A Progress Report

January 1, 1994 - June 30, 1994

NASA-UVA LIGHT AEROSPACE ALLOY AND STRUCTURES TECHNOLOGY PROGRAM (LA^2ST)

NASA-LaRC Grant NAG-1-745

Submitted to:

National Aeronautics and Space Administration
Langley Research Center
Hampton, Virginia 23681-0001

Attention:

Mr. Neil Price, Grants Officer
MS 126

For Review by:

Mr. Dennis L. Dicus, Grant Monitor
Metallic Materials Branch, MS 188A

Submitted by:

Richard P. Gangloff
Professor

Report No. UVA/528266/MSE94/116
July 25, 1994

DEPARTMENT OF MATERIALS SCIENCE
AND ENGINEERING

SCHOOL OF
ENGINEERING
& APPLIED SCIENCE

University of Virginia
Thornton Hall
Charlottesville, VA 22903

UNIVERSITY OF VIRGINIA
School of Engineering and Applied Science

The University of Virginia's School of Engineering and Applied Science has an undergraduate enrollment of approximately 1,500 students with a graduate enrollment of approximately 600. There are 160 faculty members, a majority of whom conduct research in addition to teaching.

Research is a vital part of the educational program and interests parallel academic specialties. These range from the classical engineering disciplines of Chemical, Civil, Electrical, and Mechanical and Aerospace to newer, more specialized fields of Applied Mechanics, Biomedical Engineering, Systems Engineering, Materials Science, Nuclear Engineering and Engineering Physics, Applied Mathematics and Computer Science. Within these disciplines there are well equipped laboratories for conducting highly specialized research. All departments offer the doctorate; Biomedical and Materials Science grant only graduate degrees. In addition, courses in the humanities are offered within the School.

The University of Virginia (which includes approximately 2,000 faculty and a total of full-time student enrollment of about 17,000), also offers professional degrees under the schools of Architecture, Law, Medicine, Nursing, Commerce, Business Administration, and Education. In addition, the College of Arts and Sciences houses departments of Mathematics, Physics, Chemistry and others relevant to the engineering research program. The School of Engineering and Applied Science is an integral part of this University community which provides opportunities for interdisciplinary work in pursuit of the basic goals of education, research, and public service.

A Progress Report

January 1, 1994 to June 30, 1994

NASA-UVA LIGHT AEROSPACE ALLOY AND STRUCTURES TECHNOLOGY PROGRAM (LA^2ST)

NASA-LaRC Grant NAG-1-745

Submitted to:

National Aeronautics and Space Administration
Langley Research Center
Hampton, Virginia 23665

Attention:

Mr. Neil Price
Grants Officer
MS 126

For Review by:

Mr. Dennis L. Dicus
Grant Monitor
Metallic Materials Branch, MS 188A

Submitted by:

Richard P. Gangloff
Professor
Department of Materials Science and Engineering
School of Engineering and Applied Science
University of Virginia

Report No. UVA/528266/MS94/116
July 25, 1994

NASA-UVA LIGHT AEROSPACE ALLOY AND STRUCTURES TECHNOLOGY PROGRAM

LA^2ST

Program Director:

Richard P. Gangloff

Co-principal Investigators:

Carl T. Herakovich
John R. Scully
Edgar A. Starke, Jr.
Glenn E. Stoner
John A. Wert

NASA-LaRC Grant Monitor:

Dennis L. Dicus

TABLE OF CONTENTS

TABLE OF CONTENTS (continued)

NASA-UVa LIGHT AEROSPACE ALLOY AND STRUCTURES TECHNOLOGY PROGRAM

(LA^2ST)

EXECUTIVE SUMMARY

The NASA-UVa Light Aerospace Alloy and Structures Technology (LA^2ST) Program was initiated in 1986 and continues with a high level of activity. Projects are being conducted by graduate students and faculty advisors in the Department of Materials Science and Engineering, as well as in the Department of Civil Engineering and Applied Mechanics, at the University of Virginia. This work is funded by the NASA-Langley Research Center under Grant NAG-1-745. Here, we report on progress achieved between January 1 and June 30, 1994. These results were presented at the Fifth Annual NASA-UVa LA^2ST Grant Review Meeting held at the Langley Research Center in July of 1994.

The objective of the LA^2ST Program is to conduct interdisciplinary graduate student research on the performance of next generation, light-weight aerospace alloys, composites and thermal gradient structures in collaboration with NASA-Langley researchers. Specific technical objectives are presented for each research project. We generally aim to produce relevant data and basic understanding of material mechanical response, environmental/corrosion behavior, and microstructure; new monolithic and composite alloys; advanced processing methods; new solid and fluid mechanics analyses; measurement and modeling advances; and a pool of educated graduate students for aerospace technologies.

The accomplishments presented in this report are summarized as follows.

- oo Three research areas are being actively investigated, including: (1) Mechanical and Environmental Degradation Mechanisms in Advanced Light Metals and Composites, (2) Aerospace Materials Science, and (3) Mechanics of Materials and Composites for Light Aerospace Structures.

- oo Ten research projects are being conducted by 7 PhD and 5 MS level graduate students, with 6 faculty members from 2 departments in the School of Engineering and Applied Science at UVa. Each project is

planned and executed in conjunction with a specific branch and technical monitor at NASA-LaRC.

oo Two undergraduates are conducting research in the Metallic Materials Branch at NASA-LaRC during the Summer of 1994. No undergraduates are currently participating in LA^{2}ST research at UVa.

oo Collective accomplishments between January and June of 1994 include: 9 journal or proceedings publications, 2 NASA progress reports, 9 presentations at national technical meetings, 1 MS thesis and 2 PhD dissertations. One student graduated during this reporting period with the Masters of Science Degree and two graduated with the Doctor of Philosophy Degree, each in Materials Science and Engineering at UVa. The LA^{2}ST totals since 1986 are 80 publications (43 archival journal or book publications), 17 PhD dissertations or MS theses, 90 external technical presentations, 17 NASA progress reports, and 3 NASA Contractor Reports. Since 1986, 29 graduate students, including 26 citizens of the United States, have been involved with LA^{2}ST research; 17 have received the MS or PhD degree. Four post-doctoral research associates have participated in LA^{2}ST research. A total of 12 different faculty have worked on the LA^{2}ST program.

oo ***Research on mechanisms of localized corrosion and environmental fracture in Al-Cu-Li-Mg-Ag alloy X2095 and compositional variations*** identified environmental conditions which result in subcritical crack growth in alloy 2095 under constant immersion conditions. The necessary hardware and software have been configured for real-time monitoring of crack length and control of applied stress intensity during environmental cracking under controlled electrochemical conditions. In the next reporting period, this system will be used to quantify crack propagation rates at constant stress intensity levels for various Al–Li–Cu alloys and tempers in selected electrolytes.
(Project 4)

oo ***Research on hydrogen interactions with Al-Li alloys and hydrogen embrittlement of AA2090*** has identified several hydrogen trapping sites in aluminum alloy 2090. Direct evidence was obtained for significant hydrogen absorption during SCC, particularly during alternate immersion in chloride, which strongly implicates a hydrogen-based failure mode. Thermal desorption spectroscopy measurements and hydrogen trapping analyses are being correlated with mechanical tests in order to develop a more complete understanding of hydrogen

environment-assisted cracking of aluminum-lithium alloys. (Project 5)

- oo ***Research on metastable pitting of aluminum alloys*** has identified factors which promote the transition from metastable to stable pitting for pure Al. Understanding of these factors improves our ability to design corrosion resistant alloys or devise pitting inhibitors. An evaluation has been performed on the most effective electrochemical noise method for forecasting the transition from metastable to stable pitting. Lastly, there is a limited memory associated with metastable pitting events, indicating that pitting events are not random. Moreover, feedback models that address pit stabilization need to consider pit interdependency. This work is enabled by a NASA Graduate Student Researchers Program Fellowship (Under-Represented Minority Focus). (Project 6)

- oo ***Research on the cryogenic fracture of Al-Cu-Li-In alloys*** is focusing on the microstructural fracture-path aspects of transgranular shear cracking that is uniquely prevalent in Al-Li-Cu alloys such as Vintage III 2090-T8, particularly at cryogenic temperatures. Delaminations occur along high angle boundaries (of 25 to 40° misorientation), but not necessarily at boundaries with the highest misorientation, as determined by the Electron Backscattered Pattern technique. Transgranular shear fracture, linking delaminations along grain boundaries, was qualitatively examined using the SEM/BSe technique and shown to cross numerous grain boundaries, regardless of grain orientation. (Project 2)

- oo ***Research on the fracture toughness of Weldalite™*** shows that fracture toughness variability is in part explained by modest differences in aged specimen yield strength, coupled with strength-dependent K_{JIC}, particularly for alloy 2195 with low Cu and Li. For a given aging condition, the fracture toughnesses of 4.6Li-1.5Cu (Cu/Li rich AA2095) and 4.0Li-1.0Cu (AA2195) are constant with decreasing test temperature from 25 to -185°C, in spite of higher yield strengths at the cryogenic temperature. Toughness increases substantially with reduced aging time for AA2195 at 25 and -185°C, in spite of relatively high tensile strengths. (Project 3)

- oo ***Research on the elevated temperature fracture toughness of advanced I/M aluminum alloys*** further establishes that a critical plastic strain-

controlled micromechanical model predicts the temperature independence of the initiation toughness of 2519, modified with Mg and Ag. Increasing intrinsic fracture resistance with increasing temperature prevents fracture toughness from declining at elevated temperatures. Data correlation, fracture surface analysis and plasticity considerations suggest that fracture resistance is enhanced by increasingly strain rate sensitive flow in wrought Al alloys at elevated temperatures. Deleterious strain localization between growing microvoids is retarded for alloys that harden in response to this high strain rate event, void growth is sustained to higher strains, and fracture resistance increases. Temperature-independent fracture toughness is predicted for spray formed aluminum alloy N203, based on these ideas. (Project 1)

- oo ***Research on the precipitation hardening and microstructural stability of Al-Si-Ge-Cu alloys*** shows that the cube of the average radii of SiGe precipitates in ternary and quaternary alloys coarsens linearly with time, as predicted by Lifshitz and Wagner. The yield strengths of all peak-aged alloys agree with the theoretical upper limit described by the modified Orowan equation. The volume fraction of microvoids in Al-Si-Ge decreases with increasing aging time (i.e., increasing diameter of the SiGe precipitates) at a given true strain value, and correlates with decreasing tensile ductility. The critical strain to nucleate cavities, measured by a density technique, corresponds approximately to a theoretical prediction of the Brown and Stobbs energy-based cavity nucleation model. (Project 8)

- oo ***Research to evaluate wide-panel aluminum alloy extrusions*** has developed models to predict the stress axis orientation dependence of the average Taylor factor and precipitate strengthening. Combining these models enables an accurate prediction of the yield strength anisotropy in aluminum alloys. Wide and integrally stiffened panels of two Al-Li-Cu-Mg-Ag alloys (AA2195 and AA2096 cast by Reynolds Metals) were extruded in the former USSR, and are available for laboratory characterizations under LA^{2}ST auspices. (Project 7)

- oo ***Research to incorporate environmental effects into fracture mechanics fatigue life prediction codes such as NASA FLAGRO*** is progressing in two directions.

++ Environmental fatigue cracking in the 7075-T6 (S-L)/NaCl system is adequately described for life prediction by linear superposition for prolonged load-cycle periods, and by a time-independent upper bound relationship between da/dN and ΔK for moderate loading times. Environmental fatigue is independent of crack orientation in contrast to SCC. On a detailed level, the frequency-dependence of da/dN is mild, but complex; the rate of rising load (or rise-time, t_R) dictates the enhancement, with da/dN proportional to $t_R^{-0.1}$. Various 7000-T6 alloys exhibit different frequency dependencies, with the f- and alloy-dependencies of da/dN speculatively rationalized based on a crack tip hydrogen diffusion model.. (Project 9a)

++ An undergraduate team-research project yielded a NASA-Contractor Report and Fortran computer program that estimate environmental effects on time-dependent fatigue crack propagation kinetics. The program has the capability for: (1) digitizing literature data into an ASCII file, (2) predicting environmental da/dN based on the Wei-Landes linear superposition model of mechanical fatigue with stress corrosion cracking, and (3) empirically relating da/dN to stress intensity range by regression and interpolation analyses of input data in conjunction with five literature fatigue crack growth relationships. This program was written compatibly with NASA-FLAGRO and bench-mark tested. These methods are not, however, sufficient to broadly predict environmental fatigue in aerospace materials and aggressive environments. (Project 9b)

INTRODUCTION

Background

In 1986 the Metallic Materials Branch in the Materials Division of the NASA-Langley Research Center initiated sponsorship of graduate student engineering and scientific research in the Department of Materials Science and Engineering at the University of Virginia[1]. This work emphasized the mechanical and corrosion behavior of light aerospace alloys, particularly Al-Li-Cu based compositions, in aggressive aerospace environments[2-4].

In the Fall of 1988, the scope of this program increased to incorporate research at UVa on the development and processing of advanced aerospace materials[5]. Additional funding was provided by the Metallic Materials and Mechanics of Materials Branches at NASA-LaRC. In early 1989 the program was further enhanced to include interdisciplinary work on solid mechanics and thermal structures, with funding from several Divisions within the Structures Directorate at NASA-LaRC[6]. The Departments of Civil Engineering (Applied Mechanics Program) and of Mechanical and Aerospace Engineering at UVa participated in this expanded program. With this growth, the NASA-UVa Light Aerospace Alloy and Structures Technology Program (or LA^{2}ST Program) was formed within the School of Engineering and Applied Science at UVa.

Since 1989, the LA^{2}ST program has operated with full participation from 6 to 12 faculty and 10 to 15 graduate students, yearly, as outlined in the last nine progress reports[7-16] and five grant renewal proposals[17-21]. Some contraction in the scope of the LA^{2}ST Program occurred in 1993, with the elimination of two programs in solid mechanics and thermal structures[20]. One of these programs was restored in 1994[21]. In mid-1994, Professor Thornton's work on thermal structures modeling was transferred from the LA^{2}ST Program to a project funded separately by a NASA-LaRC branch. Four 2-day Grant Review Meetings were held in July of 1989, 1990, 1991, and 1993 at the Langley Research Center, with over 25 faculty and graduate students from UVa participating at each meeting[15]. Since 1990, undergraduate engineering students have been involved in research projects at both NASA-

LaRC and UVa.

In October of 1991, E.A. Starke proposed a substantial enhancement to the base LA^{2}ST Program[22,23]. The objective of this supplement was to involve UVa faculty with engineering scientists from aluminum alloy producers and airframe manufacturers in a broad research program to develop aluminum alloys and composites for elevated temperature High Speed Civil Transport applications. This research began in January of 1992 and the results are separately reported.

Problem and Needs

Future aerospace structures require high performance light alloys and metal matrix composites with associated processing and fabrication techniques; new structural design methods and concepts with experimental evaluations; component reliability/durability/damage tolerance prediction procedures; and a pool of masters and doctoral level engineers and scientists. Work on advanced materials and structures must be interdisciplinary and integrated. The thermal and chemical effects of aerospace environments on light metals and composites are particularly important to material performance. Nationally, academic efforts in these areas are limited. The NASA-UVa LA^{2}ST Program addresses these needs.

LA^{2}ST Program

As detailed in the original proposal[6] and affirmed in the most recent renewal[21], faculty from the Departments of Materials Science and Engineering, Mechanical and Aerospace Engineering, and Civil Engineering and Applied Mechanics at UVa are participating in the LA^{2}ST research and education program focused on high performance, light weight, aerospace alloys and structures. We aim to develop long term and interdisciplinary collaborations between graduate students, UVa faculty, and NASA-Langley researchers.

Our research efforts are producing basic understanding of materials performance, new monolithic and composite alloys, advanced processing methods, solid and fluid mechanics analyses, and measurement advances. A major product of the LA^{2}ST program is graduate students with

interdisciplinary education and research experience in materials science, mechanics and mathematics. These advances should enable various NASA technologies.

The scope of the LA^{2}ST Program is broad. Four research areas are being investigated, including:

- oo Mechanical and Environmental Degradation Mechanisms in Advanced Light Metals and Composites,
- oo Aerospace Materials Science,
- oo Mechanics of Materials and Composites for Light Aerospace Structures,
- oo Thermal Gradient Structures.

Ten research projects are currently ongoing within three of these four areas, and are reported here. These projects involve six faculty, and twelve graduate students. Over one-half the graduate students are currently at the doctoral level (7 of 12), all but one are citizens of the United States, one is supported by the NASA Minority Grant Program, two are cosponsored by private industry, and two are conducting all research at the Langley Research Center. In each case the research provides the basis for the thesis or dissertation requirement of graduate studies at the University of Virginia. Each project is developed in conjunction with a specific LaRC researcher. Research is conducted at either UVa or LaRC, and under the guidance of UVa faculty and NASA staff. Participating students and faculty are closely identified with a NASA-LaRC branch.

Organization of Progress Report

This progress report first provides LA^{2}ST Program administrative information including statistics on the productivity of faculty and graduate student participants, a history of current and graduated students, refereed or archival publications, and a list of ongoing projects with NASA and UVa advisors.

Nine sections summarize the technical accomplishments of each

research project, emphasizing the period from January 1 to June 30, 1994. Each section contains a brief narrative of objective, recent progress, conclusions and immediate milestones; coupled with a set of visual aids presented at the Fifth Annual NASA-UVa LA^{2}ST Grant Review Meeting held at NASA-LaRC in July of 1994. The agenda of this meeting is presented in Appendix IV. Appendices I through III document grant-sponsored publications, conference participation and citations of all LA^{2}ST Progress Reports produced since 1986.

References

1. R.P. Gangloff, G.E. Stoner and M.R. Louthan, Jr., "Environment Assisted Degradation Mechanisms in Al-Li Alloys", University of Virginia, Proposal No. MS-NASA/LaRC-3545-87, October, 1986.

2. R.P. Gangloff, G.E. Stoner and R.E. Swanson, "Environment Assisted Degradation Mechanisms in Al-Li Alloys", University of Virginia, Report No. UVA/528266/MS88/101, January, 1988.

3. R.P. Gangloff, G.E. Stoner and R.E. Swanson, "Environment Assisted Degradation Mechanisms in Advanced Light Metals", University of Virginia, Report No. UVA/528266/MS88/102, June, 1988.

4. R.P. Gangloff, G.E. Stoner and R.E. Swanson, "Environment Assisted Degradation Mechanisms in Advanced Light Metals", University of Virginia, Report No. UVA/528266/MS89/103, January, 1989.

5. T.H. Courtney, R.P. Gangloff, G.E. Stoner and H.G.F. Wilsdorf, "The NASA-UVa Light Alloy Technology Program", University of Virginia, Proposal No. MS NASA/LaRC-3937-88, March, 1988.

6. R.P. Gangloff, "NASA-UVa Light Aerospace Alloy and Structures Technology Program", University of Virginia, Proposal No. MS NASA/LaRC-4278-89, January, 1989.

7. R.P. Gangloff, "NASA-UVa Light Aerospace Alloy and Structures Technology Program", University of Virginia, Report No. UVA/528266/MS90/104, August, 1989.

8. R.P. Gangloff, "NASA-UVa Light Aerospace Alloy and Structures Technology Program", University of Virginia, Report No. UVA/528266/MS90/105, December, 1989.

9. R.P. Gangloff, "NASA-UVa Light Aerospace Alloy and Structures Technology Program", UVa Report No. UVA/528266/MS90/106, June, 1990.

10. R.P. Gangloff, "NASA-UVa Light Aerospace Alloy and Structures Technology Program", UVa Report No. UVA/528266/MS91/107, January, 1991.

11. R.P. Gangloff, "NASA-UVa Light Aerospace Alloy and Structures Technology Program", UVa Report No. UVA/528266/MS91/108, July, 1991.

12. R.P. Gangloff, "NASA-UVa Light Aerospace Alloy and Structures Technology Program", UVa Report No. UVA/528266/MS92/109, January, 1992.

13. R.P. Gangloff, "NASA-UVa Light Aerospace Alloy and Structures Technology Program", UVa Report No. UVA/528266/MS93/111, July, 1992.

14. R.P. Gangloff, "NASA-UVa Light Aerospace Alloy and Structures Technology Program", UVa Report No. UVA/528266/MSE93/112, March, 1993.

15. R.P. Gangloff, "NASA-UVa Light Aerospace Alloy and Structures Technology Program", UVa Report No. UVA/528266/MSE93/113, July, 1993.

16. R.P. Gangloff, "NASA-UVa Light Aerospace Alloy and Structures Technology Program", UVa Report No. UVA/528266/MSE93/114, March, 1994.

17. R.P. Gangloff, "NASA-UVa Light Aerospace Alloy and Structures Technology Program", University of Virginia, Proposal No. MS-NASA/LaRC-4512-90, November, 1989.

18. R.P. Gangloff, "NASA-UVa Light Aerospace Alloy and Structures Technology Program", University of Virginia, Proposal No. MS-NASA/LaRC-4841-91, September, 1990.

19. R.P. Gangloff, "NASA-UVa Light Aerospace Alloy and Structures Technology Program", University of Virginia, Proposal No. MS-NASA/LaRC-5219-92, October, 1991.

20. R.P. Gangloff, "NASA-UVa Light Aerospace Alloy and Structures Technology Program", University of Virginia, Proposal No. MSE-NASA/LaRC-5691-93, November, 1992.

21. R.P. Gangloff, "NASA-UVa Light Aerospace Alloy and Structures Technology Program", Proposal No. MSE-NASA/LaRC-6074-94, University of Virginia, Charlottesville, VA, November, 1993.

22. R.P. Gangloff, E.A. Starke, Jr., J.M. Howe and F.E. Wawner, "NASA-UVa Light Aerospace Alloy and Structures Technology Program: Supplement on Aluminum Based Materials for High Speed Aircraft", University of Virginia, Proposal No. MS NASA/LaRC-5215-92, October, 1991.

23. R.P. Gangloff, E.A. Starke, Jr., J.M. Howe and F.E. Wawner, "NASA-UVa Light Aerospace Alloy and Structures Technology Program: Supplement on Aluminum Based Materials for High Speed Aircraft", University of Virginia, Proposal No. MSE NASA/LaRC-5691-93, November, 1992.

SUMMARY STATISTICS

Table I documents the numbers of students and faculty who have participated in the LA^{2}ST Program, both during this reporting period and since the program inception in 1986. Academic and research accomplishments are indicated by the degrees awarded, publications and presentations. Graduate students and research associates who participated in the LA^{2}ST Program are named in Tables II and III, respectively.

TABLE I: LA^{2}ST Program Statistics

	Current 1/1/94 to 6/30/94	Cumulative 1986 to 6/30/94
PhD Students--UVa:	6	18
--NASA-LaRC:	1	1
MS Students--UVa:	4	8
--NASA:	1	1
--VPI:	0	1
Undergraduates--UVa:	0	9
--NASA-LaRC:	2	13
Faculty--UVa:	6	11
--VPI:	0	1
Research Associates--UVa:	0	4
PhD Awarded:	2	12
MS Awarded:	1	5

TABLE I: LA²ST Program Statistics (continued)

	Current 1/1/94 to 6/30/94	Cumulative 1986 to 6/30/94
Employers--NASA:	0	2
--Federal:	1	4
--University:	0	1
--Industry:	1	5
--Next degree:	0	3
Publications:	9	80
Presentations:	9	90
Dissertations/Theses:	3	17
NASA Reports:	2	18

TABLE II

GRADUATE STUDENT PARTICIPATION IN THE NASA-UVa LA^{2}ST PROGRAM

June, 1994

POS #	GRADUATE STUDENT EMPLOYER	ENTERED PROGRAM	DEGREE COMPLETED	LANGLEY RESIDENCY	RESEARCH TOPIC	UVa/NASA-LaRC ADVISORS
1.	R. S. Piascik NASA-Langley	6/86	Ph.D. 10/89		Damage Localization Mechanisms in Corrosion Fatigue of Aluminum-Lithium Alloys	R. P. Gangloff D. L. Dicus
2.	J. P. Moran NIST	9/88	Ph.D. 12/89		An Investigation of the Localized Corrosion and Stress Corrosion Cracking Behavior of Alloy 2090	G. E. Stoner W. B. Lisagor
3.	R. G. Buchheit Sandia National Laboratories	6/87	Ph.D. 12/90		Measurements and Mechanisms of Localized Aqueous Corrosion in Aluminum-Lithium Alloys	G. E. Stoner D. L. Dicus
4.	D. B. Gundel Ph.D.-UVa	9/88	M.S. 12/90		Investigation of the Reaction Kinetics Between SiC Fibers and Titanium Matrix Composites	F. E. Wawner W. B. Brewer
5.	F. Rivet (VPI)	9/88	M.S. 12/90		Deformation and Fracture of Aluminum-Lithium Alloys: The Effect of Dissolved Hydrogen	R. E. Swanson (VPI) D. L. Dicus
6.	C. Copper Ph.D.-UVa	4/89	M.S. 12/90		Design of Cryogenic Tanks for Space Vehicles	W. D. Pilkey J. K. Haviland D. R. Rummler M.J. Shuart
7.	J. A. Wagner NASA-Langley	6/87	Ph.D.	PhD Research @ LaRC	Temperature Effects on the Deformation and Fracture of Al-Li-Cu-In Alloys	R. P. Gangloff W. B. Lisagor J. C. Newman
8.	W. C. Porr, Jr. David Taylor Naval Ship R&DC	1/88	Ph.D. 6/92		Elevated Temperature Facture of an Advanced Powder Metallurgy Aluminum Alloy	R. P. Gangloff C. E. Harris

TABLE II (continued)
GRADUATE STUDENT PARTICIPATION IN THE NASA-UVa LA^{2}ST PROGRAM
(continued)

POS #	GRADUATE STUDENT EMPLOYER	ENTERED PROGRAM	DEGREE COMPLETED	LANGLEY RESIDENCY	RESEARCH TOPIC	UVa/NASA-LaRC ADVISORS
9.	J. B. Parse Consultant	9/88	Ph.D. 6/92		Quantitative Characterization of the Spatial Distribution of Particles in Materials	J. A. Wert D. R. Tenney
10.	D. C. Slavik Knolls Atomic Power Laboratory	9/89	Ph.D. 6/93		Environment Enhanced Fatigue of Advanced Aluminum Alloys and Composites	R. P. Gangloff D. L. Dicus
11.	C. L. Lach NASA-Langley	9/89	M.S.	MS Research @LaRC	Effect of Temperature on the Fracture Toughness of Weldalite^{TM} 049	R. P. Gangloff W. B. Lisagor
12.	R. J. Kilmer General Motors	11/89	Ph.D. 9/93		Effect of Zn Additions on the Environmental Stability of Alloy 8090	G. E. Stoner W. B. Lisagor
13.	M. F. Coyle	12/89	Ph.D.		Visoplastic Response of High Temperature Structures	E. A. Thornton J. H. Starnes, Jr.
14.	C. J. Lissenden University of Kentucky; Engineering Mechanics	9/90	Ph.D. 6/93		Inelastic Response of Metal Matrix Composites Under Biaxial Loading	C. T. Herakovich M. J. Pindera W. S. Johnson
15.	C. Cooper AMP Incorporated	1/91	Ph.D. 6/93		Shell Structures Analytical Modeling	W. D. Pilkey J. K. Haviland M. Shuart J. Stroud

TABLE II (continued)
GRADUATE STUDENT PARTICIPATION IN THE NASA-UVa LA^{2}ST PROGRAM
(continued)

16.	Douglas Wall	4/91	Ph.D.		Measurements and Mechanisms of Localized Corrosion in Al-Li-Cu Alloys	G. E. Stoner D. L. Dicus
17.	S. W. Smith	4/91	Ph.D.		Hydrogen Interactions with Al-Li Alloys	J. R. Scully W. B. Lisagor
18.	D. B. Gundel Wright Laboratories US Air Force	4/91	Ph.D. 9/94		Effect of Thermal Exposure on the Mechanical Properties of Titanium/SiC Composites	F. E. Wawner W. B. Brewer
19.	K. McCarthy	5/91	M.S. 6/93 (Nonthesis)		Shell Structures Analytical Modeling	W. D. Pilkey M. J. Shuart J. Stroud
20.	M. Lyttle	12/91	M.S. 12/93		Superplasticity in Al-Li-Cu Alloys	J. A. Wert T. T. Bales
21.	T. Johnson NASA-LaRC	12/91	Ph.D. 6/93	(NASA Minority Grantee)	Shell Structures Analytical Modeling	W. D. Pilkey M. J. Shuart J. Stroud
22.	S. T. Pride Rohm and Haas	12/91	Ph.D. 6/94	(NASA Minority Grantee)	Metastable Pitting of Al Alloys	J. R. Scully D. L. Dicus
23.	M. A. Rowley	1/92	M.S. 12/93	(UVa AEP Sponsored)	Viscoplasticity of Metals	E. A. Thornton J. H. Starnes, Jr.
24.	M. J. Haynes	9/92	M.S.		Elevated Temperature Fracture of Advanced IM Al Alloys	R. P. Gangloff TBD
25.	M. Mason	9/92	M.S.		Environmental Effects in Fatigue Life Prediction	R. P. Gangloff R. S. Piascik

TABLE II (continued)

GRADUATE STUDENT PARTICIPATION IN THE NASA-UVa LA^{2}ST PROGRAM

(continued)

26.	H.J. Koenigsmann	6/93	Ph.D.	Precipitation Hardening and Microstructural Stability in Al-Si-Ge-Cu	E.A. Starke, Jr. W.B. Lisagor
27.	E. Richey	9/93	M.S.	Computer Modeling of Environmental Fatigue Crack Propagation	R.P. Gangloff R.S. Piascik
28.	M. Lyttle	1/94	Ph.D.	Wide-Panel Aluminum Alloy Extrusions	J.A. Wert W.B. Lisagor
29.	Z. Gasem	1/94	Ph.D.	Time-Dependent Environmental Fatigue in 7000-Series Al Alloys	R.P. Gangloff R.S. Piascik

TABLE III

Post-Doctoral Research Associate Participation in NASA-UVA LA^{2}ST Program

Pos #	Research Assoc.	Tenure	Research	Supervisor
1.	Yang Leng	3/89 to 12/91	Elevated Temperature Deformation and Fracture of PM AL Alloys and Composites	R. P. Gangloff
2.	Farshad Mizadeh	7/89 to 12/91	Deformation of Metal Matrix Composites	C. T. Herakovich and Marek-Jerzy Pindera
3.	A.K.Mukhopadhyay	6/91 to 6/92	Aluminum Alloy Development	E. A. Starke, Jr.
4.	Sang-Shik Kim	12/91 to 2/94	Environmental Fatigue Life Prediction	R. P. Gangloff

GRANT PUBLICATIONS: (REFEREED JOURNALS, ARCHIVAL VOLUMES AND NASA CONTRACTOR REPORTS)

The following papers are based on research conducted under LA^{2}ST Program support, and are published in the referred or archival literature.

43. S.T. Pride, J.R. Scully and J.L. Hudson, "Analysis of Electrochemical Noise from Metastable Pitting in Al, Aged Al-2%Cu and AA 2024-T3, ASTM STP," in Electrochemical Noise Methods in Corrosion, ASTM, Philadelphia, PA, in review (1994).

42. R.P. Gangloff, "Corrosion Fatigue Cracking", in Manual on Corrosion Tests: Application and Interpretation, R. Baboian, ed., ASTM, Philadelphia, PA, in review (1994).

41. S.S. Kim and R.P. Gangloff, "Localized Deformation Control of Elevated Temperature Fracture in Submicron Grain Aluminum with Dispersoids", Materials Science and Engineering A, in review (1994).

40. R.G. Buchheit, G.E. Stoner and G.J. Shiflet, "Corrosion Properties of a Rapidly Solidified $Al_{90}Fe_5Gd_5$ Alloy", J. Electrochem. Soc., in revision (1994).

39. R.S. Piascik and R.P. Gangloff, "Environmental Fatigue of an Al-Li-Cu Alloy: Part III - Modeling of Crack Tip Hydrogen Damage", Metallurgical Transactions A, in revision (1994).

38. S.T. Pride, J.R. Scully and J.L. Hudson, "Metastable Pitting of Aluminum and Criteria for the Transition to Stable Pit Growth," Journal of the Electrochemical Society, in press (1994).

37. E.A. Thornton and J.D. Kolenski, "Viscoplastic Response of Structures with Intense Local Heating", Journal of Aerospace Engineering, in press (1994).

36. E.A. Thornton, M.F. Coyle, and R.N. McLeod, "Experimental Study of Plate Buckling Induced by Spatial Temperature Gradients," Journal of Thermal Stresses, in press (1994).

35. Edward Richey, III, A.W. Wilson, J.M. Pope, and R.P. Gangloff, "Computer Modeling the Fatigue Crack Growth Rate Behavior of Metals in Corrosive Environments", NASA CR, NASA-Langley Research Center, in press (1994).

34. R.G. Buchheit, J.P. Moran and G.E. Stoner, "The Electrochemical Behavior of the T_1 (Al_2CuLi) Intermetallic Compound and Its Role in Localized Corrosion of Al-3Cu-2Li Alloys", Corrosion, Vol. 50, pp. 120-130 (1994).

33. D. Gundel, P. Taylor and F. Wawner, "The Fabrication of Thin Oxide Coatings on Ceramic Fibers by a Sol-Gel Technique", Journal of Materials Science, Vol. 29, pp. 1795-1800 (1994).

32. M.T. Lyttle and J.A. Wert, "Simulative Modeling of Continuous Recrystallization of Aluminum Alloys", in Advances in Hot Deformation Textures and Microstructures, J.J. Jonas, T.R. Bieler and K.J. Bowman, eds., TMS-AIME, Warrendale, PA, pp. 373-383 (1994).

31. M.T. Lyttle and J.A. Wert, "Modeling of Continuous Recrystallization in Aluminum Alloys," Journal of Materials Science, Vol. 29, pp. 3342-3350 (1994).

30. R.P. Gangloff, R.S. Piascik, D.L. Dicus and J.C. Newman, "Fatigue Crack Propagation in Aerospace Aluminum Alloys", Journal of Aircraft, Vol. 31, pp. 720-729 (1994).

29. W.C. Porr, Jr. and R.P. Gangloff, "Elevated Temperature Fracture of RS/PM Alloy 8009: Part I-Fracture Mechanics Behavior", Metall. Trans. A, Vol. 25A, pp. 365-379 (1994).

28. E.A. Thornton, "Thermal Buckling of Plates and Shells," Applied Mechanics Reviews, Vol. 46, No. 10, pp. 485-506 (1993).

27. R.P. Gangloff and Sang Shik Kim, "Environment Enhanced Fatigue Crack Propagation in Metals: Inputs to Fracture Mechanics Life Prediction", NASA CR-191538, NASA-Langley Research Center, Hampton, VA (1993).

26. R.S. Piascik and R.P. Gangloff, "Environmental Fatigue of an Al-Li-Cu Alloy: Part II - Microscopic Hydrogen Cracking Processes", Metall. Trans. A, Vol. 24A, pp. 2751-2762 (1993).

25. D.C. Slavik, J.A. Wert and R.P. Gangloff, "Determining Fracture Facet Crystallography Using Electron Back Scatter Patterns and Quantitative Tilt Fractography", Journal of Materials Research, Vol. 8, pp. 2482-2491 (1993).

24. D.C. Slavik, C.P. Blankenship, Jr., E.A. Starke, Jr. and R.P. Gangloff, "Intrinsic Fatigue Crack Growth Rates for Al-Li-Cu-Mg Alloys in Vacuum", Metall. Trans. A, Vol. 24A, pp. 1807-1817 (1993).

23. D. Gundel and F. Wawner, "The Influence of Defects on the Response of Titanium/SiC Fiber Composites to Thermal Exposure", Composites Engineering, Vol. 4, No. 1, pp. 47-65 (1993).

22. J.B. Parse and J.A. Wert, "A Geometrical Description of Particle Distributions in Materials", Modeling and Simulation in Materials Science and Engineering, Vol. 1, pp. 275-296 (1993).

21. D.C. Slavik and R.P. Gangloff, "Microscopic Processes of Environmental Fatigue Crack Propagation in Al-Li-Cu Alloy 2090", in Fatigue '93, Vol. II, J.-P. Bailon and J.I. Dickson, eds., EMAS, West Midlands, UK, pp. 757-765 (1993).

20. C.J. Lissenden, M-J. Pindera and C.T. Herakovich, "Response of SiC/Ti Tubes Under Biaxial Loading in the Presence of Damage," Damage Mechanics in Composites, D.H. Allen and D.C. Lagoudas, Eds., ASME-AMD-Vol. 150, pp. 73-90 (1992).

19. J.A. Wagner and R.P. Gangloff, "Fracture Toughness of Al-Li-Cu-In Alloys", Scripta Metallurgica et Materialia, Vol. 26, pp. 1779-1784 (1992).

18. R.G. Buchheit, Jr., J.P. Moran, F.D. Wall, and G.E. Stoner, "Rapid Anodic Dissolution Based SCC of 2090 (Al-Li-Cu) by Isolated Pit Solutions," Parkins Symposium on Fundamental Aspects of Stress Corrosion Cracking, S.M. Bruemmer, E.I. Meletis, R.H. Jones, W.W. Gerberich, F.P. Ford and R.W. Staehle, eds., TMS-AIME, Warrendale, PA, p. 141 (1992).

17. J.P. Moran, R.G. Buchheit, Jr., and G.E. Stoner, "Mechanisms of SCC of Alloy 2090 (Al-Li-Cu) - A Comparison of Interpretations from Static and Slow Strain Rate Techniques", Parkins Symposium on Fundamental Aspects of Stress Corrosion Cracking, S.M. Bruemmer, E.I. Meletis, R.H. Jones, W.W. Gerberich, F.P. Ford and R.W. Staehle, eds., TMS-AIME, Warrendale, PA, p. 159 (1992).

16. R.J. Kilmer, T.J. Witters and G.E. Stoner, "Effect of Zn Additions on the Precipitation Events and Implications to Stress Corrosion Cracking Behavior in Al-Li-Cu-Mg-Zn Alloys", Proceedings of the Sixth International Al-Li Conference, M. Peters and P.J. Winkler, eds., DGM Informationsgesellschaft, Verlag, pp. 755-760 (1992).

15. C.T. Herakovich and J.S. Hidde, "Response of Metal Matrix Composites with Imperfect Bonding", Ultramicroscopy, Vol. 40, pp. 215-228 (1992).

14. R.G. Buchheit, Jr., F.D. Wall, G.E. Stoner and J.P. Moran, "Stress Corrosion Cracking of Al-Li-Cu-Zr Alloy 2090 in Aqueous Cl^- and Mixed Cl^-/CO_3^{-2} Environments", CORROSION/91, Paper No. 99, NACE, Houston, TX (1991).

13. R.P. Gangloff, D.C. Slavik, R.S. Piascik and R.H. Van Stone, "Direct Current Electrical Potential Measurement of the Growth of Small Fatigue Cracks", in Small Crack Test Methods, ASTM STP 1149, J.M. Larsen and J.E. Allison, eds., ASTM, Philadelphia, PA, pp. 116-168 (1992).

12. R.J. Kilmer and G.E. Stoner, "The Effect of Trace Additions of Zn on the Precipitation Behavior of Alloy 8090 During Artificial Aging", Proceedings, Light Weight Alloys for Aerospace Applications II, E.W. Lee, ed., TMS-AIME, Warrendale, PA, pp. 3-15, 1991.

11. W.C. Porr, Jr., Anthony Reynolds, Yang Leng and R.P. Gangloff, "Elevated Temperature Cracking of RSP Aluminum Alloy 8009: Characterization of the Environmental Effect", Scripta Metallurgica et Materialia, Vol. 25, pp. 2627-2632 (1991).

10. J. Aboudi, J.S. Hidde and C.T. Herakovich, "Thermo-mechanical Response Predictions for Metal Matrix Composites", in Mechanics of Composites at Elevated and Cryogenic Temperatures, S.N. Singhal, W.F. Jones and C.T. Herakovich, eds., ASME AMD, Vol. 118, pp. 1-18 (1991).

9. R.S. Piascik and R.P. Gangloff, "Environmental Fatigue of an Al-Li-Cu Alloy: Part I - Intrinsic Crack Propagation Kinetics in Hydrogenous Environments", Metallurgical Transactions A, Vol. 22A, pp. 2415-2428 (1991).

8. W.C. Porr, Jr., Y. Leng, and R.P. Gangloff, "Elevated Temperature Fracture Toughness of P/M Al-Fe-V-Si", in Low Density, High Temperature Powder Metallurgy Alloys, W.E. Frazier, M.J. Koczak, and P.W. Lee, eds., TMS-AIME, Warrendale, PA, pp. 129-155 (1991).

7. Yang Leng, William C. Porr, Jr. and Richard P. Gangloff, "Time Dependent Crack Growth in P/M Al-Fe-V-Si at Elevated Temperatures", Scripta Metallurgica et Materialia, Vol. 25, pp. 895-900 (1991).

6. R.J. Kilmer and G.E. Stoner, "Effect of Zn Additions on Precipitation During Aging of Alloy 8090", Scripta Metallurgica et Materialia, Vol. 25, pp. 243-248 (1991).

5. D.B. Gundel and F.E. Wawner, "Interfacial Reaction Kinetics of Coated SiC Fibers", Scripta Metallurgica et Materialia, Vol. 25, pp. 437-441 (1991).

4. R.G. Buchheit, Jr., J.P. Moran and G.E. Stoner, "Localized Corrosion Behavior of Alloy 2090-The Role of Microstructural Heterogeneity", Corrosion, Vol. 46, pp. 610-617 (1990).

3. Y. Leng, W.C. Porr, Jr. and R.P. Gangloff, "Tensile Deformation of 2618 and Al-Fe-Si-V Aluminum Alloys at Elevated Temperatures", Scripta Metallurgica et Materialia, Vol. 24, pp. 2163-2168 (1990).

2. R.P. Gangloff, "Corrosion Fatigue Crack Propagation in Metals", in Environment Induced Cracking of Metals, R.P. Gangloff and M.B. Ives, eds., NACE, Houston, TX, pp. 55-109 (1990).

1. R.S. Piascik and R.P. Gangloff, "Aqueous Environment Effects on Intrinsic Corrosion Fatigue Crack Propagation in an Al-Li-Cu Alloy", in Environment Induced Cracking of Metals, R.P. Gangloff and M.B. Ives, eds., NACE, Houston, TX, pp. 233-239 (1990).

COMPLETED PROJECTS: (1986 to present reporting period)

1. DAMAGE LOCALIZATION MECHANISMS IN CORROSION FATIGUE OF ALUMINUM-LITHIUM ALLOYS
   Faculty Investigator: R.P. Gangloff
   Graduate Student: Robert S. Piascik
   Degree: PhD
   UVa Department: Materials Science and Engineering (MS&E)
   NASA-LaRC Contact: D. L. Dicus (Metallic Materials)
   Start Date: June, 1986
   Completion Date: November, 1989
   Employment: NASA-Langley Research Center

2. AN INVESTIGATION OF THE LOCALIZED CORROSION AND STRESS CORROSION CRACKING BEHAVIOR OF ALLOY 2090 (Al-Li-Cu)
   Faculty Investigator: Glenn E. Stoner
   Graduate Student: James P. Moran
   Degree: PhD
   UVa Department: MS&E
   NASA-LaRC Contact: W.B. Lisagor (Metallic Materials)
   Start Date: September, 1988
   Completion Date: December, 1989
   Co-Sponsor: ALCOA
   Employment: ALCOA Laboratories

3. MECHANISMS OF LOCALIZED CORROSION IN AL-LI-CU ALLOY 2090
   Faculty Investigator: G.E. Stoner
   Graduate Student: R.G. Buchheit
   Degree: PhD
   UVa Department: MS&E
   NASA-LaRC Contact: D.L. Dicus (Metallic Materials)
   Start Date: June, 1987
   Completion Date: December, 1990
   Cosponsor: Alcoa
   Employment: Sandia National Laboratories

4. DEFORMATION AND FRACTURE OF ALUMINUM-LITHIUM ALLOYS: THE EFFECT OF DISSOLVED HYDROGEN
   Faculty Investigator: R.E. Swanson (VPI)
   Graduate Student: Frederic C. Rivet
   Degree: MS
   VPI Department: Materials Engineering
   NASA-LaRC Contact: D.L. Dicus (Metallic Materials)
   Start Date: September, 1988
   Completion Date: December, 1990
   Employment: Not determined

5. INVESTIGATION OF THE REACTION KINETICS BETWEEN SiC FIBERS AND SELECTIVELY ALLOYED TITANIUM MATRIX COMPOSITES AND DETERMINATION OF THEIR MECHANICAL PROPERTIES

Faculty Investigator: F.E. Wawner
Graduate Student: Douglas B. Gundel
Degree: MS
UVa Department: MS&E
NASA-LaRC Contact: D.L. Dicus and W.B. Brewer (Metallic Materials)

Start Date: January, 1989
Completion Date: December, 1990
Employment: Graduate School, University of Virginia; PhD candidate on LA^{2}ST Program; Department of Materials Science

6. DESIGN OF CRYOGENIC TANKS FOR SPACE VEHICLES

Faculty Investigators: W.D. Pilkey and J.K. Haviland
Graduate Student: Charles Copper
Degree: MS
UVa Department: Mechanical and Aerospace Engineering (MAE)
NASA-LaRC Contact: D.R. Rummler (Structural Mechanics Division), R.C. Davis and M.J. Shuart (Aircraft Structures)

Start Date: April, 1989
Completion Date: December, 1990
Employment: Graduate School, University of Virginia; PhD candidate on NASA-Headquarters sponsored program; Department of Mechanical and Aerospace Engineering

7. ELEVATED TEMPERATURE FRACTURE OF AN ADVANCED RAPIDLY SOLIDIFIED, POWDER METALLURGY ALUMINUM ALLOY

Faculty Investigator: R.P. Gangloff
Graduate Student: William C. Porr, Jr.
Degree: PhD
UVa Department: MS&E
NASA-LaRC Contact: C.E. Harris (Mechanics of Materials)
Start Date: January, 1988
Completion Date: June, 1992
Employment: David Taylor Naval Ship R&D Center

8. QUANTITATIVE CHARACTERIZATION OF THE SPATIAL DISTRIBUTION OF PARTICLES IN MATERIALS: APPLICATION TO MATERIALS PROCESSING
   Faculty Investigator: John A. Wert
   Graduate Student: Joseph Parse
   Degree: PhD
   UVa Department: MS&E
   NASA-LaRC Contact: D.R. Tenney (Materials Division)
   Start Date: September, 1988
   Completion Date: June, 1992
   Employment: Private Consultant

9. ENVIRONMENTAL FATIGUE CRACK GROWTH AND CRACKING MECHANISMS IN Al-Li-Cu Alloy 2090
   Faculty Investigator: R.P. Gangloff
   Graduate Student: Donald C. Slavik
   Degree: PhD
   UVa Department: MS&E
   NASA-LaRC Contact: D.L. Dicus (Metallic Materials)
   Start Date: September, 1989
   Completion Date: June, 1993
   Employment: Knolls Atomic Power Laboratory

10. INELASTIC DEFORMATION OF METAL MATRIX COMPOSITES UNDER BIAXIAL LOADING
   Faculty Investigators: Carl T. Herakovich and Marek-Jerzy Pindera
   Graduate Student: Mr. Clifford J. Lissenden
   Degree: PhD
   UVa Department: Civil Engineering and the Applied Mechanics Program
   NASA-LaRC Contact: W.S. Johnson (Mechanics of Materials)
   Start Date: September, 1990
   Completion Date: June, 1993
   Employment: University of Kentucky, Department of Engineering Mechanics

11. EFFECT OF TEMPERATURE ON THE RESPONSE OF METALLIC SHELL STRUCTURES
   Faculty Investigators: W.D. Pilkey and J.K. Haviland
   Graduate Student: Karen McCarthy
   Degree: MS (non-thesis)
   Graduate Student: Theodore Johnson (NASA Minority Grantee)
   Degree: PhD
   Employment: NASA-LaRC

Graduate Student: Charles Copper
Degree: PhD
Employment: AMP Incorporated
UVa Department: MAE
NASA-LaRC Contact: M.J. Shuart and Jeffrey Stroud (Aircraft Structures)
Start Date: April, 1991
Completion Date: May, 1993

12. EFFECTS OF Zn ADDITIONS ON THE PRECIPITATION AND STRESS CORROSION CRACKING BEHAVIOR OF ALLOY 8090
Faculty Investigator: Glenn E. Stoner
Graduate Student: Raymond J. Kilmer
Degree: PhD
Department: MS&E
NASA-LaRC Contact: W.B. Lisagor (Metallic Materials)
Start Date: September, 1989
Completion Date: September, 1993
Cosponsor: Alcoa
Employment: General Motors

13. PROCESSING AND SUPERPLASTIC PROPERTIES OF WELDALITE™ SHEET
Faculty Investigator: John A. Wert
Graduate Student: Mark Lyttle
Degree: MS
Department: MS&E
NASA-LaRC Contact: T.T. Bales (Metallic Materials)
Start Date: September, 1991
Completion Date: December, 1993
Employment: Graduate School, University of Virginia; PhD Candidate in Materials Science and Engineering

15. METASTABLE PITTING OF Al ALLOYS AND CRITERIA FOR THE TRANSITION TO STABLE PITTING
Faculty Investigators: John R. Scully and J.L. Hudson
Graduate Student: Sheldon T. Pride; PhD Candidate
Department: Chemical Engineering
NASA-LaRC Contact: D.L. Dicus (Metallic Materials)
Start Date: September, 1991
Completion Date: May, 1994
Cosponsor: NASA Graduate Student Researchers Program; Under Represented Minority Emphasis
Employment: Rohm and Haas Chemical Company

15. THE EFFECT OF THERMAL EXPOSURE ON THE MECHANICAL PROPERTIES OF Ti-1100/SCS-6 COMPOSITES

Faculty Investigator: F.E. Wawner
Graduate Student: Douglas B. Gundel; PhD candidate
UVa Department: MS&E
NASA-LaRC Contact: D.L. Dicus and W.B. Brewer (Metallic Materials)
Start Date: April, 1991
Completion Date: June, 1994
Employment: Wright Laboratories (WL/MLLM), US Air Force Materials Laboratory

ADMINISTRATIVE PROGRESS

Faculty Participation

Professor Herakovich resumed participation in the 1994 program, with a research project examining damage evolution in a polymeric composite under strain. Professor Thornton transferred his research program on thermal structures modeling from the LA^{2}ST Program to individual sponsorship by a NASA-Langley branch.

Brochure

The brochure prepared in March of 1991 was employed to advertise the LA^{2}ST program during this reporting period. Copies were distributed nationally to stimulate graduate and undergraduate recruitment.

Graduate Student Recruitment

The LA^{2}ST Program has encountered no problems in recruiting the best graduate students entering the participating Departments at UVa, and in sufficient numbers to achieve our education and research objectives. Professor Gangloff recently recruited Mr. Sean Hayes into the PhD program in Materials Science and Engineering at UVa under LA^{2}ST sponsorship. Mr. Hayes will receive the MS degree in Materials Science and Engineering at Lehigh University in August 1994, and will enter UVa in September. His LA^{2}ST research will focus on elevated temperature and hydrogen effects on the fracture toughness of α/β titanium alloys.

Undergraduate Research Participation

In April of 1990, the LA^{2}ST Program was increased in scope to include undergraduate engineering students. Four students worked at NASA-LaRC during the Summer of 1990, none were recruited for the 1991 program, and seven were successfully recruited to work at NASA-LaRC during the Summer of 1992. Each student was a rising senior in an engineering or science major closely related to aerospace materials and mechanics. Represented universities have included Harvard, Georgia Institute of Technology, Virginia Polytechnic Institute, Duke, the University of Missouri, California Polytechnical Institute, and North Carolina State University.

Professor Glenn E. Stoner assumed responsibility for the 1993 Summer

Undergraduate Program. No qualified applicants were identified for 1993 Summer employment at NASA-LaRC. During this reporting period, he successfully recruited two undergraduates in Materials Science and Engineering at Duke and North Carolina State University. These students are currently conducting research at the Langley Research Center.

CURRENT PROJECTS

MECHANICAL AND ENVIRONMENTAL DEGRADATION MECHANISMS IN ADVANCED LIGHT METALS AND COMPOSITES

1. ELEVATED TEMPERATURE DAMAGE TOLERANCE OF ADVANCED INGOT METALLURGY WROUGHT ALUMINUM ALLOYS
   Faculty Investigator: R.P. Gangloff
   Graduate Student: Michael J. Haynes
   UVa Department: MS&E
   NASA-LaRC Contact: To be determined (Metallic Materials)
   Start Date: September, 1992
   Completion Date: September, 1994
   Project #1

2. CRYOGENIC TEMPERATURE EFFECTS ON THE DEFORMATION AND FRACTURE OF Al-Li-Cu and Al-Li-Cu-In ALLOYS
   Faculty Investigator: R.P. Gangloff
   Graduate Student: John A. Wagner; PhD candidate and NASA-LaRC employee
   UVa Department: MS&E
   NASA-LaRC Contacts: W.B. Lisagor (Metallic Materials) and J.C. Newman (Mechanics of Materials)
   Start Date: June, 1987
   Anticipated Completion Date: December, 1994
   Project #2

3. THE EFFECTS OF CRYOGENIC TEMPERATURE AND AGING ON THE FRACTURE TOUGHNESS OF WELDALITE™ X2095
   Faculty Investigator: R.P. Gangloff
   Graduate Student: Cynthia L. Lach; MS candidate and NASA-LaRC employee
   UVa Department: MS&E
   NASA-LaRC Contacts: W.B. Lisagor (Metallic Materials)
   Start Date: August, 1990
   Anticipated Completion Date: December, 1994
   Project #3

4. MECHANISMS OF LOCALIZED CORROSION IN 2090 AND X2095
   Faculty Investigator: G.E. Stoner
   Graduate Student: Douglas Wall; PhD candidate
   UVa Department: MS&E
   NASA-LaRC Contact: M.S. Domack (Metallic Materials)
   Start Date: April, 1991
   Completion Date: December, 1994
   Cosponsor: Reynolds Metals Company (A. Cho)
   Project #4

5. HYDROGEN INTERACTIONS IN ALUMINUM-LITHIUM ALLOYS AND HYDROGEN EMBRITTLEMENT OF AA2090
   Faculty Investigator: John R. Scully
   Graduate Student: Stephen W. Smith; PhD Candidate
   Department: MS&E
   NASA-LaRC Contact: W.B. Lisagor and D.L. Dicus (Metallic Materials)
   Start Date: April, 1991
   Anticipated Completion Date: December, 1994
   Cosponsor: Virginia CIT
   Project #5

6. METASTABLE PITTING OF Al ALLOYS AND CRITERIA FOR THE TRANSITION TO STABLE PITTING
   Faculty Investigators: John R. Scully and J.L. Hudson
   Graduate Student: Sheldon T.; PhD Candidate
   Department: Chemical Engineering
   NASA-LaRC Contact: D.L. Dicus (Metallic Materials)
   Start Date: September, 1991
   Anticipated Completion Date: September, 1994
   Cosponsor: NASA Graduate Student Researchers Program; Under Represented Minority Emphasis
   Project #6

AEROSPACE MATERIALS SCIENCE

7. EVALUATION OF WIDE-PANEL ALUMINUM ALLOY EXTRUSIONS
   Faculty Investigator: John A. Wert
   Graduate Student: Mark T. Lyttle, Ph.D. Candidate
   UVa Department: Materials Science and Engineering
   NASA-LaRC Contact: T. Bales
   Start Date: September, 1993
   Completion Date: August, 1996
   Project #7

8. PRECIPITATION HARDENING AND MICROSTRUCTURAL STABILITY IN Al-Si-Ge AND Al-Si-Ge-Cu ALLOYS
   Faculty Investigator: E.A. Starke, Jr.
   Graduate Student: H.J. Koenigsmann, Ph.D. Candidate
   UVa Department: Materials Science and Engineering
   NASA-LaRC Contact: W.B. Lisagor
   Start Date: September, 1993
   Completion Date: To be determined
   Project #8.

MECHANICS OF MATERIALS FOR LIGHT AEROSPACE STRUCTURES

9. ENVIRONMENTAL EFFECTS IN FATIGUE LIFE PREDICTION: MODELING ENVIRONMENTAL CRACK PROPAGATION IN LIGHT AEROSPACE ALLOYS

Faculty Investigator: R.P. Gangloff
Graduate Students: Mark E. Mason; MS Candidate
Zuhair Gasem; PhD Candidate
Edward Richey III; MS Candidate (Mechanical and Aerospace Engineering)
Post Doctoral Research Associate: Dr. Sang-Shik Kim
UVa Department: MS&E
NASA-LaRC Contact: R.S. Piascik (Mechanics of Materials)
Start Date: January, 1992
Anticipated Completion Date: September, 1994 (Mason)
December, 1994 (Richey)
December, 1996 (Gasem)

Project #9

THERMAL GRADIENT STRUCTURES

None

RESEARCH PROGRESS AND PLANS . (January 1 to June 30, 1994)

Research progress, recorded during the period from January 1, 1994 to June 30, 1994, is summarized for each project in the following sections. The standard format includes the program objective, recent progress, conclusions, and immediate milestones; coupled with a set of visual aids given in graduate student presentations at the Fifth Annual NASA-UVa LA^{2}ST Grant Review Meeting held at NASA-LaRC in July of 1994. The agenda of this meeting is presented in Appendix IV.

Project #1 Elevated Temperature Damage Tolerance of Advanced Ingot Metallurgy Wrought Aluminum Alloys

Michael J. Haynes and Richard P. Gangloff

Objective

The objective of this study is to quantitatively characterize plane strain initiation (K_{JICi}) and plane stress growth fracture toughnesses as a function of temperature and loading rate. The effect of temperature on K_{JICi} is micromechanically modeled employing temperature dependent measurements of intrinsic fracture strain, elastic modulus, yield strength, and work hardening, coupled with an estimate of the critical microstructural distance relevant to dimpled rupture. Metallurgical aspects of elevated temperature microvoid fracture; including second phase particle distributions, shear localization during coalescence, and dynamic recovery; are identified and incorporated into explanations of time-temperature dependent fracture processes.

Recent Findings

K_{JICi} of AA2519-T87 (modified with Mg plus Ag additions and produced by Alcoa) is substantial (> 30 MPa$\sqrt{m}$) and is temperature independent up to 175°C for a load-line displacement rate of 0.26 μm/sec. At 175°C, Ω

strengthened AA2519-T87 (+Mg+Ag) displays superior initiation and growth toughness over Θ' strengthened AA2519-T87 (plus Mg only). Fractographic analyses show intergranular components of fracture for the Θ' strengthened alloy at 175°C, while the Ω strengthened alloy fractures by transgranular dimpled rupture at this and all lower temperatures. The superior elevated temperature R-curve behavior of 2519+Mg+Ag is probably due to the large volume fraction of Ω. Because the Ω plane coincides with slip planes, dislocations must bypass precipitate plates frequently; a process requiring thermally assisted climb and which somewhat stabilizes the microstructure against dislocation creep and creep damage.

For a constant C(T) load-line displacement rate of 0.26 μm/sec, microvoid coalescence is the operating fracture mechanism in 2519-T87 (+Mg+Ag) at every temperature studied. Voids initiate at large processing-cracked, undissolved Θ particles, with some contribution from manganese and iron bearing constituents. Void sheets connect clusters of Θ nucleated voids and contain smaller dimples (0.5 to 5.0 μm) initiated from smaller second phase particles in the strain localized region between primary voids. As temperature increases, fracture is more homogenous, and enhanced stable void growth produces larger dimples and reduced void sheeting.

The critical plastic strain controlled model accurately predicts the temperature (in)dependence of the measured K_{JICi}, with a calculated critical distance (l^*) approximately equalling the average undissolved Θ particle spacing. The model attributes constant initiation toughness to a rising fracture strain with temperature that counteracts the declining flow strength and elastic modulus. The critical distance has been classically treated as an adjustable parameter in the micromechanical model. Preliminary studies of independently measured l^*, taken as the measured void-nucleating particle spacing (excluding smaller Θ particles), have been conducted with notched tensile bars interrupted at peak load. Average void spacing is directly measured from a metallographic section and l^* is estimated. A closed form prediction of K_{JICi} = 32.2 MPa√m at 25°C shows excellent agreement with measured values, without adjustable parameters.

The possibility of enhanced dynamic recovery is primarily responsible for increased strain rate hardening (m, the exponent in the power-law relationship between stress and strain rate) at elevated temperatures. Changes in slip mode (e.g., climb or cross slip) may also affect m. The intrinsic fracture strain of wrought precipitation hardened aluminum alloys is proportional to m for a range of temperatures. At elevated temperatures, enhanced strain rate hardening, coupled with strain rate amplification, produces increased hardening in the strain-localized intravoid ligament. The flow stress ($\Delta\sigma$) differential between the intravoid microstructure and the more homogeneously deforming bulk retards strain localization if m and $\Delta\sigma$ are sufficiently high. The flow stress differential due to m is higher at 150°C, consistent with reduced void sheeting observed in elevated temperature crack profiles. Accordingly, fracture strain increases with increasing m at increasing temperatures. The converse is true for aluminum alloys that suffer from dynamic strain aging, or that exhibit nil work hardening due to submicron grain size and contain a population of dispersoid-sources of mobile dislocations.

Milestones

A paper, prepared for submittal to *Metallurgical Transactions A*, has been written and is in the revision process. Final work on AA2519+Mg+Ag will focus on direct current potential drop monitoring of notched tensile bars, to more accurately determine the intrinsic fracture strain and critical distance. The effect of preexposure on R-curve behavior will also be investigated.

In the next reporting period, we will begin work on spray formed aluminum alloy N203 (Al-6.2Cu-0.4Mg-0.8Mn-0.4Ag-0.3Zr-0.3V-0.2Ti). Initial work will involve characterization of the alloy; including R-curve measurements, SEM fractography, and micromechanical modelling. The long-term goal is to enhance understanding of strain localization in aluminum alloys, through systematic variations in alloy microstructure and deformation behavior.

Presentation Viewgraph Captions

1. Title.

2. Project objectives.

3. Presentation outline.

4. Compositions of the alloys studied (AA2024, AA2650, AA2519+Mg, and AA2519 +Mg+Ag).

5. Photograph illustrating the experimental set up for fracture toughness testing of C(T) specimens. Load, crack length from electrical potential and crack mouth opening displacement are digitally recorded for input to the calculation of J versus Δa.

6. J-Δa curves for AA2519+Mg+Ag as a function of temperature. This plot demonstrates the decrease in crack growth toughness, at high temperatures and particularly for the alloy without silver. The highest damage tolerance is seen at 75°C, and the lowest at 175°C. Data for AA2519+Mg at 175°C are included for comparison; note the superior R-curve behavior of the Ag containing alloy.

7. Summary bar chart of initiation fracture toughness (K_{JICi}) values for each of three alloys and six temperatures. These data show the high temperature retention of K_{JICi} for the Ag bearing AA2519 alloy.

8. This summary of K @ 4mm for each alloy and test temperature, shows the superior high temperature crack growth toughness of the AA2650 alloy, and the better behavior of Ag bearing AA2519 relative to the non-Ag bearing variant.

9. Optical micrographs illustrating the distribution of undissolved Θ particles and the internal cracks induced by the hot rolling process.

10. Room temperature fracture surface morphology of AA2519+Mg+Ag showing two features: primary microvoid dimples nucleated at undissolved Θ particles and "void sheets" of smaller dimples nucleated at smaller second phase particles.

11. High magnification SEM void sheet observations and fracture surface particle size correlations with TEM measurements of Al-Cu-Mn dispersoids.

12. Photograph of the compression test-fixture with a linear variable differential transducer (LVDT) mounted on the inner plates.

13. Summary of the effect of temperature on the mechanical properties of AA2519+Mg+Ag, including tensile and compressive yield strengths, smooth bar reduction in area and notched bar reduction in area.

14. Schematic illustration of the critical plastic strain controlled micromechanical model of K_{JICi}; crack tip strain must exceed a critical fracture strain over a critical distance. The algebraic model formulation is also included, based on a crack tip strain field reported by McMeeking.

15. Critical plastic strain controlled model predictions of the temperature (in)dependence of K_{JICi}, based on either uniaxial tensile or notched bar reduction in area measurements. ε^* (from Figure 14) may be calculated from reduction in area of the fractured bars, or from diametral displacement measurements of interrupted test specimens, yielding two separate estimates of the critical distance (l^*). The trends remain the same for either case, and l^* is treated as an adjustable parameter.

16. Independent measurement of l^* from an interrupted notched tensile bar experiment. l^* is equated to the spacing of Θ particles that nucleate voids at near peak load, as measured directly from a metallographic section. ε_i^* is also estimated from the final diameter, and a closed form prediction of K_{JICi} (32.2 MPa$\sqrt{m}$) is made.

17. Strain rate hardening measurements for AA2219 and AA2618, plotted together with notched bar reduction in area measurements for AA2519+Mg+Ag, each as a function of temperature. Note the similar trends and specifically the rapid increase of both values between 150°C and 175°C.

18. Correlation between strain rate hardening exponent, m, and reduction in area for AA2519 strained at a variety of temperatures between 25 and 175°C..

19. The characteristics of intravoid strain localization, as shown schematically, including strain rate amplification and intravoid flow strength increase.

20. A metallurgical explanation of strain localization between growing microvoids in AA2519+Mg+Ag at ambient and elevated temperatures. Increased strain rate hardening at 150°C retards void sheeting and acts to increase both the intrinsic fracture resistance and fracture toughness.

21. Plot of the calculated intravoid flow stress differential at ambient and elevated temperatures, as affected by strain rate hardening coupled with strain rate amplification.

22. Microscopic evidence of reduced void sheeting at 150°C from crack tip profiles of compact tension specimens.

23. Conclusions: Toughness and Fractography.

24. Conclusions: Modelling and Microscopic Fracture.

25. Characteristics of spray formed aluminum alloys.

26. Alcan-Cospray N203 composition and microstructure. The micrograph reported by Li and Wawner at UVa shows a fine grain size (1 to 5 μm) and a high dispersoid content.

27. A plot of normalized fracture strain versus temperature for I/M 2519+Mg+Ag, ultra fine grain size RS/PM 8009, and spray formed N203. Fracture strain rises with temperature for I/M 2519 and spray formed N203, in contrast to the declining fracture strain of 8009. The strain rate hardening exponent for the ingot metallurgy alloy is substantially higher than m for the rapidly solidified alloy at elevated temperatures.

28. *Apriori* predictions of elevated temperature K_{JICi}, based on tensile data, for N203. A constant initiation toughness is predicted, equal to the measured room temperature value, with an estimated critical distance of approximately 50 μm.

29. Proposed Work on N203.

ELEVATED TEMPERATURE FRACTURE OF AN ADVANCED INGOT METALLURGY WROUGHT Al-Cu-Mg-Ag ALLOY

Michael J. Haynes and Richard P. Gangloff

Funded by NASA Langley Research Center
W.B. Lisagor, Project Monitor

Objectives

- Measure initiation and growth fracture toughness of an advanced ingot metallurgy Al-Cu-Mg-Ag Alloy as a function of temperature and loading rate.

- Identify metallurgical aspects of time-temperature dependent fracture

- Model initiation fracture toughness (K_{JICI}) as a function of temperature with tensile data and compression flow curves.

Outline

I. Initiation and Growth Toughness Characterization:

- J-Integral resistance curves
- Characterize I/M 2XXX alloys (2650, 2519+Mg, 2519+Mg+Ag)

II. Fractography - 2519+Mg+Ag

III. Micromechanical Modeling - 2519+Mg+Ag

IV. Strain Localization \ Void Coalescence Mechanisms

- Effect of strain rate sensitivity

V. Conclusions

VI. Spray Formed Al-Cu-Mg-Ag-Mn Alloys: The Next Generation?

Alloy Compositions

	Cu	Mg	Mn	Ag	Zr	V	Fe	Ni	Si
AA2024-T3	4.4	1.5	0.6	—	—	—	—	—	—
AA2519-T87 w/ Mg	5.83	0.52	0.30	—	0.15	0.10	—	—	—
AA2519-T87 w/ Mg, Ag	5.75	0.52	0.30	0.5	0.16	0.09	—	—	—
AA2650-T6	2.71	1.64	—	—	—	—	0.20	0.21	0.21

C(T) Specimen Detail For J-Δa Curve Determination

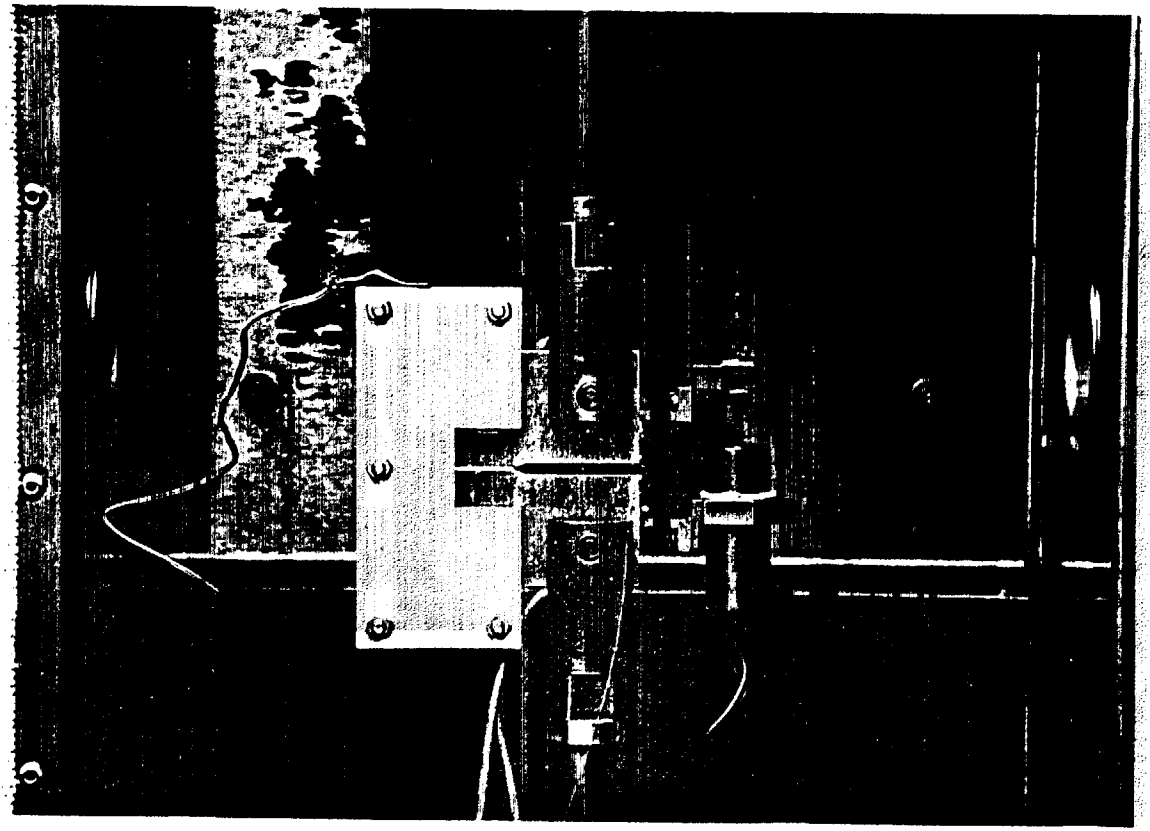

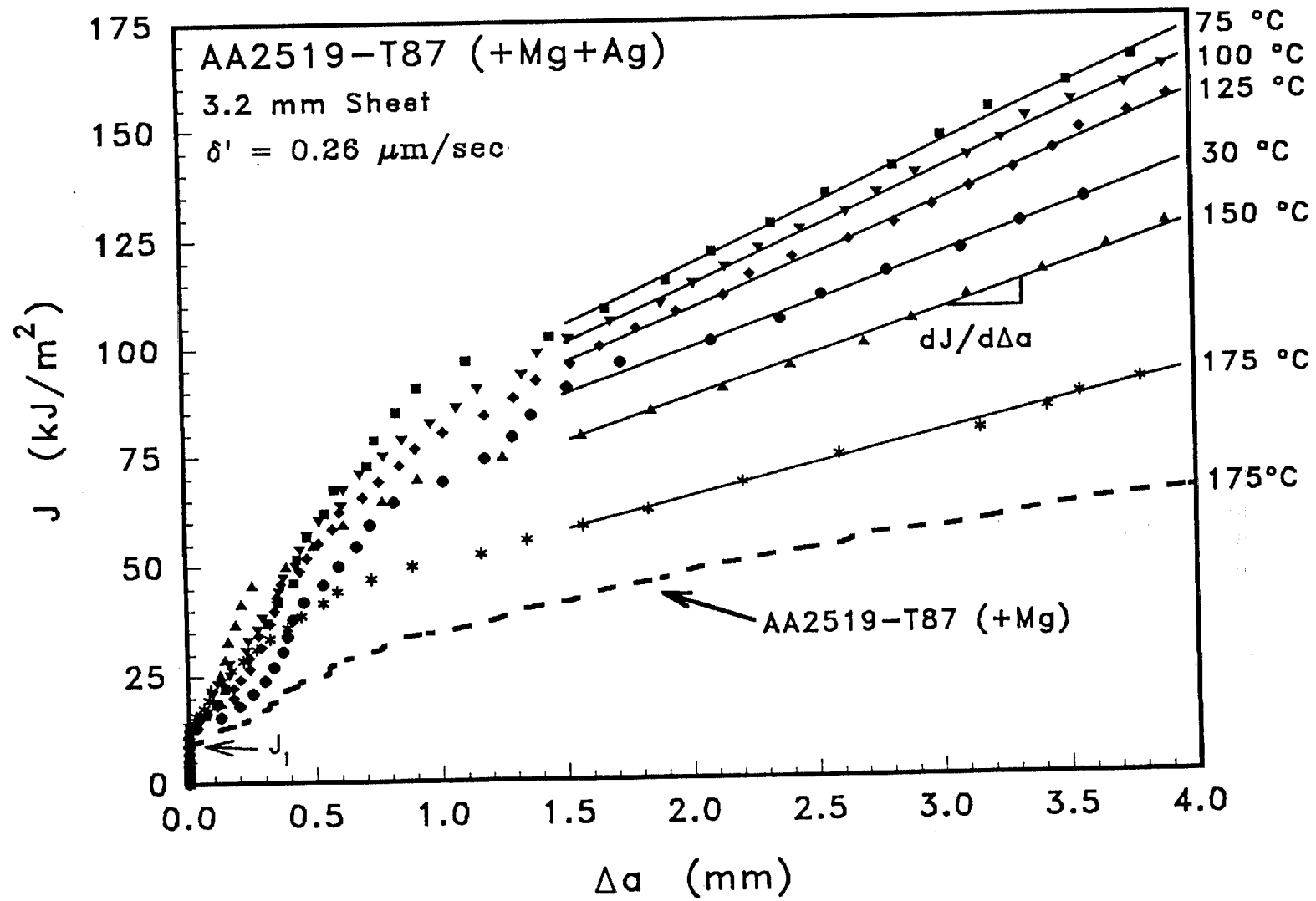
AA2519–T87 (+Mg+Ag)
3.2 mm Sheet
δ' = 0.26 μm/sec
75 °C
100 °C
125 °C
30 °C
150 °C
175 °C
175°C
dJ/dΔa
AA2519–T87 (+Mg)
J1
J (kJ/m2)
Δa (mm)
0
25
50
75
100
125
150
175
0.0
0.5
1.0
1.5
2.0
2.5
3.0
3.5
4.0

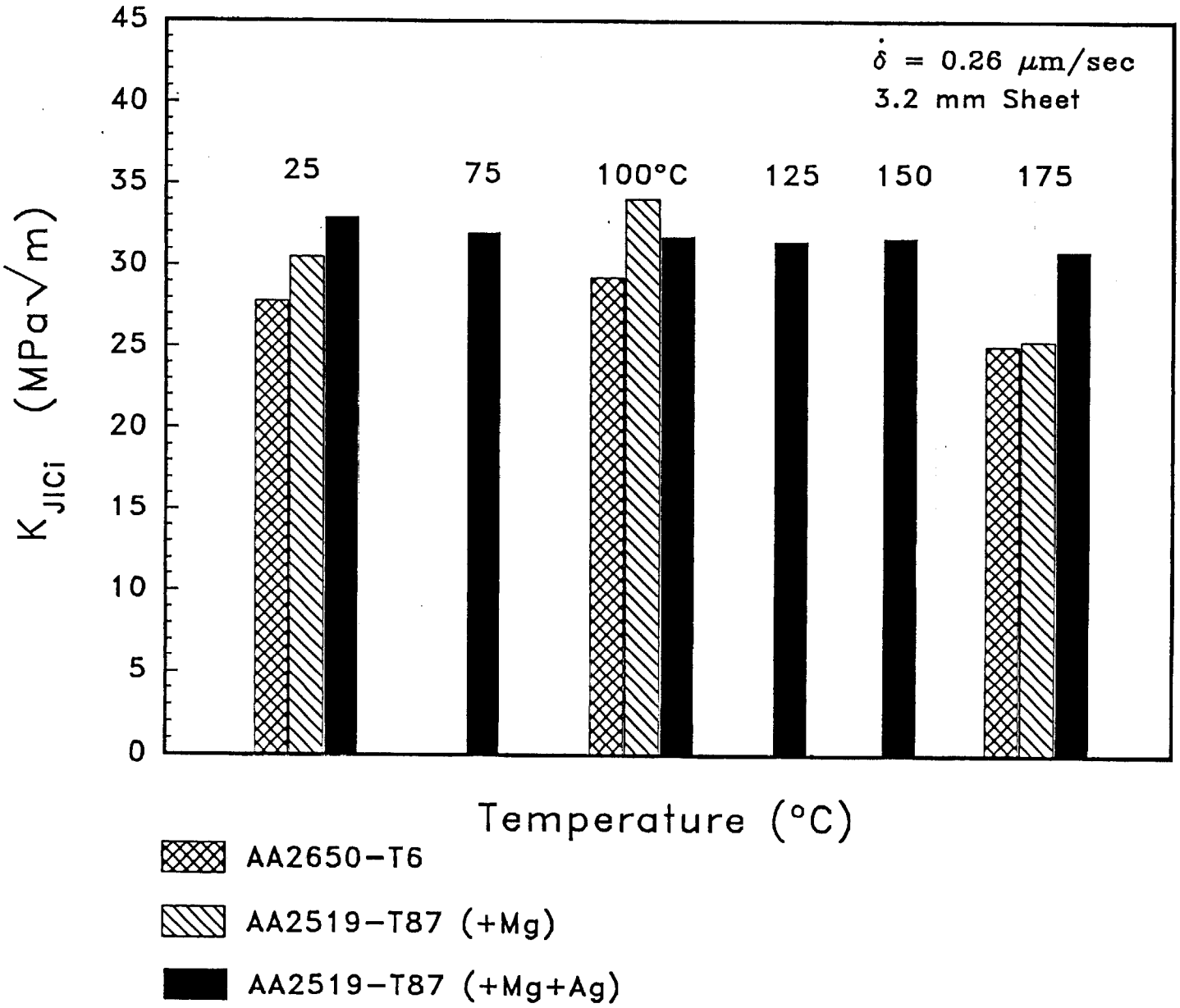
$\dot{\delta}$ = 0.26 μm/sec
3.2 mm Sheet
25
75
100°C
125
150
175
45
40
35
30
25
20
15
10
5
0
K_{JICi} (MPa√m)
Temperature (°C)
AA2650-T6
AA2519-T87 (+Mg)
AA2519-T87 (+Mg+Ag)

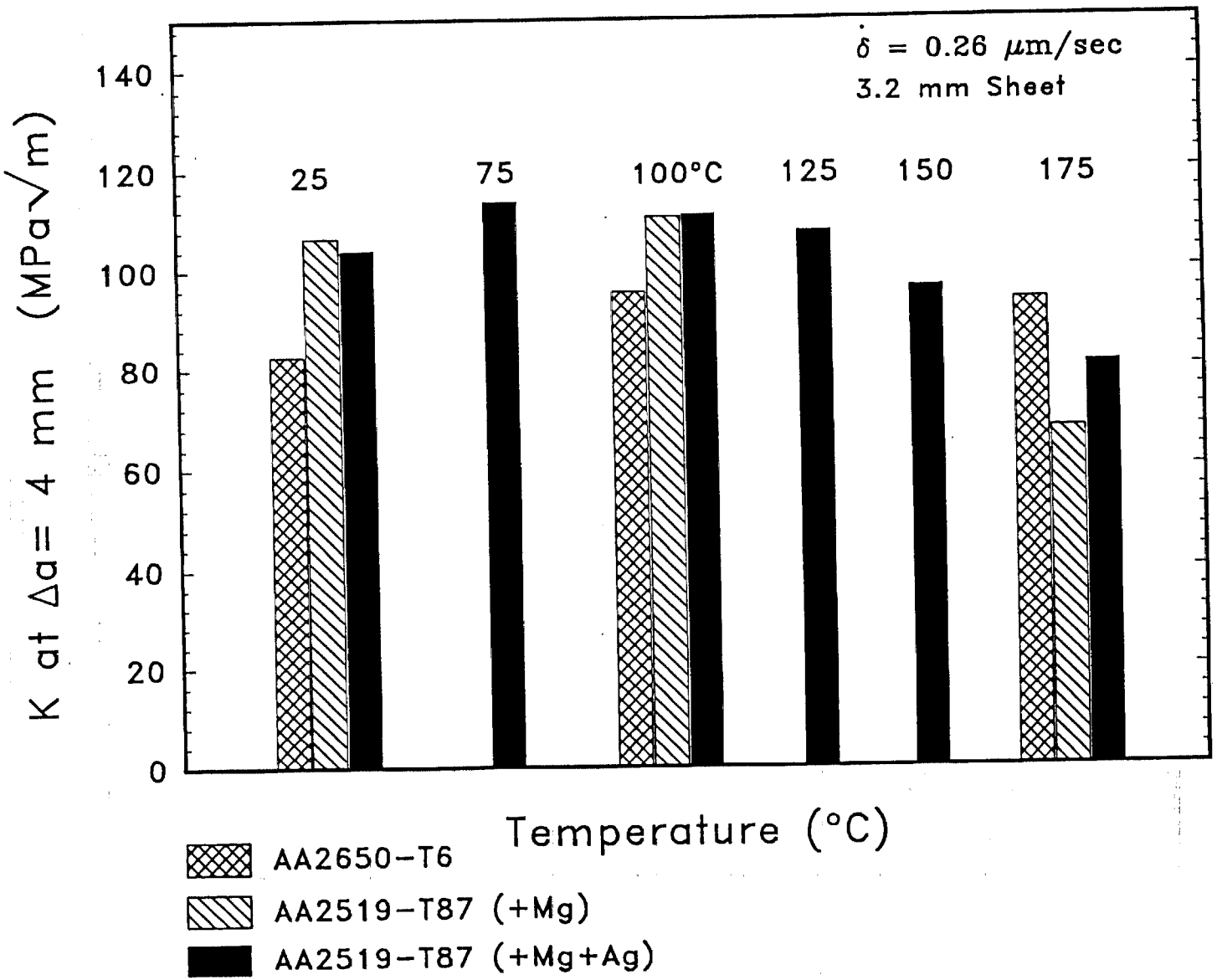
$\dot{\delta}$ = 0.26 μm/sec
3.2 mm Sheet
140
120
100
80
60
40
20
0
25
75
100°C
125
150
175
K at Δa = 4 mm (MPa√m)
Temperature (°C)
AA2650-T6
AA2519-T87 (+Mg)
AA2519-T87 (+Mg+Ag)

Undissolved θ Particles Were Cracked During the Rolling Process

RD

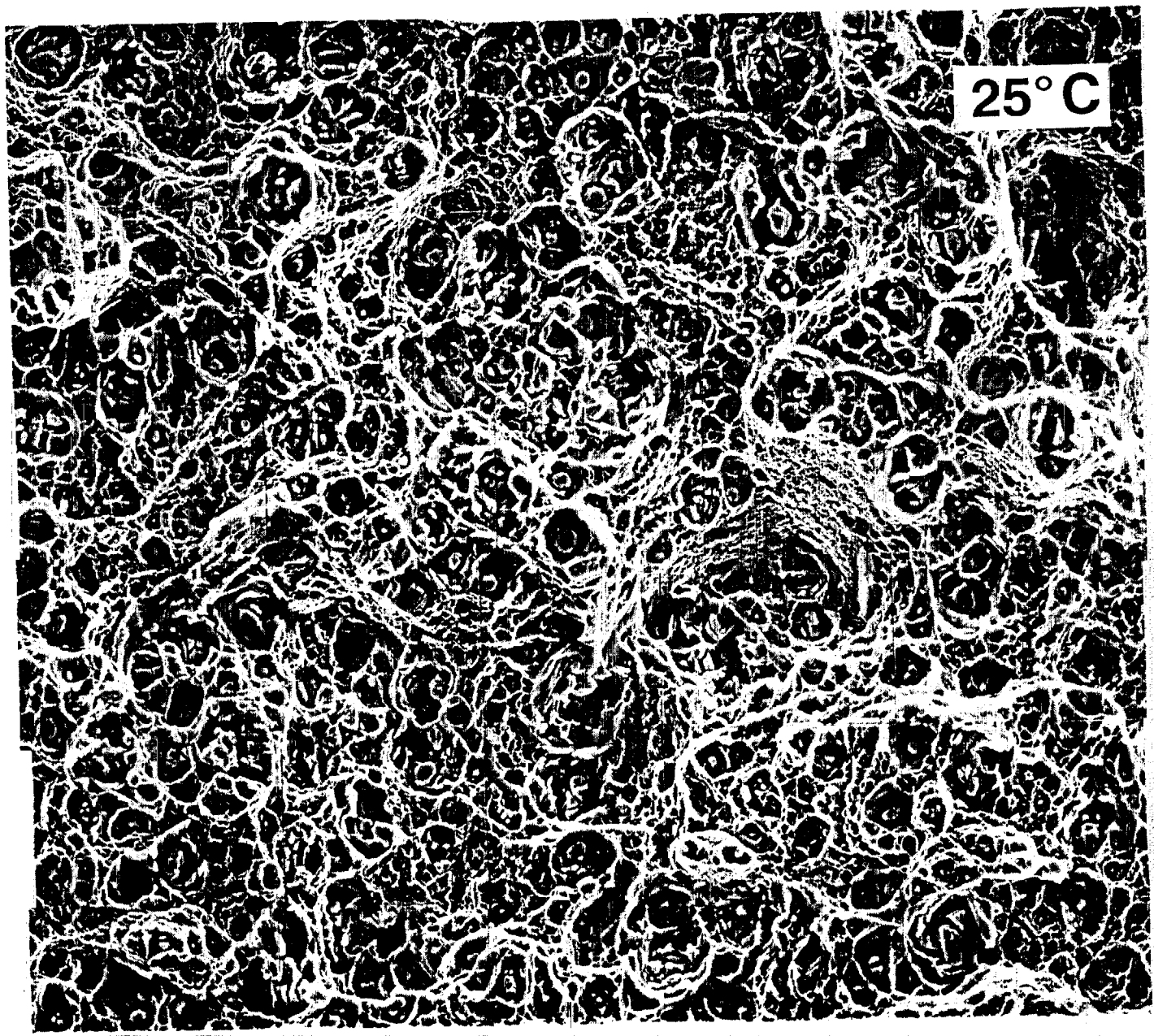
25° C

High Magnification SEM Void Sheet Observations

Tilted 75° about Axis Parallel to Crack Front

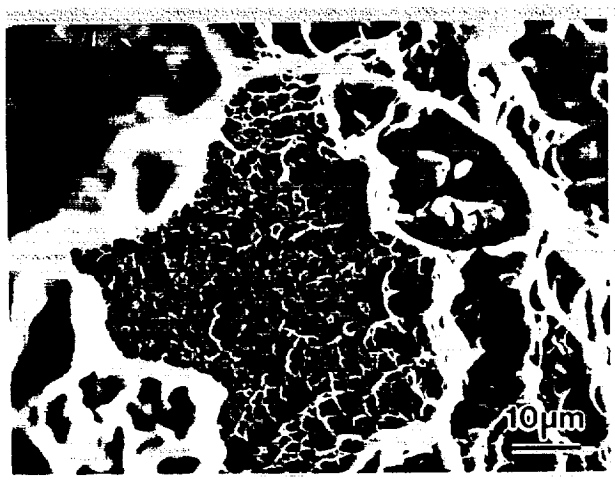

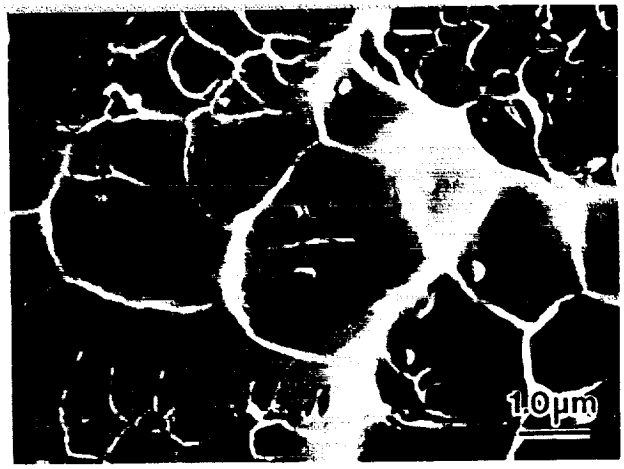

Particle Size Statistics

Particles on Fracture Surface

Avg. Diameter = 0.234 μm

Std. Deviation = 0.090 μm

# of Particles = 22

T.E.M. Al-Cu-Mn Dispersoid Sizes

Avg. Diameter = 0.168 μm

Std. Deviation = 0.077 μm

# of Particles = 21

Compression Test Fixture

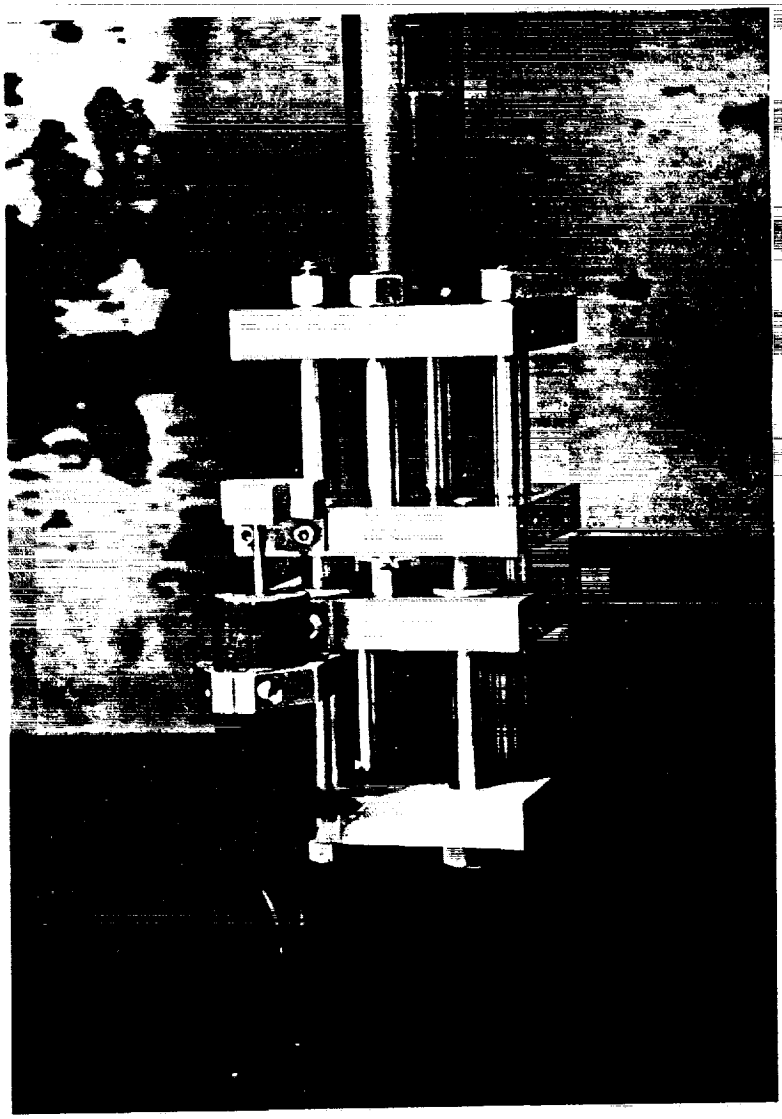

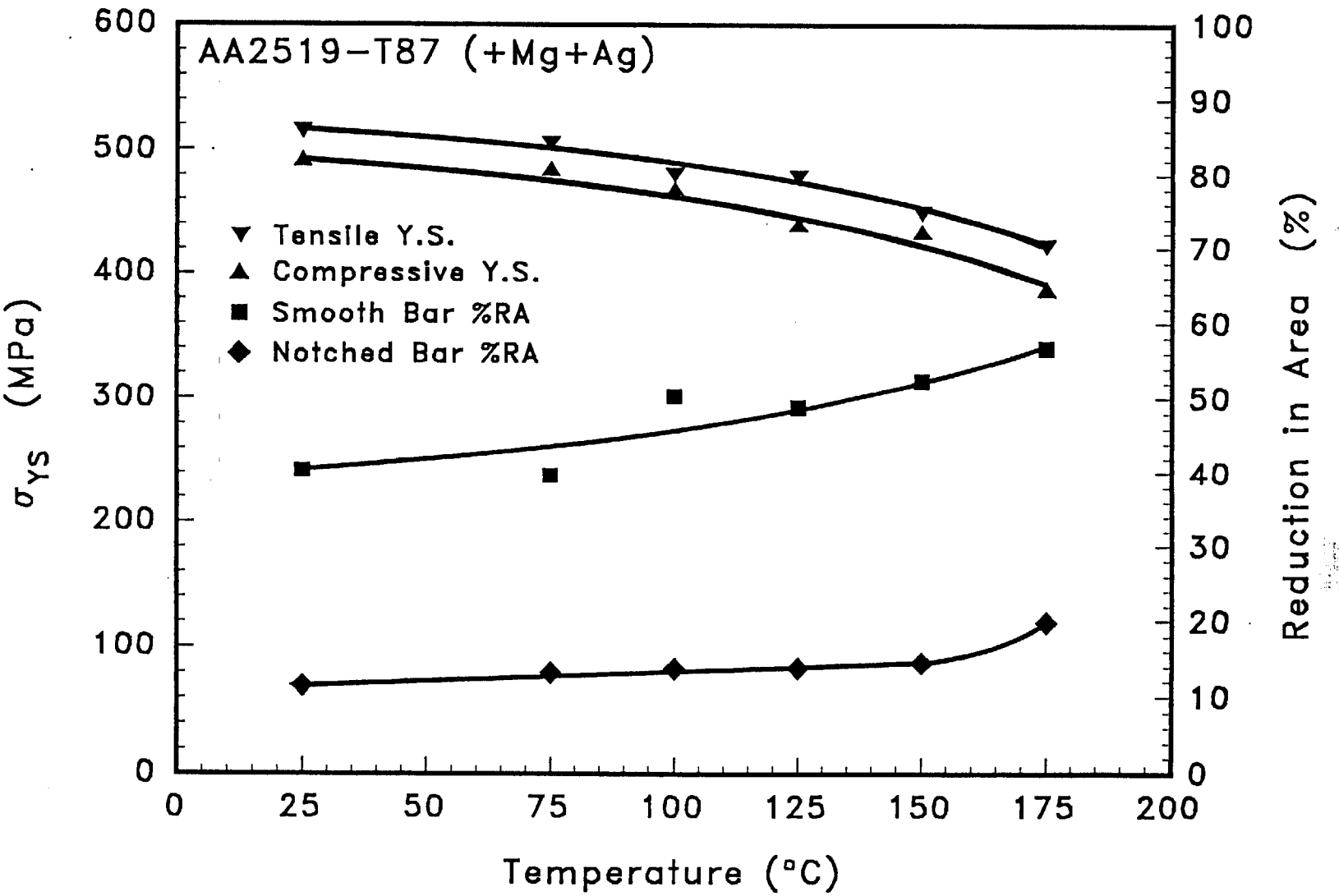
AA2519–T87 (+Mg+Ag)
Tensile Y.S.
Compressive Y.S.
Smooth Bar %RA
Notched Bar %RA
σYS (MPa)
Reduction in Area (%)
Temperature (°C)
600
500
400
300
200
100
0
100
90
80
70
60
50
40
30
20
10
0
0
25
50
75
100
125
150
175
200

Critical Plastic Strain Controlled Model

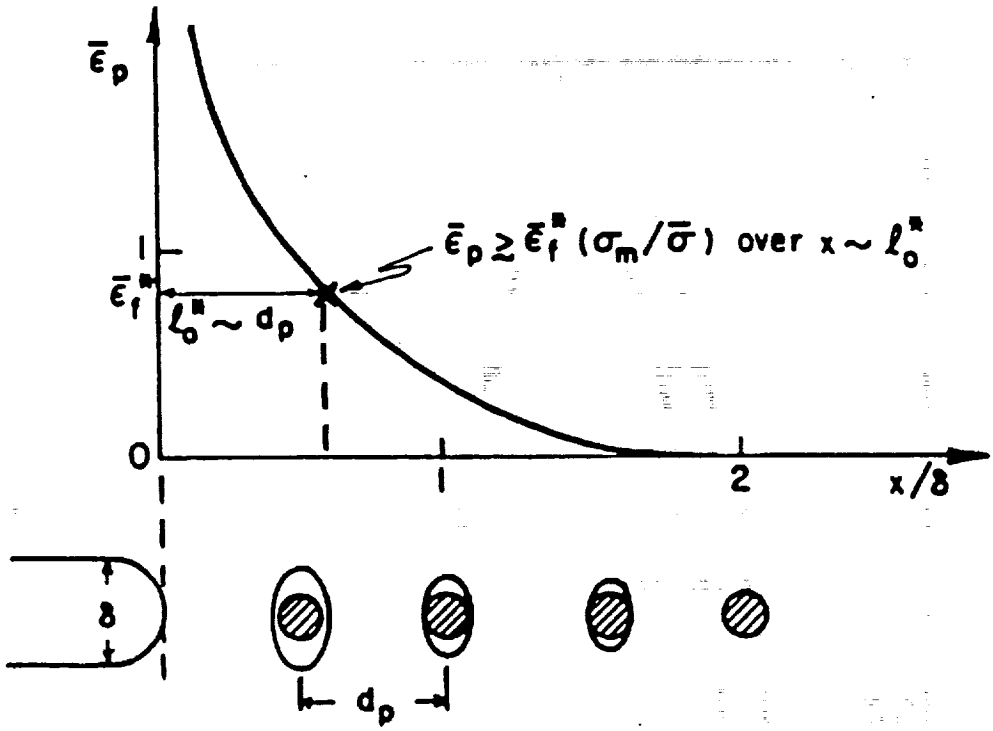

$$K_{JICi} = \sqrt{\frac{\sigma_{ys} E I^*}{(1-\nu^2) d_n} \left(\frac{\bar{\epsilon}_f^*}{C1} \right)^{\frac{1}{C2}}}$$

$$\bar{\epsilon}_f^* = (1/\gamma)\,(-\ln(1-\%RA))$$

MODEL PREDICTIONS

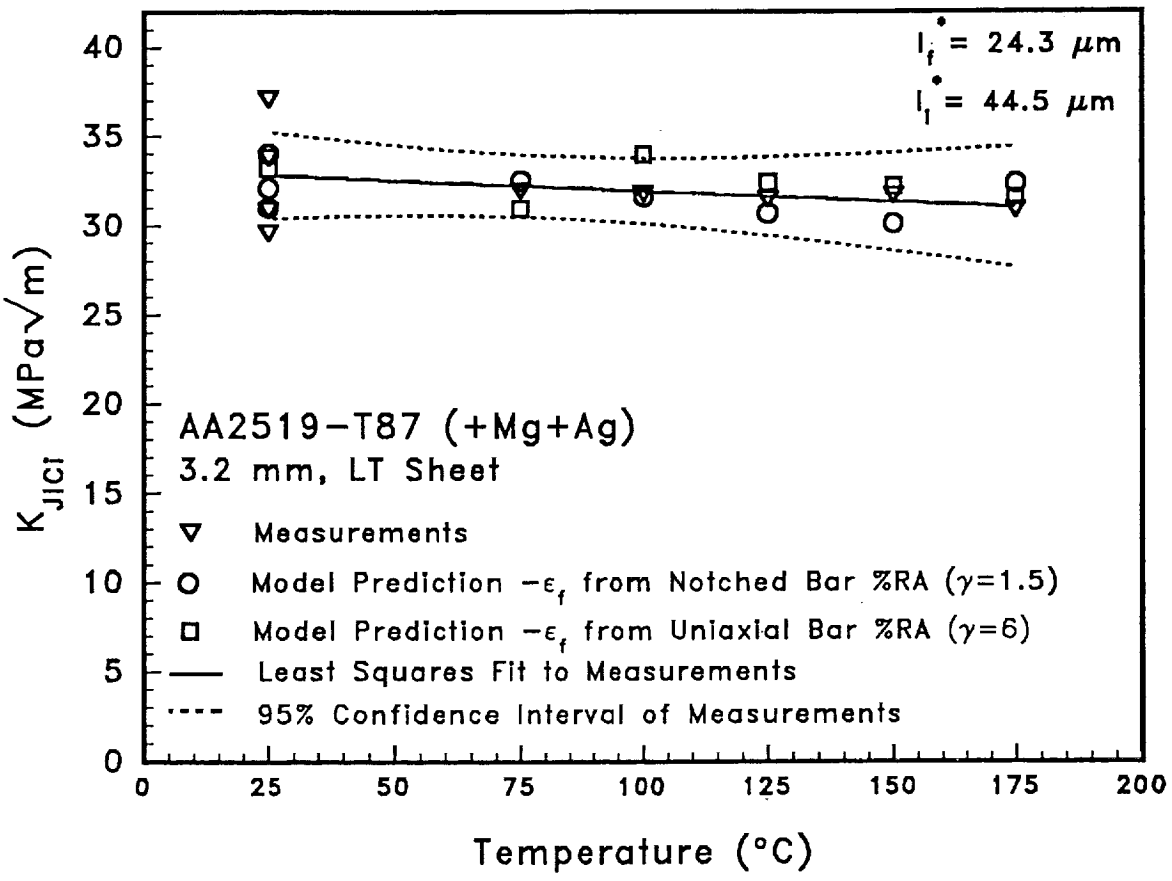

l^* "back-calculated" by normalizing measured and predicted K_{JICI} at 25°C

- **l_f^*: back-calculated with $\bar{\epsilon}_f^*$ determined from fractured notched bar**
- **l_i^*: back-calculated with $\bar{\epsilon}_i^*$ determined from interrupted notched bar**

Critical Distance and Initiation Strain Determinations From Interrupted Notched Bar Tensile Test (Stopped At Peak Load - 25°C)

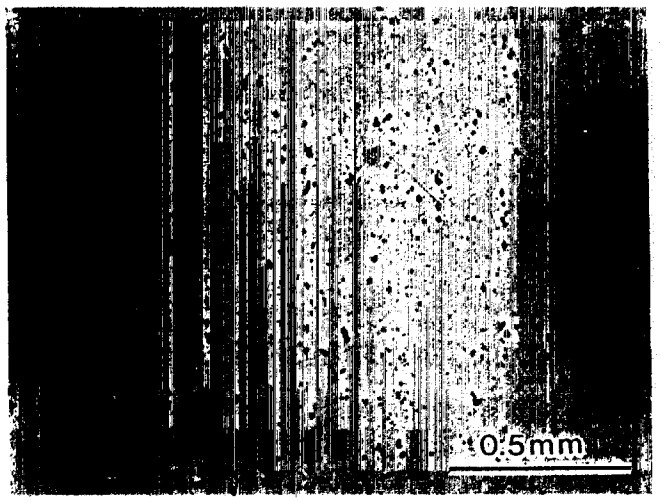

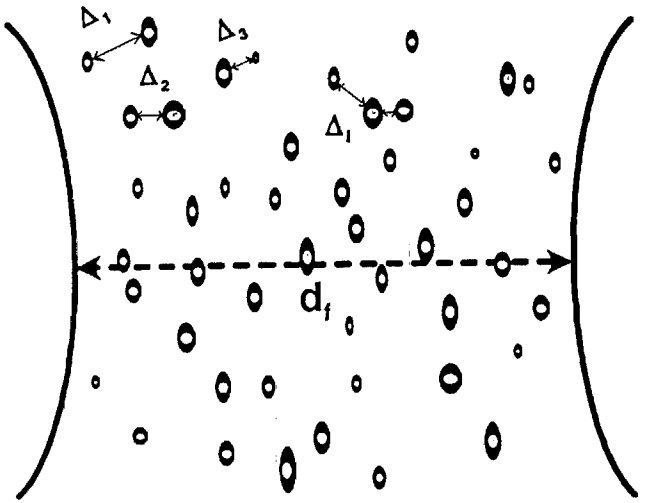

$$\bar{\epsilon}_i^{\,*} = 2 \ln\left(\frac{d_o}{d_f}\right) \approx 4\%$$

$$l_i^{\,*} = \frac{(\Delta_1 + \Delta_2 + \Delta_3 \ldots \Delta_i)}{N} \approx 43\ \mu m$$

$$K_{JICi}^{predicted}(25^\circ C) = 32.2\ MPa\sqrt{m}$$

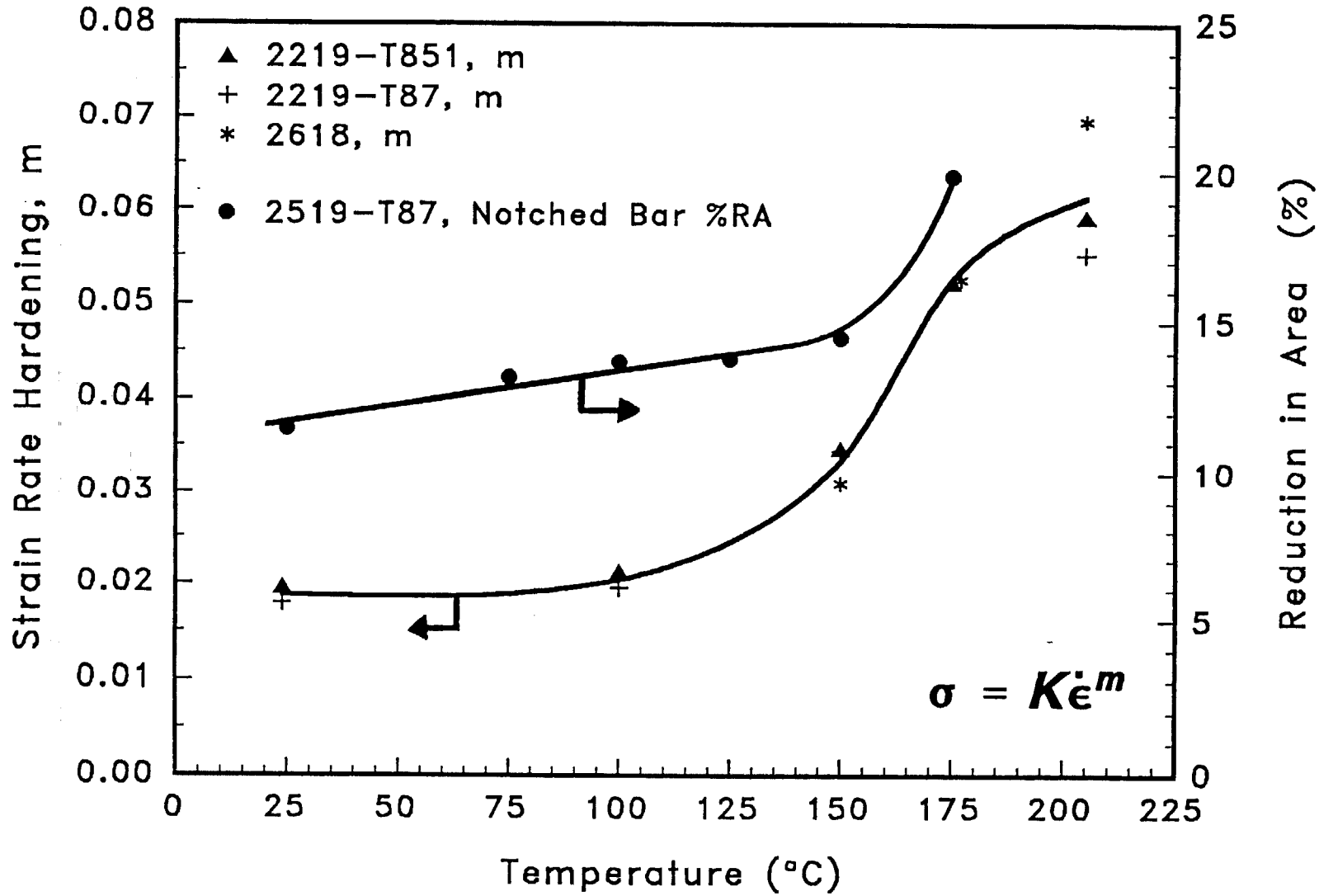
▲ 2219–T851, m
+ 2219–T87, m
* 2618, m
● 2519–T87, Notched Bar %RA
$\sigma = K\dot{\epsilon}^m$
Strain Rate Hardening, m
Reduction in Area (%)
Temperature (°C)
0.00
0.01
0.02
0.03
0.04
0.05
0.06
0.07
0.08
0
5
10
15
20
25
0
25
50
75
100
125
150
175
200
225

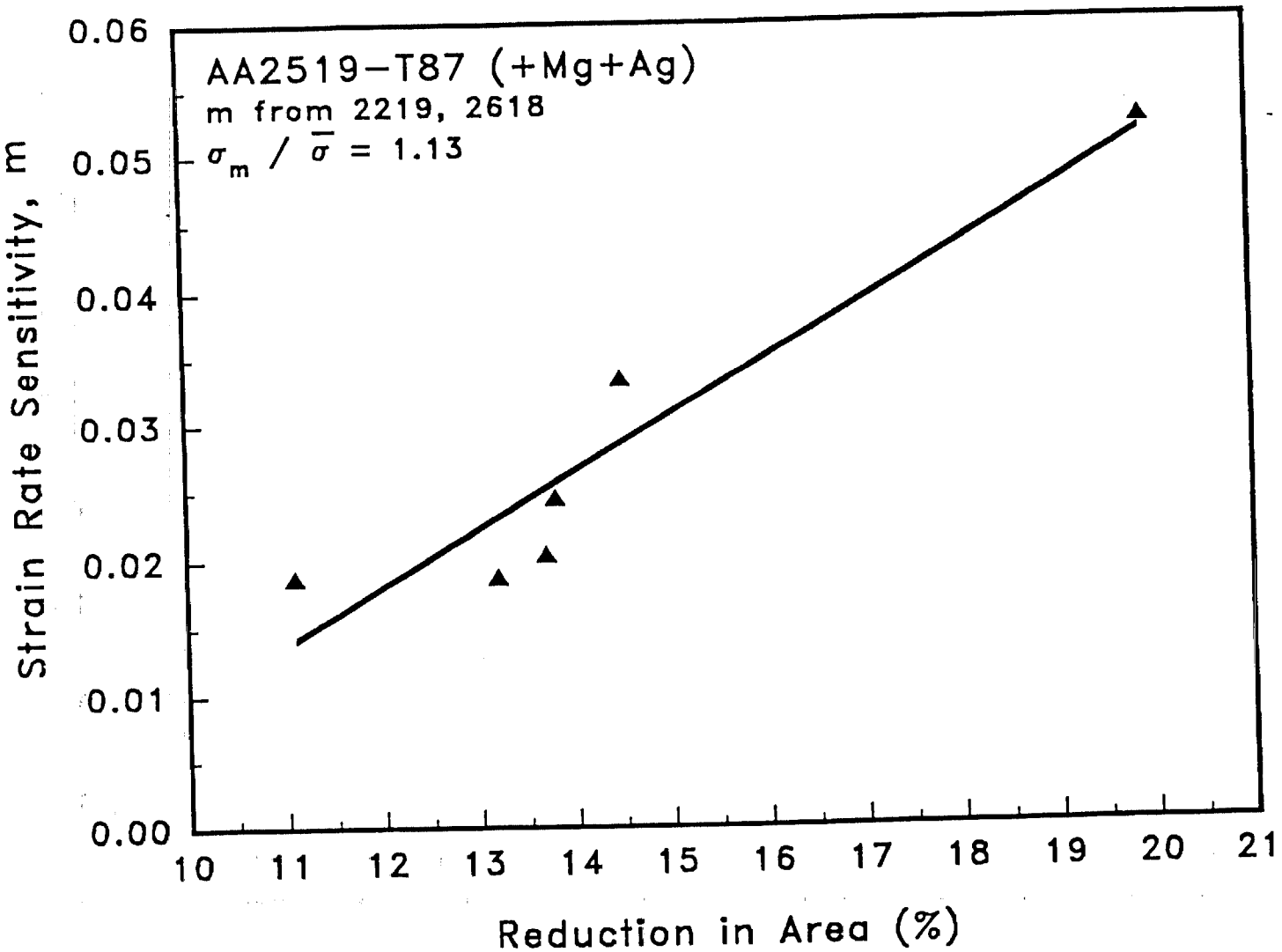
AA2519–T87 (+Mg+Ag)
m from 2219, 2618
σ_m / $\overline{\sigma}$ = 1.13
Strain Rate Sensitivity, m
0.06
0.05
0.04
0.03
0.02
0.01
0.00
10
11
12
13
14
15
16
17
18
19
20
21
Reduction in Area (%)

INTRAVOID STRAIN LOCALIZATION

- Localization is governed by differences in flow properties within the intravoid strain band (flow strength, $\sigma_{o:L}$ and strain hardening, n_L) versus global flow properties ($\sigma_{o:gl}$ and n_{gl})

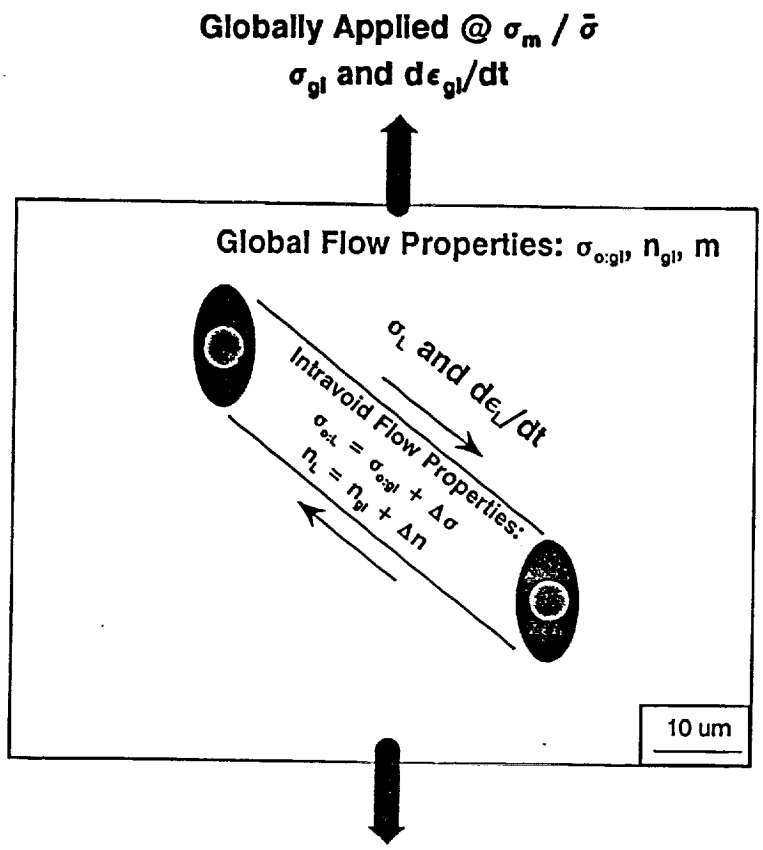

- Strain rate is amplified by λ in the intravoid region:

$$\frac{d\,\epsilon_L}{dt} = \lambda \frac{d\,\epsilon_{gl}}{dt} \qquad (100 < \lambda < 10{,}000)$$

- $\Delta\sigma$ is directly related to λ and the strain rate hardening, m:

$$\Delta\sigma = K\left(\lambda \dot{\epsilon}_{nominal}\right)^m - \sigma_{o:gl}$$

- Localization occurs at a critically low $\Delta\sigma$ or Δn; $\Delta\sigma, \Delta n \rightarrow 0$

INTRAVOID STRAIN LOCALIZATION

In AA2519-T87 & other precipitation hardened I/M Al alloys, the critical macroscopic effective strain to failure ($\bar{\varepsilon}_f^*$) rises moderately with temperature.

<u>At Ambient Temperature:</u>

- Strain rate hardening is low and dynamic dislocation recovery is limited.
- Increased strain rate in the localized strain band between voids does not significantly alter the degree of dynamic recovery nor sufficiently stabilize flow by hardening relative to global deformation.
- Strain concentrates in void sheets, resulting in premature coalescence and lower fracture strains.

<u>At Elevated Temperatures:</u>

- Dynamic recovery is significant and strain rate hardening increases.
- Dynamic recovery decreases significantly with increasing intravoid strain rate and flow strength within the localized band rises.
- Intravoid flow stabilization homogenizes slip, postpones void sheeting, and raises the fracture strain.

Evidence of dynamic strain aging was not observed for peak aged AA2519 (+Mg+Ag).

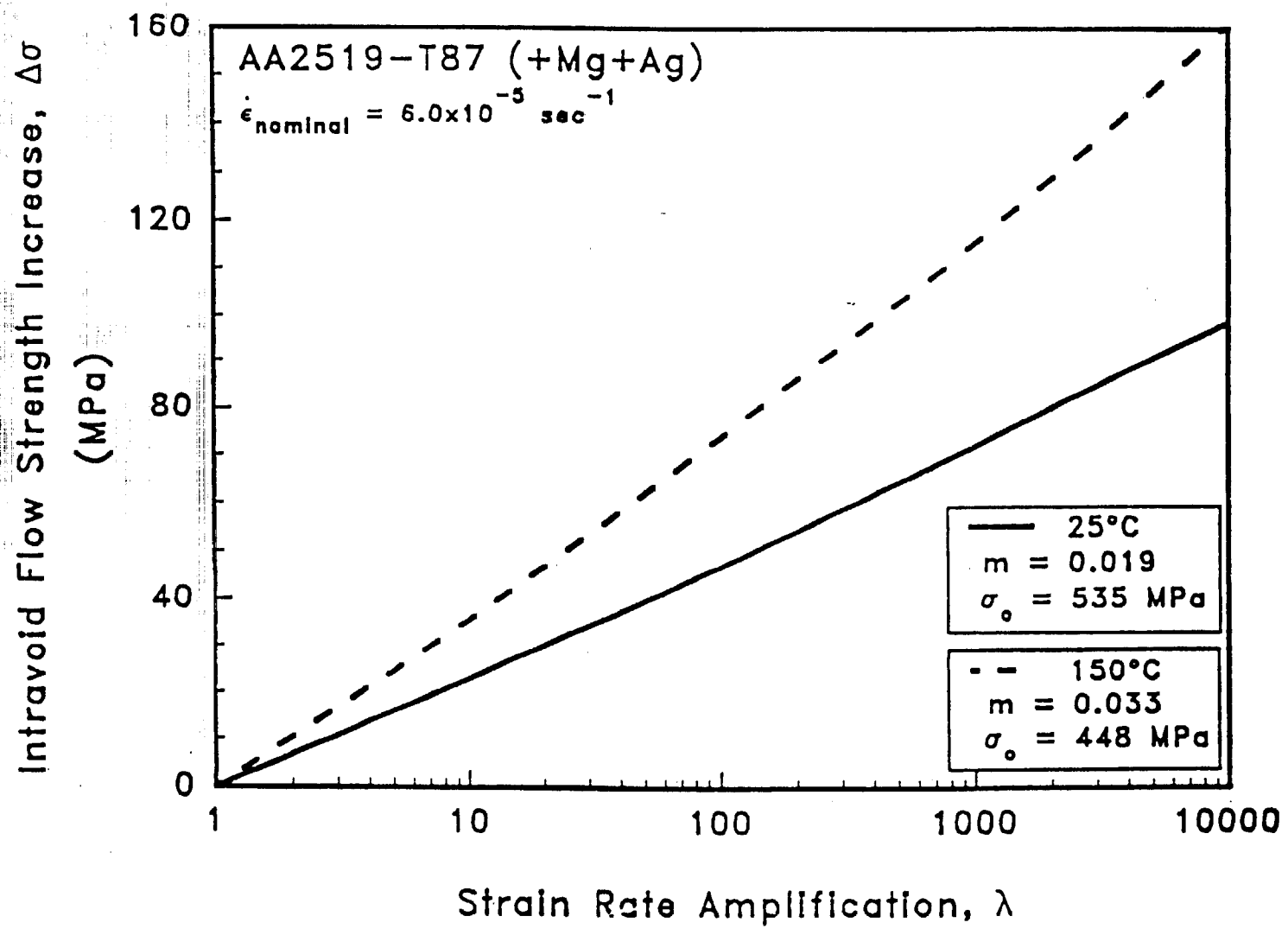
AA2519-T87 (+Mg+Ag)
$\dot{\epsilon}_{nominal} = 6.0 \times 10^{-5}\ sec^{-1}$
Intravoid Flow Strength Increase, Δσ (MPa)
160
120
80
40
0
1
10
100
1000
10000
Strain Rate Amplification, λ
25°C
m = 0.019
σ_o = 535 MPa
150°C
m = 0.033
σ_o = 448 MPa

Crack Tip Profiles from C(T) Specimen Midplanes

Room Temperature

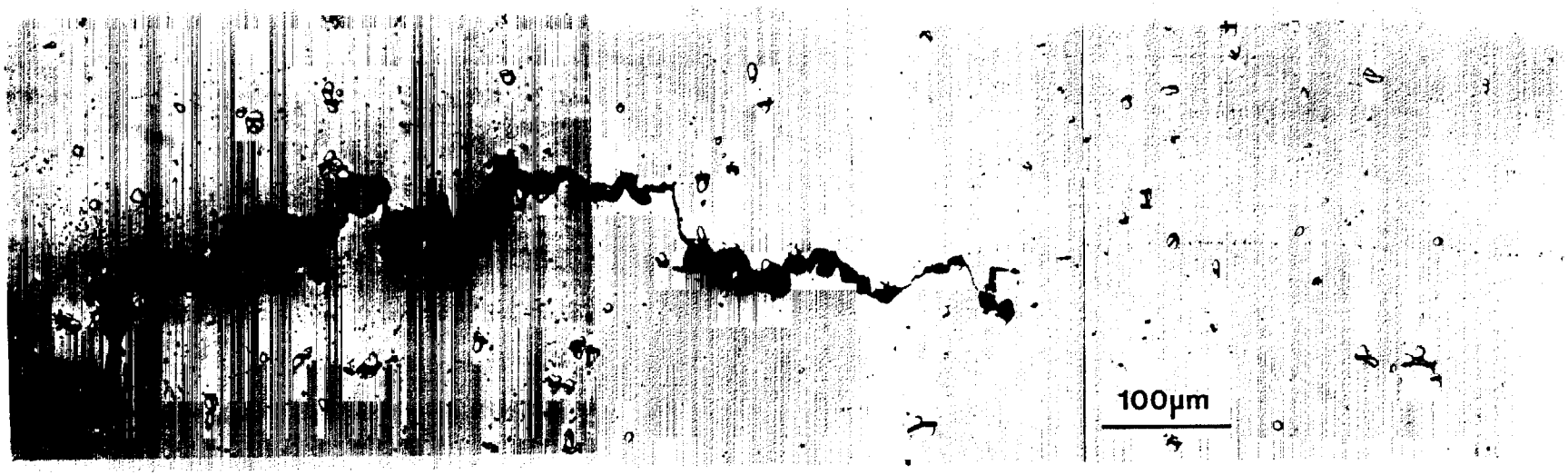

150 °C

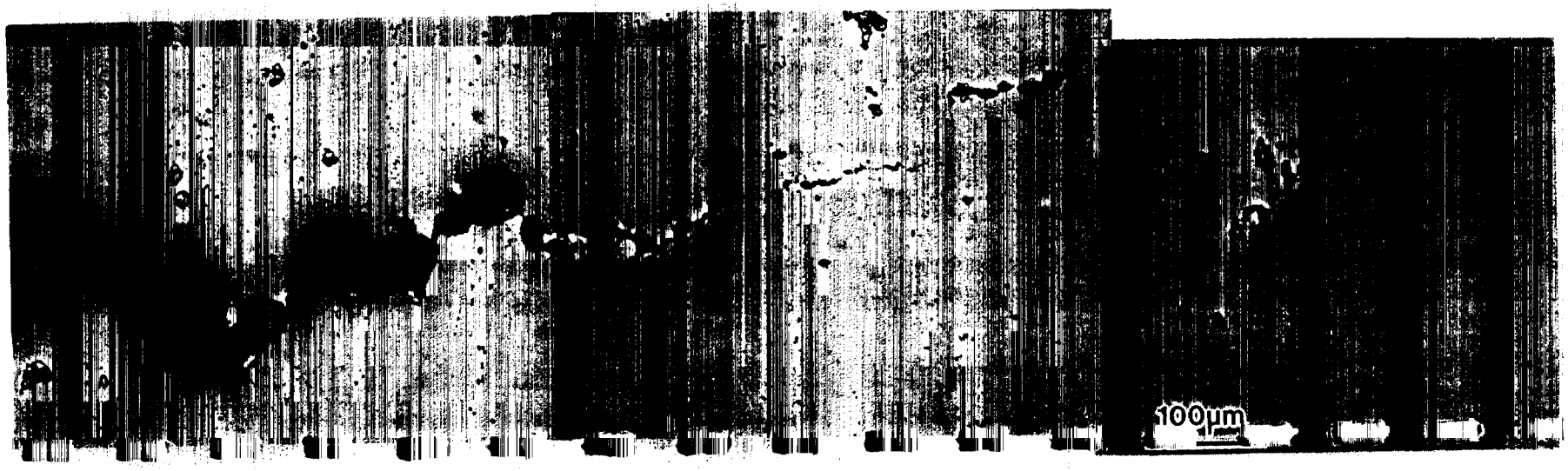

Conclusions: Toughness and Fractography

- Fracture initiation toughness is relatively high (K_{JICI} > 30 MPa√m) for high strength 2519-T87 (+Mg+Ag) in spite of large Θ particles, and is invariant with increasing temperature to 175°C at normal loading rates.

- Fracture surfaces are characterized by a bimodal distribution of dimples. Fracture evolved by primary void initiation at undissolved Al_2Cu particles, followed by limited void growth and unstable coalescence through propagation of fine dimpled void sheets nucleated at Al-Cu-Mn dispersoids.

- Elevated temperature fracture surfaces are more "homogenous". Enhanced stable void growth produces larger dimples and reduced void sheeting.

- At 175°C, Ω phase strengthened AA2519-T87 (+Mg+Ag) displays higher initiation and growth toughnesses than Θ' strengthened AA2519-T87 (+Mg). Intergranular fracture facets were observed for AA2519-T87 (+Mg), consistent with the lower toughnesses.

Conclusions: Modeling and Microscopic Fracture

- The critical plastic strain-controlled micromechanical model of initiation toughness accurately predicts temperature (in)dependent K_{JICI}, whether smooth or notched bars are employed to estimate the intrinsic fracture resistance, $\bar{\epsilon}_f^*$.

- Critical distances are reasonably similar based on either "toughness fitting" or direct measurements from polished sections of notched bars. l^* is directly related to the average spacing of void-nucleating Θ particles.

- The model attributes temperature independent K_{JICI} to rising fracture strain with temperature, that counteracts declining flow strength and elastic modulus.

- At elevated temperatures, enhanced strain rate hardening and consequently enhanced intravoid ligament hardening are responsible for higher $\bar{\epsilon}_f^*$. m provides a flow stress differential between intravoid microstructure and the homogeneously deforming bulk that retards intravoid strain localization.

Spray Formed Aluminum Alloys: The Next Generation?

Processing:

- Spray Deposition, Osprey process, and Atomized Melt Deposition (AMD)
- Cooling Rates of 10^3-10^4 °C/sec (10^1-10^3 °C/sec slower than rapid solidification processes)

Potential Advantages:

- Reduction in the size of intermetallic constituent particles
- Reduction in volume fraction and size of powder particle surface oxides and hydrated oxides
- Extended solid solubility of transition elements; higher volume fraction of dispersoids for grain refinement
- Reduction in grain size, from levels typical of I/M aluminum alloys (e.g.-50 μm)
- Reduced solute segregation at grain boundaries and other interfaces
- Improved isotropy of strength and fracture toughness

Present Limitations

- Spray processed microstructures are not reproducibly homogenous.
- Microstructures contain high volume fractions of large constituent and dispersoid particles that degrade fracture toughness.

Alcan-Cospray Spray Formed N203: The Next Generation?

- Composition: Al-6.3Cu-0.36Mg-0.80Mn-0.40Ag-0.31Zr-0.27V-0.19Ti by wt%
- Preliminary TEM study of alloy microstructure (Q. Li and F.E Wawner; UVA)
  - → Refined Grain Size (1 - 5 μm)
  - → Mn, Ti, V, and Zr bearing Dispersoids (0.1 - 0.5 μm)
  - → Ω precipitates
  - → Constituent Particle Distributions?

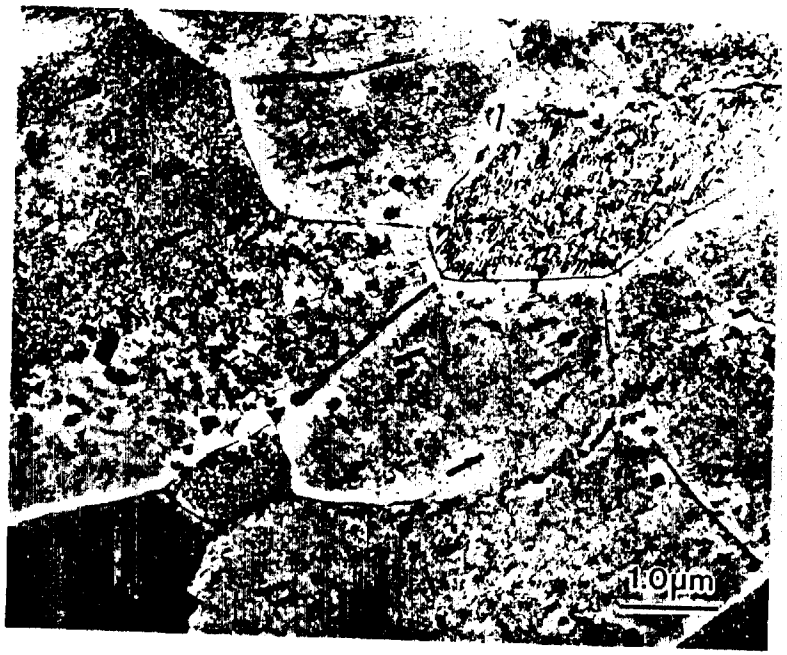

Rationale for Study: N203 grain size is small relative to I/M grain sizes, but it is presumably large enough to facilitate a dislocation substructure that subsequently precludes strain localization observed in advanced, sub-micron grain size, powder metallurgy aluminum alloys.

- How will alloying elements in solution and fine grain size affect strain rate hardening?
- Thermal stability and low deformation rate toughness unexplored.

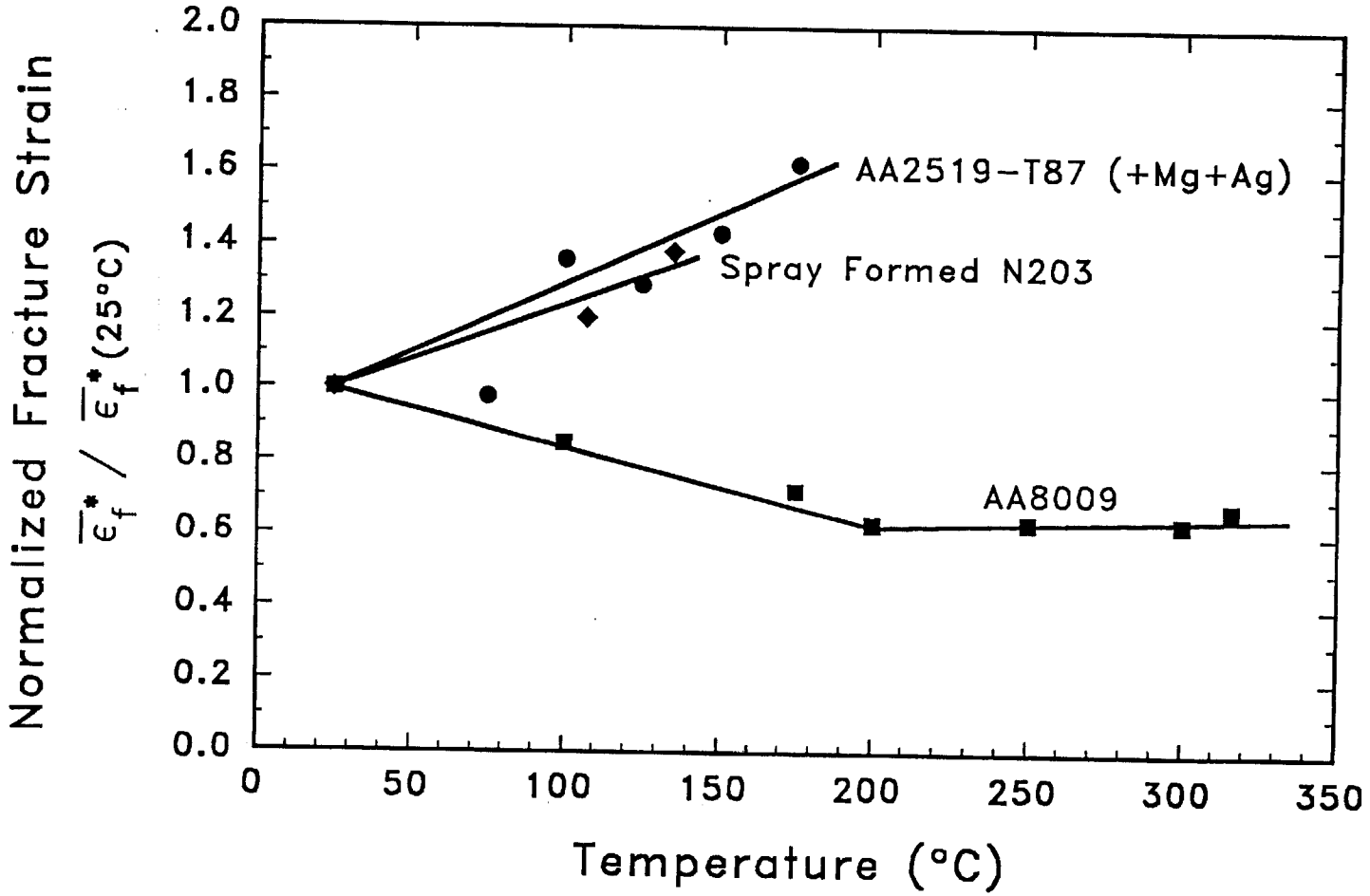
Normalized Fracture Strain
$\overline{\epsilon}_f^* / \overline{\epsilon}_f^*(25°C)$
2.0
1.8
1.6
1.4
1.2
1.0
0.8
0.6
0.4
0.2
0.0
0
50
100
150
200
250
300
350
Temperature (°C)
AA2519-T87 (+Mg+Ag)
Spray Formed N203
AA8009

Elevated Temperature K_{JICi} Predictions

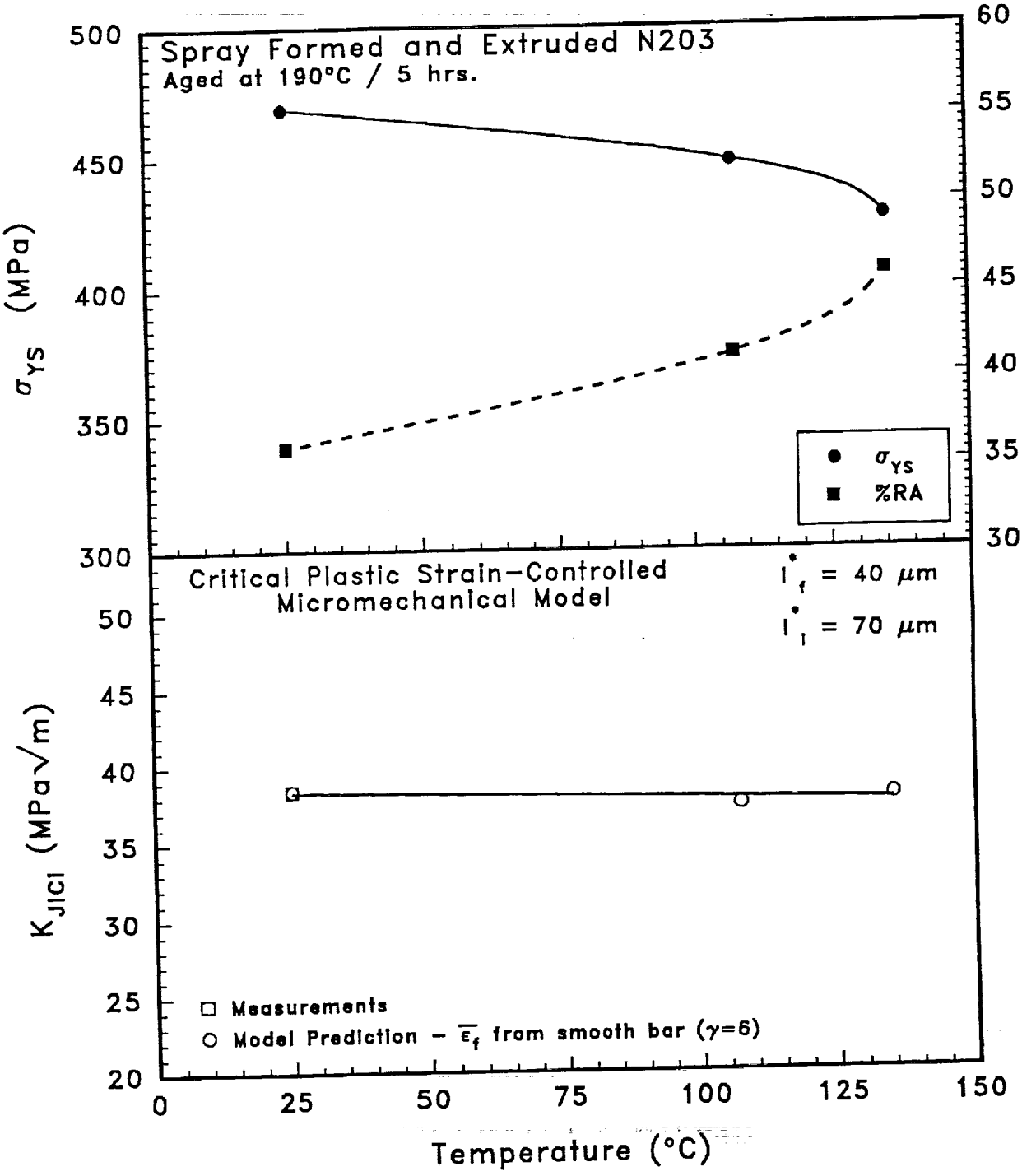

Proposed Work on Spray Formed N203

STAGE I:

- Measure N203 initiation (K_{JICI}) and growth (T_R) fracture toughnesses versus temperature and actuator displacement rate.
- Determine effect of pre-exposure on K_{JICI} and T_R.
- Predict temperature dependence of K_{JICI} through micromechanical modelling.
- Investigate metallurgical fracture mechanisms.

STAGE II:

Hypothesis: *The critical factor governing K_{JICI} is the strain at which primary, stable void growth is interrupted by strain localized coalescence. Important variables include inclusion distribution, strain hardening, strain rate sensitivity, slip mode, triaxiality, and microstructure within the strain localized band.*

- Study strain localization as a function of:
  - → rolling reduction / cold work (effects on precipitate and particle distributions)
  - → specimen orientation: LT, TL, SL (differing inclusion distributions)

Project #2 Cryogenic Temperature Effects on the Deformation and Fracture of Al-Li-Cu and Al-Li-Cu-In Alloys

John A. Wagner and R.P. Gangloff

Objective

The objective of this PhD research is to characterize and optimize the crack initiation and growth fracture resistance Al-Li-Cu (alloy 2090) and Al-Li-Cu-In (alloy 2090+In) for cryogenic tank applications. The program aims to understand microscopic fracture events; as influenced by ambient to cryogenic temperatures, stress state and microstructure. The specific goal is to determine the mechanisms associated with transgranular shear (TGS) fracture.

Status

This presentation provides a review of the initial work conducted on the fracture of 2090 and 2090+ In at ambient and cryogenic temperatures. It was observed that indium additions to 2090-based alloys increase T_1 number density with no change in yield strength. The toughness of 2090+In-T6 is low and characterized by intersubgranular fracture.

The current work in this project has been focusing on the details of the mechanisms associated with fracture of 2090-T81 at ambient and cryogenic temperatures. Crack growth resistance was correlated with fracture and grain morphology under nominal plane stress and plain strain conditions for tests conducted at 25 and -185°C to define the physical basis for fracture. The 2090-T81 plate studied in this investigation exhibited four different fracture modes:

- -delaminations
- -Intersubgranular (ISG) cracking
- -TGS fracture
- -slip band cracking (SBC)

Recent Results

Relative grain orientation in the region of TGS fracture was investigated

to gain insight regarding the underlying fracture mechanisms. Examination of electropolished specimen in the SEM BSe- mode showed that although this alloy is highly textured, the majority of grains within a TGS region were qualitatively of differing orientation and suggests that the propagation of the crack in the TGS region does not occur solely by cooperative SBC parallel to (111) planes within individual grains.

The delamination fracture process was examined by crystallographic characterization of regions around the delaminations. Electron Backscattered Patterns (EBSP) were obtained across the tips of several delaminations associated with an L-S section of a compact tension specimen. It was observed that delaminations occurred along high angle boundaries (27 to 40° misorientation), but not necessarily at boundaries with the highest misorientation. This suggest that other factors such as stress state, precipitate distribution and morphology also influence the initiation of delaminations.

Milestones

Future work will focus on completing the development of a physical model to describe the evolution of fracture in 2090-T81 at ambient and cryogenic temperatures. The EBSP technique will be used to examine grain orientation in the TGS fracture region.

Presentation Graphics Captions

1. Title.
2. Problem statement and program objective.
3. Presentation outline.
4. Material available from 350 lb. DC castings produced by Reynolds Metals.
5. Hardness behavior at 160°C of 2090+In-T6 is similar to 2090-T8.

6. Indium additions increase the ultimate strength at longer aging times, but yield strength is unaffected.

7. Ultimate and yield strength of 2090-T8 and 2090+In-T6 increase with decreasing temperature.

8. The table presented summarizes the test results from various laboratories on 2090+In-T6.

9. Tear strength to yield strength ratio, determined by Kahn Tear tests, of 2090+In-T6 increases with increasing temperature and shorter aging times.

10. Fracture of both baseline 2090 and 2090+In sheets is primarily intersubgranular.

11. Optical photomicrographs of the plate alloys investigated.

12. R-curve behavior of 1.6 mm (0.06") thick compact tension specimens from plate alloys tested at 25°C.

13. R-curve behavior of 12.0 mm (0.47") thick compact tension specimens from plate alloys tested at 25°C.

14. R-curve behavior of 12.0 mm (0.47") thick compact tension specimens from 2090 and 2090+In plate alloys tested at 25°C.

15. R-curve behavior and fracture cross sections of 2090-T81 1.6 mm (0.06") thick compact tension specimens tested at 25°C and -185°C.

16. R-curve behavior and fracture cross sections of 2090-T81 12.0 mm (0.47") thick compact tension specimens tested at 25°C and -185°C.

17. This figure shows delaminations along with TGS fracture in matched pairs of SEM fractographs together with the corresponding etched cross sections of the grain structure. In the location marked A is a small delamination with shear fracture across two grains. Location B is also a region of TGS fracture which shows that the shear fracture can propagate across several grains before arresting.

18. To qualitatively examine the orientation of grains in the region of 2090-T81 fracture where TGS was the dominate fracture mode, cross sections of 12.0 mm specimens tested at 25°C were electroetched and examined in cross polarized light or electropolished and examined in the SEM BSe- mode.

19. Fracture in areas which had a well defined substructure, in general, was characterized by ISG fracture. On the right side of cross sections in this figure is a region where fracture has been confined to a single grain in which the subboundaries are, in comparison, not decorated.

20. These are sectioned notched tensile optical and BSe images. The bottom three photomicrographs are of the smaller crack which is more centrally located. The crack tends to primarily follow grain boundaries typical of delamination fracture.

21. The bottom left photomicrograph shows two delamination cracks along boundaries being linked by a shear crack similar to what was observed in fracture toughness specimens. The photomicrograph on the right shows cracking along decorated substructure.

22. Recent results on intermediate temperature tests and EBSP crystallographic characterization of 2090-T81.

23. In intermediate temperature tensile tests, there is an increase in yield strength, modulus and work hardening exponent with a decrease in temperature.

24. R-curve fracture toughness behavior increases with decreasing temperature with the largest increase between -155°C and -185°C.

25. The increase in fracture toughness at cryogenic temperatures is associated with an increase in the level of delamination behavior.

26. EBSP patterns were obtained from an L-S fracture section of a specimen tested at -185°C.

27. Misorientation across delamination labeled "x" was 30°.

28. Summary

FRACTURE OF Al-Li ALLOYS 2090 AND 2090+In AT CRYOGENIC TEMPERATURES

John A. Wagner

LA^{2}ST Program Review

NASA Langley Research Center

July 25-26, 1994

FRACTURE OF 2090 AND 2090+In ALLOYS

Problem

- No systematic investigation conducted to determine the interactive effects of:
  - Temperature
  - Delamination
  - Indium addition
  - Microstructure

  on the fracture of 2090-based alloys

Objective

- Determine the influences of microstructure, stress state and temperature on the occurrence of various fracture modes in Al-Li-Cu-X alloys. Understand the mechanism(s) associated with transgranular shear fracture

FRACTURE OF 2090 AND 2090+In ALLOYS AT CRYOGENIC TEMPERATURES

OUTLINE

- Summary of tensile and fracture properties of 2090+In-T6
- Intermediate temperature tests of 2090-T81
- Electron Backscatter Patterns(EBSP's) from 2090-T81 Metallographic Sections

CHEMICAL COMPOSITIONS AND PROCESS HISTORIES OF AVAILABLE ALLOYS

Alloy 2090: Al-2.65Cu-2.17Li-0.13Zr-0.06Fe-0.05Si (wt%)
2090+In: Al-2.60Cu-2.34Li-0.16Zr-0.05Fe-0.04Si-0.17In (wt%)

Material available:

1. 2090 Base chemistry

-3.2 mm sheet	TMT C	SHT	3% stretch
-3.2 mm sheet		TMT C	SHT @ LaRC
-12.7 mm plate		SHT	3% stretch

2. 2090+In

-3.2 mm sheet	TMT C	SHT	3% stretch
-3.2 mm sheet		TMT C	SHT @ LaRC
-12.7 mm plate		SHT	3% stretch
-12.7 mm plate		SHT	0% stretch

HARDNESS, R_B AS A FUNCTION OF AGING TIME FOR 2090 AND 2090+In AGED AT 160°C

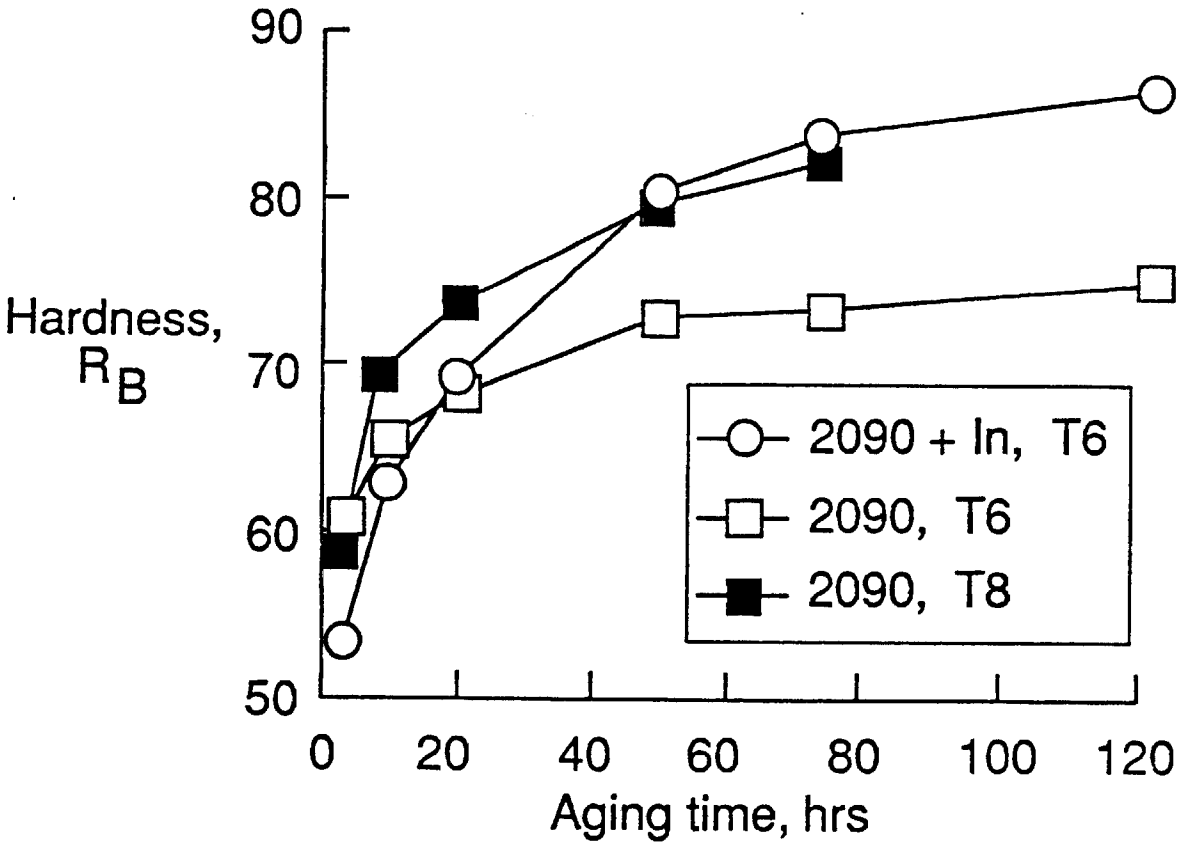

VARIATION OF ROOM TEMPERATURE STRENGTH WITH AGING TIME AT 160°C

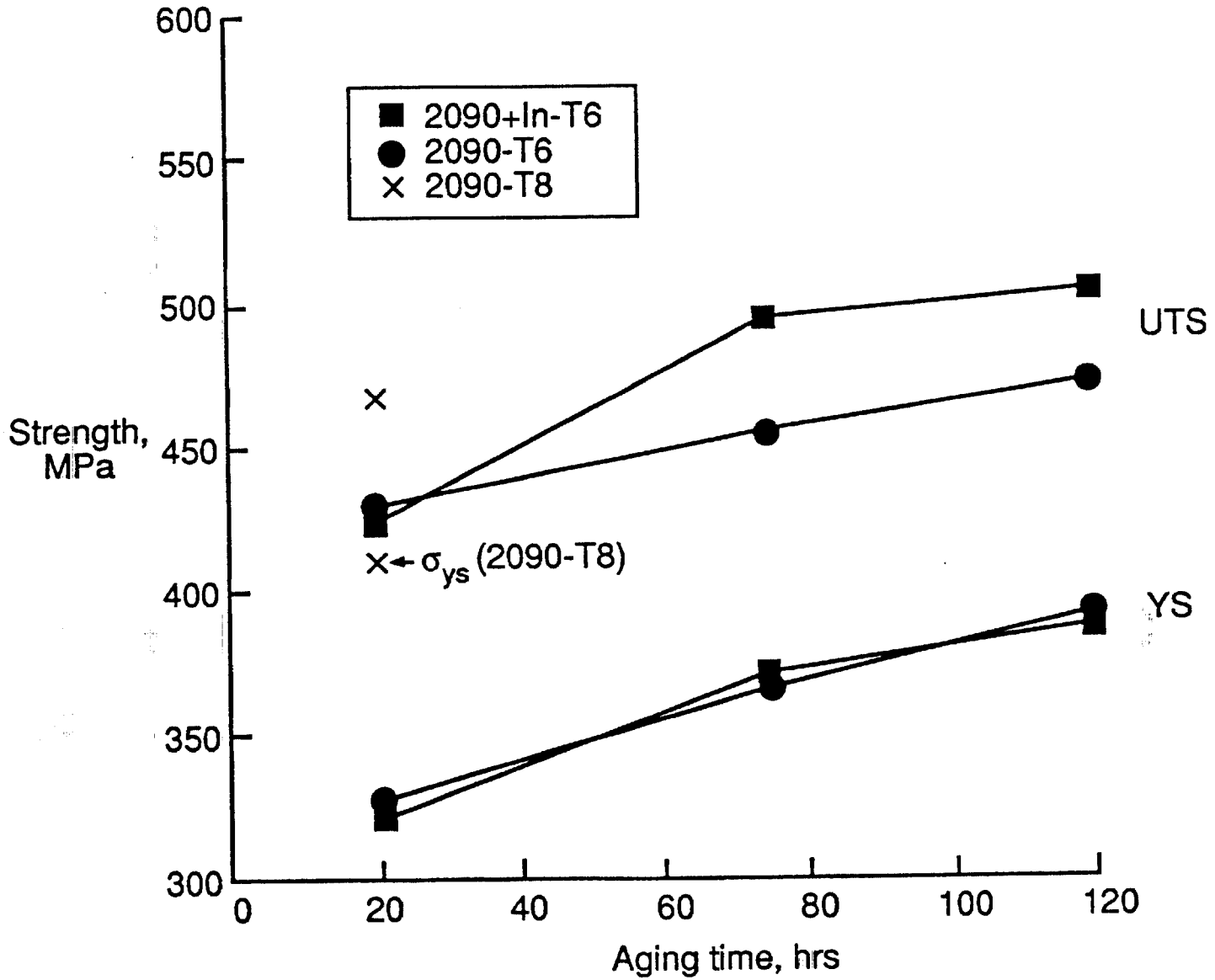

AMBIENT AND CRYOGENIC TENSILE PROPERTIES OF 2090 AND 2090+In AGED AT 160°C FOR 75 HOURS

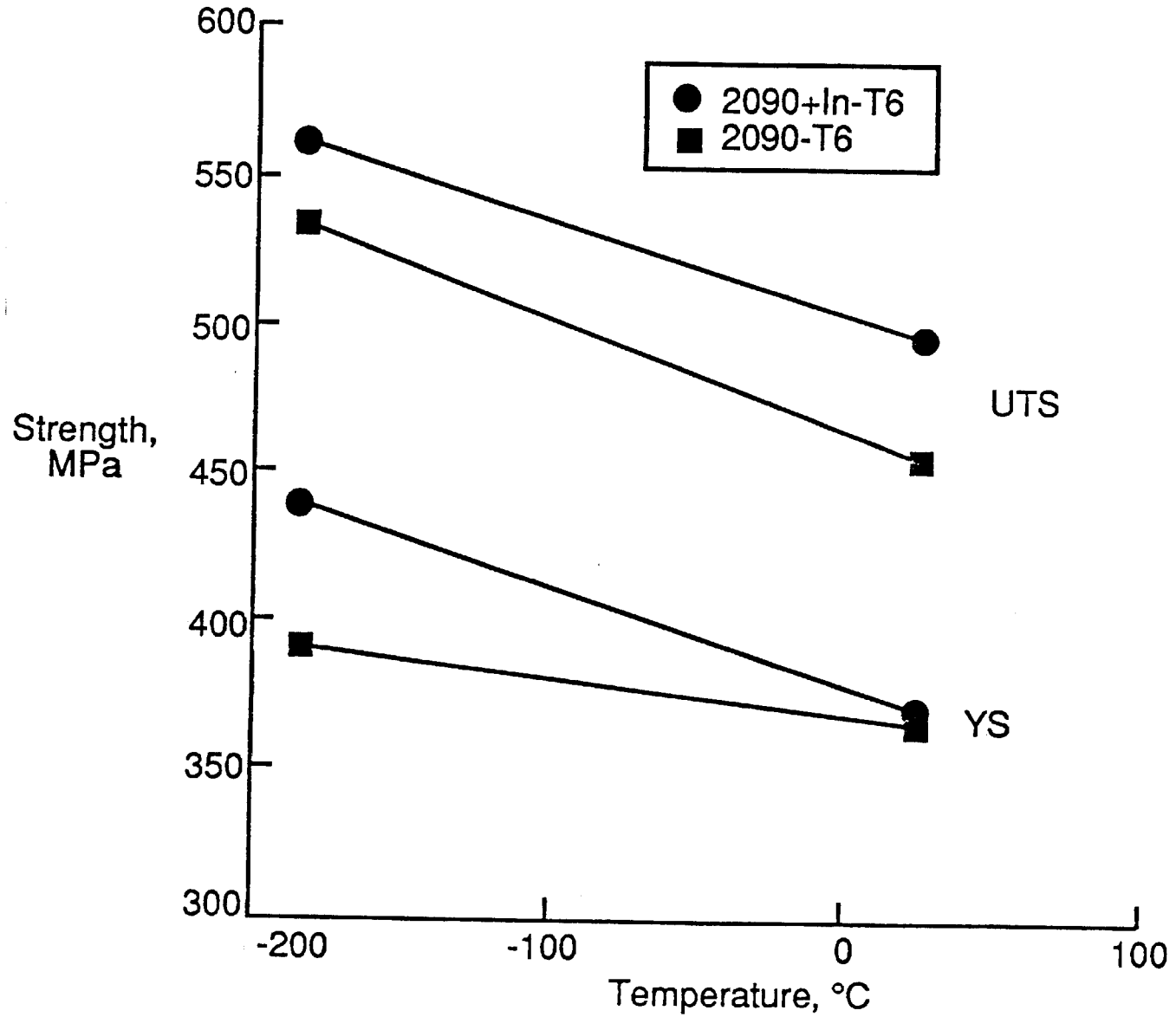

2090 + In - T6 TENSILE PROPERTIES

(SHT = 538-560°C, 160°C 72-100 hrs)
2090-T81: σ_{ys} = 559MPa
2090-T6: σ_{ys} =476MPa

Lab	Ingot Size	Material Condition	σ_{ys}	σ_{ult}
Northrop	160kg	SPF 150%	400MPa	531MPa
			407	517
		TMTC	372	482
Reynolds	14	Sheet	441	510
			448	496
LBL (Bradley)	160	SPF 90%	386	538
		TMTC	386	517
LBL (Verzsconi)	160	SPF Thermal No Strain	365	461
NASA (Wagner)	160	TMTC	372	496
		12.7mm plate	400	559
NASA (Wagner)	14	12.7mm plate	434	517
NASA (Blackburn)	14	12.7mm plate	490	538
Boeing	160	no data available; but no increase in properties observed		

TEAR STRENGTH TO YIELD STRENGTH RATIO OF 2090+In-T6

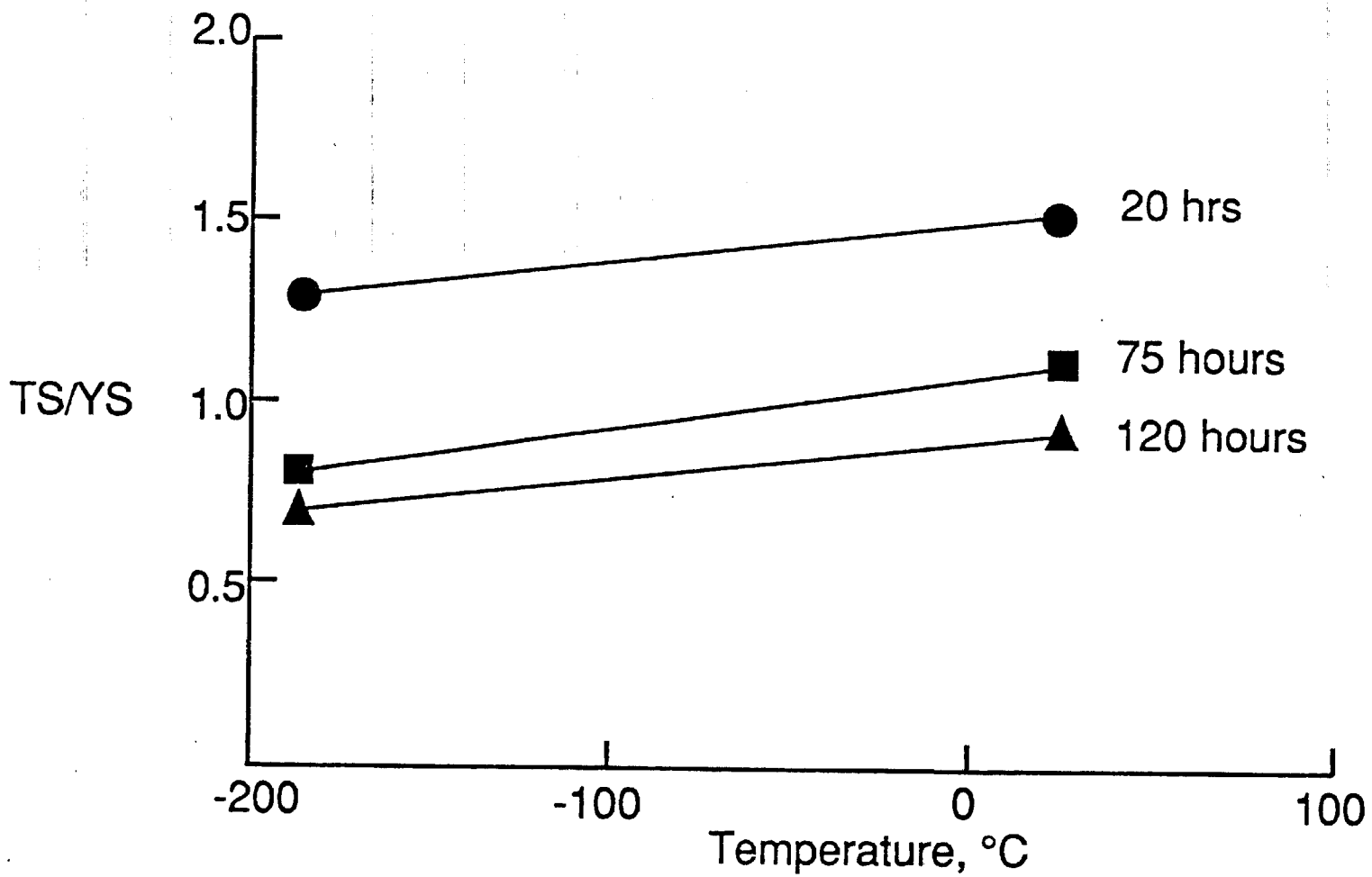

FRACTURE PATH AND FRACTURE SURFACE MORPHOLOGY OF R2090 BASELINE TESTED AT CRYOGENIC TEMPERATURES

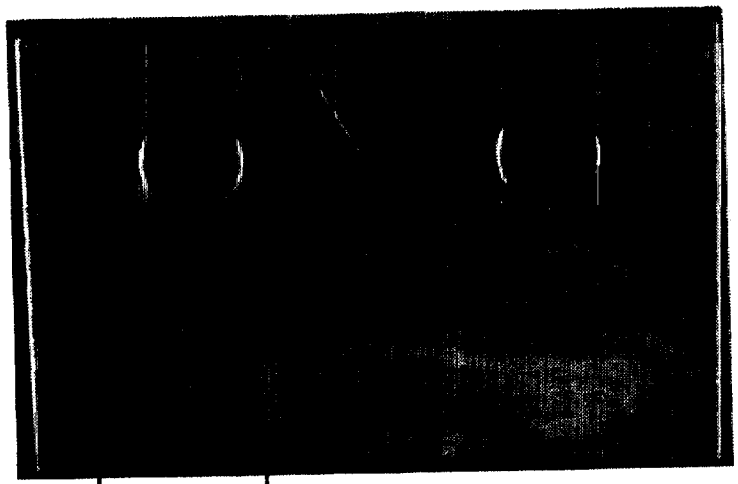

0.562 in.

A

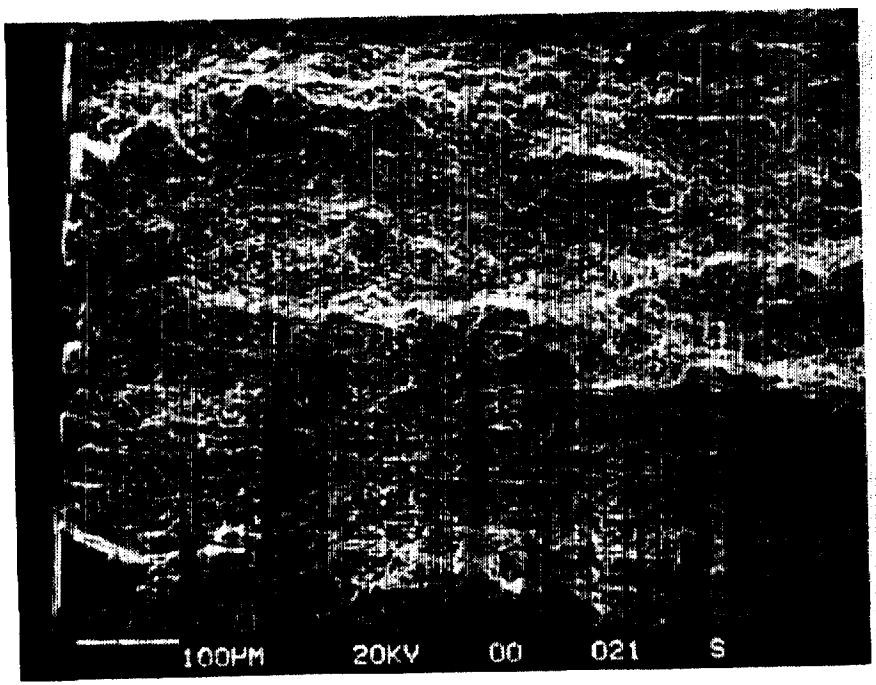

B

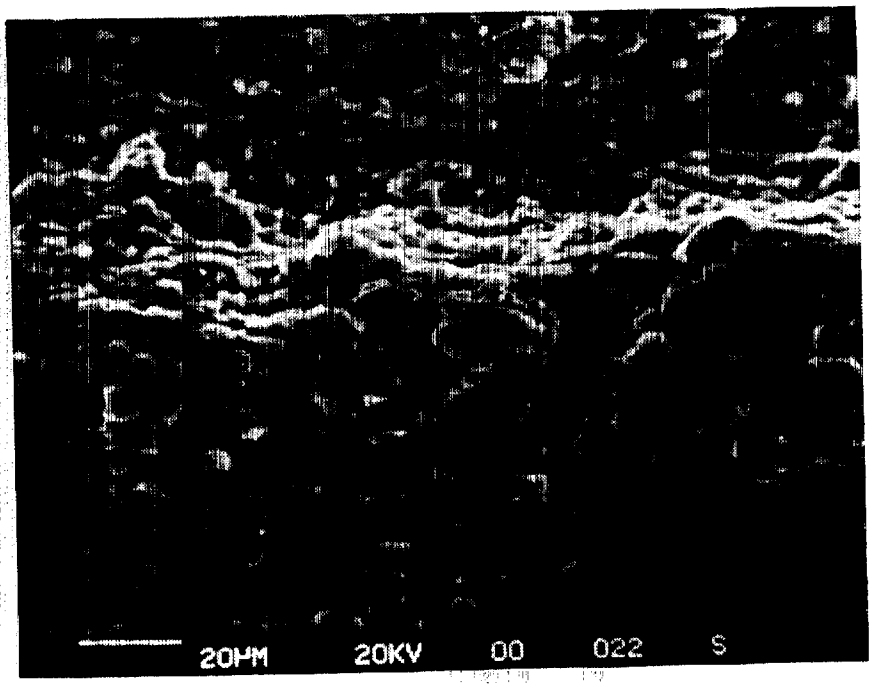

C

MICROSTRUCTURES OF PLATE ALLOYS

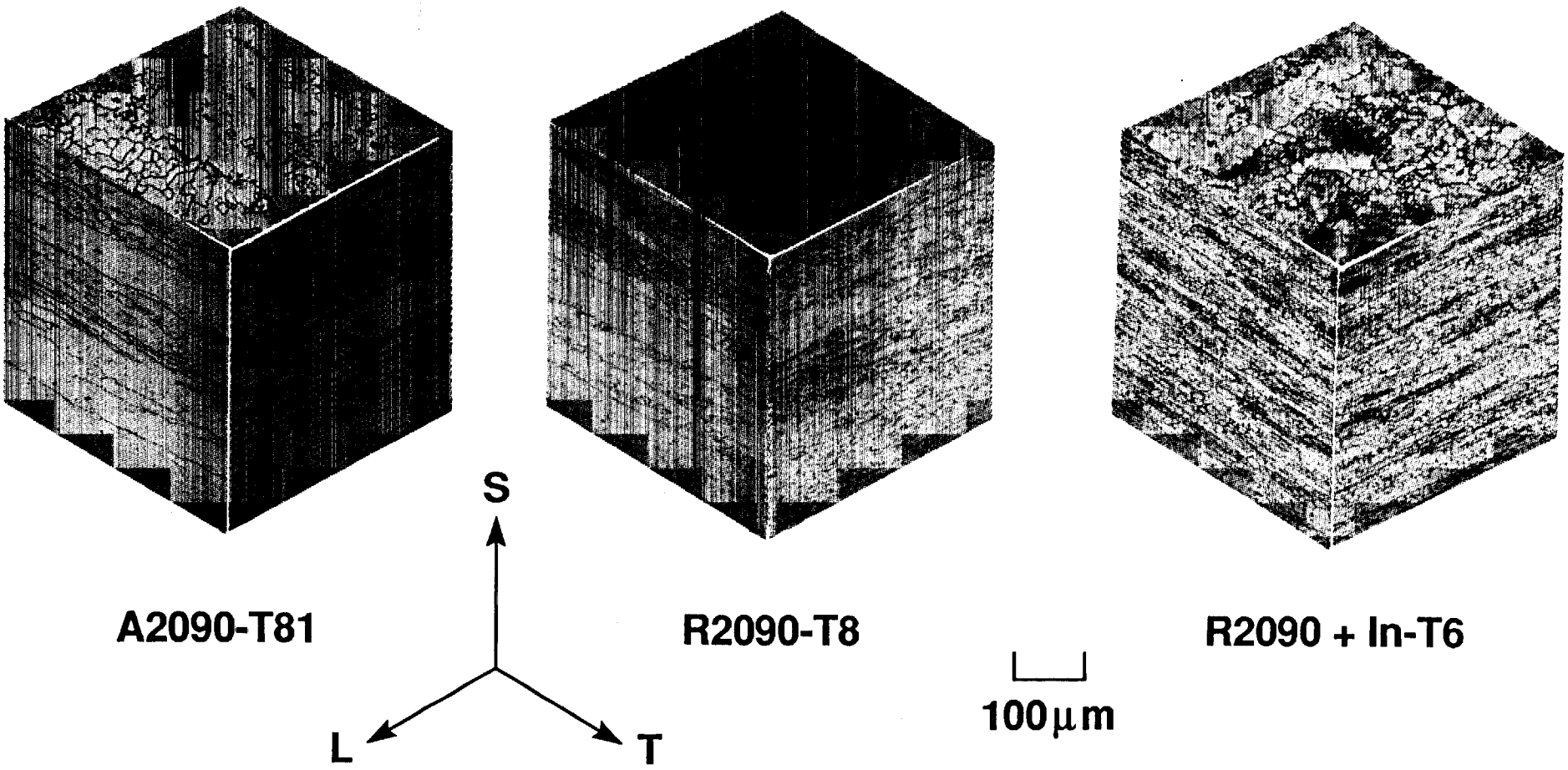

FRACTURE TOUGHNESS R-CURVE FOR 0.06" THICK SPECIMENS

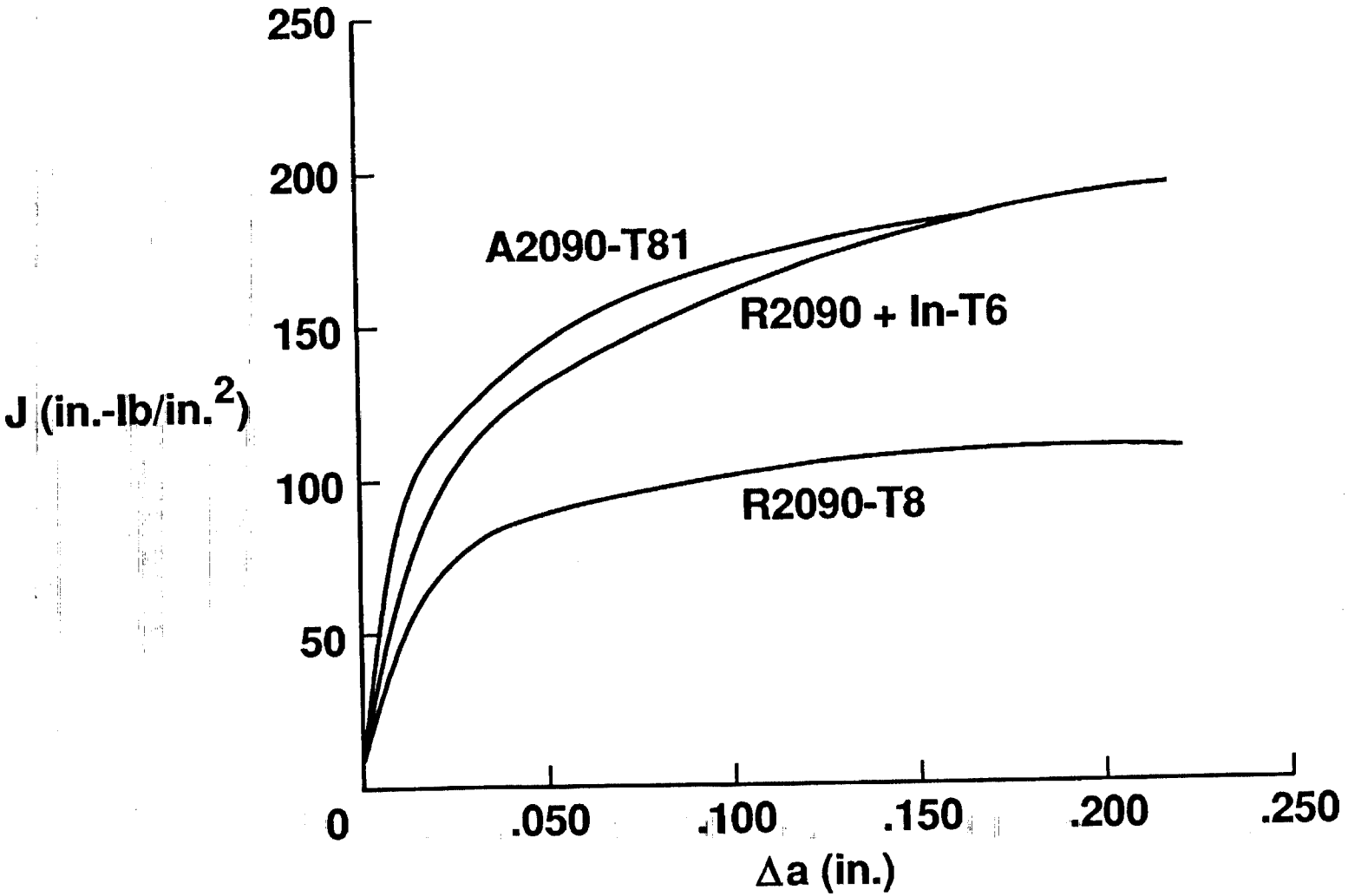

FRACTURE TOUGHNESS R-CURVE FOR 0.47" THICK SPECIMENS

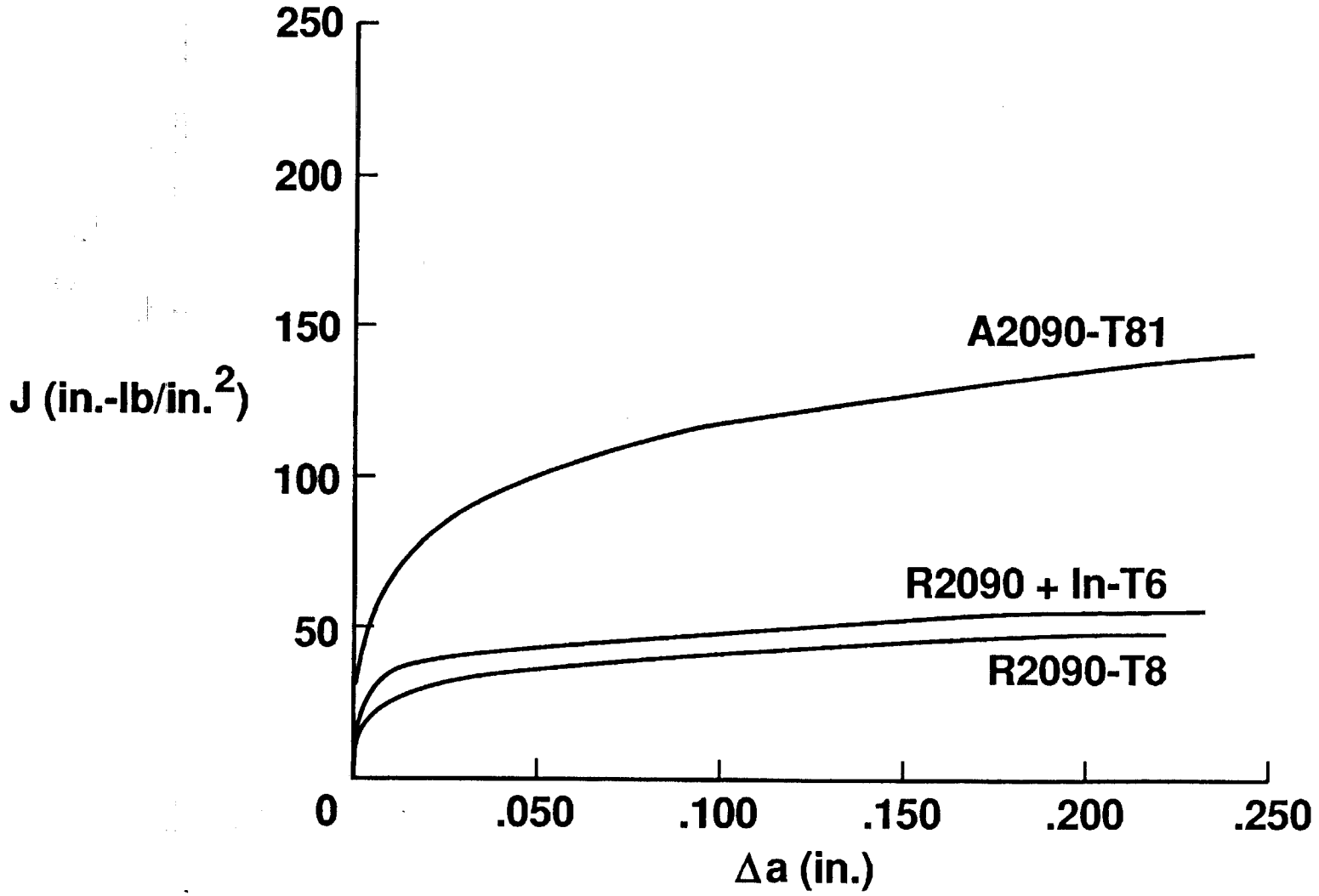

FRACTURE TOUGHNESS OF CONVENTIONAL AND CHEMISTRY MODIFIED 2090 Al-Li ALLOY

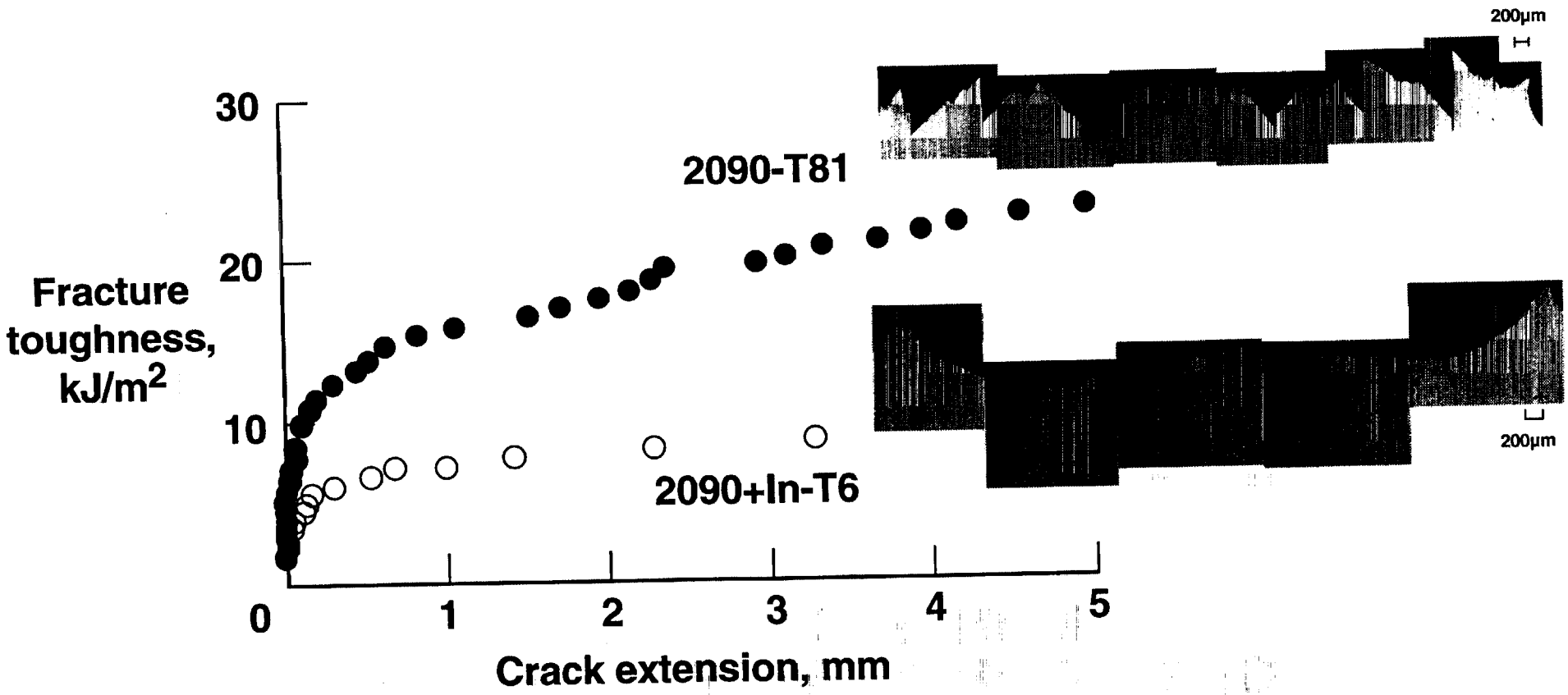

R-CURVES FOR 1.6MM 2090-T81 SPECIMENS TESTED AT 25°C AND -185°C

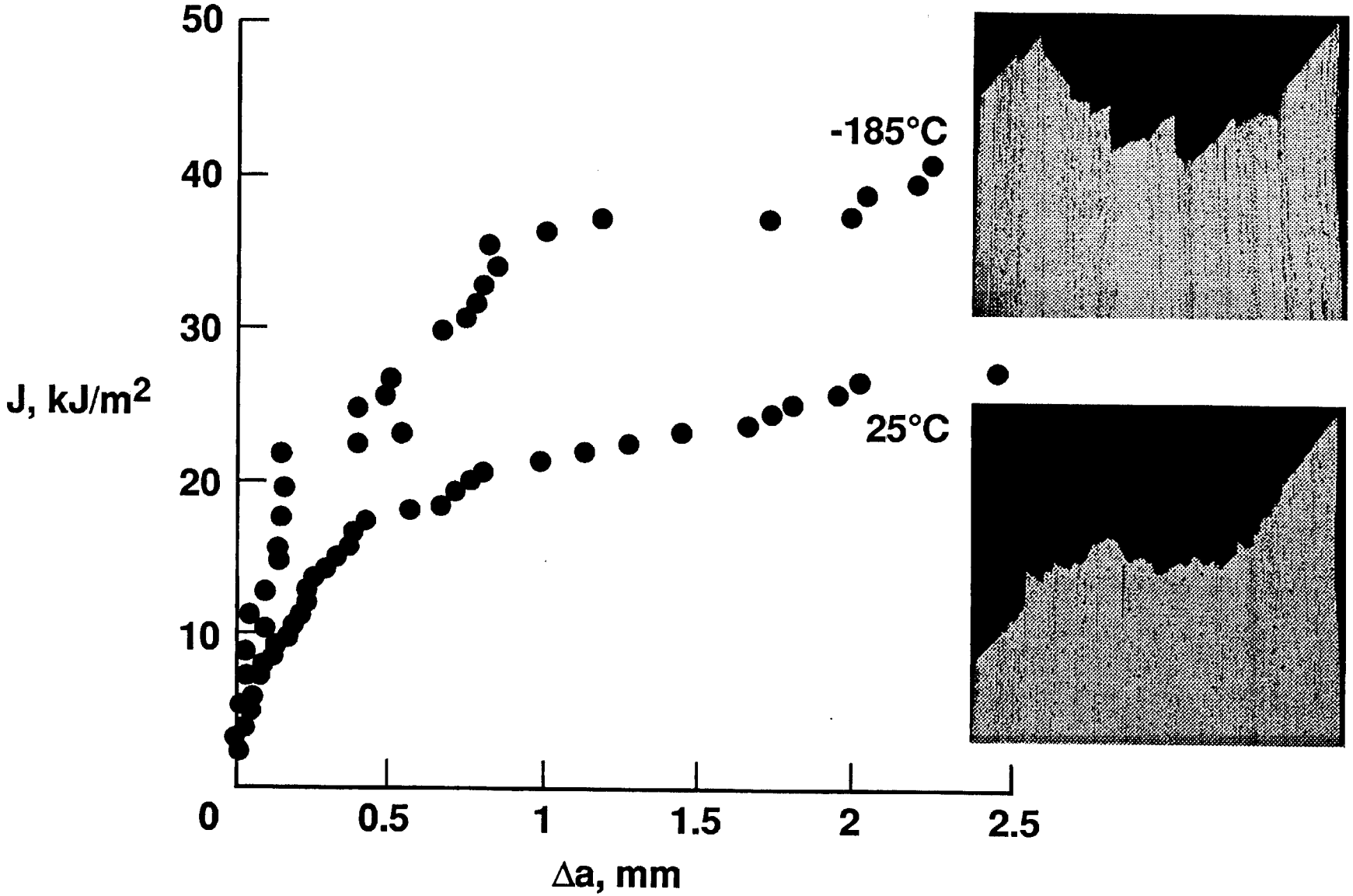

r-crvs 1.6mm 2090-t81

R-CURVES FOR 12MM 2090-T81 SPECIMENS TESTED AT 25°C AND -185°C

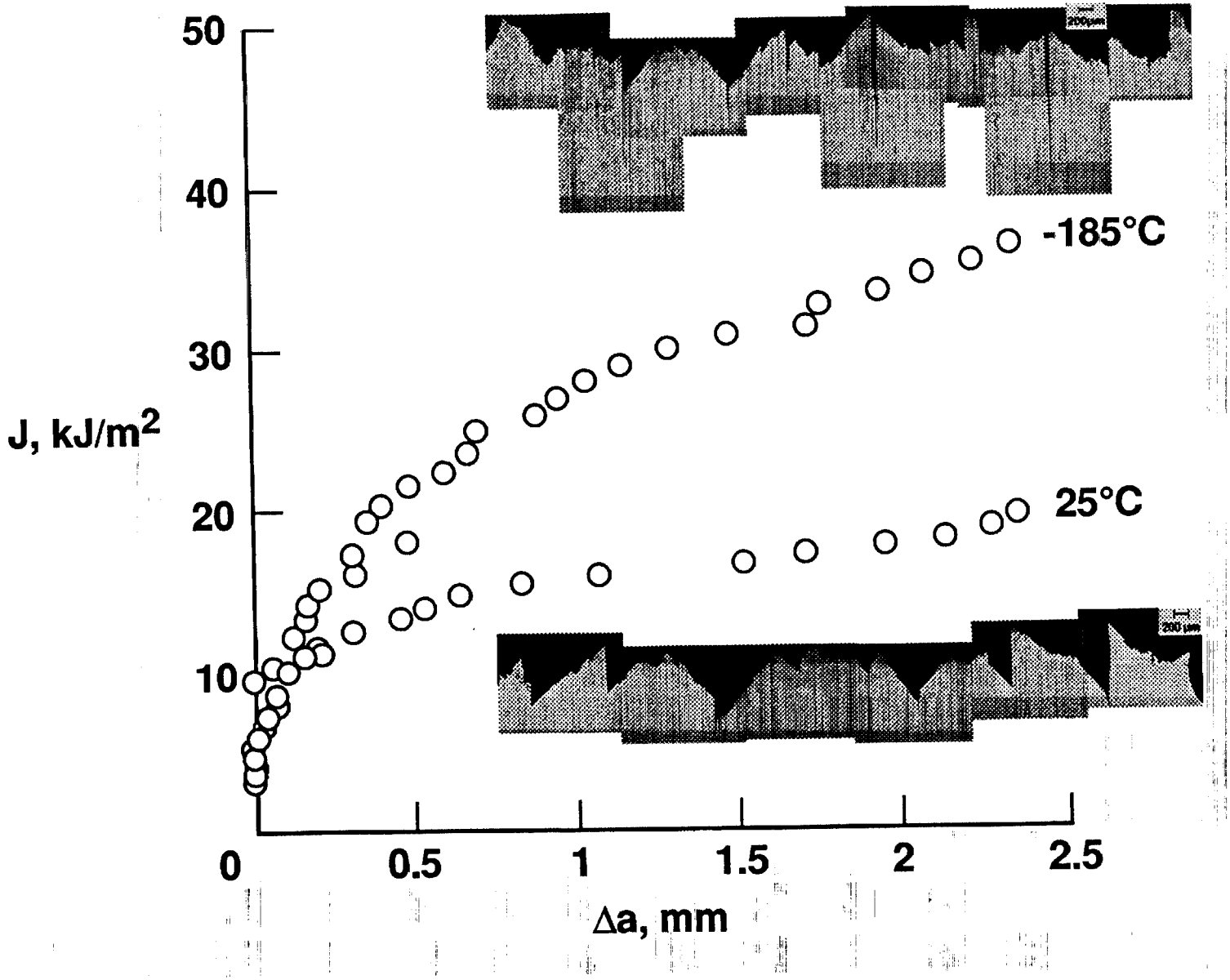

TRANSGRANULAR SHEAR FRACTURE IN 2090-T81 AT -185°C

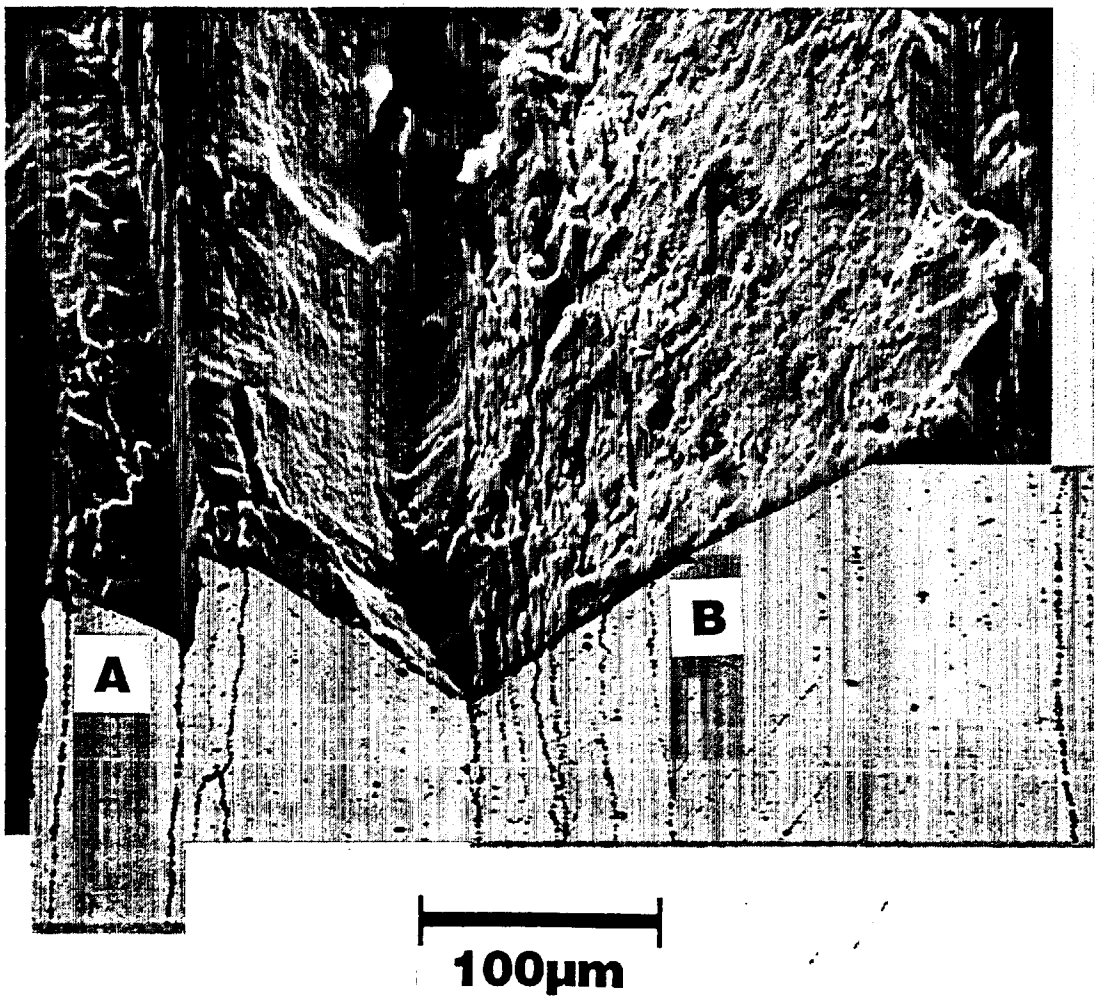

Figure 4

paste up Fig 4

CROSS SECTIONS OF TRANSGRANULAR SHEAR FRACTURE REGION IN 2090-T81

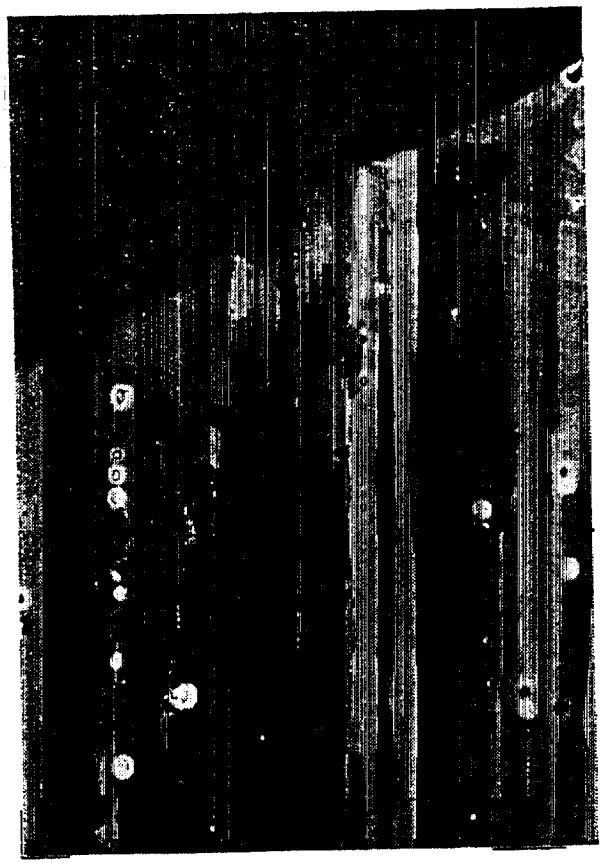

20μm

Backscattered electron image

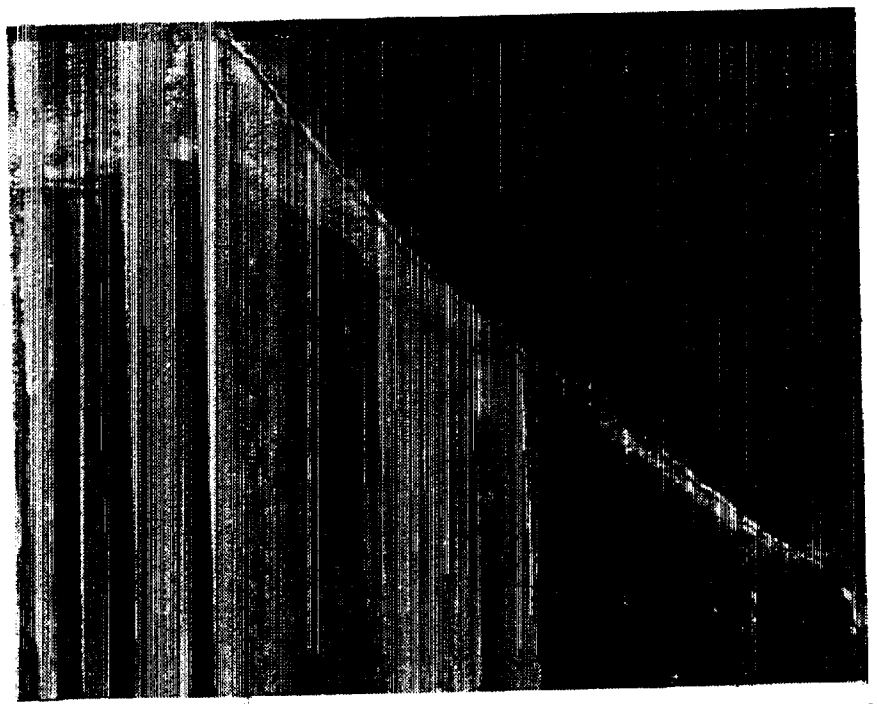

10μm

Cross polarized light image

Figure 5

INTERSUBGRANULAR FRACTURE AND AND SLIP BAND CRACKING 2090-T81

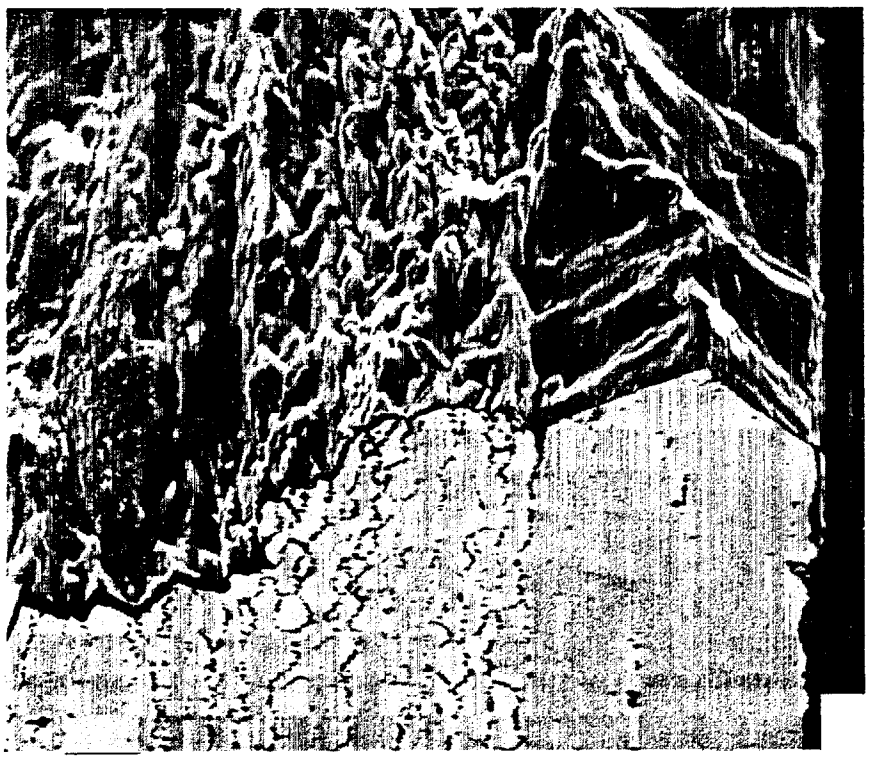

3A

40µm

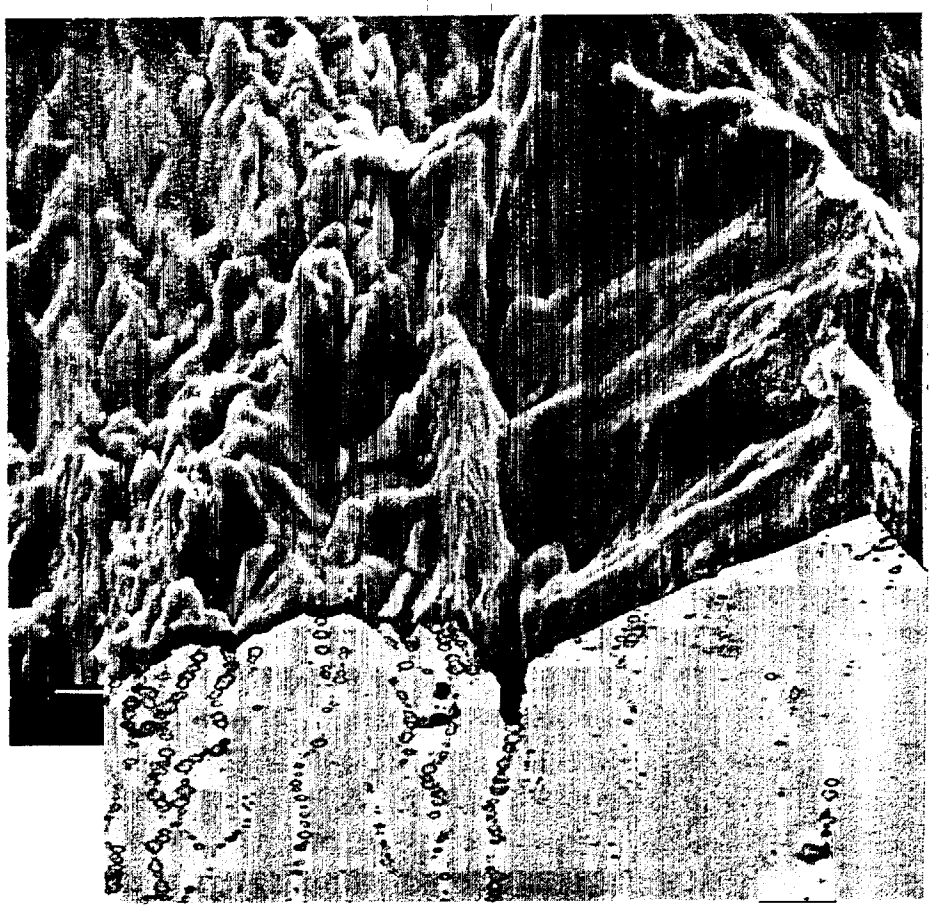

3B

10µm

Figure 3

OPTICAL AND BACK SCATTERED IMAGES OF THE MIDPLANE OF INTERUPTED NOTCH TENSILE TEST AT -185°C

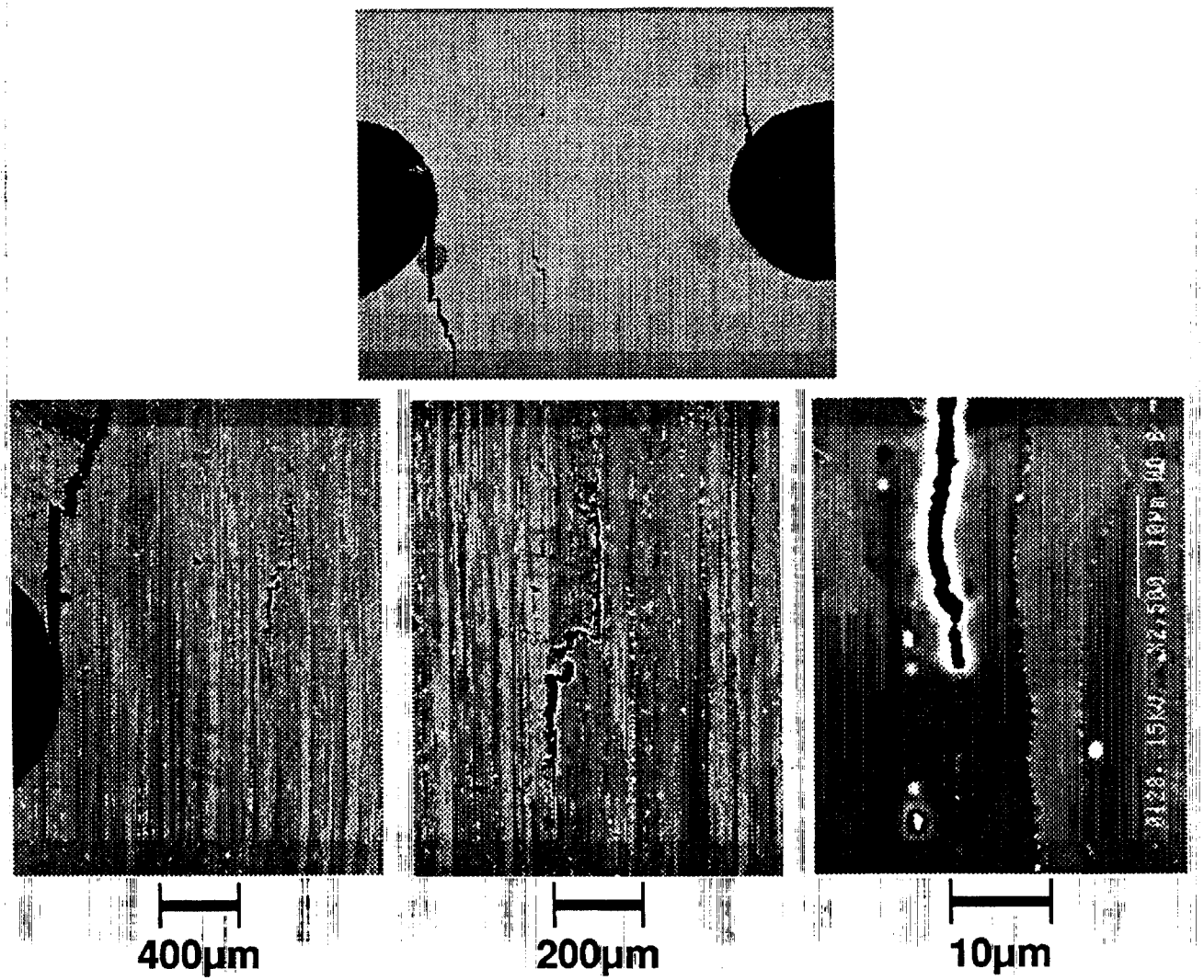

ptcl & bck scttrd mgs

CROSS SECTION OF NOTCHED TENSILE SPECIMEN TESTED TO FAILURE AT -185°C

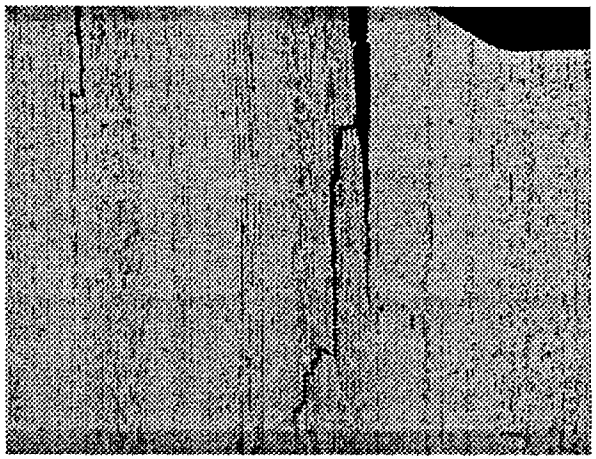

200µm

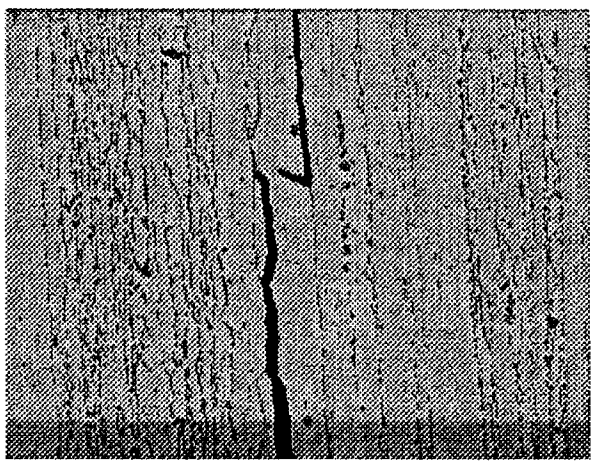

50µm

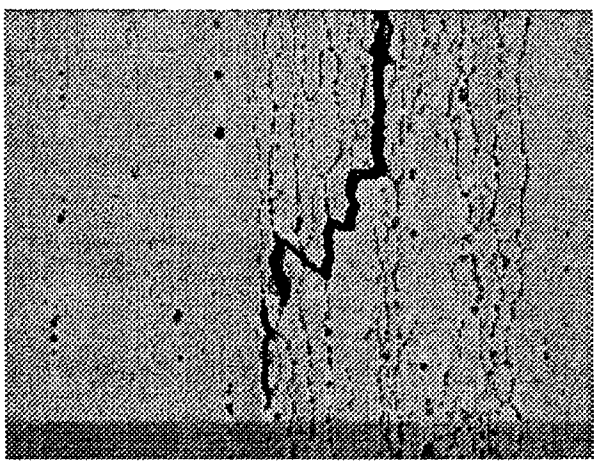

20µm

crss sctn ntchd tnsl spcmn

FRACTURE OF Al-Li ALLOYS 2090 AND 2090+In AT CRYOGENIC TEMPERATURES

RECENT RESULTS

- Intermediate Temperature Tests
- EBSP of Metallographic Fracture Cross Sections

TRANSVERSE TENSILE PROPERTIES OF 2090-T81 AT INTERMEDIATE TEMPERATURES

TEMPERATURE T, °C	YIELD STRENGTH σys, MPa	MODULUS E, GPa	WORK HARDENING EXPONENT, n
25°	537	77.2	0.052
-25°	548	81.4	0.054
-75°	570	83.4	0.055
-125°	588	84.1	0.062
-155°	595	85.5	0.076
-185°	607	87.6	0.081

R-CURVES OF 12MM THICK SPECIMENS AT -185°C T0 25°C

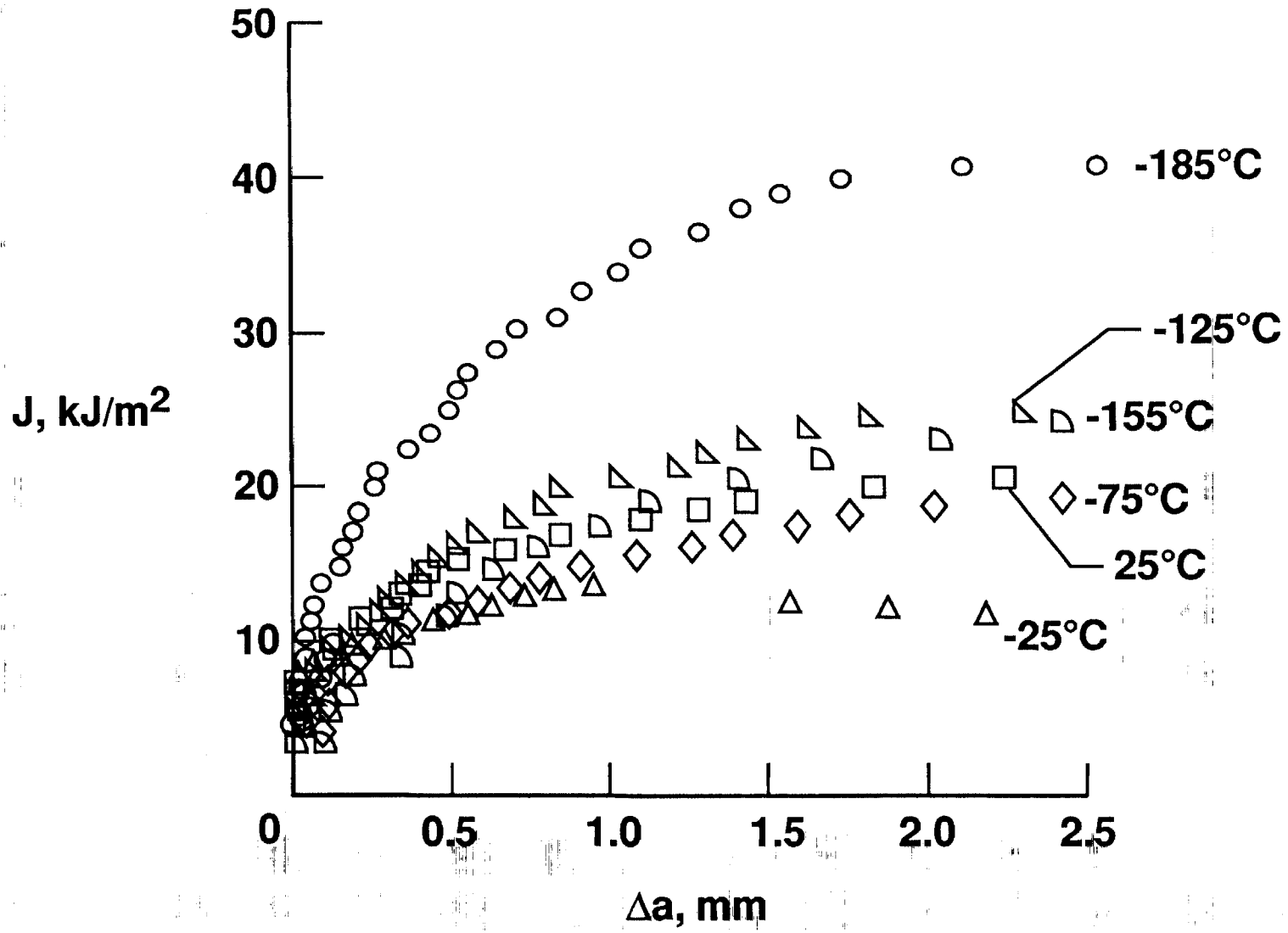

r-crvs 12mm/7.94

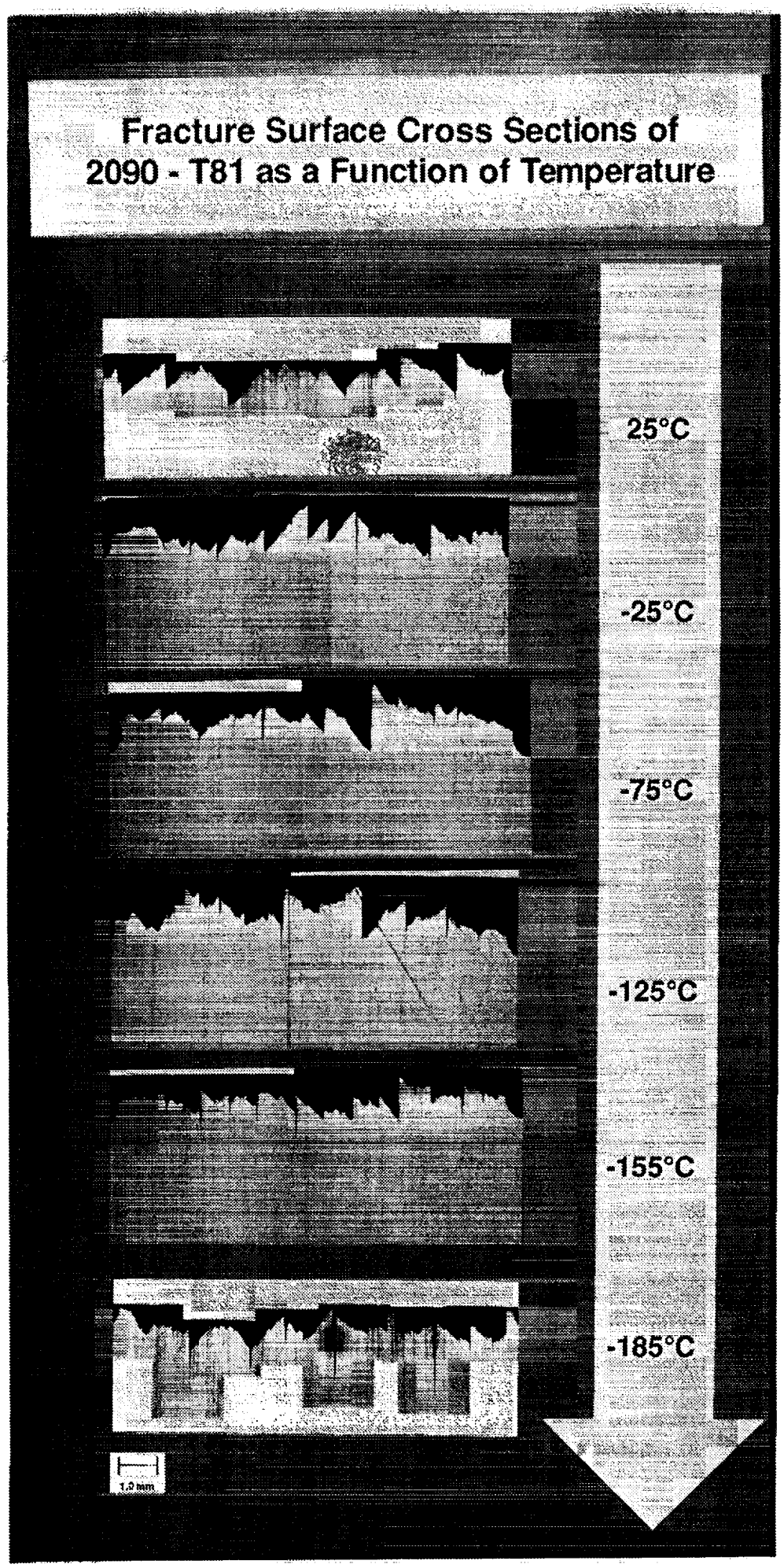
Fracture Surface Cross Sections of
2090 - T81 as a Function of Temperature
25°C
-25°C
-75°C
-125°C
-155°C
-185°C
1.0 mm

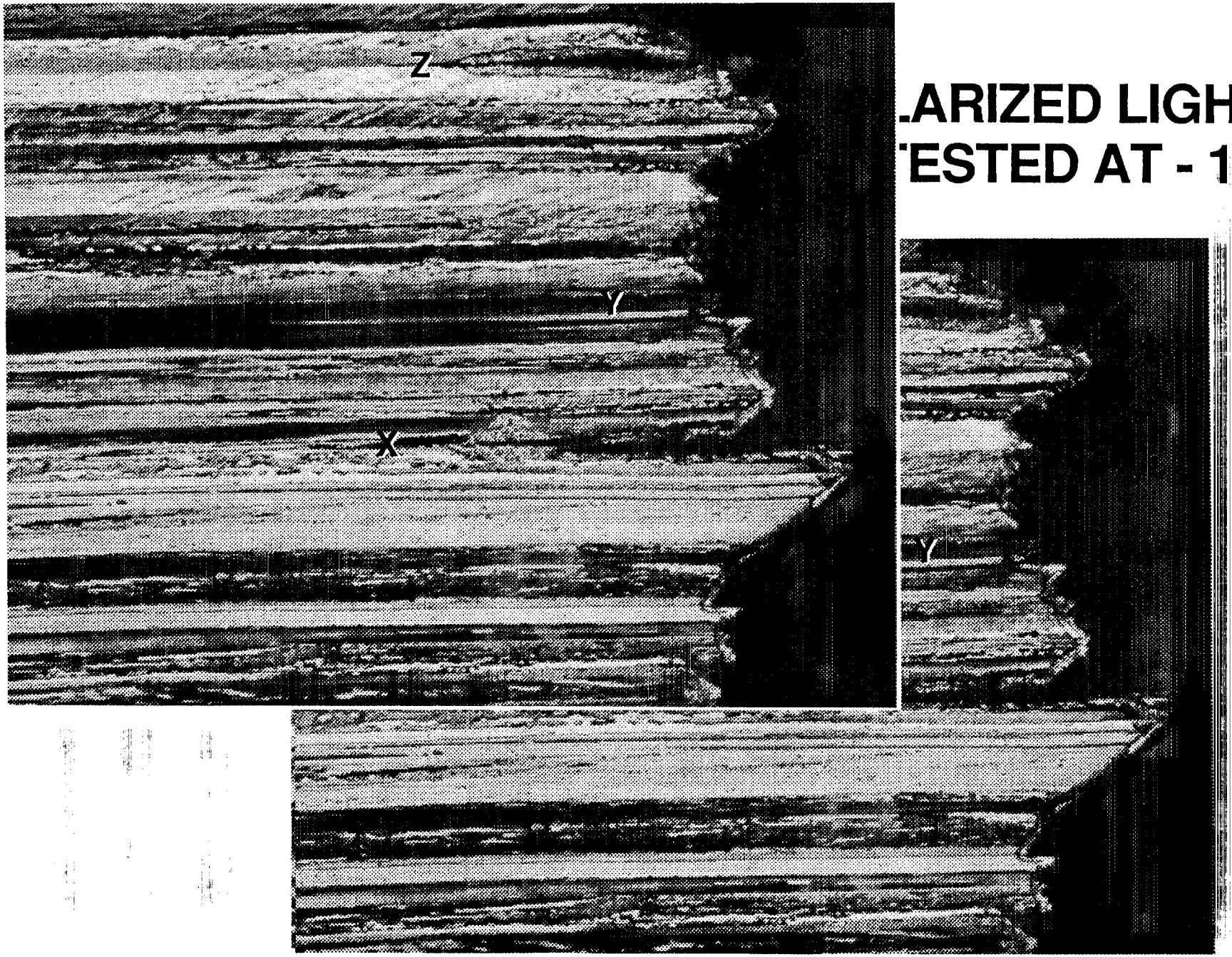

_ARIZED LIGHT OF
'ESTED AT - 185°C

400 µm

MISORIENTATION ANGLE AS A FUNCTION OF THE (SUB)GRAIN NUMBER, ALONG ND

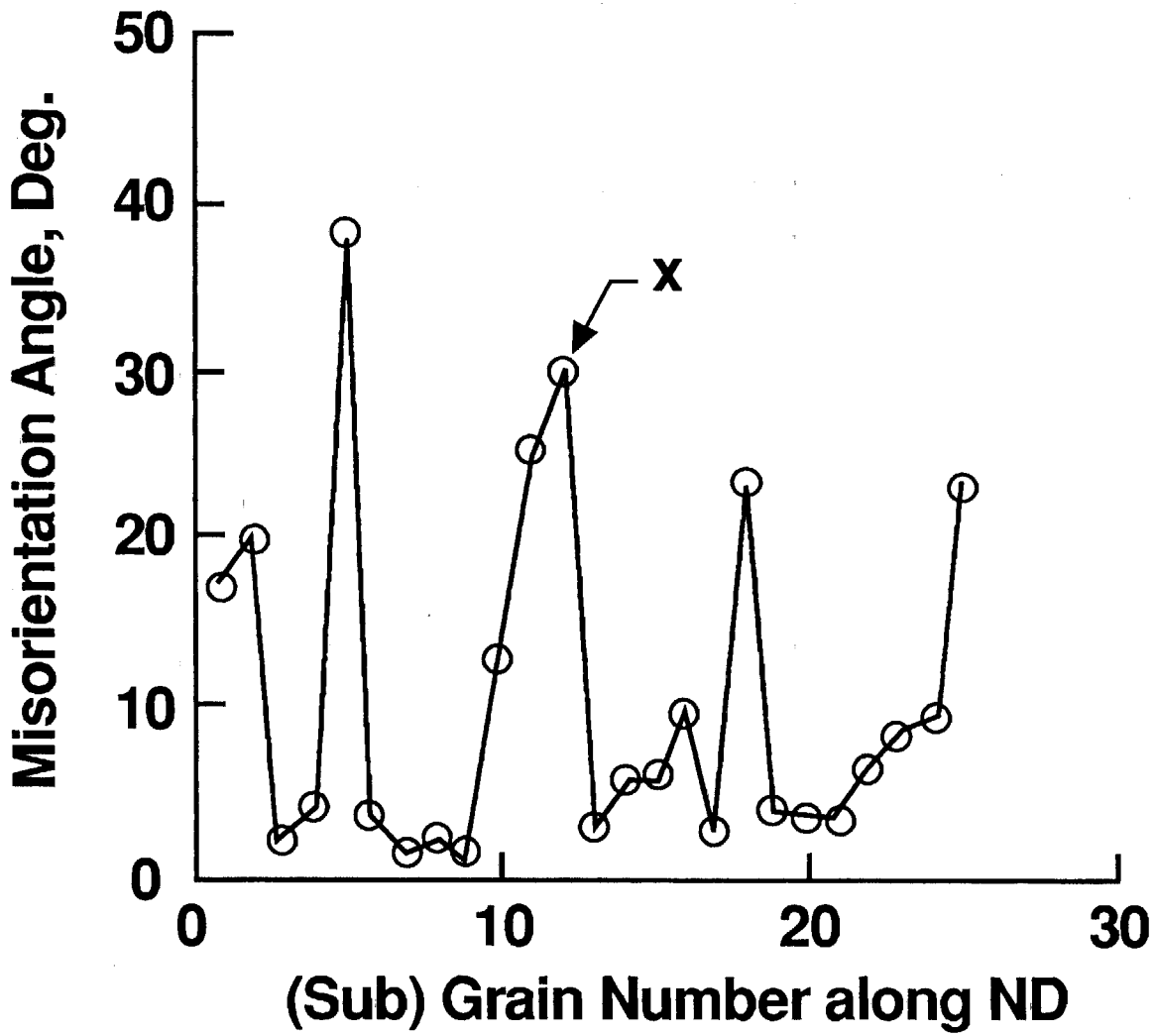

MISOR

FRACTURE OF 2090-T81 AT CRYOGENIC TEMPERATURES

SUMMARY

- Fracture in 2090-T81 is characterized by four fracture modes:
  - -Intersubgranular
  - -Slip band cracking
  - -Delamination
  - -Transgranular shear

- All 2090-T81 specimens exhibit an increase in toughness at -185C and is primarily associated with an increase in the level of delamination and work hardening

- Delaminations occur along high angle boundaries but not necessarily at boundaries with the highest misorientation

- Transgranular shear fracture across multiple grains of different orientations suggests a macroscopic shearing event and not cooperative slip band cracking

Project #3 The Effects of Cryogenic Temperature and Aging on the Fracture Toughness of Weldalite™ X2095

Cynthia L. Lach and Richard P. Gangloff

Objective

The objective of this research is to characterize the effect of cryogenic to mildly elevated temperature on the tensile fracture toughness of an emerging composition of Weldalite™-type alloys. We will determine quantitative initiation and growth fracture toughness data, as well as the associated microscopic fracture mechanisms and micromechanical models in order to understand temperature dependent fracture.

Status

Two Weldalite™ X2095 compositions were selected for study to examine the limits of the Li and Cu levels for the alloy registered as AA2095. Specifically, a high Li-Cu alloy (Al-4.64Cu-1.53Li-0.34Ag-0.37Mg-0.17Zr; wt%) at the upper extreme of the AA2095 composition specification, and a low copper alloy (Al-4.04Cu-1.00Li-0.37Ag-0.36Mg-0.15Zr; wt%) in the middle of the AA2195 specification were chosen for evaluation. Fracture toughness is investigated for peak-strength aged AA2195 as a function of test temperature and in terms of applied J-integral versus crack extension.

The following experiments were conducted on the alloy variants during this reporting period: optical microscopy and image analysis in the as-received (-T3) condition, texture analysis at various locations through the thickness of the plate, ambient and cryogenic hardness measurements of tensile and compact tension specimens, and uniaxial tensile tests from -185°C to 135°C. Fracture toughness tests of the peak-strength aged AA2195 are 80% complete.

Recent Results

The through-thickness microstructure of the low Cu-Li alloy (AA2195)

is inhomogeneous, varying from fully recrystallized at the surface to completely unrecrystallized at the mid-plane. The high Cu-Li alloy (AA2095) is essentially recrystallized throughout the entire cross-section of the plate. Image analysis revealed that the average undissolved-phase particle size for AA2195 was 0.7 μm, with about 90% of the particles less than 1.0 μm in size. The average particle size for AA2095 was 4.5 μm with about 95% greater than 1.0 μm. The textures of both AA2195 and AA2095 were inhomogeneous through the thickness of the plate. The two alloy variants demonstrated different types of textures, but at the mid-plane both alloys exhibited a strong Brass deformation texture component. Microstructure and texture were affected by the amounts of Cu and Li present in the alloys. As a result of the texture, microstructural, and image analyses, it can be concluded that AA2095 recrystallized (throughout) by particle stimulated nucleation, while AA2195 recrystallized (near-surface) by strain induced grain boundary migration.

The alloy variants exhibited a nearly linear correlation of tensile bar hardness to yield strength, regardless of temperature. Fracture toughness results were plotted as a function of the calculated yield strength of the C(T) specimens. The scatter in toughness reported in the last progress report was somewhat reduced. For the peak-strength aging condition (AA2195 aged for 30 hours at 143°C), as test temperatures decreased, the yield and ultimate tensile strengths increased, as did the extent of work hardening.

Milestones

Fracture toughness experiments will measure the J-crack growth response, based on the automated unloading compliance method, for cryogenic to mildly elevated temperatures for AA2195 aged at 143°C for 30 hours.

The deformation behavior of AA2195 will be characterized at several temperatures, (-185, -140, -125, -75, -25, 25, 107, and 135°C). Tensile yield strength, work hardening, and fracture strain (reduction in area) will be measured as a function of temperature for the constant alloy composition and

age of the toughness-temperature study. The fracture surfaces will be examined by SEM to detect temperature dependent changes in the details of the microvoid-based fracture process.

Presentation Graphics Captions

1. Title.

2. Objective.

3. Approach.

4. Issues.

5. The table displays the registered compositional limits of Weldalite™ 049 alloys. The original lean and rich chemistries were chosen to reflect the upper and lower limits of the X2095 alloy. The lean variant chemistry (4.0 wt% Cu-1.0 wt% Li) also happens to fall in the middle of the AA2195 specification.

6. The optical micrograph cubes of both variants of as-received X2095-T3 (magnification 100X) show the amount and relative size of the primary phase present in each chemistry. It has been confirmed through EDAX analysis that the primary phase is Cu-rich. The low Cu alloy (AA2195) contains on average 0.4 volume percent of primary phase, while the high Cu alloy (AA2095) contains 1.9 average volume percent.

7. The through-thickness microstructures of the entire thickness (12.7mm) are shown in the optical micrographs of anodized specimens for both alloy variants. The through-thickness microstructure of the low Cu-Li alloy (AA2195) is inhomogeneous. The mid-plane of the plate is completely unrecrystallized. From the mid-plane toward the outer surfaces, the plate exhibits a mixture of unrecrystallized and recrystallized grain structures. At the outer surfaces, the microstructure is completely recrystallized. The microstructure of the high Cu-Li alloy (AA2095) is essentially recrystallized throughout the entire cross-section of the plate.

8. The microstructures corresponding to the mid-plane of the 12.7mm plate for the two alloy variants in the as-received condition are shown in these optical micrographs of anodized specimens. The compact tension specimens were machined from the mid-plane (3.9mm thick), and are representative of these two microstructures. At the mid-plane, AA2195 is unrecrystallized while AA2095 is completely recrystallized.

9. Image analysis was conducted on polished and lightly etched samples of the two alloy variants in the as-received condition. The average particle size for AA2195 was 0.7 microns, with ~90% of the particles less than 1.0 micron in size. The average particle size for AA2095 was 4.5 microns with ~95% greater than 1.0 micron in size.

10. The Weldalite™ alloy plates were produced commercially by Reynolds Metals Company from 10,000 lb ingots. The two ingots underwent the same thermomechanical process (TMP) to produce the 12.7mm plates, which were then solution heat treated and stretched 6% (-T3 temper). The resulting microstructure and texture was affected by the amounts of Cu and Li present in the alloys. The low Cu alloy (AA2195) had a low volume fraction of small (0.7 micron) primary particles, while the high Cu alloy (AA2095) had a high volume fraction of large (4.5 microns) primary particles. Humphreys and Kalu have shown that the critical particle size for recrystallization by particle stimulated nucleation (PSN) is 1 to 5 microns. The effect of large primary particles during TMP can be to create deformation adjacent to the large particles, which in turn create nucleation sites that can cause recrystallization via PSN. Thus, alloy AA2095 recrystallized by PSN. AA2195 was found to have recrystallized by strain induced grain boundary migration. For the processing condition used, the critical particle size is estimated to equal 2.6μm.

11&12. Texture analysis using crystallite orientation distribution functions (CODF) was conducted on the 12.7mm thick plate at the T/2(mid-plane), T/4, and the surface for both Weldalite™ alloy variants. The through-thickness texture of the AA2195 alloy was inhomogeneous. The mid-plane consisted of an FCC deformation texture (strong Brass {110}<112> and S={123}<634> components) along with a weak Copper {112}<111> orientation. At T/4 a significant reduction in the deformation texture components was observed and the development of a new {001}<320> orientation. The surface consisted of primarily the {001}<320> texture component with negligible amounts of the deformation textures remaining. The through-thickness of the AA2095 alloy was also inhomogeneous. At the mid-plane a strong Brass component was observed with weak recrystallization (Cube and Goss) textures. The Brass deformation texture significantly decreased at T/4 and the Cube component was slightly larger; the overall texture is described to be random. The texture at the surface was similar to that at T/4 with approximately equivalent intensities of the Brass and Cube components.

13. An aging study was conducted at 143°C for the Weldalite™ alloy variants and times between 1 and 100 hours. Based on hardness,

neither alloy overaged within the 100 hour time frame. The high Cu alloy (AA2095) had somewhat higher hardness values, at least for times less than 10 hours. The aging kinetics of both alloys were similar. Aging times of 10, 20, 30 and 72 hours were selected to determine the interactive effects of yield strength, work hardening, subgrain boundary T_1, and δ' precipitation (for AA2095).

14. Uniaxial tensile deformation behavior of AA2095 and AA2195 was characterized for the four aging conditions at 25°C to -185°C. The yield and ultimate tensile strengths increased with increasing aging time and increasing Cu and Li levels. At both test temperatures, as the aging time increased, and the yield strength increased, there was a corresponding reduction in the work hardening exponent from a power-law hardening relationship. An increase in yield strength and work hardening was observed for each alloy with decreasing temperature to cryogenic levels. Elongation generally decreased with increasing aging time and with increasing Li + Cu. Elongation increased modestly with decreasing temperature, except for 2195 aged at times of 20 hours and longer. Notably, for the 20 hour aging time, elongation increases with decreasing temperature for AA2095 but not for AA2195. Tensile data for AA2195 aged for 30 hours exhibit comparable properties to the AA2095 aged for 20 hours.

15. The fracture toughness of the alloy variants increased with decreasing aging time and the associated increase in yield strength. For each test temperature and aging condition, K_{IC} of AA2195 is substantially higher than the values for AA2095. The large primary particles most likely play a substantial role in degrading fracture toughness. Delamination was observed for AA2095 at -185°C, but is not an important factor in the fracture toughness of these Weldalite™-type alloys. For all of the aging conditions, K_{IC} values for AA2095 and AA2195 are either essentially constant or decrease with decreasing test temperature. When toughness is considered at a constant yield strength, there is a beneficial effect of decreasing temperature for each alloy variant. The correlation in this figure is based on measured fracture toughness, and yield strength measured for separate test bars, for each aging condition and the two loading temperatures. The variability in fracture toughness is substantial, as discussed in the last progress report.

16. SEM was employed to determine if different fracture surface morphologies existed. Fractographs at the mid-plane of the alloys (aged for 20 hours) representing both test temperatures (25°C and -185°C) showed dimpled rupture. No change was observed in the fracture mode as the test temperature decreased to cryogenic levels.

17. Hardness measurements were conducted at 25°C and -185°C on the remnants of both the tensile and C(T) specimens. For the cryogenic

hardness tests, both the specimen and the brale indentor were submerged in liquid nitrogen and brought to equilibrium prior to conducting the hardness tests. (Thermocouples were imbedded in the test specimens and welded to the hardness indentor.)

18. The combined behavior of the alloy variants was typified by a nearly linear correlation of hardness to yield strength (with both measured for the tensile bars), regardless of deformation temperature or aging condition. This correlation enabled estimates of the yield strength of individual C(T) specimens, for either fracture temperature, in an attempt to explain the variability in fracture toughness.

19. The yield strength of each C(T) fracture toughness specimen was calculated by using the hardness value, measured from the specimen at either 25 or -185°C, coupled with the linear curve fit determined from the tensile bar tests (Figure 18). Fracture toughness results were plotted as a function of this calculated yield strength and scatter was somewhat reduced. At least two particularly discrepant C(T) samples from the second test set-up remain, 4072CF and 4020DF, which will be further investigated.

20. Toughness versus calculated yield strength data were replotted for each alloy, strained at 25°C, including identification of the aging time associated with each point. While the correlation is excellent for high Cu/Li AA 2095, significant variability remains for AA2195. For example, a two-fold toughness difference is associated with replicate experiments with specimens aged for 72 hours and of near-constant yield strength. Second, essentially the same fracture toughness is observed for two widely divergent strength levels, produced by aging at 30 and 72 hours. Finally, the same strength and fracture toughness are observed for two specimens aged for 30 and 72 hours. The source of this difference is not understood.

21. Future plans.

22. Conclusions.

EFFECTS OF TEMPERATURE AND AGING CONDITION ON THE FRACTURE TOUGHNESS OF AA2095

C. L. Lach

LA^{2}ST Program Review

NASA Langley Research Center

July 25-26, 1994

OBJECTIVE

To characterize the effects of temperature, alloy composition and aging condition on the deformation and fracture behavior of AA2095 from elevated to cryogenic temperatures.

APPROACH

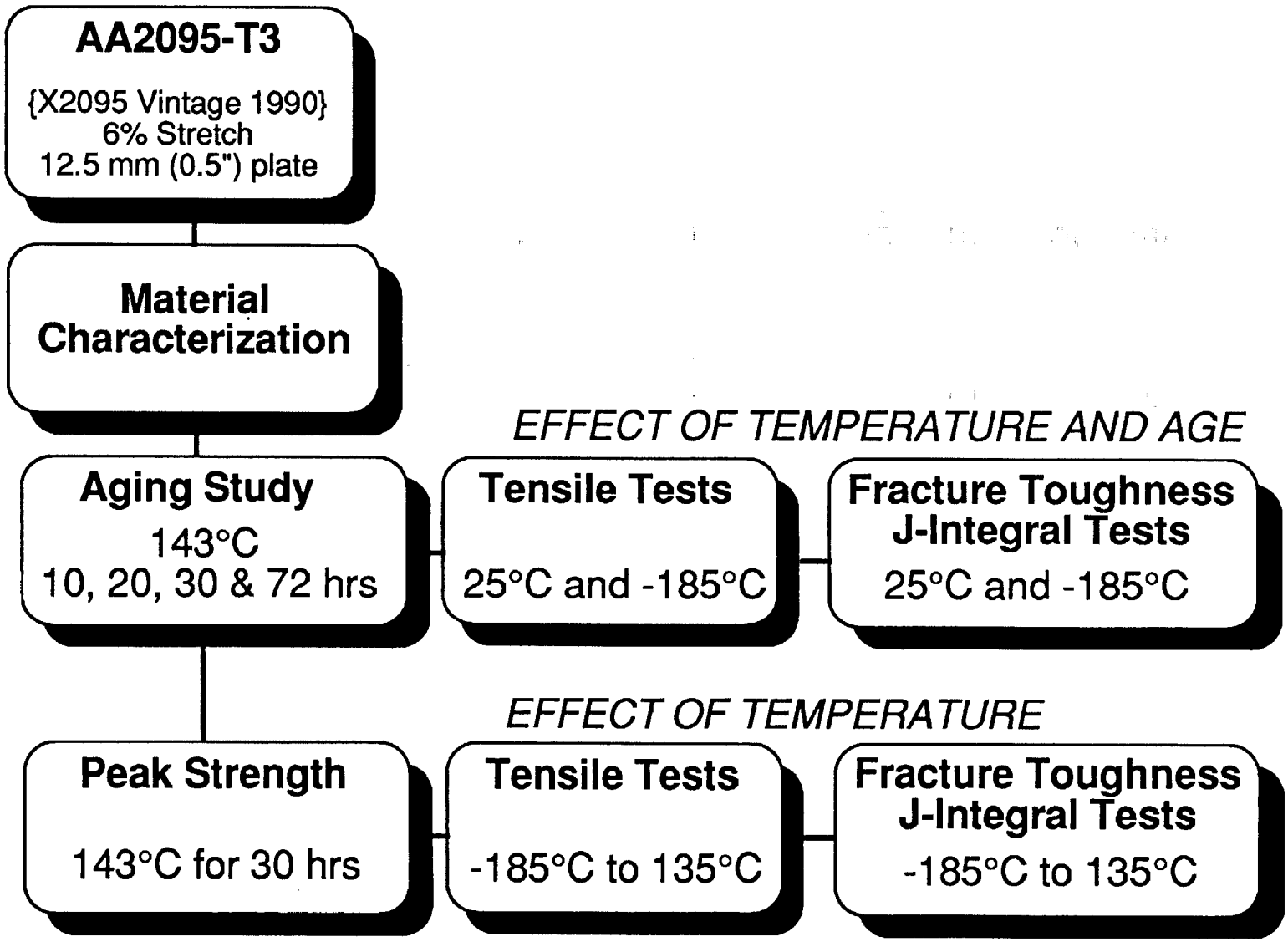
AA2095-T3
{X2095 Vintage 1990}
6% Stretch
12.5 mm (0.5") plate
Material Characterization
EFFECT OF TEMPERATURE AND AGE
Aging Study
143°C
10, 20, 30 & 72 hrs
Tensile Tests
25°C and -185°C
Fracture Toughness J-Integral Tests
25°C and -185°C
EFFECT OF TEMPERATURE
Peak Strength
143°C for 30 hrs
Tensile Tests
-185°C to 135°C
Fracture Toughness J-Integral Tests
-185°C to 135°C

ISSUES

- Why are replicate fracture toughness values variable?
- What is the effect of temperature on the toughness of peak-strength aged AA2195?
- What is the mechanism for temperature-(in)dependent fracture in peak-strength aged AA2195?

MATERIALS CHARACTERIZATION

MATERIALS CHARACTERIZATION

Registered Composition limits of Weldalite™049 Alloys

ELEMENTS	AA2094	AA2095	AA2195	Lean Variant	Rich Variant
Cu	4.4-5.2	**3.9-4.6**	**3.7-4.3**	**4.04**	**4.64**
Li	.70-1.4	**.70-1.5**	**.80-1.2**	**1.00**	**1.53**
Mg	.25-.80	.25-.80	.25-.80	0.36	0.37
Ag	.25-.60	.25-.60	.25-.60	0.37	0.35
Zr	.04-.18	.04-.18	.08-.16	0.15	0.17
Mn	.25 max	.25 max	.25 max	.25 max	.25 max
Zn	.25 max	.25 max	.25 max	.25 max	.25 max
Fe	.15 max	.15 max	.15 max	.15 max	.15 max
Si	.12 max	.12 max	.12 max	.12 max	.12 max
Ti	.10 max	.10 max	.10 max	.10 max	.10 max
Other, Each	.05 max	.05 max	.05 max	.05 max	.05 max
Other, Total	.15 max	.15 max	.15 max	.15 max	.15 max
Al	Remainder	Remainder	Remainder	Remainder	Remainder

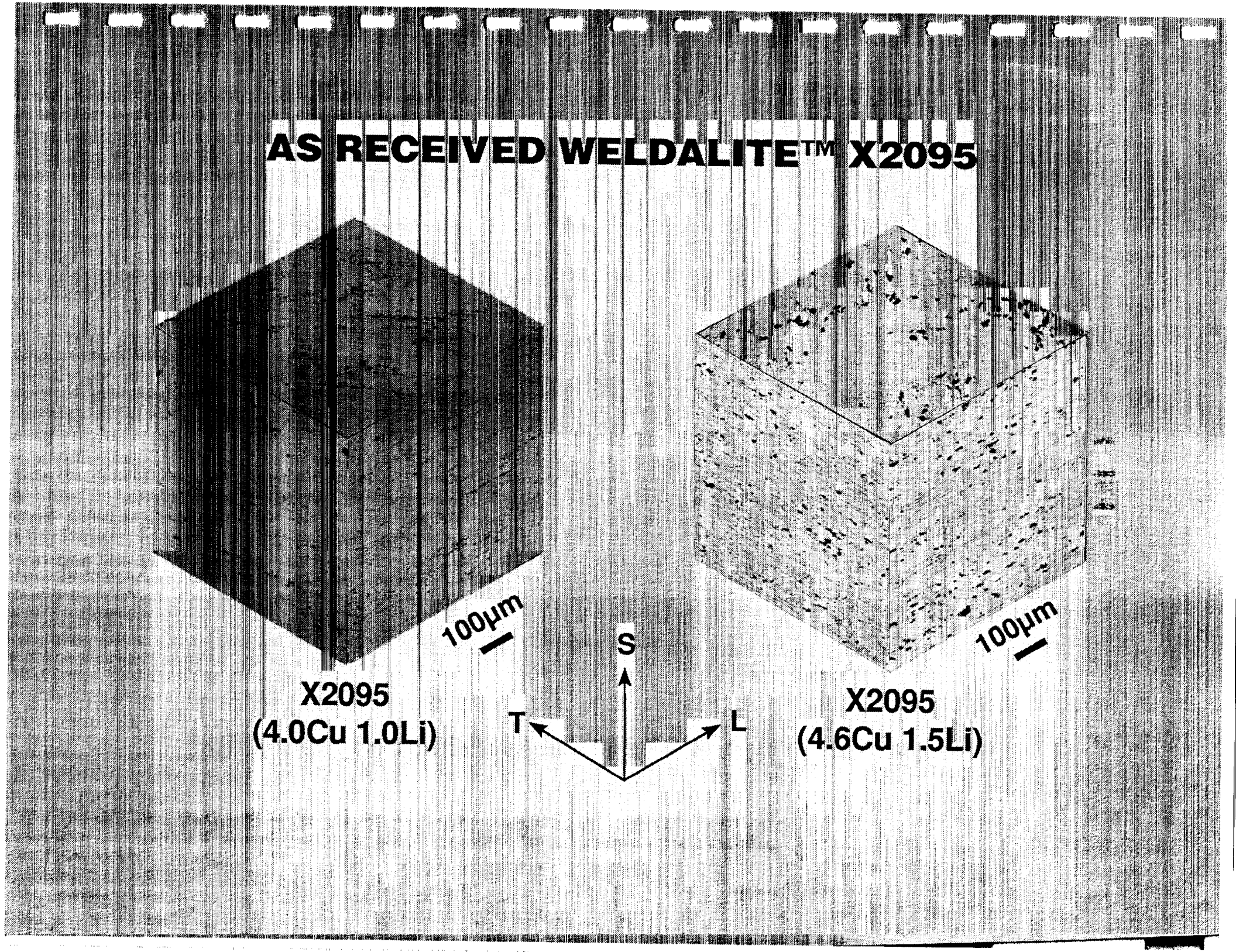
AS RECEIVED WELDALITE™ X2095
100μm
100μm
S
T
L
X2095
(4.0Cu 1.0Li)
X2095
(4.6Cu 1.5Li)

MATERIAL CHARACTERIZATION

Through Thickness Microstructure (0.5 in. plate)

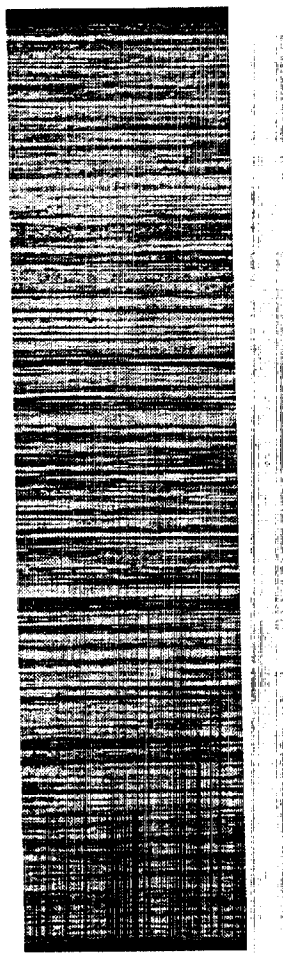

AA2195-T3

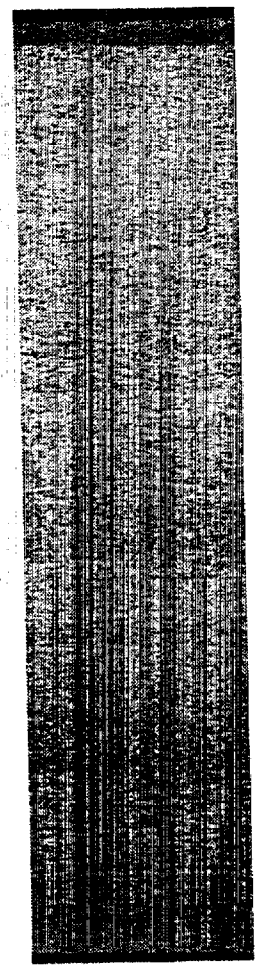

AA2095-T3

MATERIAL CHARACTERIZATION

Mid-plane (T/2) Microstructure at 200X

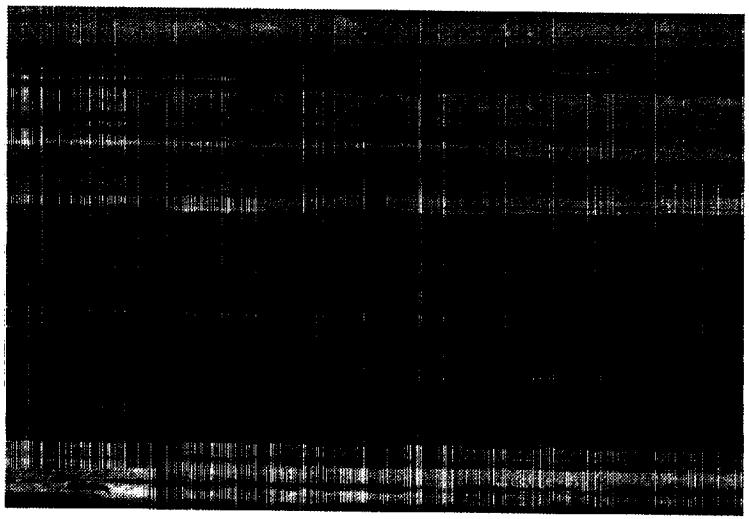

AA2195-T3

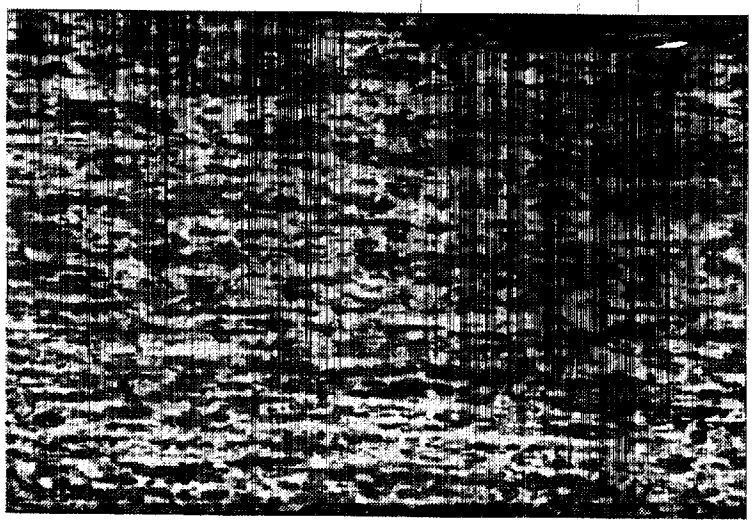

AA2095-T3

MICROSTRUCTURAL CHARACTERIZATION

Image Analysis (500X)

AA2195-T3

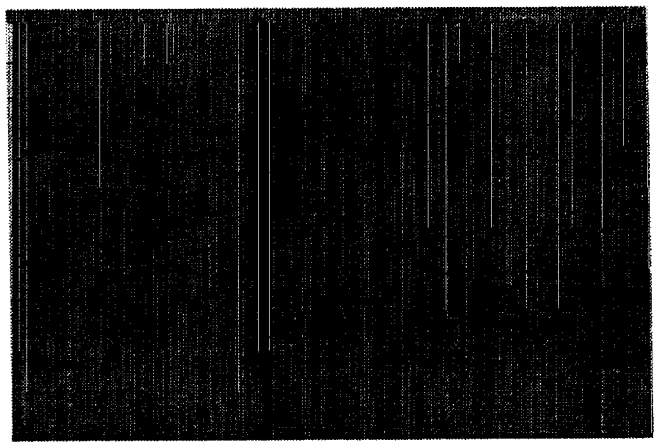

Avg. particle size 0.7 microns
90% of particles < 1.0 micron

AA2095-T3

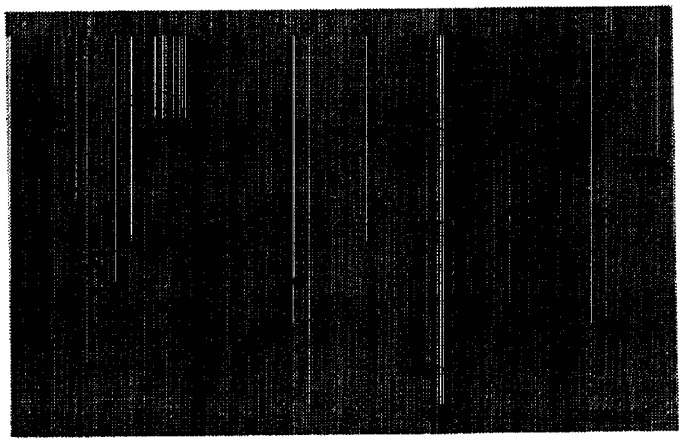

Avg. particle size 4.5 microns
95% of particles > 1.0 micron

PSN MODEL: HUMPHREYS AND KALU

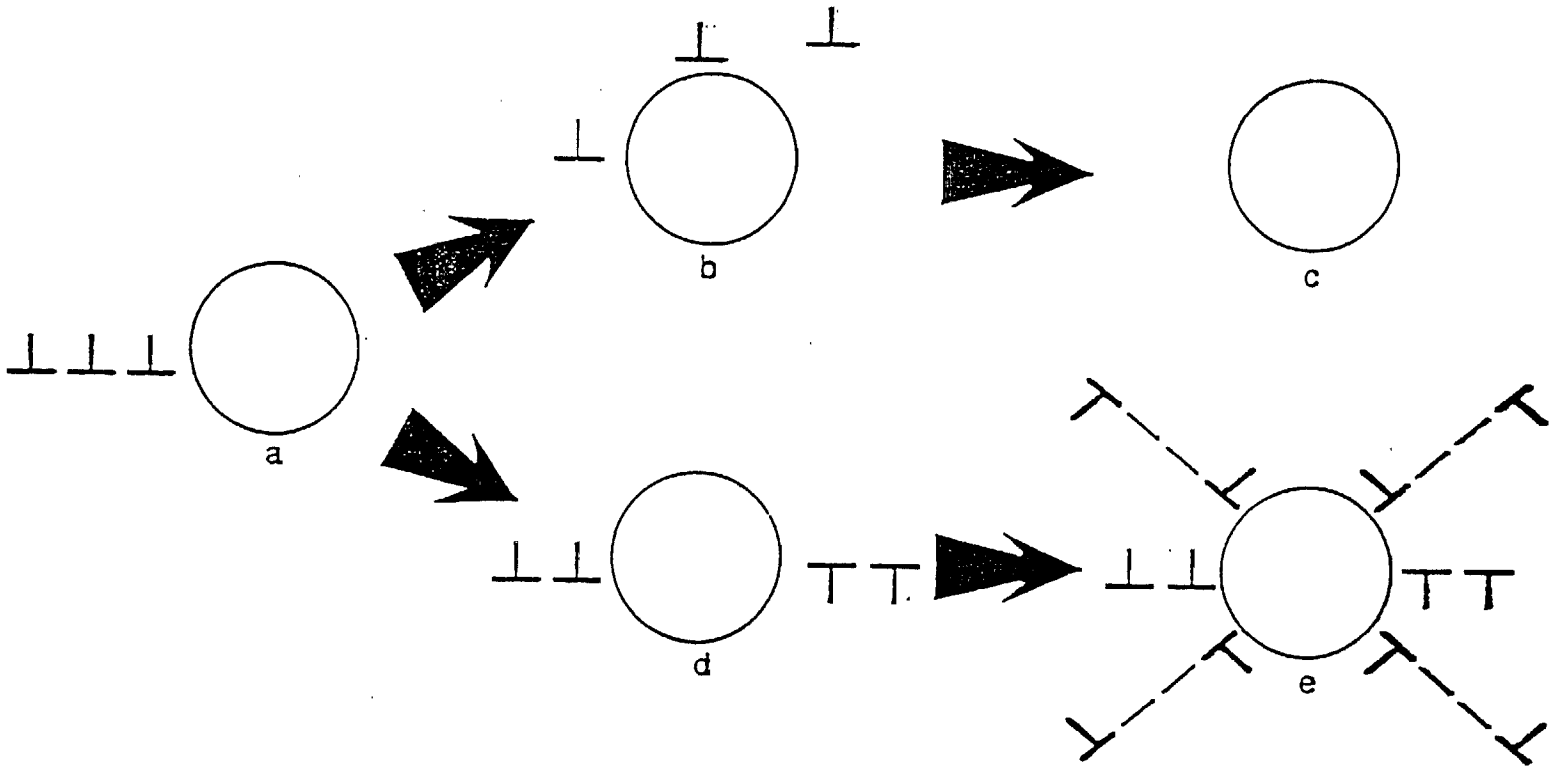

The critical particle size d_c, for the deformation zone formation is

$$d_c = \left[\frac{K\exp(-Q_V/RT)}{T\dot{\varepsilon}}\right]^{1/3}$$

K - pre exponential constant
Q_V - activation energy for bulk diffusion
R - Gas Constant

For the processing condition used $d_c = 2.6\ \mu m$

MATERIAL CHARACTERIZATION

Texture Analysis 2195-T3

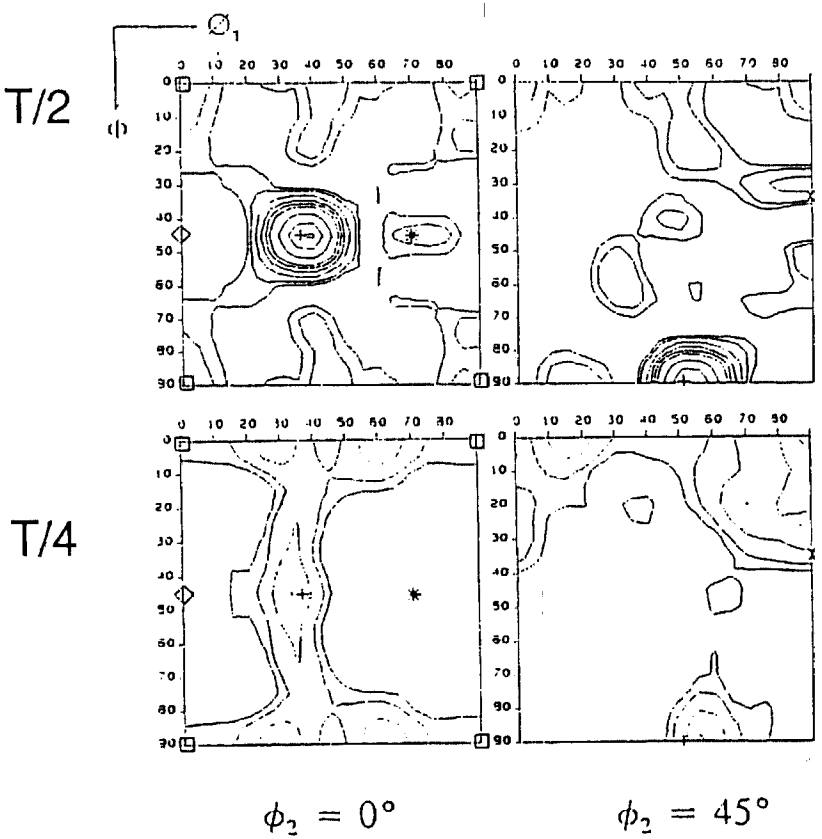

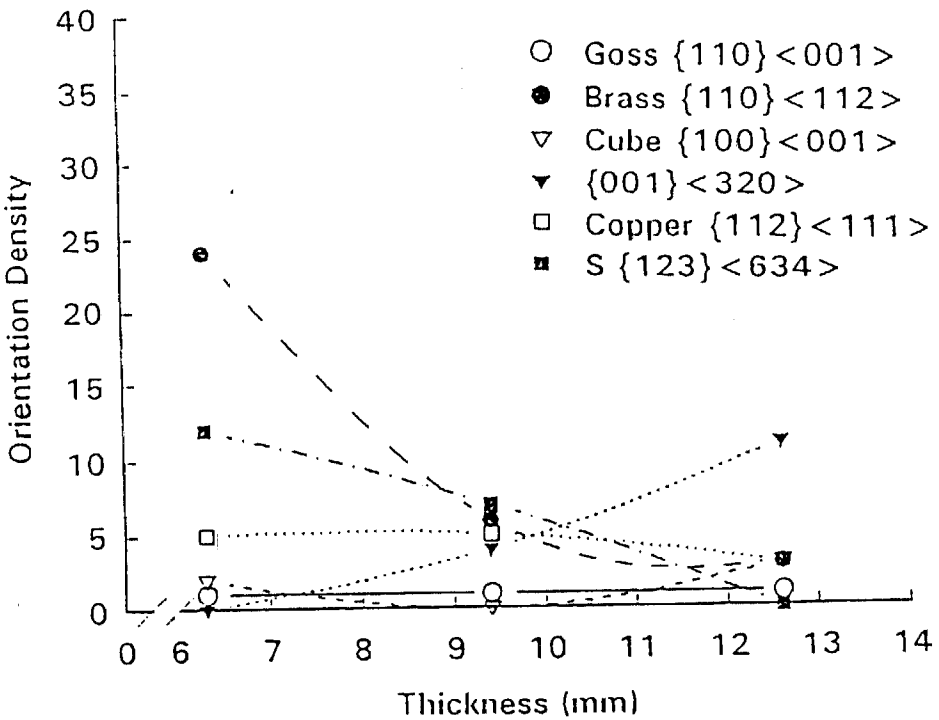

(a) ODF sections at T/2 and T/4. (b) Texture variation with location.

MATERIAL CHARACTERIZATION

Texture Analysis 2095-T3

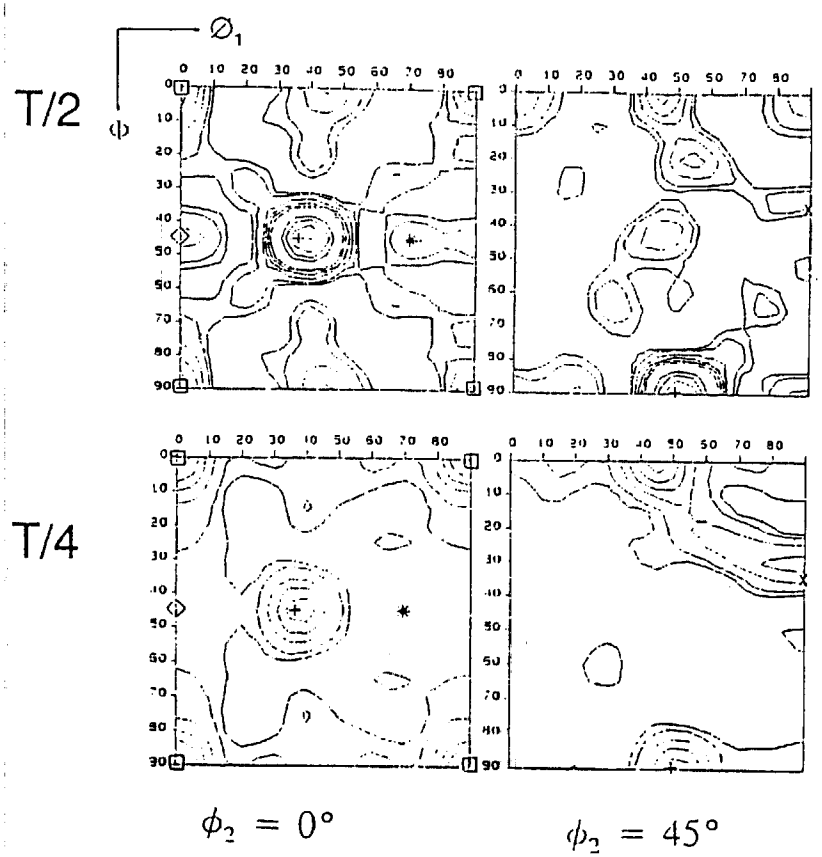

(a) ODF sections at T/2 and T/4.

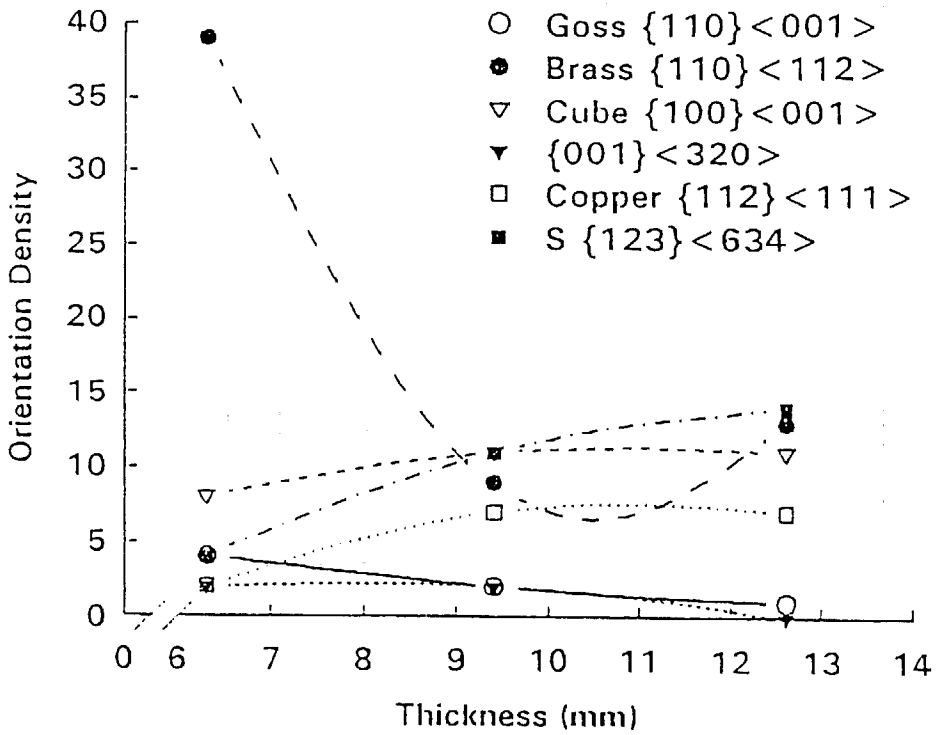

(b) Texture variation with location.

MATERIALS CHARACTERIZATION

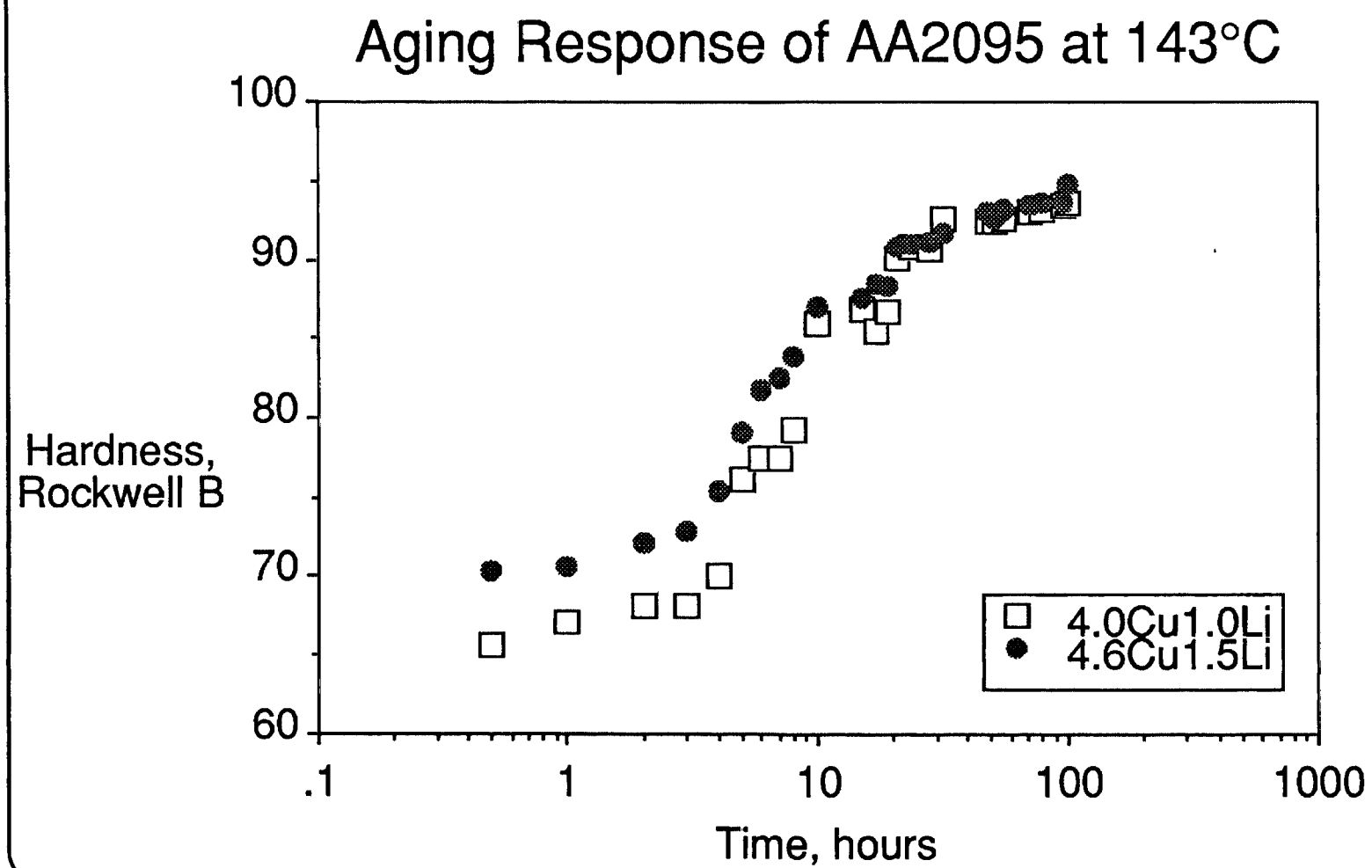

MATERIAL CHARACTERIZATION

Tensile Properties

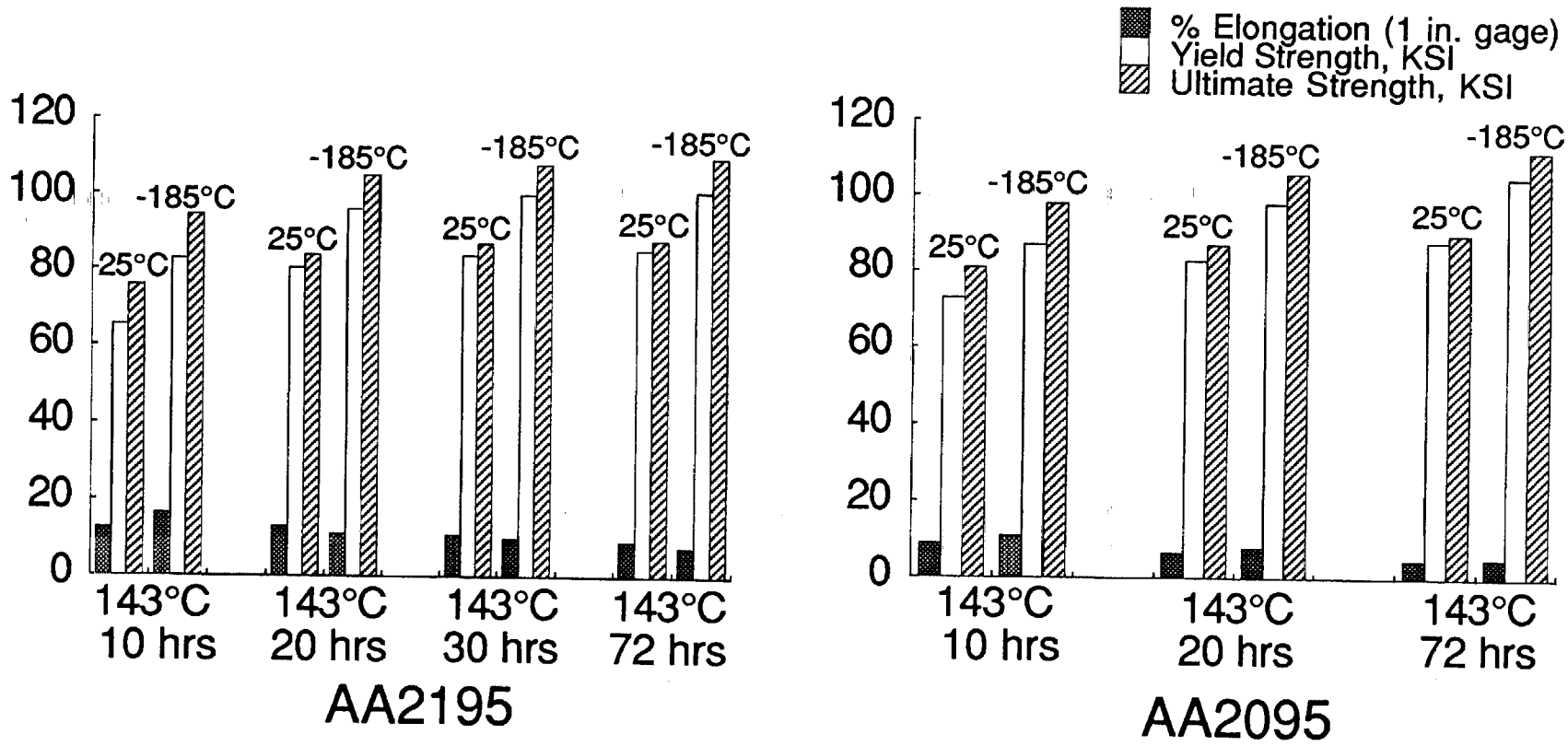

FRACTURE TOUGHNESS

J-Integral
{Compact tension}

FRACTURE TOUGHNESS

Effects of Temperature, Chemistry and Age

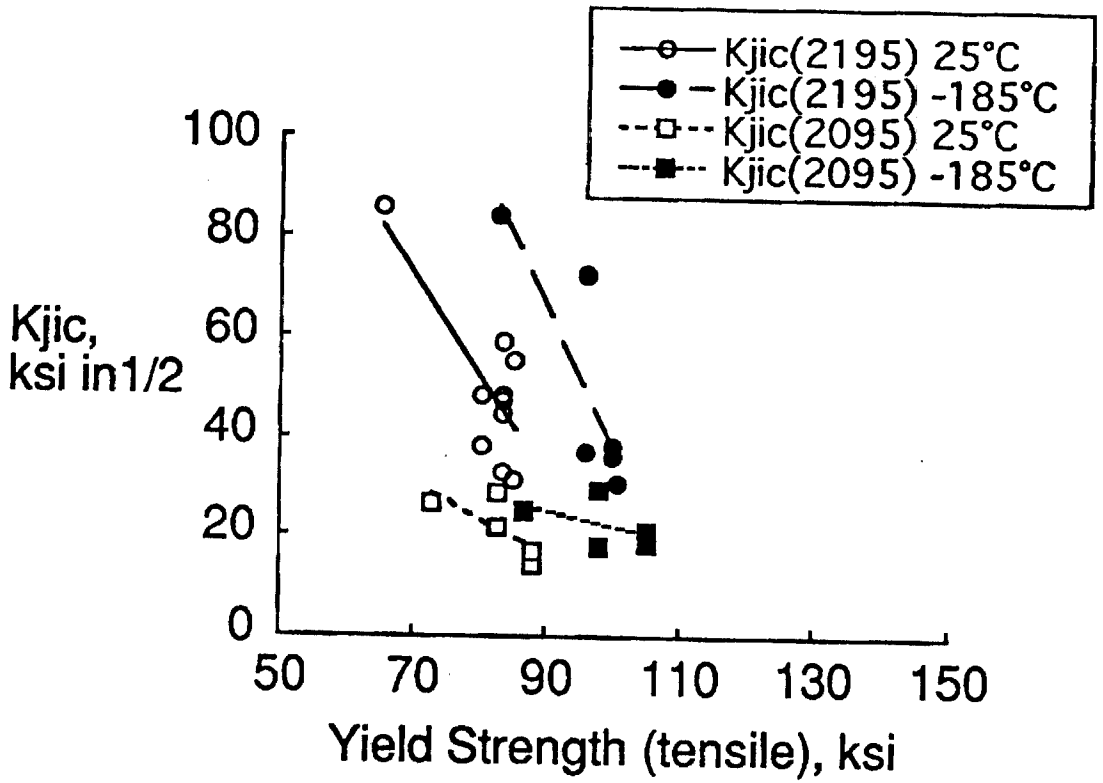

FRACTURE TOUGHNESS

SEM Fracture Surfaces

AA2195
143°C 20 hrs

25°C

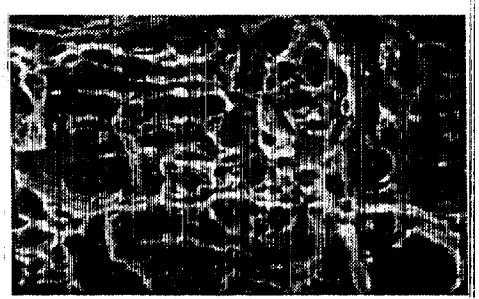

-185°C

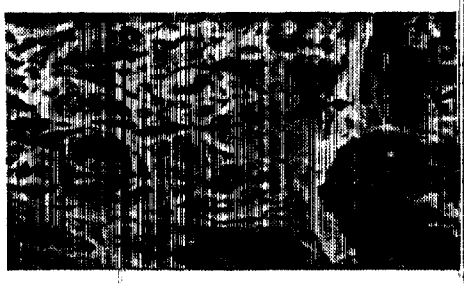

40 um

AA2095
143°C 20 hrs

25°C

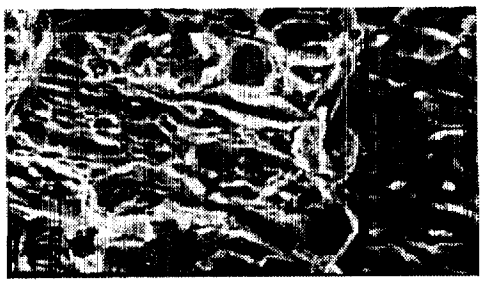

-185°C

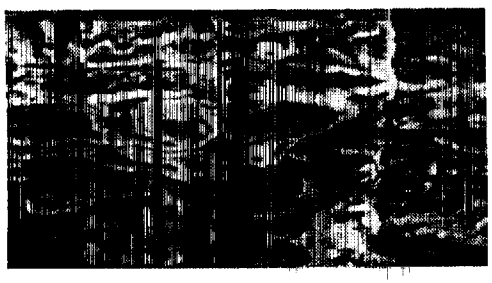

FRACTURE TOUGHNESS

Cryogenic (LN2) Hardness Test Set-up

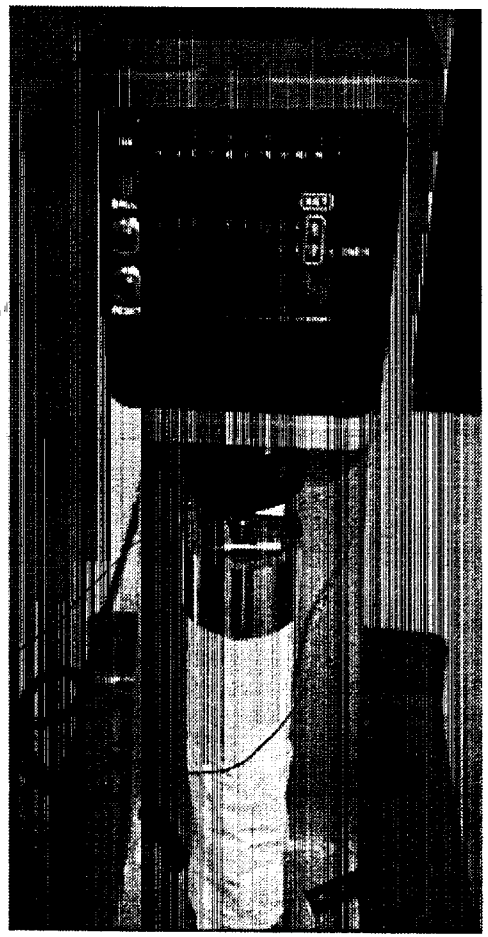

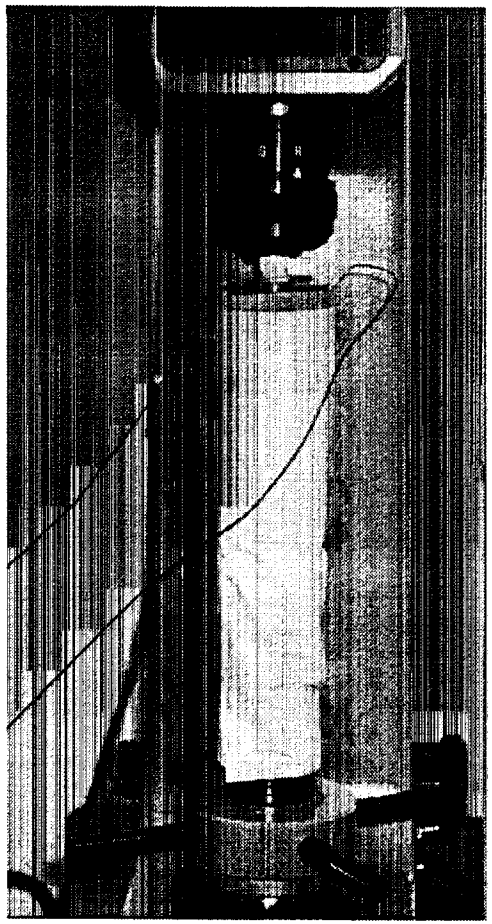

FRACTURE TOUGHNESS

Effects of Temperature, Age and Chemistry

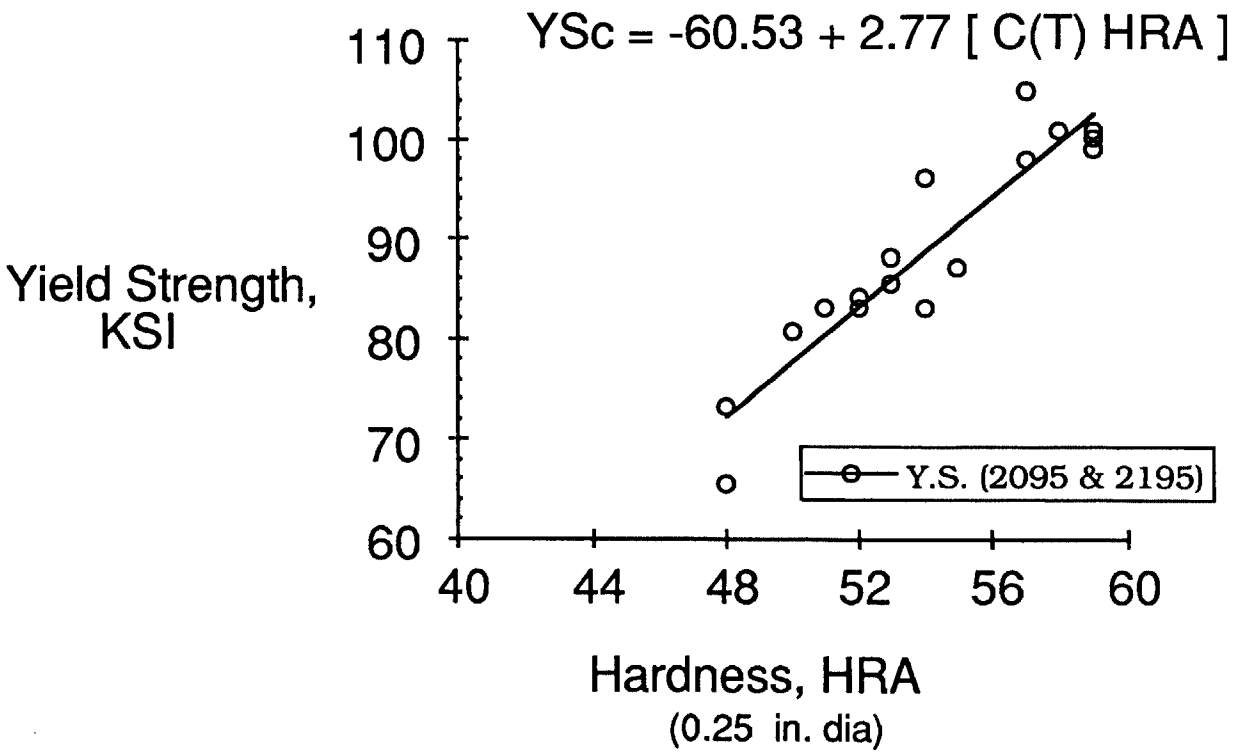

FRACTURE TOUGHNESS

Effects of Temperature, Chemistry and Age

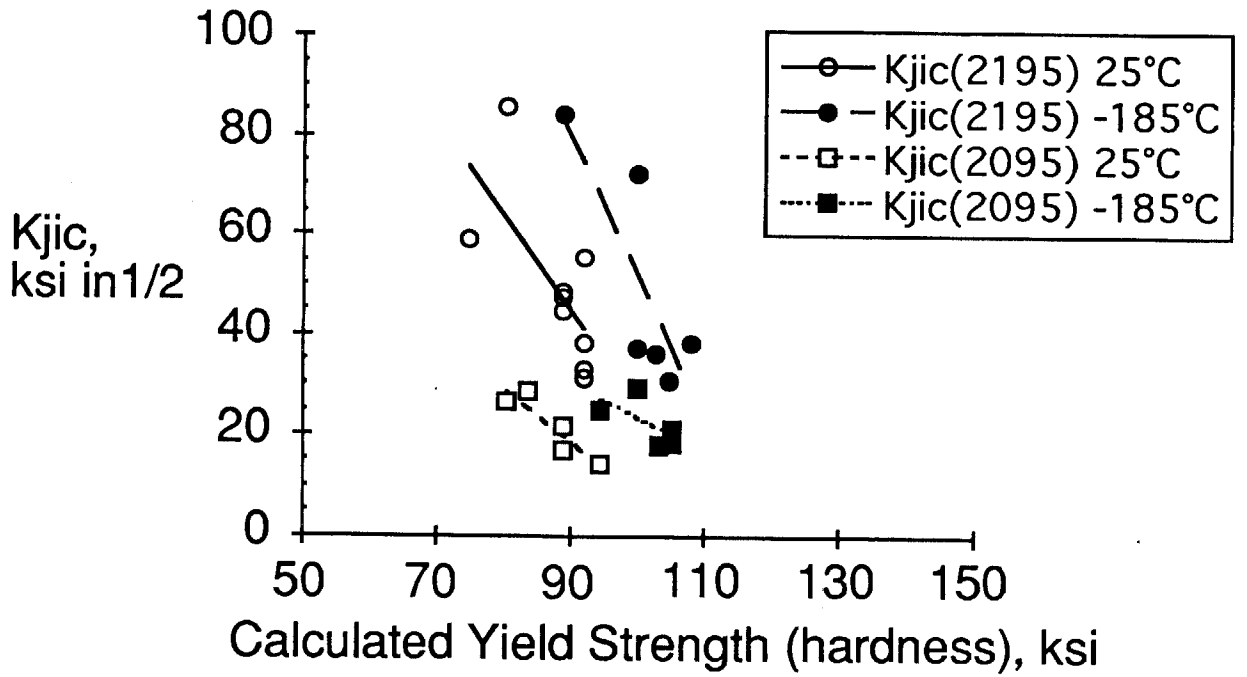

FRACTURE TOUGHNESS
Effects of Chemistry and Age

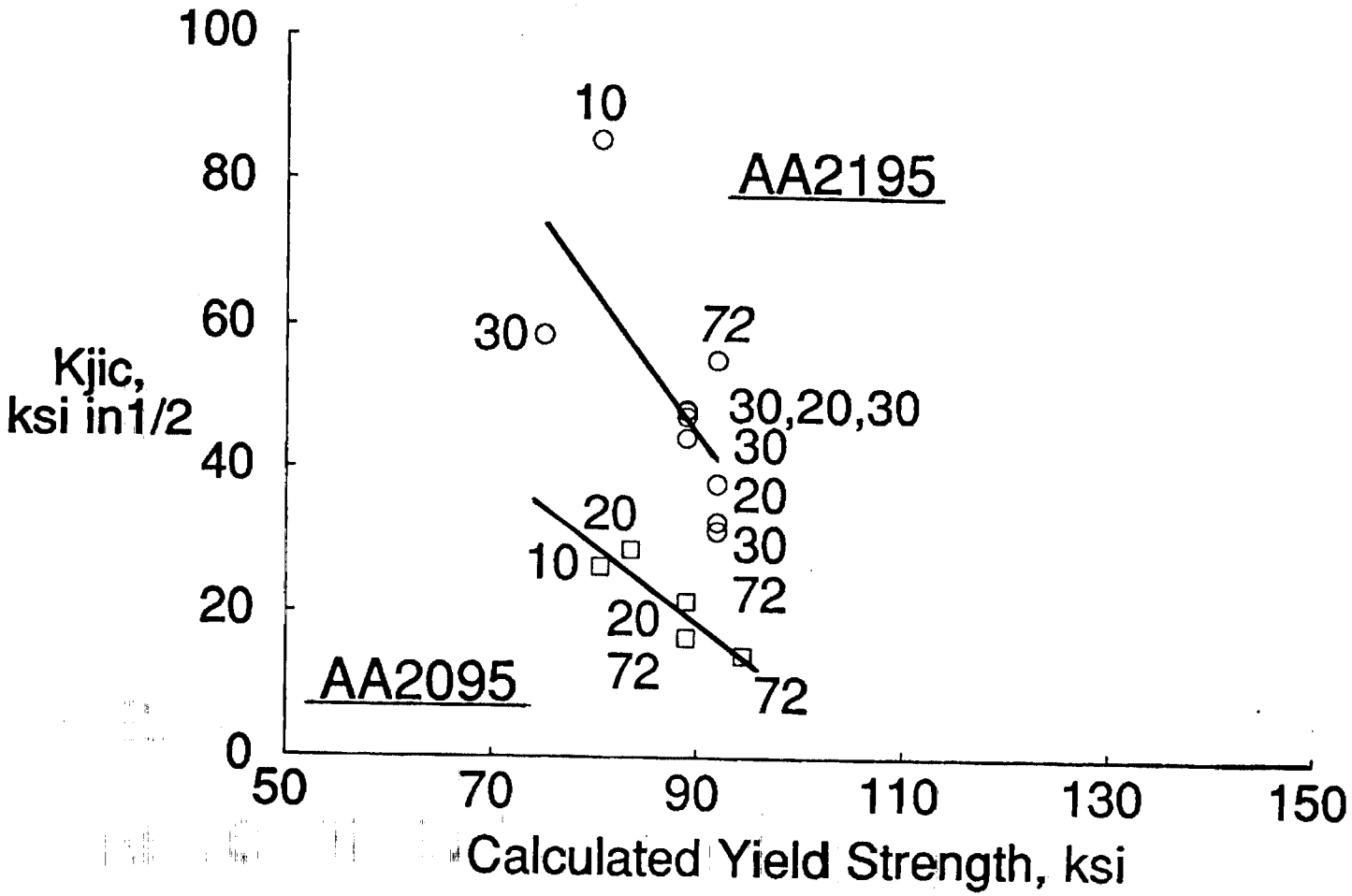

FUTURE PLANS

Fracture Toughness

- Determine the effect of temperature (-185°C to 135°C) on the toughness of peak-strength aged AA2195.

- Define the mechanism for temperature-(in)dependent fracture in peak-strength aged AA2195.

CONCLUSIONS

Material Characterization

- o The through-thickness microstructure and texture of AA2195 was inhomogeneous.
- o For AA2095 the through-thickness microstructure was homogeneous but the texture was inhomogeneous.

Tensile

- o The yield and ultimate strengths increased with increasing aging times and Cu/Li levels and decreasing temperature.

Fracture Toughness

- o For each temperature and aging time, the toughness of AA2195 was substantially higher than AA2095.
- o The underaged condition had significantly higher toughness values for both temperatures and chemistries.
- o For a constant yield strength the toughness increased with decreasing temperature, aging times and Cu/Li levels.
- o AA2195 had a high dependency of toughness on yield strength.
- o For a constant age and chemistry, as the temperature decreased the yield strength increased while maintaining toughness.

Project #4 Mechanisms of Localized Corrosion in Alloys 2090 and X2095

F. Douglas Wall and Glenn E. Stoner

Project Objective:

The objective of this research project is to determine the electrochemical conditions and microstructural features necessary for EAC failures of Al-Li-Cu alloys in several aqueous environments.

Current Status:

Efforts are being concentrated on refining a method for growing environmentally assisted cracks *in situ* with real-time monitoring of crack lengths.

Recent Findings:

Information from past stages of this project has lead to the development of an experimental technique for growing *in situ* cracks in Al-Li-Cu alloys.

Analysis of solutions from exposures of high material surface area to low solution volumes indicated that a possible occluded chemistry could contain significant Li^+ and CO_3^{2-} and have an alkaline pH. Electrochemical characterization of modeled microstructural features in a simulated occluded environment indicated the existence of a potential window in which grain interiors are predicted to be passive while boundary features such as the T_1 phase and Cu depleted Al are predicted to actively corrode. Data to support this hypothesis came from performing constant load/scratching electrode experiments on smooth bar tensile samples. It was found that rapid failures could be produced by polarizing samples to a potential where the boundary features are active and the grain interiors passive. These data suggest that electrochemical conditions can be prescribed which will result in sustained in-situ crack growth in Al-Li-Cu alloys.

Wedge opening loading (WOL) specimens have been used to examine the feasibility of growing *in situ* EAC cracks. It has been demonstrated that under the proper combination of environment, stress intensity and applied electrochemical potential that crack growth can be sustained. Cracks have been grown in WOL specimens (B=0.125 inches and W=1.44 inches) for periods of up to five days. Cracking has been confirmed through optical microscopy and scanning electron microscopy (SEM). At this time insufficient data have been collected to allow for characterization of crack growth rates and ranking of materials. This will be a primary focus over the next few months.

Future Work:

(1) Determine crack growth rates for under aged and peak aged tempers of 2090 and 2095 in $NaCl/Na_2CrO_4$ and $NaCl/Li_2CO_3$ environments as a function of applied stress intensity. Crack growth rates will be used to quantitatively rank materials/tempers in terms of susceptibility to EAC crack propagation.

(2) Perform alternate immersion of DCB specimens to establish crack growth rates in a chloride environment for comparisons with trends determined by *in situ* da/dt vs K experiments. Also examine crack chemistries using capillary electrophoresis.

(3) Variable stress level-constant load-scratching electrode experiments will be performed to determine threshold stress levels below which material failure will not occur. These experiments will provide an additional ranking of materials/tempers to EAC susceptability.

(4) An extensive matrix of constant extension rate tests will be performed on 2095-A and 2095-B to determine whether or not changes in material response as a function of applied potential are abrupt changes corresponding to unique electrochemical potentials.

(5) Scratching electrode experiments will be performed with high speed data acquisition and surface area analysis in order to quantify maximum corrosion current densities for modeled subgrain boundary features. These current densities will be used to determine if observed crack growth rates can be accounted for by an anodic dissolution process.

(6) Solution chemistry analysis of artificial occluded geometries will be performed using pH measurement and capillary electrophoresis to refine the model of the occluded environment. Experimentation will be performed on samples in constant immersion and alternate immersion.

Explanatory Text for Viewgraphs:

1. Title slide.

2. Objectives of research project.

3. Overview slide showing the contributions to EAC and the variables associated with each of the contributions.

4. Description of materials and tempers used in this research. The 99.99 Al and Al-Cu binaries are used to simulate various degrees of copper depletion along a microstructural boundary.

5. The development of a model occluded chemistry begins with the notion that Al-Li-Cu alloys do not fail in constant immersion, but do fail after removal from solution. The chemistry that develops in the absence of a bulk solution is modeled by exposing large areas of material to small volumes of solution. This has been done in three experimental configurations which are shown schematically.

6. The graphs on this page show the pH response of solution containing material shavings. In some cases the shavings were rinsed in 0.1M NaOH prior to the experiment to remove the machined oxide. Although this treatment appears to have an effect on the initial response, longer term exposures indicate less of an effect.

7. Results of capillary electrophoresis analysis of solution from a shavings experiment are shown in this graph. The data indicates the presence of lithium ions although precise quantification has not been performed

at this time.

8. This viewgraph summarizes the potentiodynamic polarization experiments which have been previously reported. The most significant result is the identification of environment and potential combinations in which Al-Li-Cu grain interiors should be passive while the T_1 phase is active.

9. The potentiostatic/scratching electrode experiments provide a refinement to the data obtained by potentiodynamic polarizations. In these experiments the behavior of bare material exposed to solution is evaluated. From these tests it was determined that Cu-depleted Al can be active under conditions where model grain interiors are passive suggesting the possible role of a Cu-depleted zone in EAC.

10. Straining electrode experiments were performed to determine if plastic deformation gave the same type of material response as observed for the scratching electrode experiments. It was determined that under certain combinations of environment, applied potential and plastic deformation Cu-depleted Al is highly active while model grain interiors spontaneously repassivate.

11. The $NaCl/Na_2CrO_4$ and $NaCl/Li_2CO_3$ environments provide conditions where modeled boundary features are active and grain interiors are passive. These conditions lend themselves well to studying anodic dissolution based EAC.

12. This slide gives an overview of the constant load / scratching electrode experiment.

13. These graphs show the critical EAC potentials (E_{crit}) for various alloys and tempers in the two test environments. The E_{crit} represents a potential where a change in behavior occurs from passivity to corrosion and material failure.

14. These graphs show the current response of UA 2090-A (top graph) and 2090-T8 (bottom graph) during a constant load / scratching electrode experiment. Note the difference in magnitude of corrosion current and length of time-to-failure between the two tempers.

15. This is a schematic diagram indicating two possible types of overload failures from EAC of smooth tensile samples. In each case there is a region of EAC which is easily identified by the prepense of corrosion products. The overload region may or may not be affected by the EAC process. If the overload region is not affected by the EAC process then the EAC region must grow to such a flaw size that the remaining ligament cannot support the residual stress on the sample. However,

if the mechanical properties (such as K_{Ic}) of the ligament are reduced due to the EAC process, then the sample may fail at what would appear to be a subcritical flaw size. In many of the observed failures it is not possible to determine if the ligament has been affected by the EAC process (top figure); however, in the case of the UA–2090–A fractography suggests that the ligament has been affected (bottom figure).

16. These micrographs are from 2095-B, ST smooth bar specimens. They are intended to show that the overall fracture morphology is similar for air fracture and overload failure due to the scratching electrode test.

17. These are micrographs from 2090-T8 smooth bar specimens. The air fracture appears similar to the overload region from the specimen which underwent corrosion induced failure.

18. These micrographs are from UA 2090-A smooth bar tensile specimens. Unlike the previous two materials, the appearance of the air fracture is markedly different from the corrosion induced failure for this specimen.

19. This slide shows a comparison of the corrosion regions from the UA 2090-A sample and the 2095-B sample. The corrosion region in the UA sample only extends about 40μm into the sample interior whereas in the 2095-B sample the corrosion region extends several hundred microns into the sample interior.

20. EDS analysis of the UA 2090-A specimen was performed to confirm the limited penetration of corrosion into the sample. The upper plot is from the corrosion region and contains peaks corresponding to the prepense of chloride and chromate. These elements are usually detected in the corrosion product from these experiments. The bottom plot is from a region approximately 55μm into the sample interior and shows no evidence of peaks corresponding to chromate or chloride.

21. This slide lists some observations based on the constant load/ scratching electrode experiments.

22. This slide summarizes the constant extension rate testing performed on 2095-A and 2095-B in the $NaCl/Na_2CrO_4$ environment.

23. These are the results from the constant extension rate testing.

24. This is the introductory slide to the da/dt vs K experimental technique.

25. This schematic of the da/dt vs K experimental set-up shows the interconnections between controlling hardware and specimen.

26. This slide shows preliminary data collected using the set-up described on the previous two slides. It is intended to demonstrate the ability to grow in-situ EAC cracks. This data is not intended to yield crack growth rate information since sufficient duplication has not been performed.

27. These pictures are SEM micrographs from a crack grown in 2095-B in the $NaCl/Na_2CrO_4$ environment.

28. These micrographs show the crack tip of a 2095-B sample. Note that the EAC region extends to a greater distance in the center of the crack than at the edges. This indicates the role of constraint in driving the cracking process.

29. This slide lists a few observations concerning the initial da/dt vs K testing.

30. Summary of progress to date.

31. Future work.

32. Future work.

Mechanisms of Localized Corrosion in Alloys 2090 and 2095

F. D. Wall
G. E. Stoner

Department of Materials Science and Engineering
University of Virginia
Charlottesville, Virginia 22901

NASA - LaRC Contact : Marsha Domac

Co-sponsor : Reynolds Metals Corporation
Technical Contact : Alex Cho

OBJECTIVES

Determine the electrochemical conditions and microstructural features necessary for EAC failures of Al–Li–Cu alloys in an aqueous environment.

* **Examine the occluded chemistries (ions present, pH) from exposure of material to small amounts of solution.**

* **Characterize the electrochemistry of alloys and modelled microstructural features.**

* **Distinguish alloys in terms of EAC susceptability and correlate susceptability to microstructural features.**

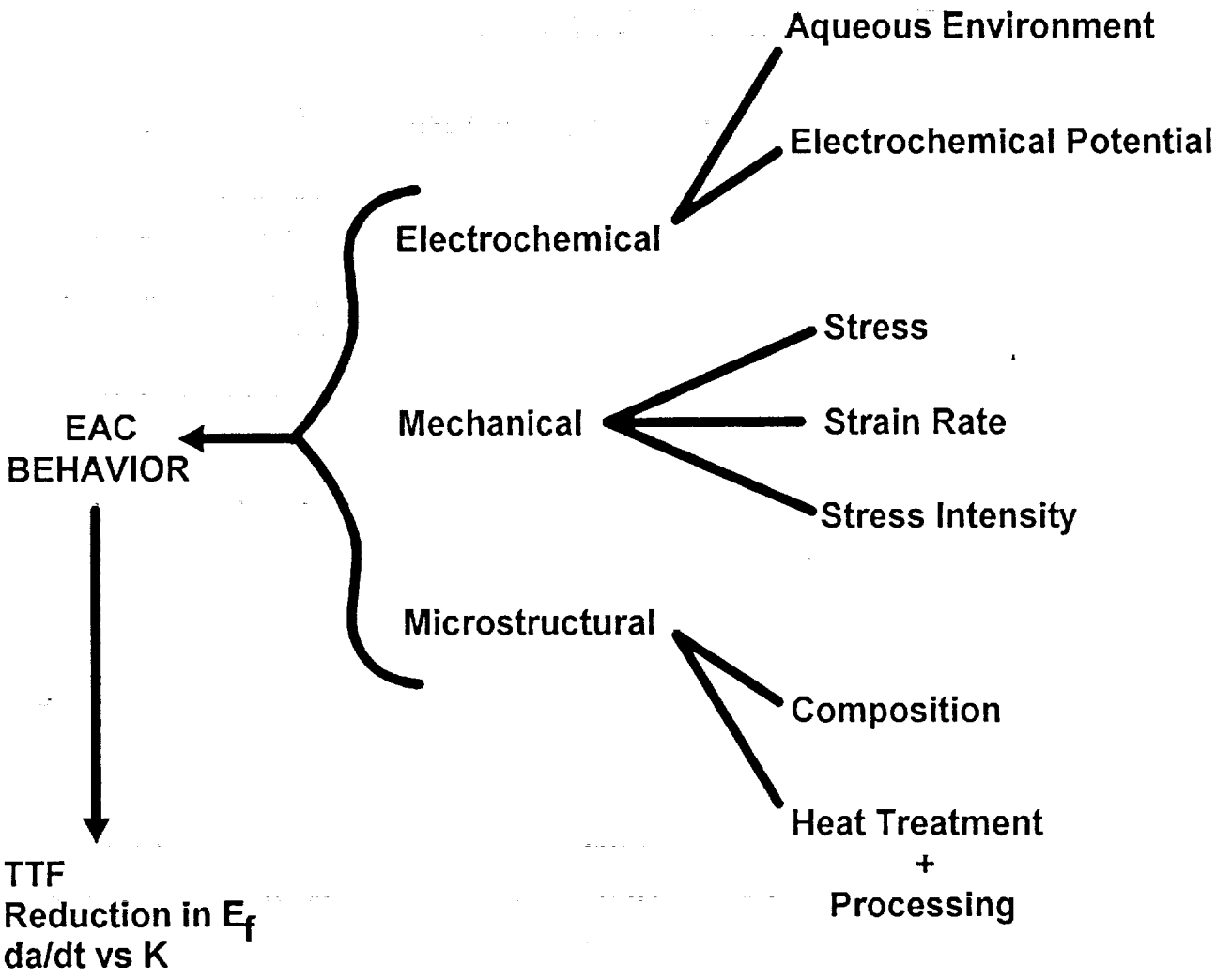
Aqueous Environment
Electrochemical Potential
Electrochemical
Stress
Mechanical
Strain Rate
Stress Intensity
EAC
BEHAVIOR
Microstructural
Composition
Heat Treatment
+
Processing
TTF
Reduction in E_f
da/dt vs K

MATERIALS

2095 (Al-4 Cu-1 Li- 0.25 Mg-0.25 Ag-0.1 Zr)

2090 (Al-2 Li-2.5 Cu-0.1 Zr)

2124 (Al-4 Cu-1.5Mg-0.25 Zn-0.2 Zr)

99.99 Al : Worst case Cu-depletion

Al-0.1 Cu ... Al-3.96 Cu : Intermediate Cu depletion

Designation	SHT	Quench	Stretch	Aging	Comments
2090-T8	1 hr/545°C	cold water	3.5%	14 hrs/ 160°C	peak-aged
2090-A	1 hr/545°C	cold water	none	1.5 hrs/ 160°C	under-aged
2090-B	1 hr/545°C	cold water	none	3.0 hrs/ 160°C	under-aged
2090-C	1 hr/545°C	cold water	none	7.0 hrs/ 160°C	under-aged
2090-SHT	1 hr/545°C	cold water	none	none	model for α-Al
2095-A	1 hr/505°C	cold water	6.5%	20 hrs/ 143°C	under-aged
2095-B	1 hr/505°C	cold water	6 %	30 hrs/ 143°C	peak-aged
2095-SHT	1 hr/505°C	cold water	none	none	model for α-Al

AQUEOUS ENVIRONMENT

Base solution : aqueous 0.6 M NaCl

Al-Cu-Li alloys generally do not fail in constant immersion but do fail under conditions of alternate immersion.

Pre-exposure embrittlement testing has identified some important solution characteristics : $[Li^+]$, $[CO_3^{2-}]$, pH

Simulate occluded solution chemistry that develops during dry cycle of AI test by exposing large material surface area to small solution volumes:

Shavings Experiment

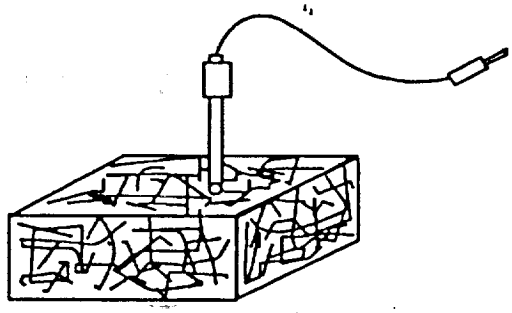

Occluded Geometry

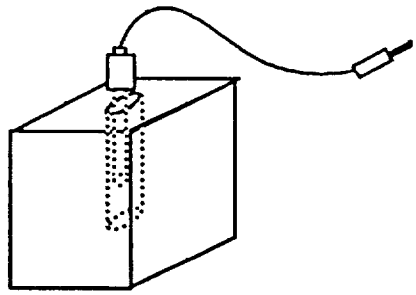

Flat Sample

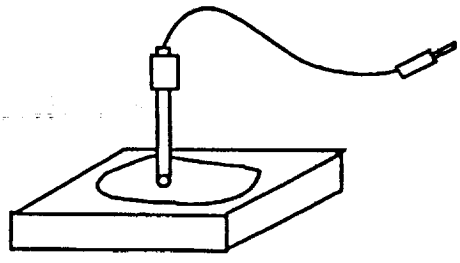

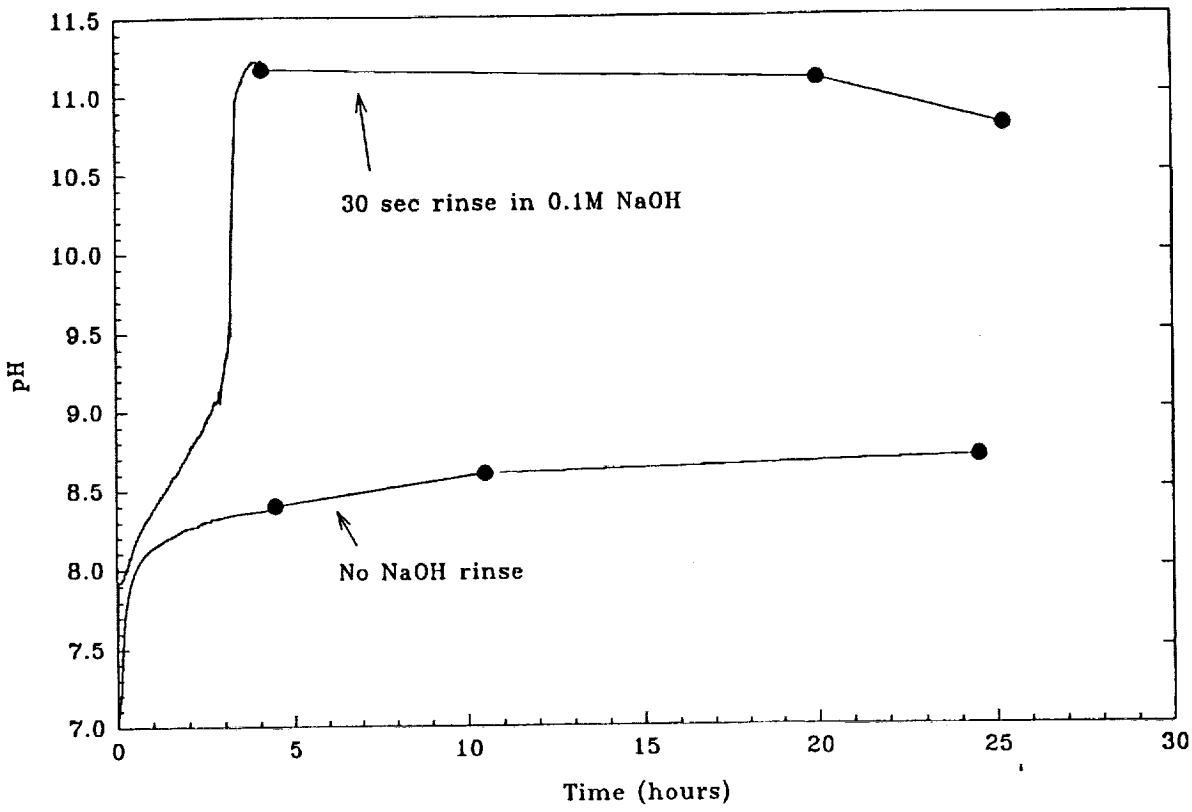

pH generated by 2090-T8 shavings exposed to 0.1 M NaCl

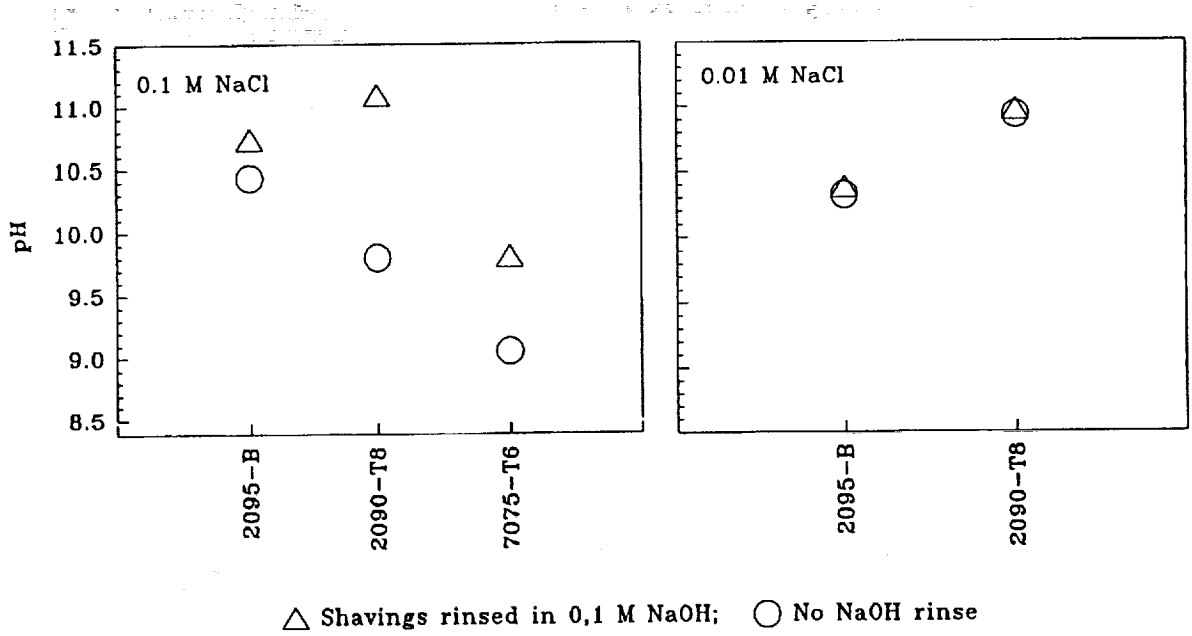

pH attained after three days exposure to NaCl solution

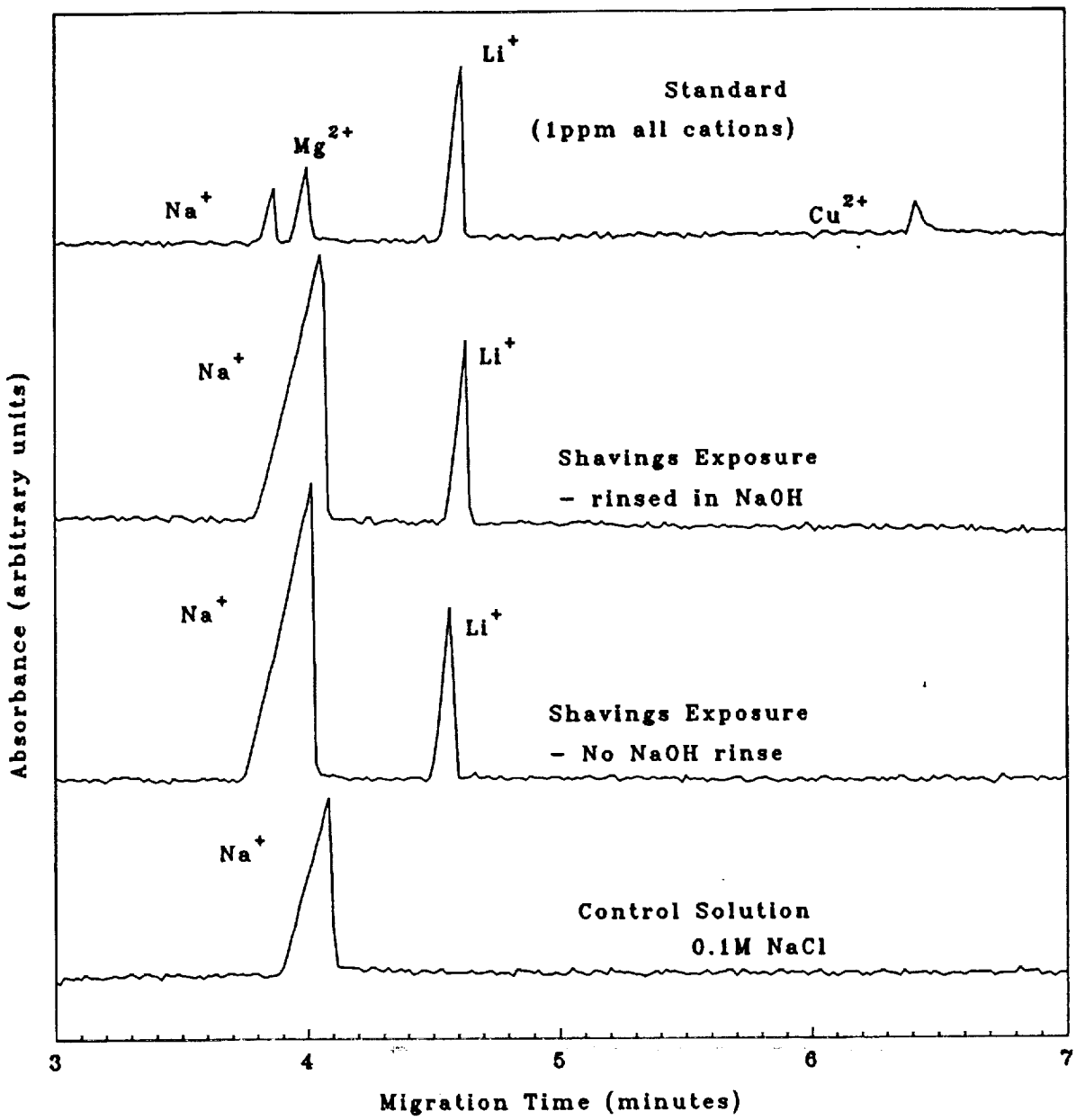

Capillary electrophoresis analysis of solution from 2095-B shavings exposed to 0.1 M NaCl for three days.

ELECTROCHEMICAL CHARACTERIZATION

Potentiodynamic Polarization:

Objective:

* **Determine the basic electrochemical response of modeled boundary features in a simulated occluded environment.**

Experimental:

* **Initial test environments 0.6M NaCL, 0.6M NaCl + 0.1M Li_2CO_3**

* **Performed on 99.99 Al (Cu DZ), SHT 2095, SHT 2090 (grain interiors), Bulk model for T_1 (T_1 phase along sub-boundaries)**

Results:

* **E_{br}-SHT 2095, E_{br}-99.99 Al > > E_{br}-model T_1 in $NaCl/Li_2CO_3$ environment.**

* **T_1 may be considered active compared to grain interiors even in "passive range" due to corrosion current densities greater than 10^{-5} A/cm^2.**

* **$NaCl/Na_2CrO_4$ comparable to $NaCl/Li_2CO_3$ and will be used as complimentary test environment.**

ELECTROCHEMICAL CHARACTERIZATION

Potentiostatic polarization / scratching electrode:

Objective:

* **Determine the potential ranges where samples will spontaneously repassivate when oxide-free surface is exposed to the environment.**

Experimental:

* **Environments tested : 0.6M NaCl + 0.1M Li_2CO_3, 0.1M NaCl + 0.1M Na_2CrO_4**

* **Materials tested : 99.99 Al, Al-0.1 Cu, Al-1.0 Cu, Al-3.96 Cu, SHT 2090, SHT 2095, 2095-A, 2095-B, 2090-T8**

Results:

* **Tested materials exhibit a repassivation potential, E_{rp}. Polarized cathodic to this value bare surface will spontaneously repassivate; polarized anodic to E_{rp} bare surface will not repassivate.**

* **E_{rp}-SHT 2095, E_{rp} SHT 2090 > > E_{br}-model T_1 > E_{rp}-99.99 Al**

* **E_{rp} of Al is a function of Cu content**

ELECTROCHEMICAL CHARACTERIZATION:

Straining Electrode:

Objective:

* **Determine if plastic deformation of materials yields the same electrochemical response as the scratching electrode experiments.**

Experimental:

* **Environments : 0.6M NaCl + 0.1M Li_2CO_3, 0.1M NaCl + 0.1M Na_2CrO_4**

* **Materials : 99.99 Al, SHT 2090**

Results:

* **There exist combination of environment, applied potential and plastic deformation which result in extensive dissolution of 99.99 Al and spontaneous respassivation of SHT 2090.**

* **The applied potentials described are accurately predicted by the scratching electrode experiments.**

Electrochemical Evidence of an Active Pathway:

* **The tip of a propagating crack must be electrochemically active relative to the material composing the crack walls.**

* **In the $NaCl/Li_2CO_3$ and $NaCl/Na_2CrO_4$ environments there are ranges of applied potential where the grain interiors should remain passive while the boundary features are active.**

These conditions are suitable for studying EAC in Al-Cu-Li alloys.

* **Constant load / scratching electrode experiments**

* **Constant extension rate testing**

* **da/dt vs applied K experiments**

ENVIRONMENTALLY ASSISTED CRACKING

Constant Load / Scratching Electrode Experiments:

Objectives:

* **Determine if the TTF behavior of tempered alloys as a function of applied potential correlates to the electrochemistry of the modeled boundary phases.**

* **Determine critical EAC potentials (E_{crit}) such that samples polarized cathodic to E_{crit} will remain passive while samples polarized anodic to E_{crit} will corrode then fracture.**

* **Examine the effect of material temper on the TTF behavior.**

* **Compare the results from lithium containing alloys to an alloy lacking lithium.**

Experimental:

* **Load sample to 60%YS in environment of interest.**

* **Potentiostatically polarize sample to target potential.**

* **Mechanically disturb sample surface to expose bare material to environment/potential combination.**

* **If the sample repassivates, increase the applied potential and repeat experiment.**

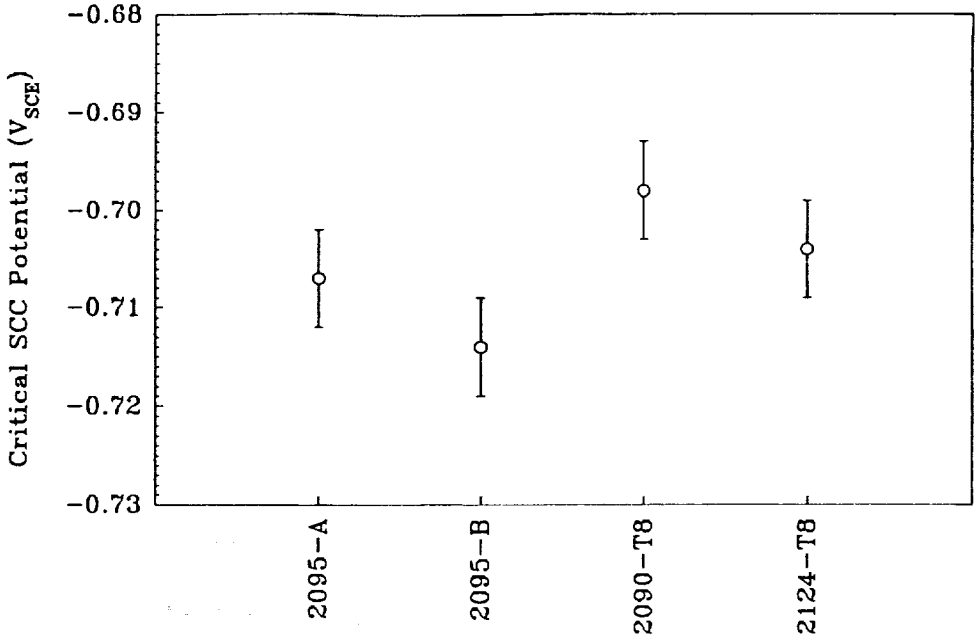

Critical EAC potentials for ST samples at 60%YS in 0.6M NaCl + 0.1M Li_2CO_3

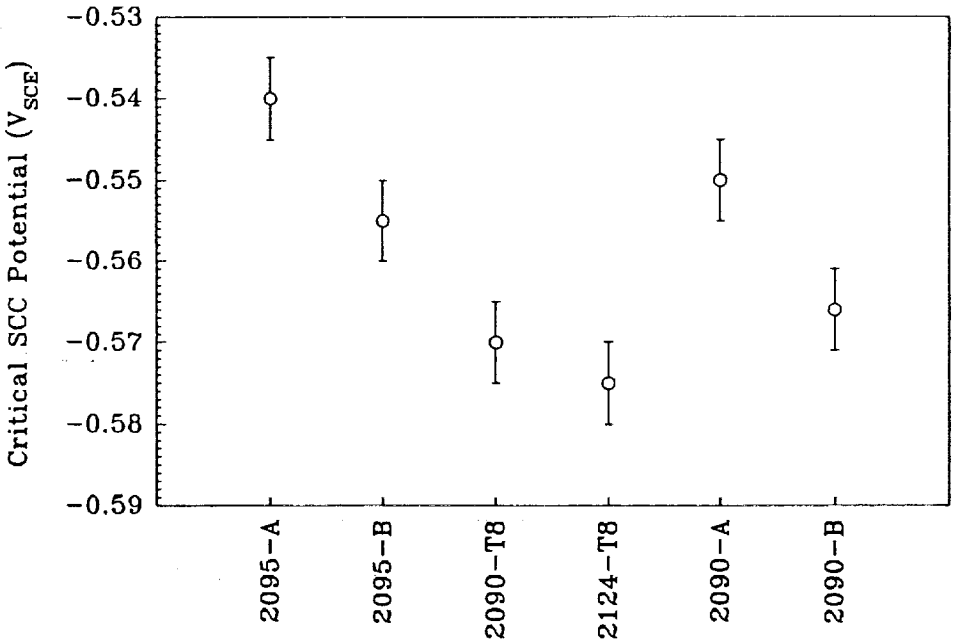

Critical EAC potentials for ST samples loaded to 60%YS in 0.1M NaCl + 0.1M Na_2CrO_4

Underaged 2090-A loaded to 60%YS in
0.1M NaCl + 0.1M Na_2CrO_4

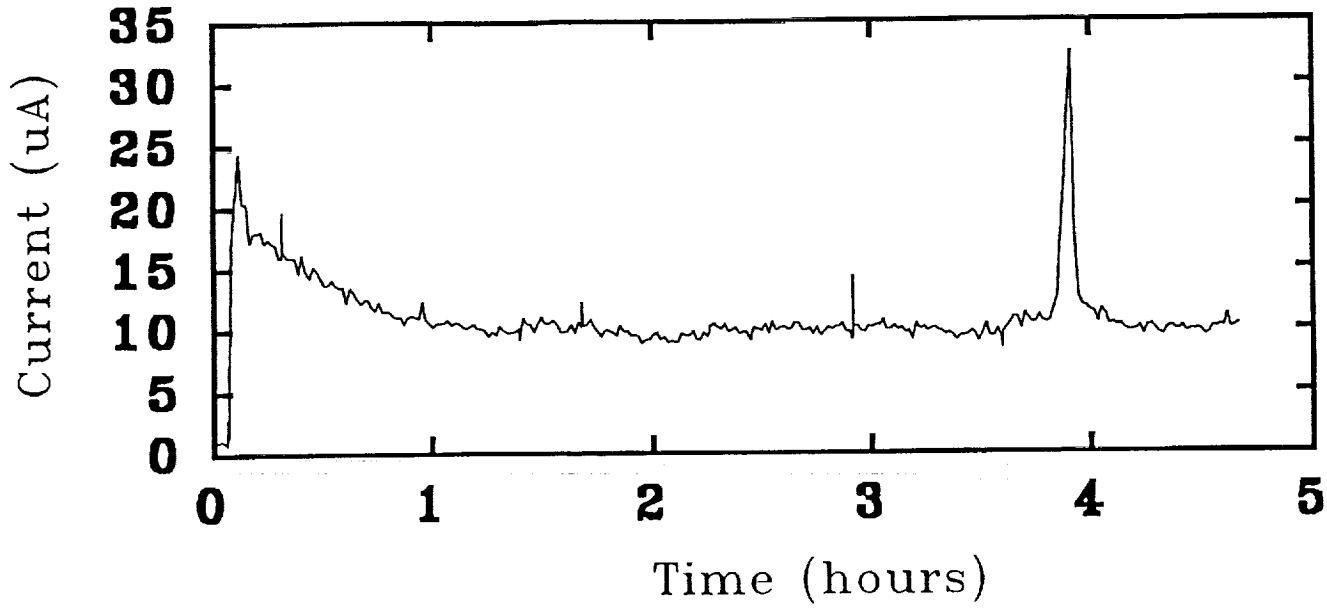

2090-T8 loaded to 60%YS in
0.1M NaCl + 0,1M Na_2CrO_4 at $-575mV_{SCE}$

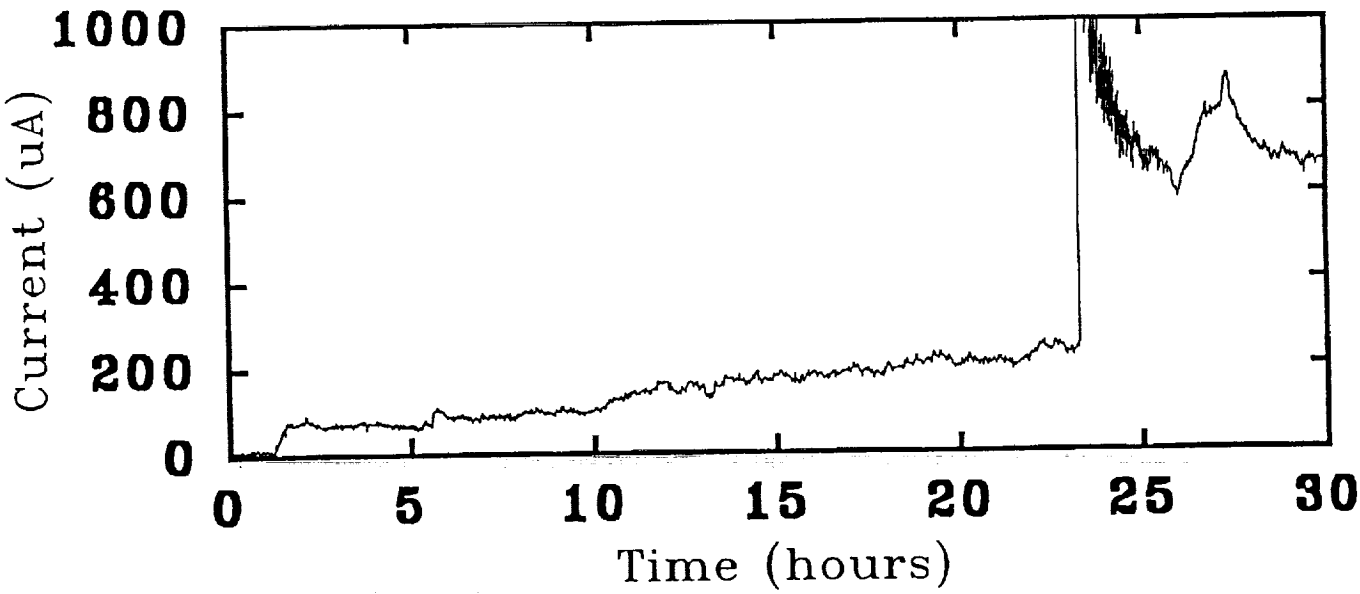

Total charge passed from scratch to failure:

2090-A (UA) : 0.018 coul

2090-T8 : 12.0 coul

Proposed types of overload failures from EAC of smooth bar tensile samples

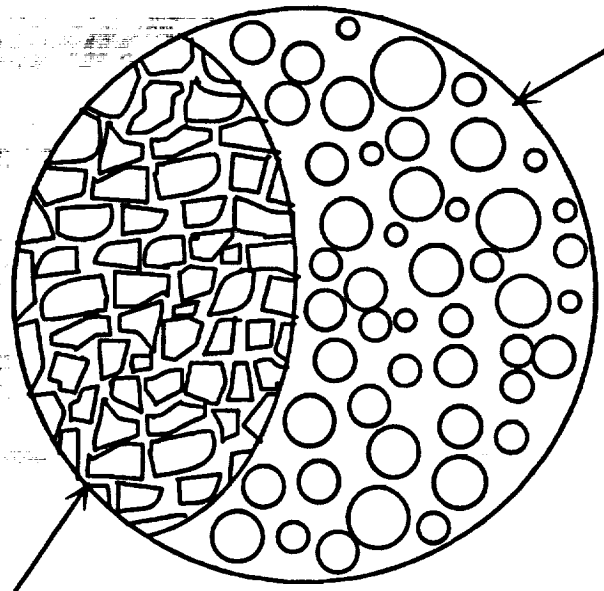

Overload region
* Same as air fracture : ?
* Material properties affected by EAC : ?

EAC region identified by presence of corrosion products

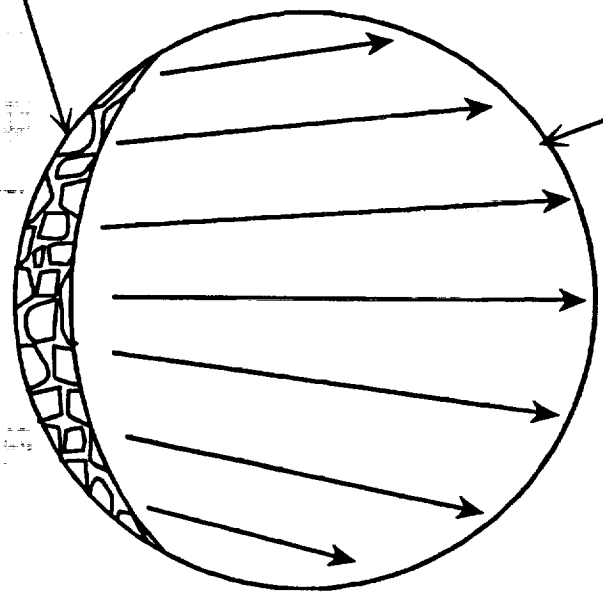

Overload region
* Same as air fracture : X
* Material properties affected by EAC :✓

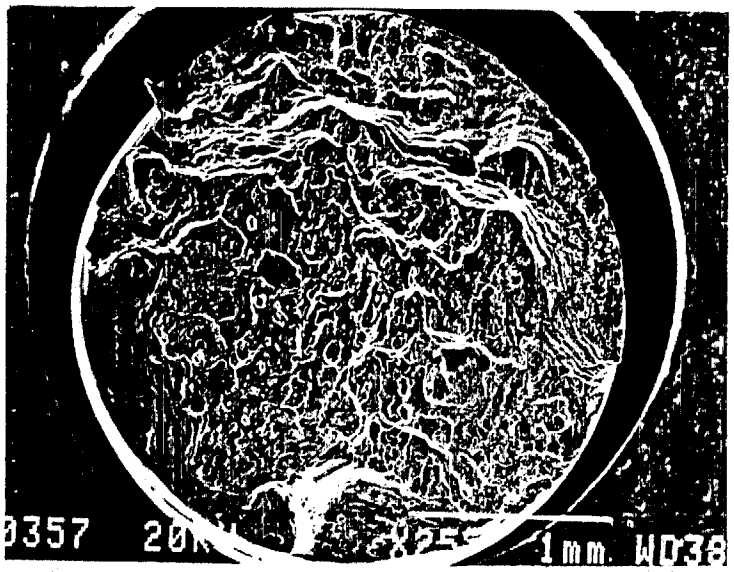

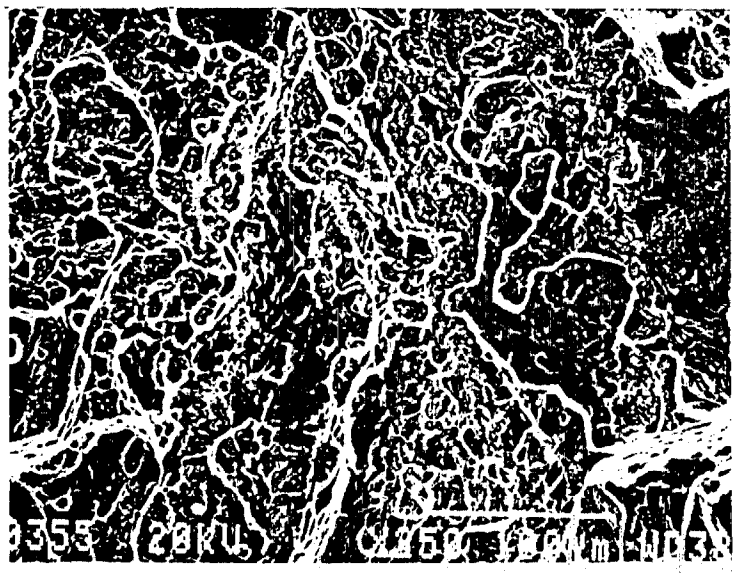

2095-B,ST : air fracture 10^{-3}/sec

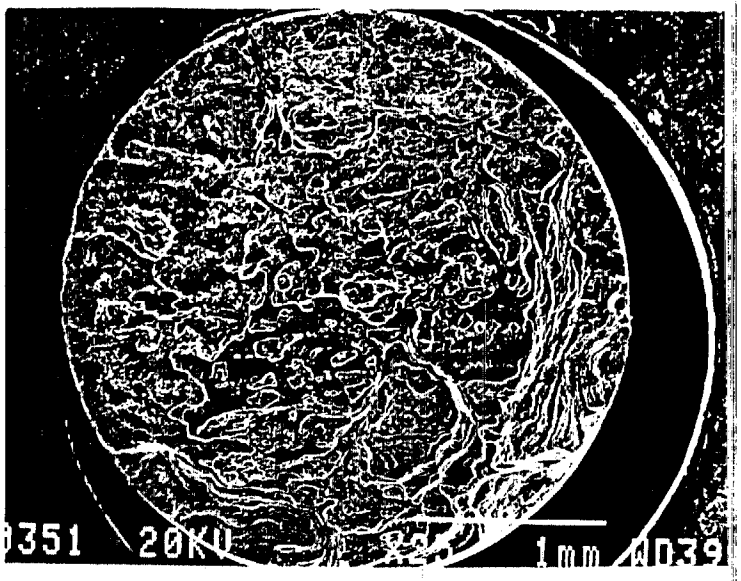

2095-B,ST : corrosion induced failure in $NaCl/Na_2CrO_4$

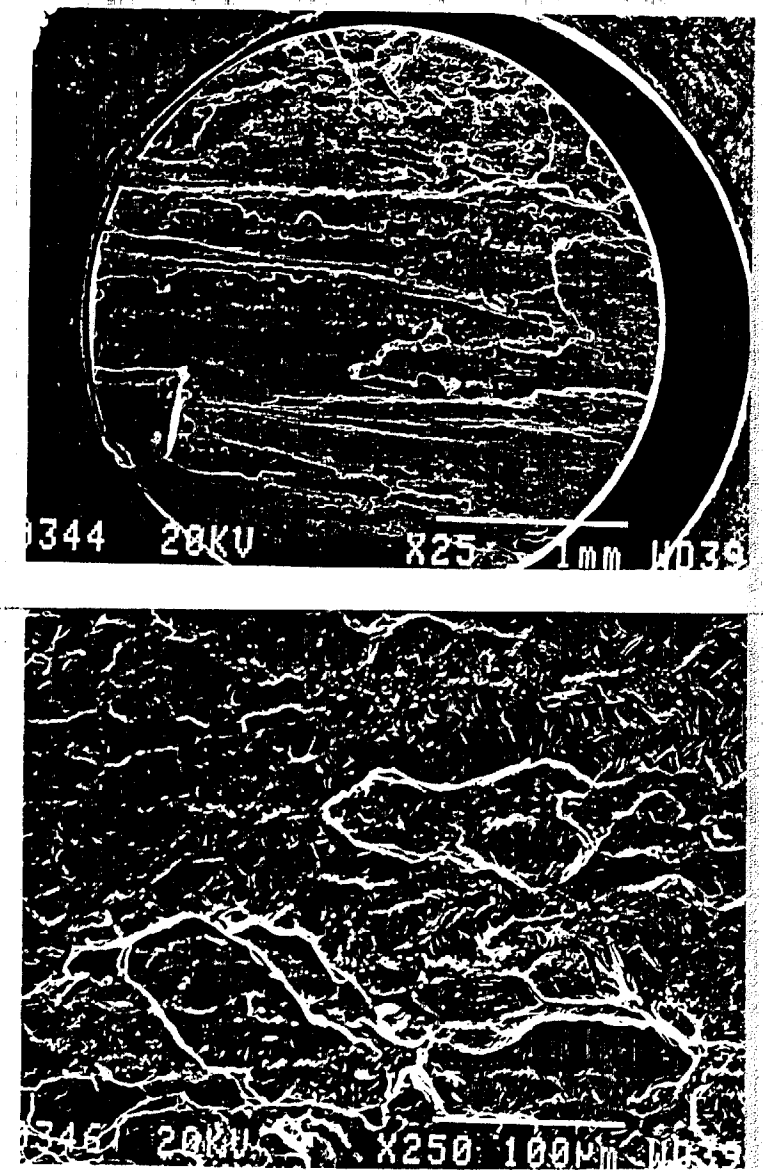

2090-T8,ST : air fracture 10^{-3}/sec

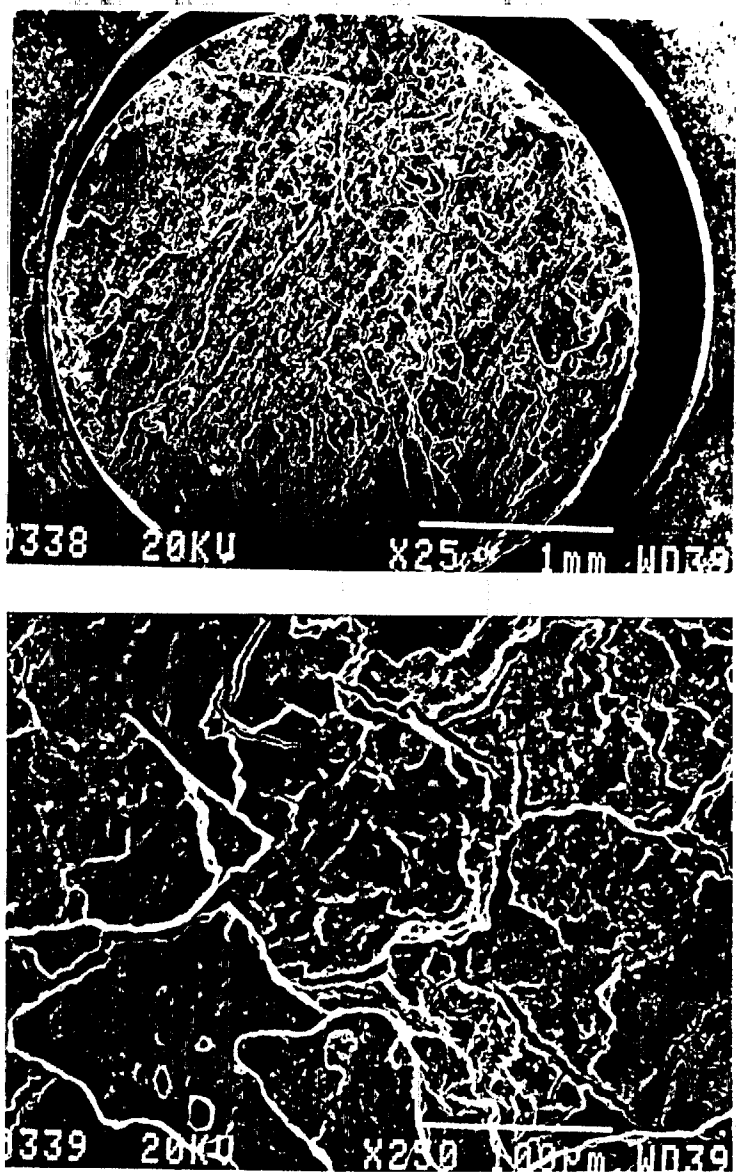

2090-T8,ST : corrosion induced failure in $NaCl/Na_2CrO_4$

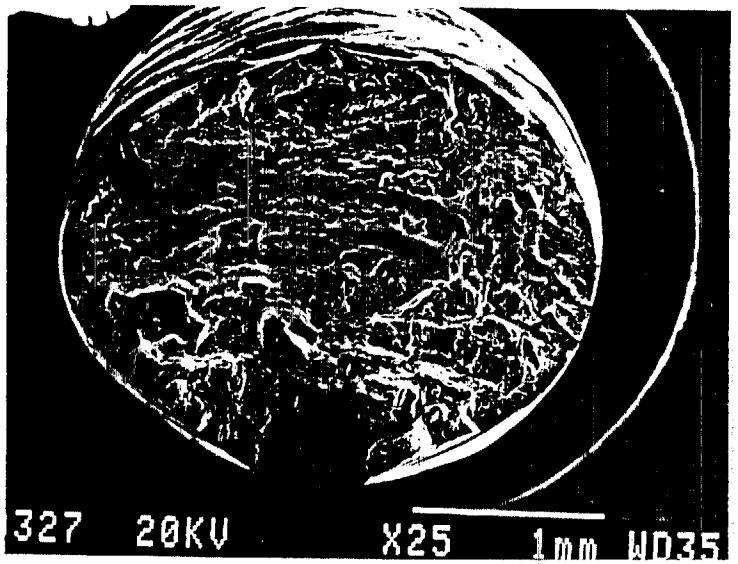

2090-A,ST : air fracture 10^{-3}/sec

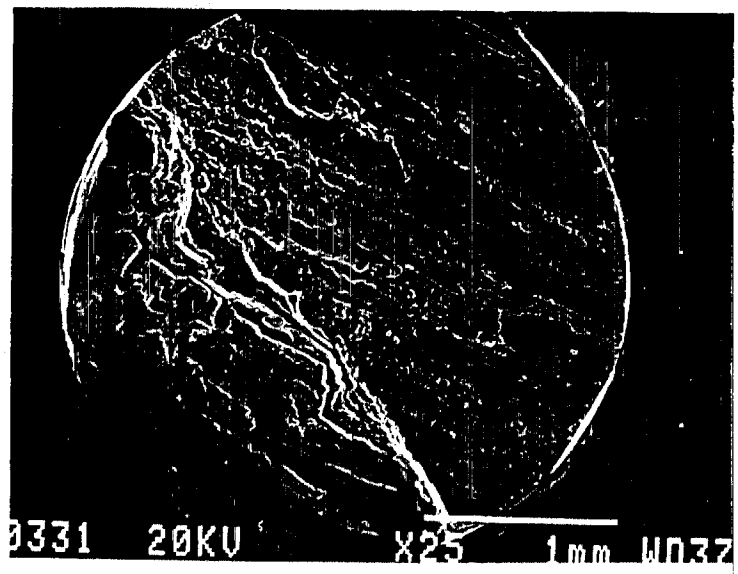

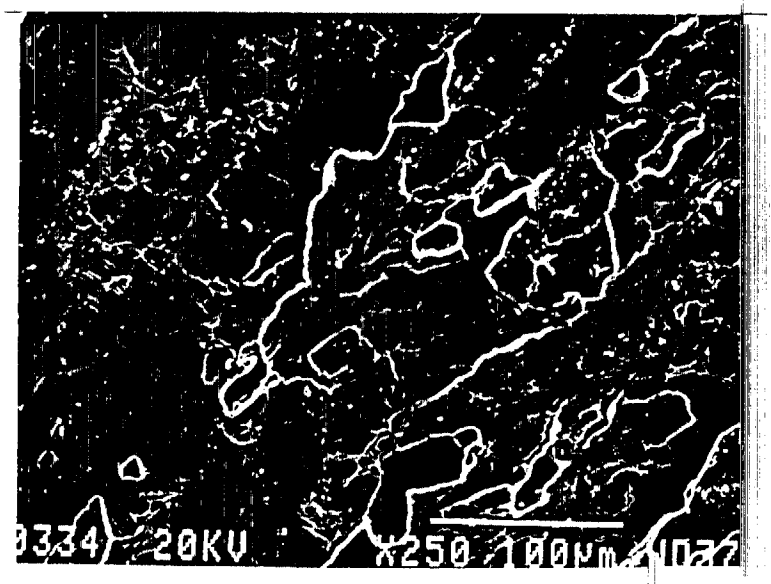

2090-A,ST : corrosion induced failure in $NaCl/Na_2CrO_4$

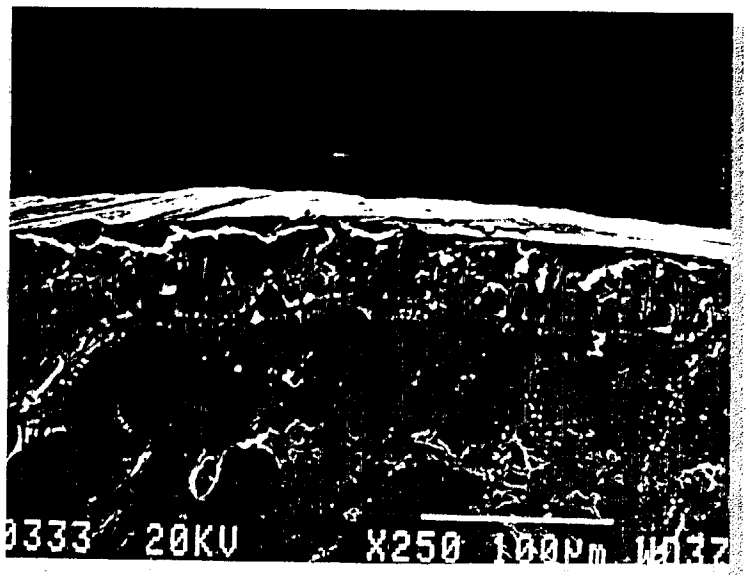

2090-A,ST : corrosion induced failure in $NaCl/Na_2CrO_4$

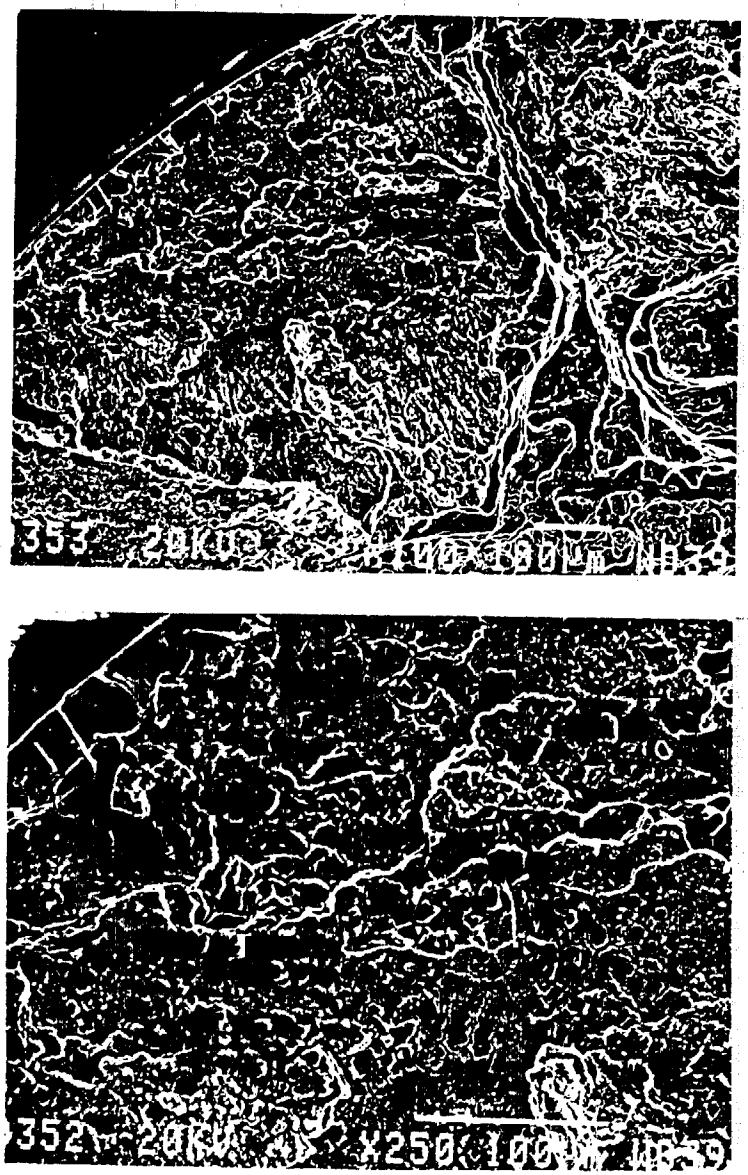

2095-B,ST : corrosion induced failure in $NaCl/Na_2CrO_4$

EDS of regions at periphery of 2090-A (UA) sample which failed in $NaCl/Na_2CrO_4$

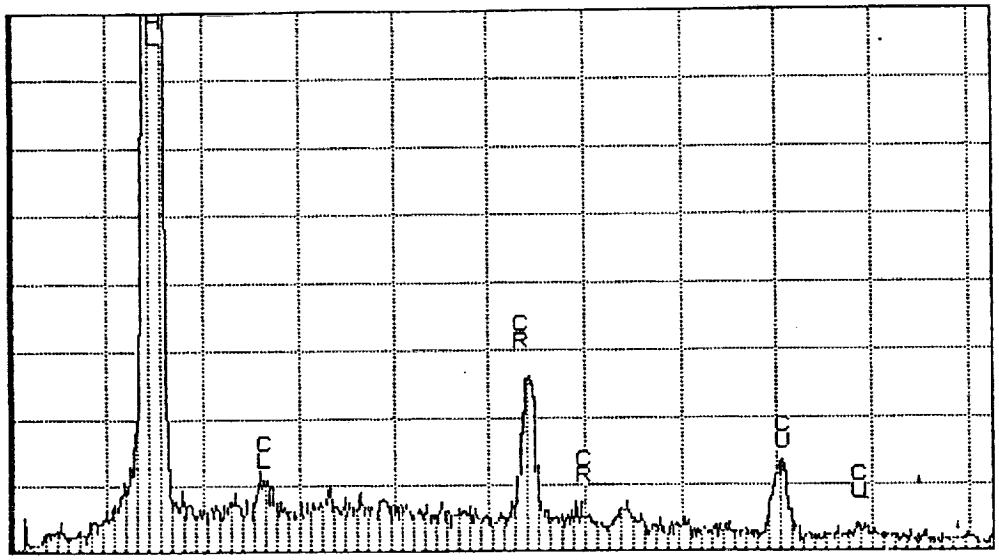

Corrosion region : corrosion product contains chloride and chromate

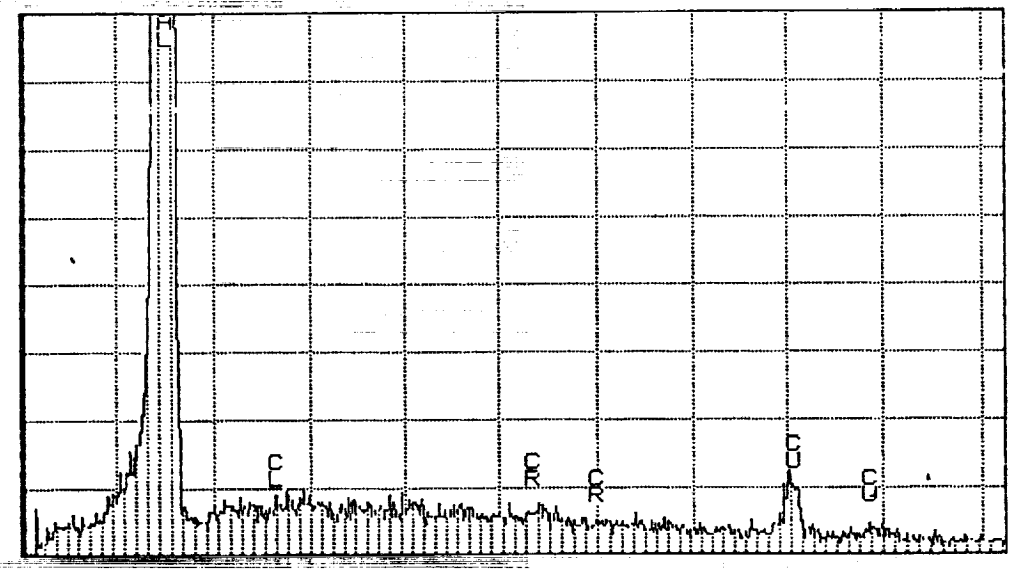

Overload region : no evidence of chloride or chromate

ENVIRONMENTALLY ASSISTED CRACKING

Constant Load / Scratching Electrode Experiment:

Results and Observations:

* Critical EAC potentials (E_{crit}) have been observed for 2095, 2090 and 2124 in $NaCl/Li_2CO_3$ and $NaCl/Na_2CrO_4$ environments.

* Samples polarized cathodic to E_{crit} spontaneously repassivate after bare surface is exposed to solution.

* Samples polarized anodic to E_{crit} corrode and fail after bare surface is exposed to solution.

* The similarity in E_{crit} values for alloys 2124, 2090 and 2095 cannot be explained by the electrochemical activity of the T_1 phase since it does not occur in alloy 2124; however, the similarity in behaviors could be accounted for by a copper depleted region.

* The critical potentials observed for alloys 2090 and 2095 shift towards more cathodic values for increased aging time. This trend can be explained by increased levels of Cu-depletion with increased aging time.

* The differences in total charge passed and fracture morphology between UA 2090 and PKA 2090 and 2095 indicate that these EAC failures are highly sensitive to material temper.

ENVIRONMENTALLY ASSISTED CRACKING

Constant Extension Rate Testing:

Objective:

* **Evaluate EAC behavior in terms of reduction in elongation to failure as a function of applied potential.**

Experimental:

* **Environment : 0.1M NaCl + 0.1M Na_2CrO_4**
* **Materials : 2095-A, 2095-B**
* **Initial strain rate : 1.18×10^{-6}/sec**

Data:

Potential (V_{SCE})	2095-A $(e_{air}-e_{env})/e_{air}$	2095-B $(e_{air}-e_{env})/e_{air}$
open circuit (-0.650)	0.01	0.01
-0.540	0.5	0.8
-0.475	1	1

ENVIRONMENTALLY ASSISTED CRACKING

Constant extension rate testing

Results:

* **Three potential regions of differing behavior:**

  (1) **At the most cathodic potentials tested specimens show negligible decrease in E_f.**

  (2) **At intermediate potentials specimens exhibit marked decrease in E_f. (Anodic to E_{rp} of Cu depleted Al)**

  (3) **At most anodic potentials samples lose all mechanical integrity. (Anodic to E_{rp} of Cu depleted Al and E_{br} of model T_1)**

ENVIRONMENTALLY ASSISTED CRACKING

da/dt vs K experiments:

Objective:

* **Quantify the EAC susceptibility of Al-Cu-Li alloys in terms of crack propagation rates and correlate trends with alloy microstructure.**

Experimental:

* **Environment : 0.1M NaCl + 0.1M Na_2CrO_4**
* **Materials : 2095-A, 2095-B**

Specimen:

* **wedge openning loading (WOL)**
* **B = 0.125", W = 1.44"**
* **Thick specimens favor plane strain fracture mechanics**
* **Thin specimens required to minimize electrochemical IR drop to crack front**

Schematic of set-up for monitoring in-situ crack growth rates

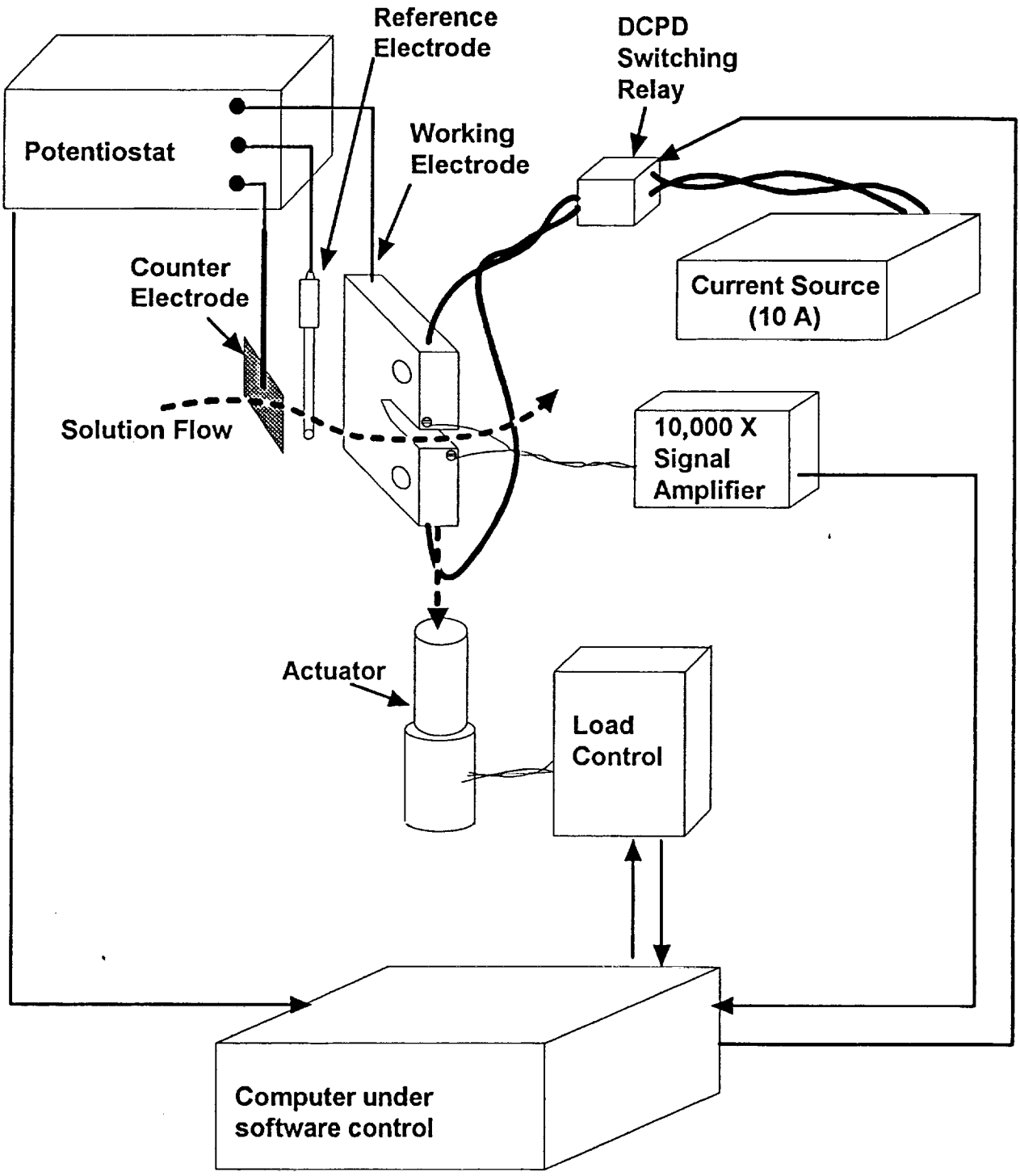

Sample #053194k1

2095-B, SL, WOL (B=0.125, W=1.44)

0.1M NaCl + 0.1M Na_2CrO_4, aerated, E_{appl}=-0.515 V_{SCE}

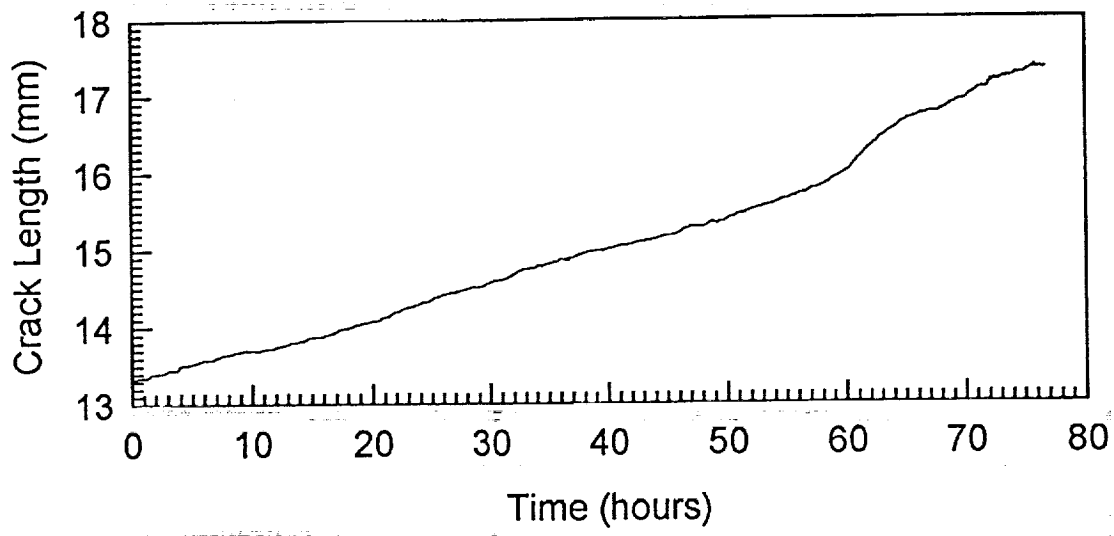

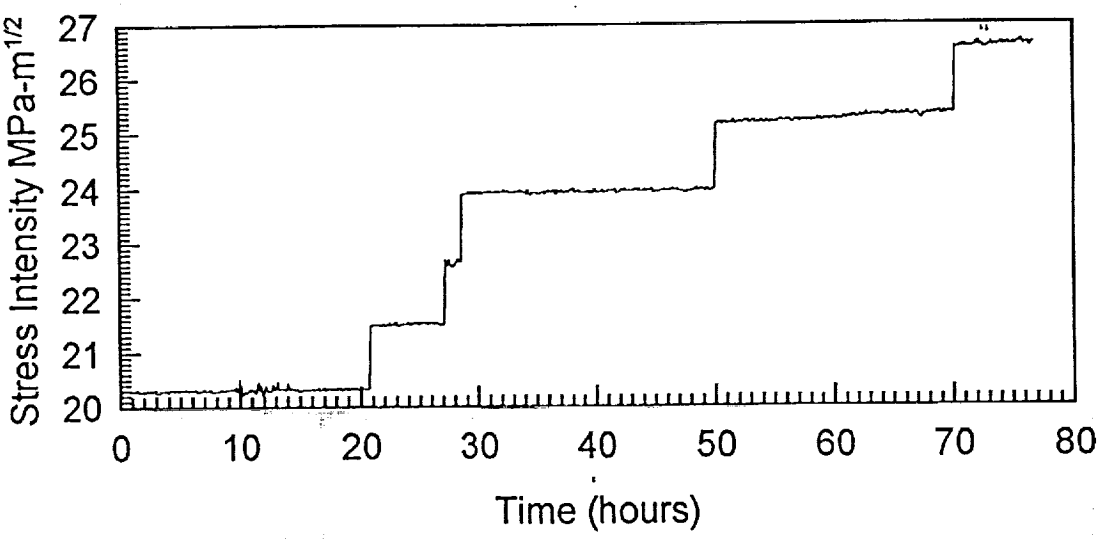

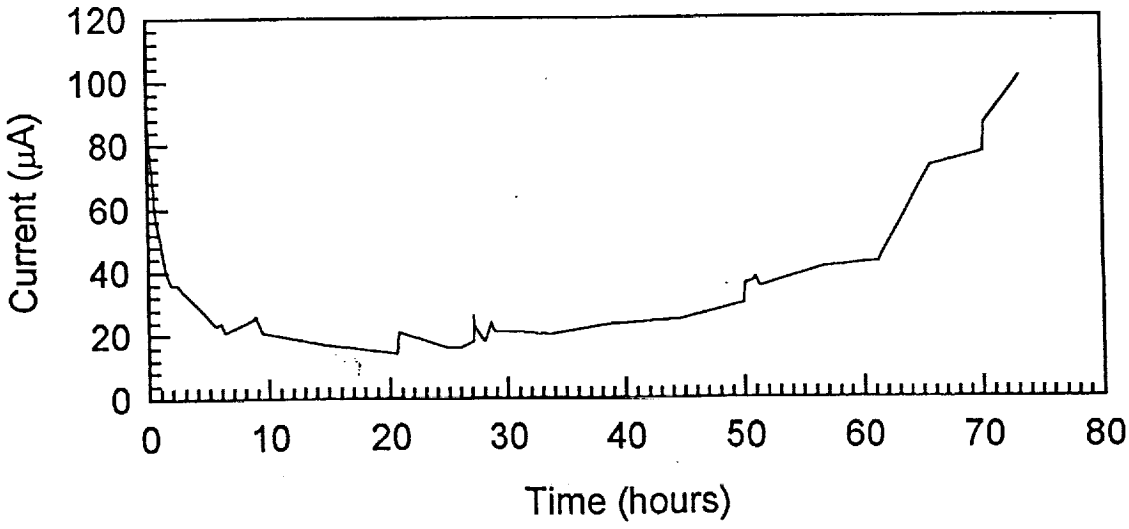

da/dt vs constant K
2095-B, WOL, ST
0.1M NaCl + 0.1M Na_2CrO_4
E_{appl} = -0.515 V_{SCE}

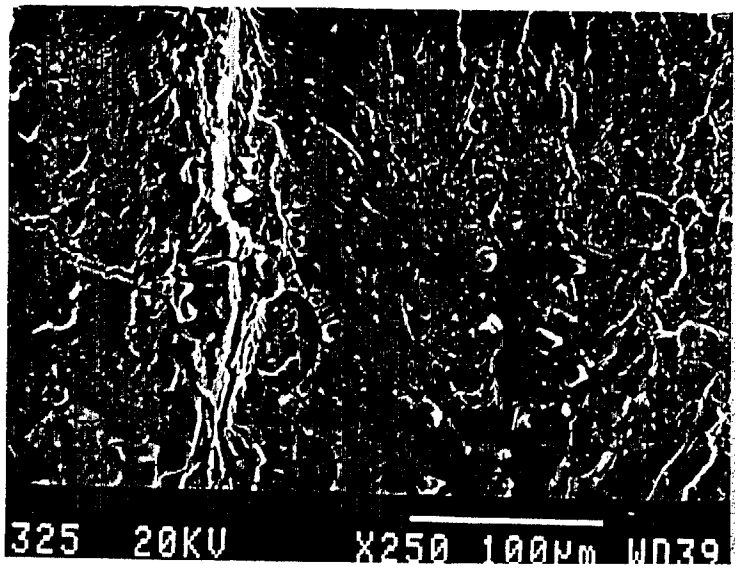

Fatigue pre-crack region

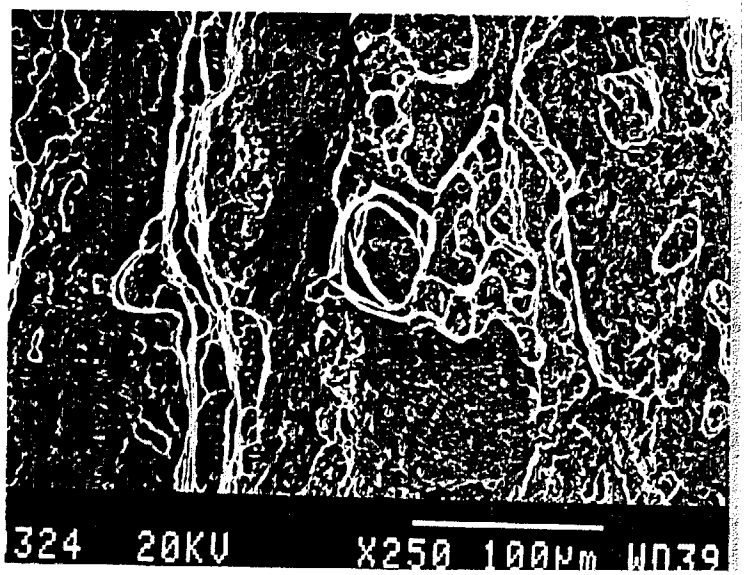

Overload region

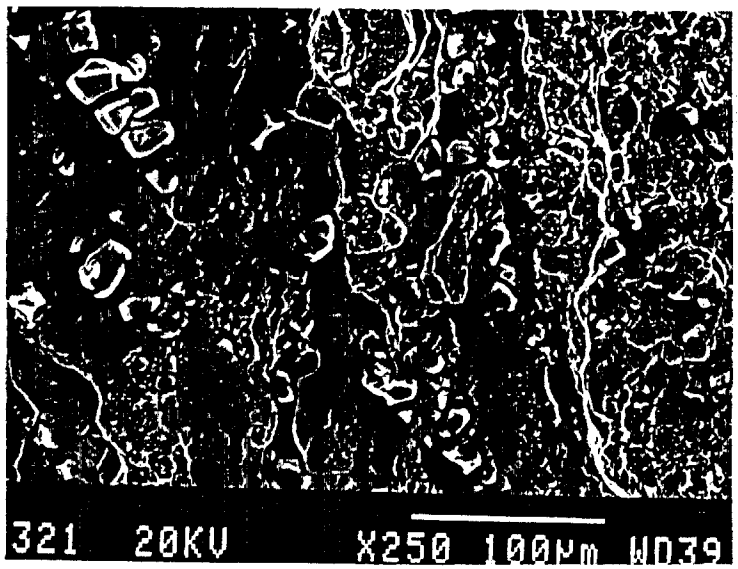

EAC region

da/dt vs constant K
2095-B, WOL, ST
0.1M NaCl + 0.1M Na_2CrO_4
E_{appl} = -0.515 V_{SCE}

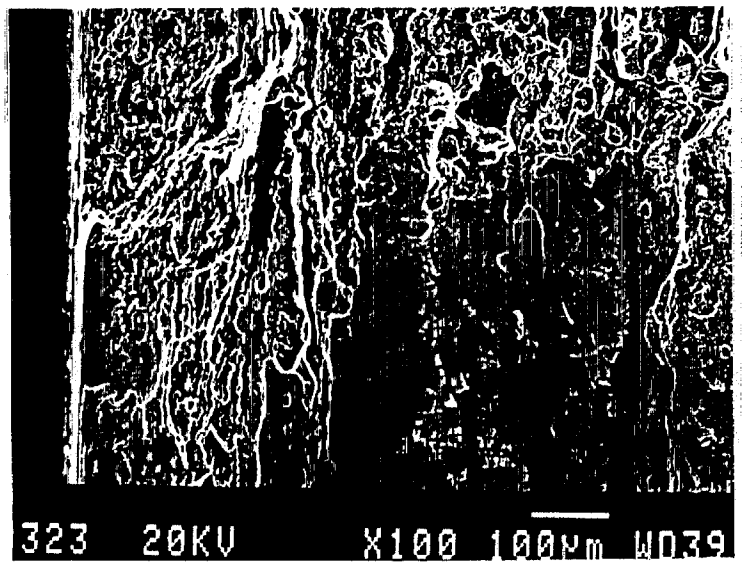

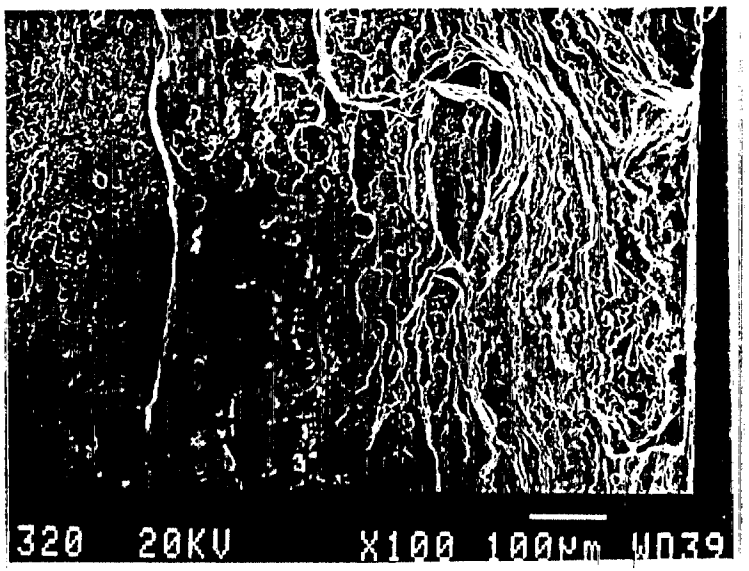

Left and right portions of crack front at experiment completion.

ENVIRONMENTALLY ASSISTED CRACKING

da/dt vs K experiments:

Observations:

* A technique has been developed by which in-situ cracks can be grown in Al-Li-Cu alloy 2095 with real-time monitoring of crack length and control of applied stress intensity.

* Cracks have been grown in two tempers of 2095 (UA and PKA).

* Initial fractography suggests that constraint contributes to crack propagation.

SUMMARY OF PROGRESS TO DATE

(1) Combinations of aqueous environment and applied electrochemical potential have been identified which are suitable for studying EAC in Al-Li-Cu alloys.

(2) Insight into the roles of electrochemical potential, material composition and material temper in EAC has been gained through constant load and constant extension rate testing.

(3) EAC cracks in Al-Li-Cu alloy 2095 have been grown and monitored in-situ through use of appropriate environment, electrochemical potential and applied stress intensity.

FUTURE WORK:

Da/dt vs applied K experiments:

* **Determine crack growth rates for UA and PKA tempers of 2095 and 2090 in $NaCl/Na_2CrO_4$ and $NaCl/Li_2CO_3$ environments as a function of applied stress intensity.**

* **Rank materials in terms of crack growth rates and propose microstructural features likely to be responsible for observed ranking.**

Alternate immersion of DCB specimens:

* **Measure crack growth rates of 2090, 2095-A and 2095–B during AI in a chloride environment for comparison with rankings provided by other test methods.**

* **Examine crack chemistries at experiment termination to refine model of occluded chemistry.**

Scratching electrode on non-T_1 containing materials:

* **Find E_{crit}/E_{rp} for Al-Cu-X alloys without lithium to provide a larger data base of critical potentials.**

Variable stress level / constant load / scratching electrode:

* **Examine the effect of stress level on the TTF behavior of smooth bar specimens under constant load.**

* **Determine threshold stress below which material failure does not occur. Rank materials in terms of TTF at low stress levels.**

Constant extension rate testing:

* Determine if critical potentials correspond to abrupt changes in material properties or if changes are gradual.

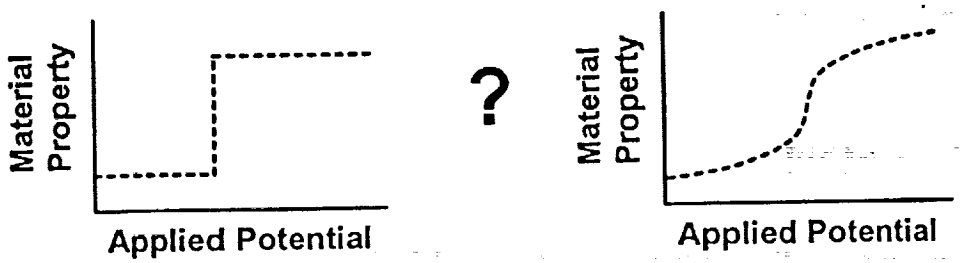

Scratching electrode with high speed data acquisition:

* Measure transients upon scratching samples during potentiostatic polarization to determine if maximum corrosion rates are sufficient to account for crack growth rates.

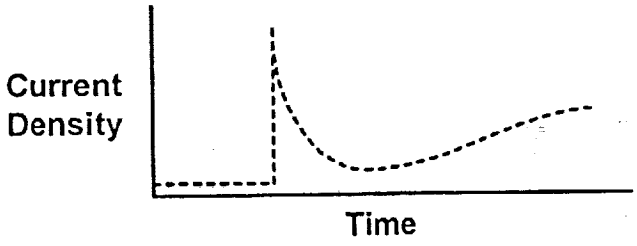

Solution chemistry analysis of artificial occluded geometries:

* pH measurement / C.E. analysis of solutions from artificial restricted geometries subjected to constant immersion or alternate immersion to refine understanding of occluded chemistries.

Project #5 Hydrogen Interactions in Aluminum-Lithium Alloys and Hydrogen Embrittlement of AA 2090

S.W. Smith and J.R. Scully

Objective

The role hydrogen plays in the environmentally assisted cracking of aluminum-lithium alloys has not been fully established. This issue must be addressed since hydrogen environmentally assisted cracking (HEAC) is an important issue concerning alloys intended for utilization in advanced aerospace applications. To date the hydrogen absorption, internal transport, trapping and resultant effects on mechanical properties have not been characterized for these alloys. We seek to develop a fundamental understanding of the effects of dissolved and trapped hydrogen on the mechanical properties of selected Al-Li-Cu-X alloys. In order to reach this goal we will study the behavior of alloy 2090.

We have established three major goals for this study. We propose to: (a) distinguish HEAC from aqueous dissolution controlled EAC, (b) correlate internal hydrogen embrittlement (IHE) with mobile and trapped hydrogen concentrations, and (c) identify significant trap sites and hydride phases (if any exist). The ultimate goal of this project is to develop deterministic models which define the effect of absorbed hydrogen on the mechanical properties of aluminum-lithium alloys.

Current Status

Research during the latest reporting period has focused on the use of thermal desorption spectroscopy (TDS) to identify operative trap sites, to determine the process by which hydrogen is absorbed and measure internal hydrogen concentrations that may be obtained for AA2090. In previous reports we have shown that absorbed hydrogen can adversely affect the mechanical behavior of this alloy. The desorption studies that we have been

conducting were performed to answer the questions; can a significant amount of hydrogen be absorbed when exposed to typical operating environments to account for the cracking behavior seen in an SCC test, once hydrogen has been absorbed into these materials where is it trapped, and can this trapping behavior be altered.

The issue of hydrogen absorption has been addressed by measuring hydrogen desorption of materials that were exposed to several different environments and tested under different tensile loading conditions. These studies have clearly shown increased absorption under conditions of dynamic loading, however, further study is required to determine the mechanism by which this accelerated absorption rate is produced. Trap site identification has been accomplished with the use of model Al-3Li binary alloys, recrystallized Al-Li-Cu-Zr alloys and by testing AA2090 under various aging conditions. This information will be used to see if any correlation between operative trap sites and HEAC can be made.

Recent Findings

Four major results have been identified recently; 1) several trapping states have been identified in AA2090, these include dislocations, high angle grain boundaries and δ′; 2) a significant level of absorbed hydrogen has been found in specimens that were exposed to environment by alternate immersion, this strongly implicates a hydrogen related mechanism contributing to SCC; 3) hydrogen absorption and possibly transport are enhanced during concurrent straining and cathodic polarization and 4) absorbed hydrogen can be repartitioned via dislocations during straining of a precharged specimen.

Future Work

Thermal desorption analysis will be used to address three major topics during the next reporting period, these are: 1) is the increased hydrogen absorption that has been identified under concurrent straining and cathodic charging due to increased hydrogen transport, mechanical destabilization of

the passive film or an increased solubility due to elastic loading; 2) what effect does unavoidable aging of a specimen during a desorption test have on trap binding energies that have been calculated and; 3) develop models for HEAC of AA2090 using the information obtained by trap analysis, hydrogen transport and absorption coupled with knowledge of the mechanical behavior of these materials.

The issue of possible increased hydrogen transport via dislocations will be studied using straining electrode tests (SET), while varying the strain rate used during a test. By modifying the SET test used, and cathodically charging specimens under varying constant loads the issue of elastic loading effects contributing to an increased hydrogen solubility may be addressed. Microhardness testing will be used in order to evaluate to what degree the materials are being aged during TDS tests, this information will be used with the information already learned about the available trapping sites as a function of aging to evaluate what effect this aging may have on the creation or elimination of trapping sites during a test.

The final and major goal of this work will be addressed, this is to develop a deterministic model for the HEAC of aluminum-lithium alloys in light of the information that has been developed on the mechanical behavior of these materials in the presence of absorbed hydrogen, the hydrogen trapping behavior of AA2090, and the process of hydrogen absorption.

Presentation Viewgraph Captions

1. Title

2. Objectives

3. Absorbed hydrogen concentrations measured for AA2090-UA under several testing conditions.

4. Mechanical data for the unrecrystallized AA2090 and the three variants of recrystallized Al-Li-Cu-Zr alloy used for mechanical testing.

5. Continuous extension rate test results for AA2090 tested as a function of absorbed hydrogen. All testing was performed at a strain rate of 2.5 x 10^{-6} sec^{-1}.

6. Results for $J_{initiation}$ values obtained from J-Integral testing for all AA2090 and Al-Li-Cu-Zr alloys studied.

7. Results for the effect of hydrogen charging on the mechanical behavior of AA2090.

8. Fractography showing the region of high triaxial constraint in a fracture toughness test of the unrecrystallized AA2090-UA-TL, charged and uncharged.

9. Fractography showing the region of high triaxial constraint in a fracture toughness test of the fine grain recrystallized Al-Li-Cu-Zr alloy in the UA temper, charged and uncharged.

10. Fractography showing the region of high triaxial constraint in a fracture toughness test of the fine grain recrystallized Al-Li-Cu-Zr alloy in the PA temper, charged and uncharged.

11. Conclusions for mechanical testing.

12. Relevant questions developed from mechanical testing that must be studied.

13. Overview of hydrogen analysis methods.

14. Schematic drawing of the thermal desorption spectroscopy system constructed at UVA.

15. Partial pressure vs. time data for several mass to charge channels sampled during desorption of an AA2090-UA sample tested at a thermal ramp rate of 10°C/min.

16. Mass balance equations used to solve for desorption rate and absorbed hydrogen concentration during a thermal desorption experiment.

17. Hydrogen desorption rate vs. time for an AA2090-UA sample tested at a thermal ramp rate of 10°C/min.

18. Desorption rate calculations for the detrapping and diffusion of a bulk species being desorbed from a metal by thermal stimulation.

19. Continuation of desorption rate calculations.

20. Deconvolution of desorption rate data for AA2090-UA and the identification of major trapping states.

21. Hydrogen partitioning among the major trapping states for AA2090 when tested in the T3, UA (T3 + 5 hrs. @ 160°C) and PA (T3 = 25 hrs. @ 160°C) tempers.

22. Binding energy calculations used to calculate trap binding energies with thermal desorption spectroscopy.

23. Normalized hydrogen desorption rate vs. time data for AA2090 tested at several thermal ramp rates.

24. Calculated binding energies for trapping states present in the AA2090 studied.

25. Hydrogen desorption rate vs. time data for an Al-3Li binary alloy tested in solution heat treated (SHT), SHT + 5 hrs. @ 160°C, and SHT + 25 hrs. @ 160°C tempers.

26. Hydrogen desorption spectra and hydrogen partitioning data for AA2090-UA. The data identified as being prestrained 3% represents specimens that were strained at a constant cross head displacement of 2×10^{-6} sec^{-1} to a total strain of 3% before being charged in order to increase the dislocation density present in those specimens.

27. Hydrogen desorption spectra and hydrogen partitioning data for the recrystallized Al-Li-Cu-Zr alloy. The fine grain recrystallized alloy has a higher total grain boundary area than the large grain material, which results in a larger number of high angle grain boundary trap sites.

28. Hydrogen desorption spectra for AA2090 specimens tested under alternate immersion. The Al tests were conducted for 84 days with the specimens being stressed in a constant displacement apparatus.

29. Hydrogen desorption spectra for AA2090 specimens cathodically charged under a straining electrode test. The specimens were preloaded to 75% σ_{ys} and strained at a constant cross head displacement rate of 2×10^{-6} sec^{-1} while being polarized at -2 V_{SCE} in a pH 1 HCl solution.

30. Hydrogen desorption spectra and hydrogen partitioning data for AA2090. The data identified as being strained to 3% represents specimens that were cathodically charged than strained at a constant cross head displacement rate of 2×10^{-6} sec^{-1} to a total strain of 3% in order to identify hydrogen transport of absorbed hydrogen via dislocations.

31. Conclusions from thermal desorption spectroscopy.

32. Future work

Hydrogen Interactions in Aluminum-Lithium Alloys and Hydrogen Embrittlement of AA2090

Stephen W. Smith
and
John R. Scully

University of Virginia
Department of Materials Science and Engineering
Center for Electrochemical Sciences and Engineering
Charlottesville, VA 22903

Sponsors:
NASA Langley Research Center
Virginia Center for Innovative Technology
Alcoa Technical Center; Contact: J.P. Moran

Objective

- Distinguish hydrogen induced EAC from aqueous dissolution
  - Mechanical Testing of pre-charged specimens
    - Continuous Extension Rate Testing (CERT)
    - J-Integral R-Curve Testing

- Identify significant hydrogen trap sites and hydride phases (if any), present in selected Al-Li-Cu-X alloys
  - Characterized hydrogen partitioning as a function of microstructural features and aging condition
    - Thermal Desorption Spectroscopy (TDS)

- Correlate hydrogen environmentally assisted cracking (HEAC) with mobile and trapped hydrogen concentrations and operative trap sites

Absorbed Hydrogen Concentrations AA2090-UA

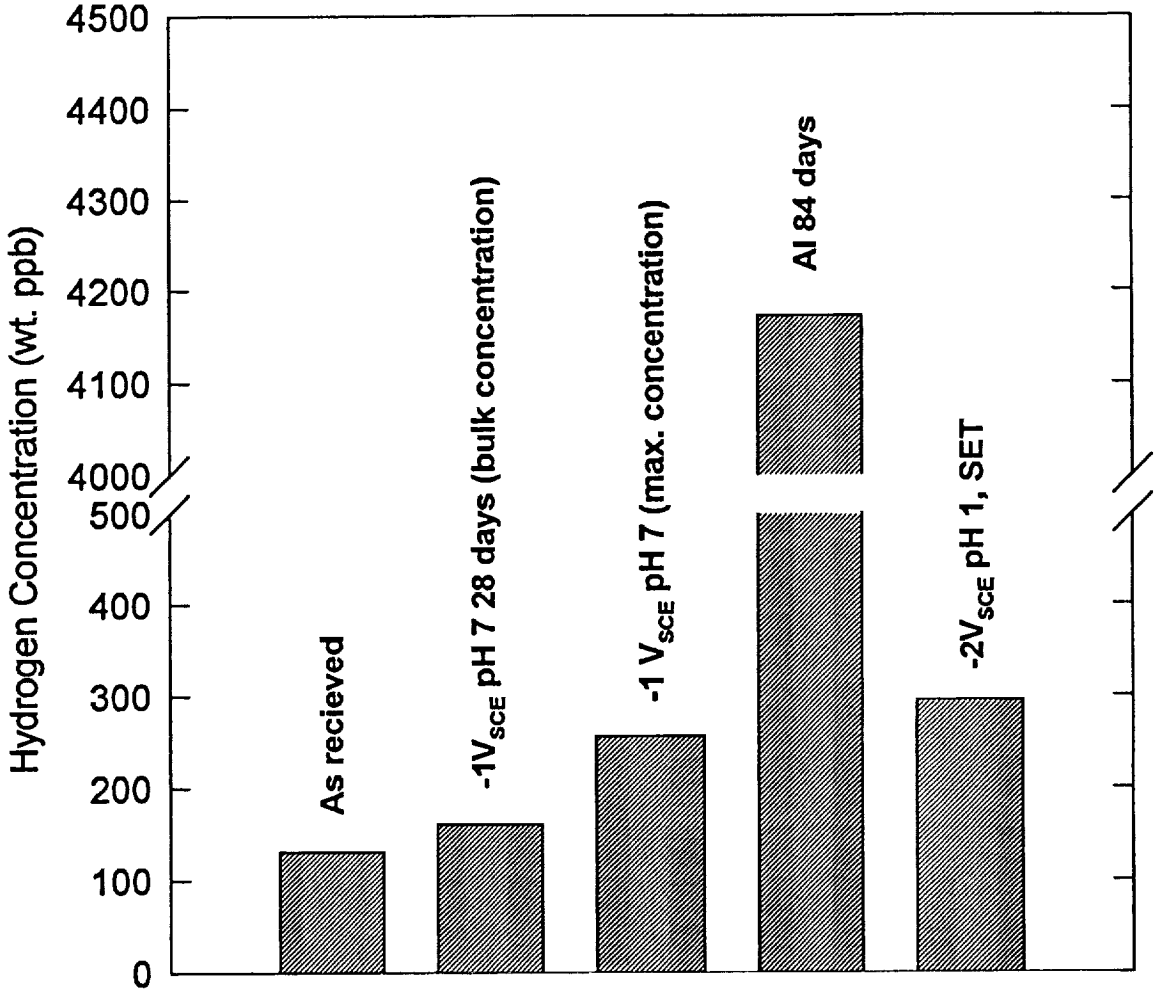

Alloys Studied

Mechanical properties of alloys being studied

Alloy	Temper	Product Form	Grain Dimensions (μm) (L x LT x ST)	σ_{YS} (Mpa)	σ_{UTS} (MPa)
Al-Li-Cu (A)	UA PA	Recrystallized	1200 x 1100 x 250	296 379	393 434
Al-Li-Cu (B)	UA PA	Recrystallized	800 x 800 x 100	241 400	379 490
Al-Li-Cu (C)	UA PA	Recrystallized	30 x 30 x 20	303 400	421 496
AA2090 (D)	T3 UA PA	Unrecrystallized	4400 x 600 x 10	255 296 434	303 476 572

temper designations:
T3 - as received (solution heat treated, cold worked, naturally aged)
UA - T3 + 5 hrs. at 160°C
PA - T3 + 25 hrs. at 160°C

CERT RESULTS
Unrecrystallized 2090 Sheet

Temper	Orientation	Charging Condition	Reduction in Area (% loss)	Fracture Mode
T3	T	Uncharged	27.98#	transgranular shear
		28 days @ -1V_{SCE}	17.49#	TGS + intersubgranular
T3	L	Uncharged	19.97#	transgranular shear
		28 days @-1V_{SCE}	9.63#	hydrogen affected TGS
UA	T	Uncharged	20.68*	transgranular shear
		28 days @-1V_{SCE}	13.85*	TGS + intersubgranular
UA	L	Uncharged	13.35*	transgranular shear
		28 days @-1V_{SCE}	11.94*	hydrogen affected TGS
PA	T	Uncharged	32.27#	transgranular shear
		28 days @-1V_{SCE}	38.40#	transgranular shear
PA	L	Uncharged	16.30#	transgranular shear
		28 days @-1V_{SCE}	14.85#	transgranular shear

All specimens charged in 0.25 M Na_2SO_4 buffered to pH 7.

- average of 3 specimens
* - single specimen tested

Results of J-Integral Testing for 2090 alloys.

Alloy	Fracture Mode* ($UA_{Charged}$)	J_i (kJ/m^2) (K_i (*MPa √m*))			
		$UA_{Uncharged}$	$UA_{Charged}$	$PA_{Uncharged}$	$PA_{Charged}$
Al-Li-Cu (A)	Transgranular	6.70 (*22.93*)	9.47 (*27.28*)	10.51 (*28.73*)	11.02 (*29.42*)
Al-Li-Cu (B)	Transgranular + Intergranular	13.71 (*32.82*)	6.87 (*23.23*)	9.86 (*27.84*)	15.12 (*34.46*)
Al-Li-Cu (C)	Intergranular	15.59 (*35.00*)	5.20 (*20.22*)	4.77 (*19.36*)	3.98 (*17.69*)
AA 2090 - LT (D)	Transgranular + Intersubgranular	18.42 (*38.04*)	17.31 (*36.88*)	5.35 (*20.51*)	5.12 (*20.06*)
AA 2090 - TL (D)	Transgranular + Intergranular	27.7 (*46.7*)	18.6 (*38.2*)	---	---

* The central plane strain dominated "pop-in" region is where fracture mode assessment was taken.

Hydrogen pre-charging influences the mechanical behavior of AA2090

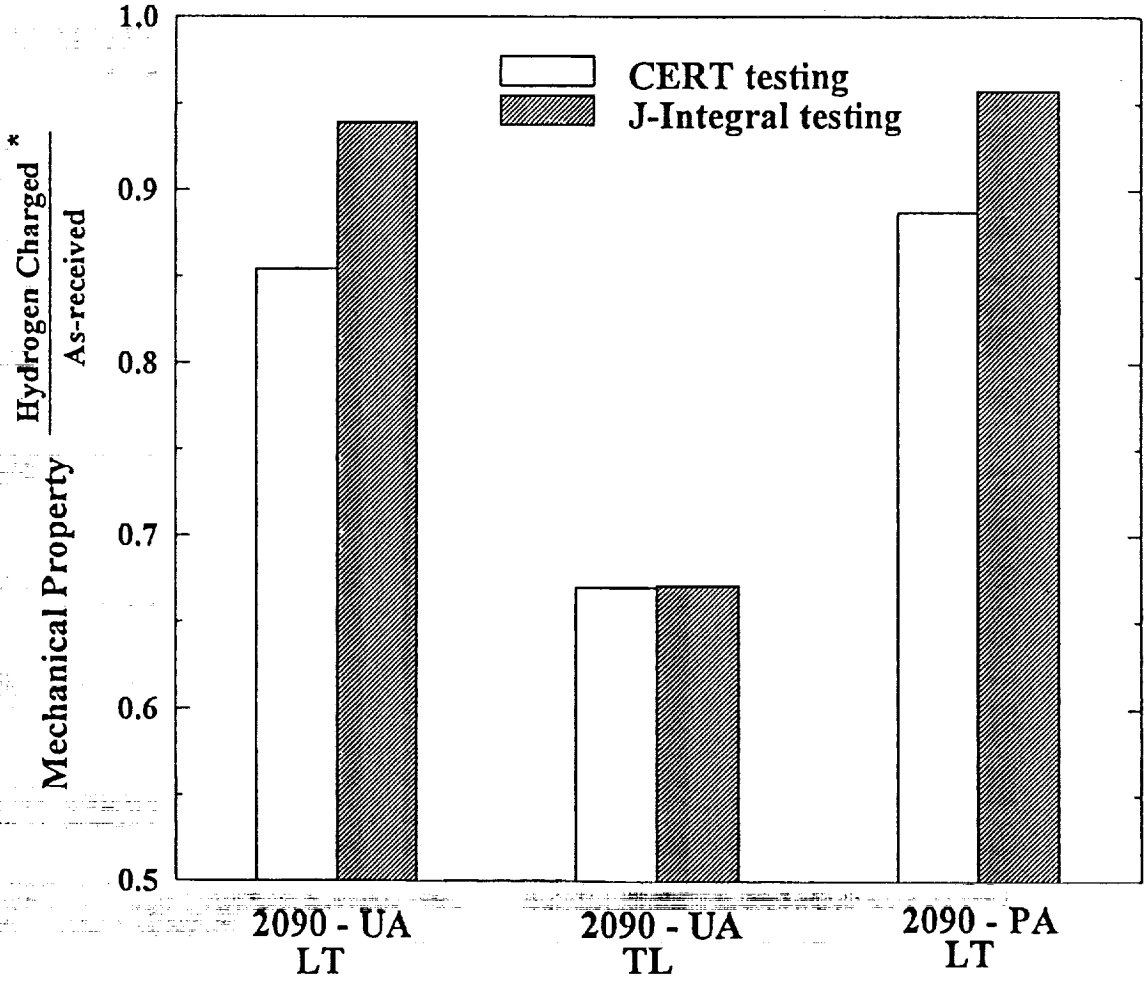

* Reduction in cross sectional area measured for CERT tests
J_i measured for J-Integral testing

All specimens pre-charged for 28 days in 0.25 M Na_2SO_4 buffered to pH 7.

2090 UNRECRYSTALLIZED UA - TL

UNCHARGED

CHARGED

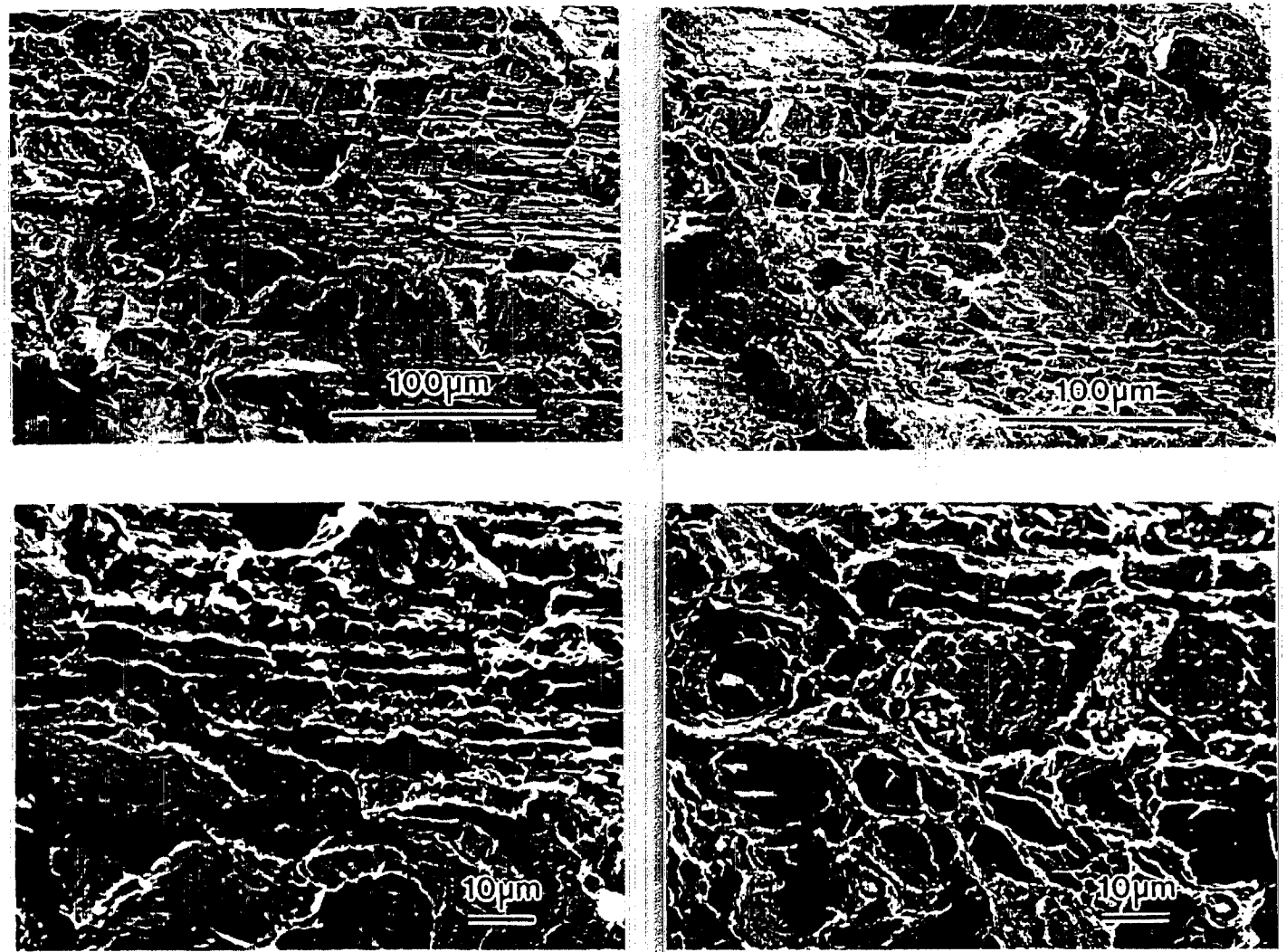

2090 FINE GRAIN RECRYSTALLIZED UA

UNCHARGED

CHARGED

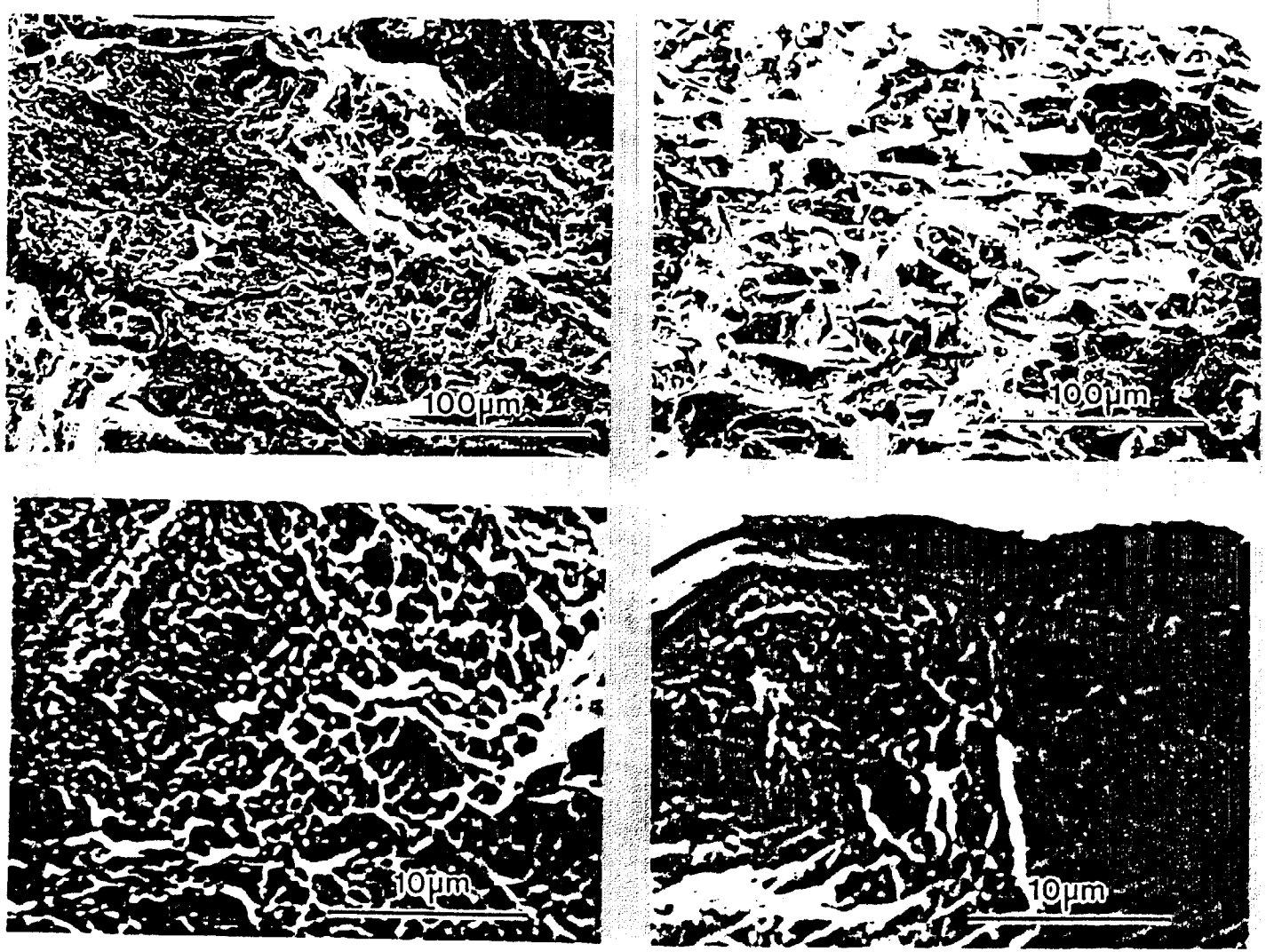

2090 FINE GRAIN RECRYSTALLIZED PA

UNCHARGED

CHARGED

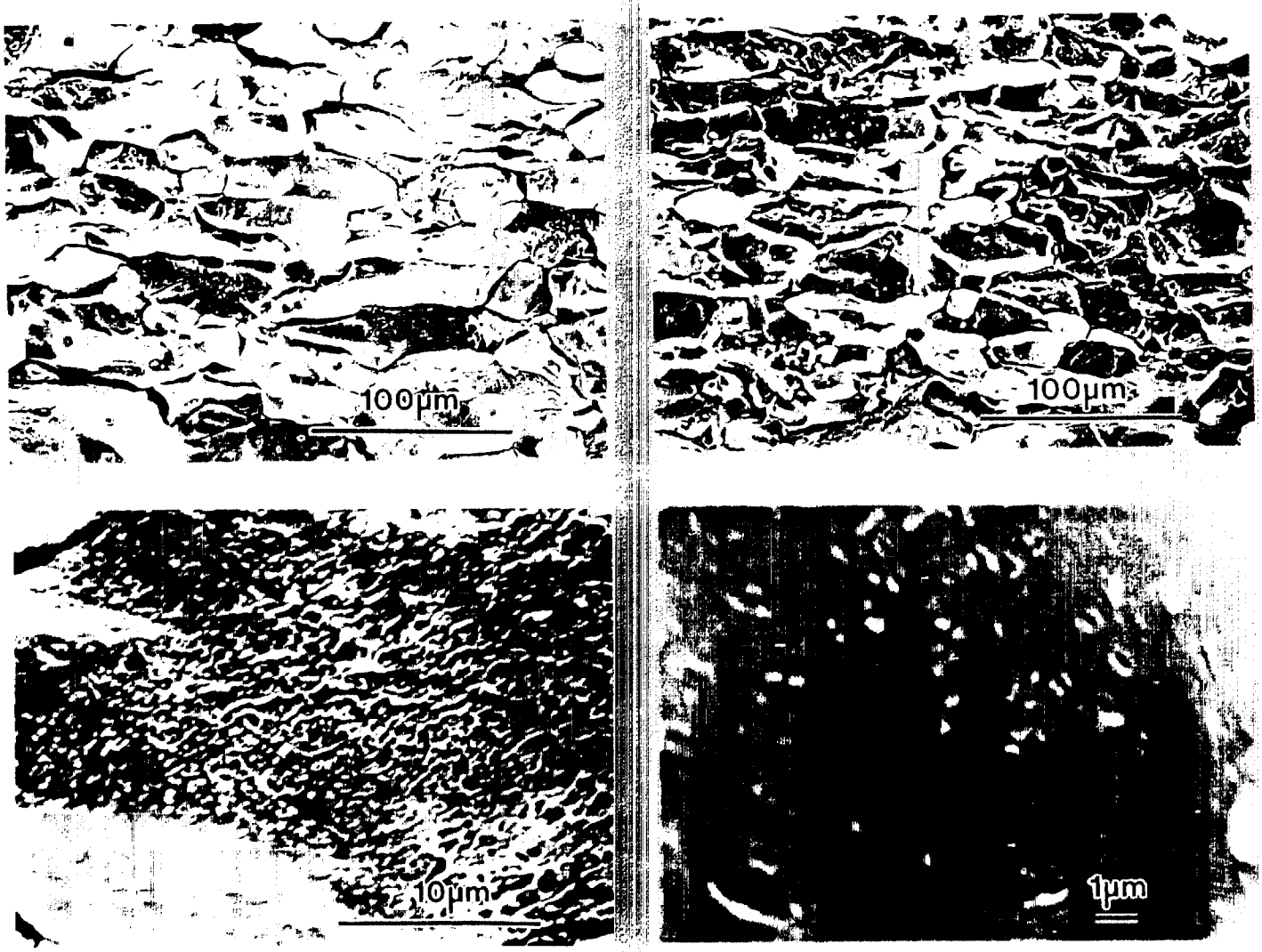

Conclusions: Mechanical Testing

- AA 2090 is susceptible to HEAC in the underaged (fracture toughness and CERT) and T3 (CERT) tempers. This behavior agrees with alternate immersion testing of these alloys as shown by Kilmer and Stoner.
- HEAC correlates well with the favorable orientation of high angle grain boundaries with respect to the crack plane.
- Intergranular fracture processes were significantly affected by hydrogen charging (fine grain recrystallized Al-Li-Cu-Zr).
- J_i was not significantly degraded upon charging when the operative fracture processes were transgranular shear (large grain recrystallized Al-Li-Cu-Zr) and intersubgranular fracture (unrecrystallized AA2090).

Questions Developed From Mechanical Testing

- How many trapping states exist in AA2090 and what microstructural features are they associated with.

  How does aging affect trapping and can this explain HEAC behavior.

- What levels of internal hydrogen are produced during AI/SCC testing and how do they compare to precharged specimens.

- Is hydrogen absorption during AI/SCC or concurrent polarization/straining dominated by dislocation transport or mechanical destabilization of passive films coupled with locally high hydrogen fugacities.

- Does a fixed concentration of internal hydrogen repartition during straining.

Hydrogen Analysis Methods

Permeation - Devanathan Stuchurski Technique

- Can only detect and quantify mobile hydrogen
- Information on irreversible trapping of hydrogen produced indirectly
- Difficult to use for materials with low D_H and low hydrogen solubility

Leco Analysis

- Can not separate contributions from mobile and trapped hydrogen
- Can not distinguish individual trap states
- Resolution for hydrogen is approximately 1 ppm

Thermal Desorption Spectroscopy

- Can identify number of trapping states
- Can determine hydrogen partitioning among several trap sites
- Can determine binding energy of trap states
- Resolution for hydrogen can be less than 1 ppb
- No spatial resolution, trap state identification by process of elimination

SCHEMATIC OF THERMAL DESORPTION SPECTROSCOPY SYSTEM

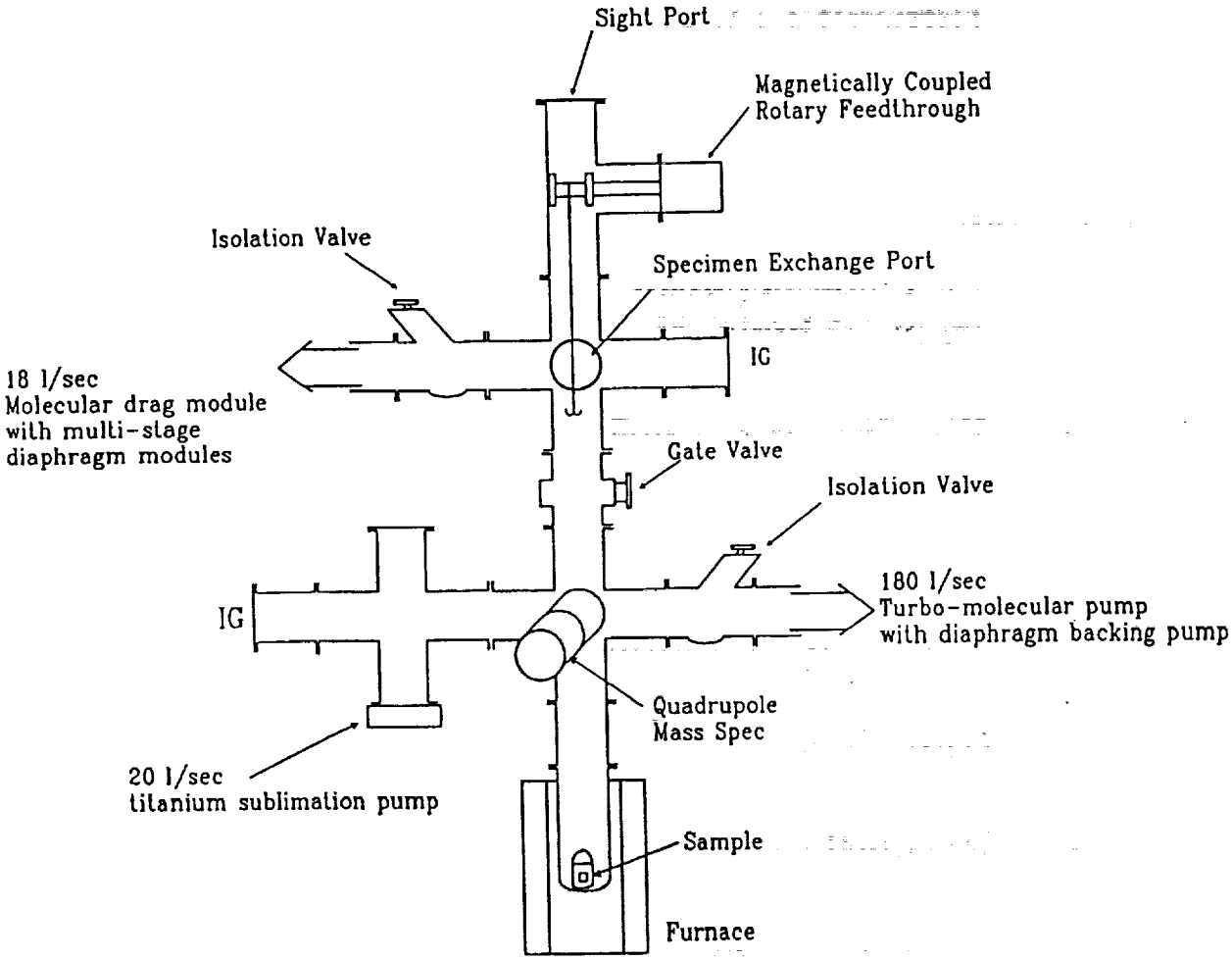

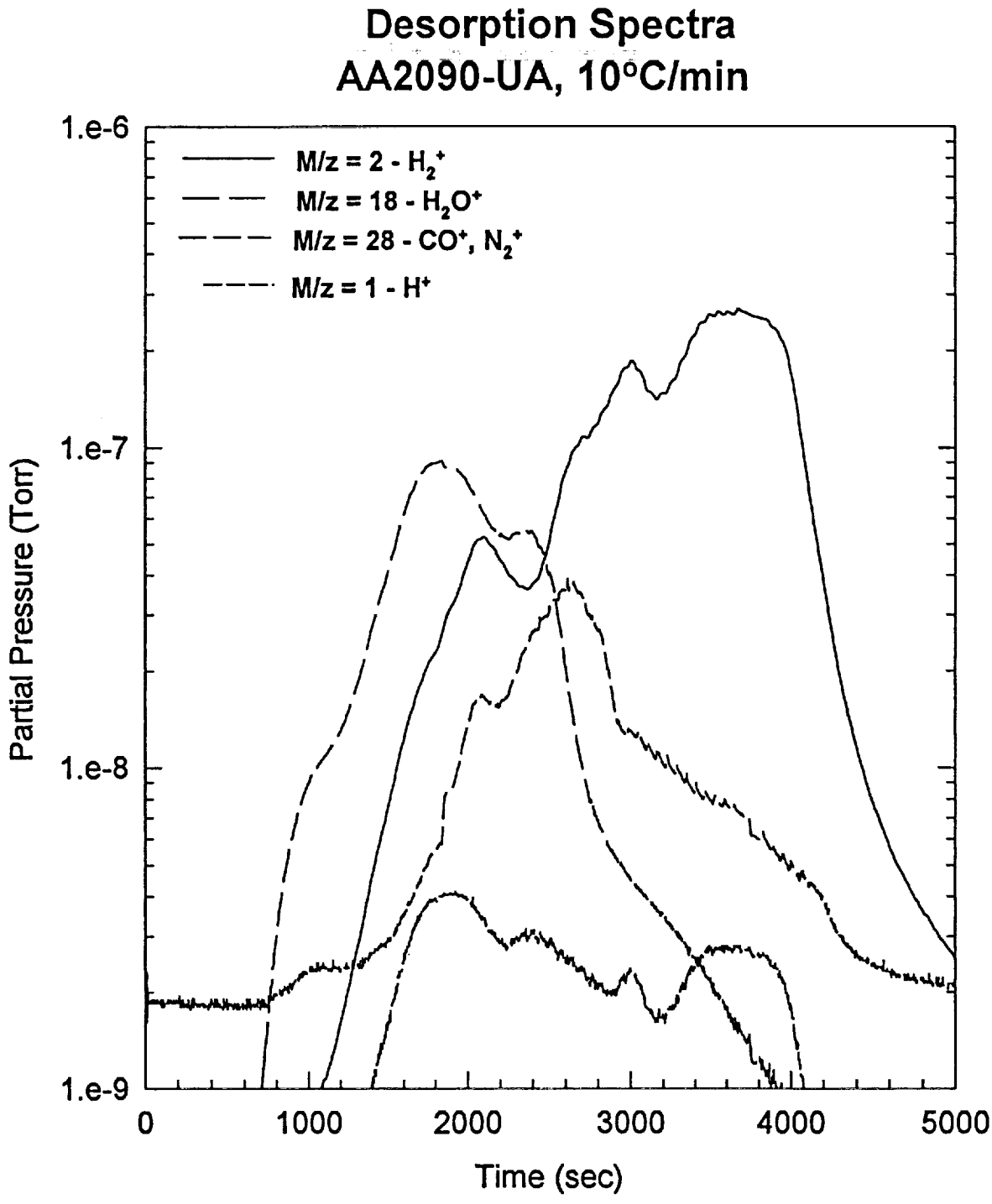
Desorption Spectra
AA2090-UA, 10°C/min
M/z = 2 - H2+
M/z = 18 - H2O+
M/z = 28 - CO+, N2+
M/z = 1 - H+
Partial Pressure (Torr)
1.e-6
1.e-7
1.e-8
1.e-9
0
1000
2000
3000
4000
5000
Time (sec)

Mass Balance During Desorption Experiments

$$V \frac{dp}{dt} = F_d - F_r + L - Sp$$

where:

V → Volume of analysis chamber (known)

p → H_2 partial pressure (measured)

F_d → instantaneous desorption rate (solve)

F_r → instantaneous re-adsorption rate ($F_r << F_d$)

L → leak rate ($L << F_d$)

S → pumping speed (known for H_2)

$$F_{d_{H_2}} = V \frac{dp_{H_2}}{dt} + S_{H_2} p_{H_2}$$

$$C_{H_2} = \int F_{d_{H_2}} dt$$

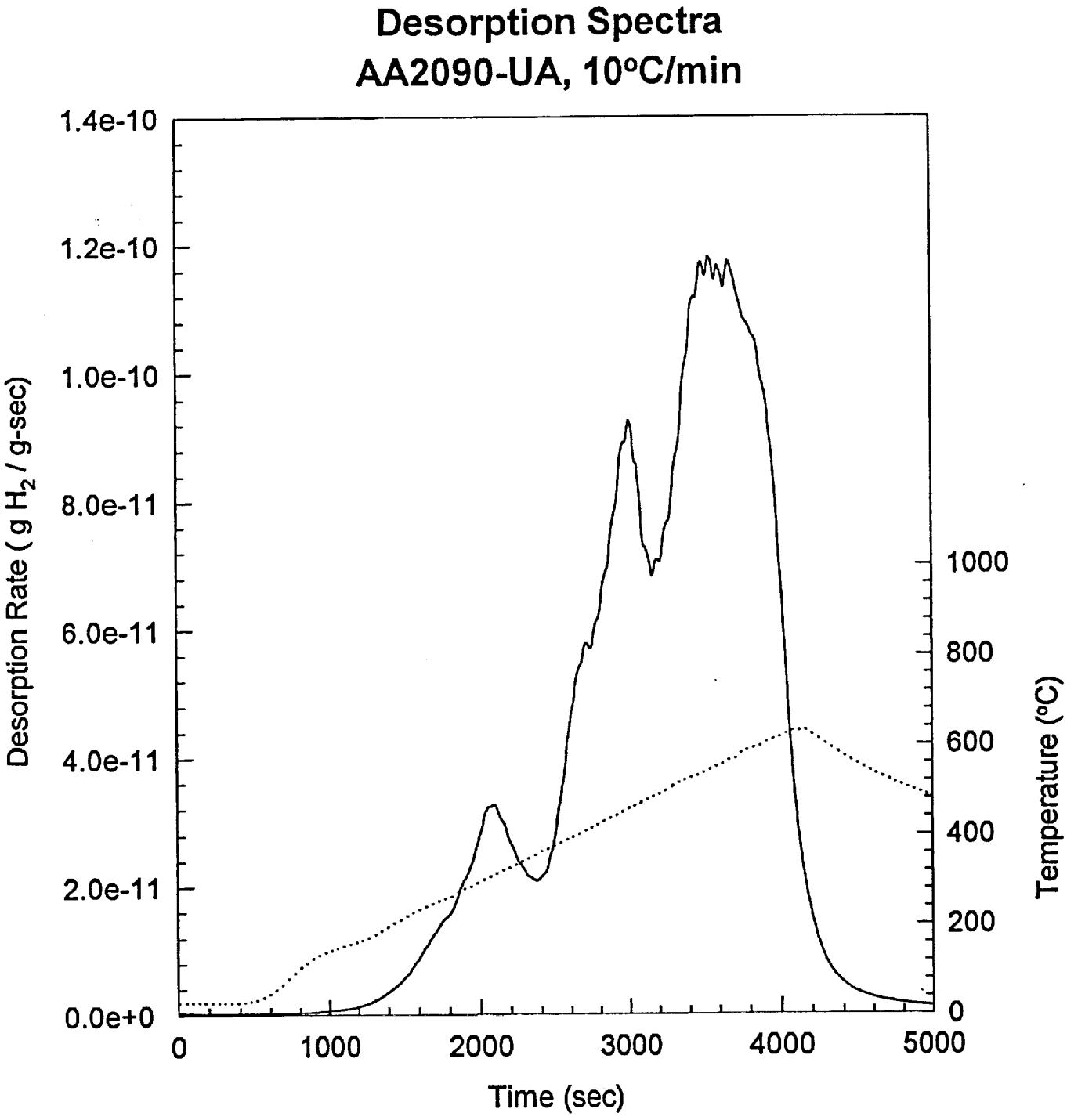
Desorption Spectra
AA2090-UA, 10°C/min
Desorption Rate (g H_2 / g-sec)
1.4e-10
1.2e-10
1.0e-10
8.0e-11
6.0e-11
4.0e-11
2.0e-11
0.0e+0
0
1000
2000
3000
4000
5000
Time (sec)
1000
800
600
400
200
0
Temperature (°C)

Desorption Rate Calculations

$$C_L + \square_T \rightleftharpoons C_X$$

where: C_L - Lattice H
C_X - trapped H
C_T - conc. of trap sites

$$\frac{K_t}{K_d} = \gamma \exp\left(\frac{E_B}{RT}\right)$$

at equil:

$$\frac{C_X}{C_L} = \frac{K_t}{K_d} C_T$$

effective diffusion coefficient

$$D_e = D_H \cdot \frac{C_L}{(C_L + C_X)}$$

Desorption Rate Calculations (cont.)

$$\frac{\partial C_L}{\partial t} = -\alpha^2 D_H (C_L - C_O) = -\alpha^2 D_* (C_H - C_O)$$

where: C_H - bulk hydrogen conc.

$$\frac{\partial C_L}{\partial t} = \left(\frac{\pi}{2d}\right)^2 D_O \exp\left(\frac{-E_m}{RT}\right)\left[\frac{1}{1+\gamma \exp(E_B/RT) C_T}\right]$$

$$(t_{n-1})[C_H(t_{n-1}) - C_O(t_{n-1})]\Delta t$$

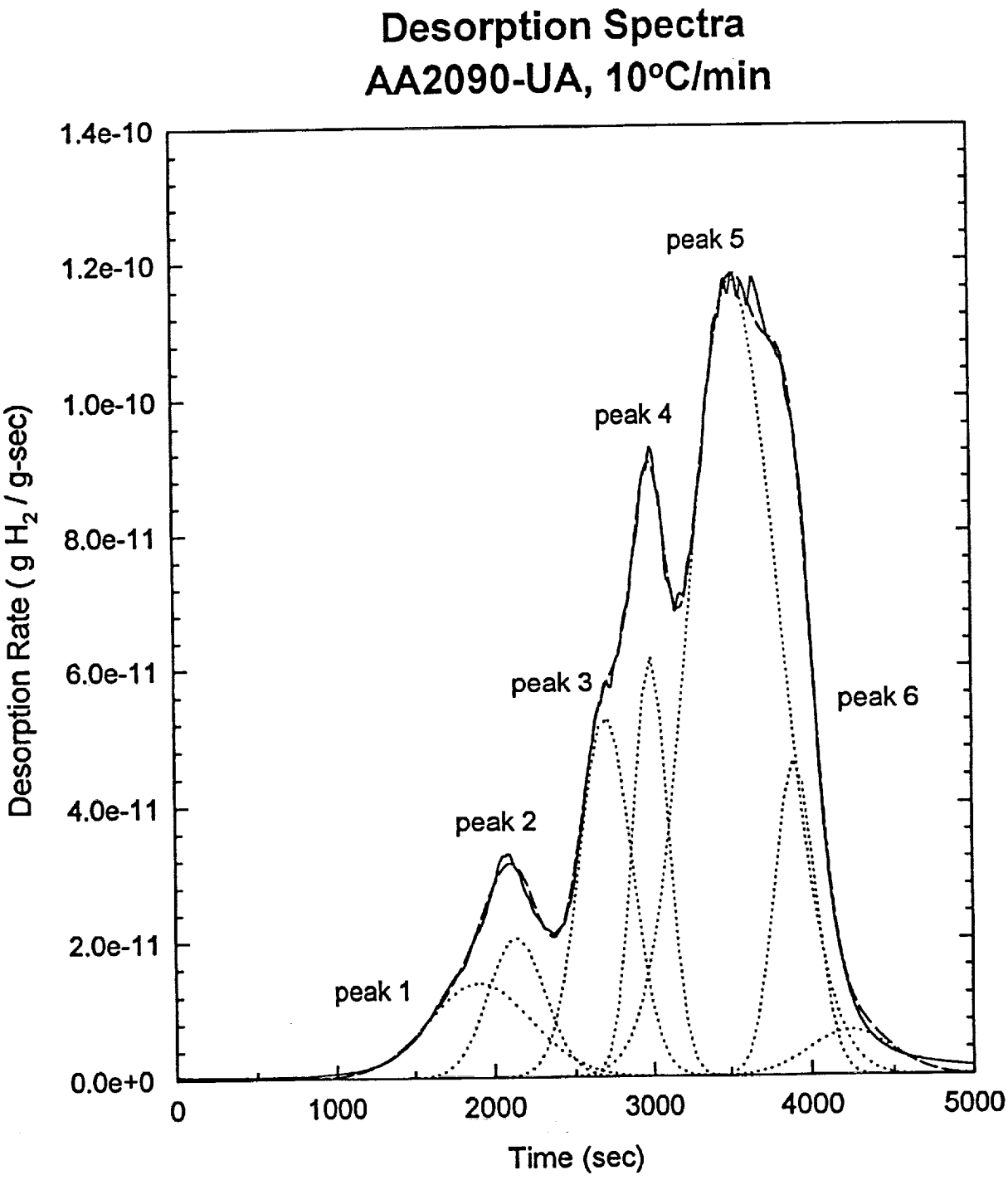
Desorption Spectra
AA2090-UA, 10°C/min
Desorption Rate (g H_2 / g-sec)
1.4e-10
1.2e-10
1.0e-10
8.0e-11
6.0e-11
4.0e-11
2.0e-11
0.0e+0
0
1000
2000
3000
4000
5000
Time (sec)
peak 1
peak 2
peak 3
peak 4
peak 5
peak 6

Hydrogen Partitioning for AA2090

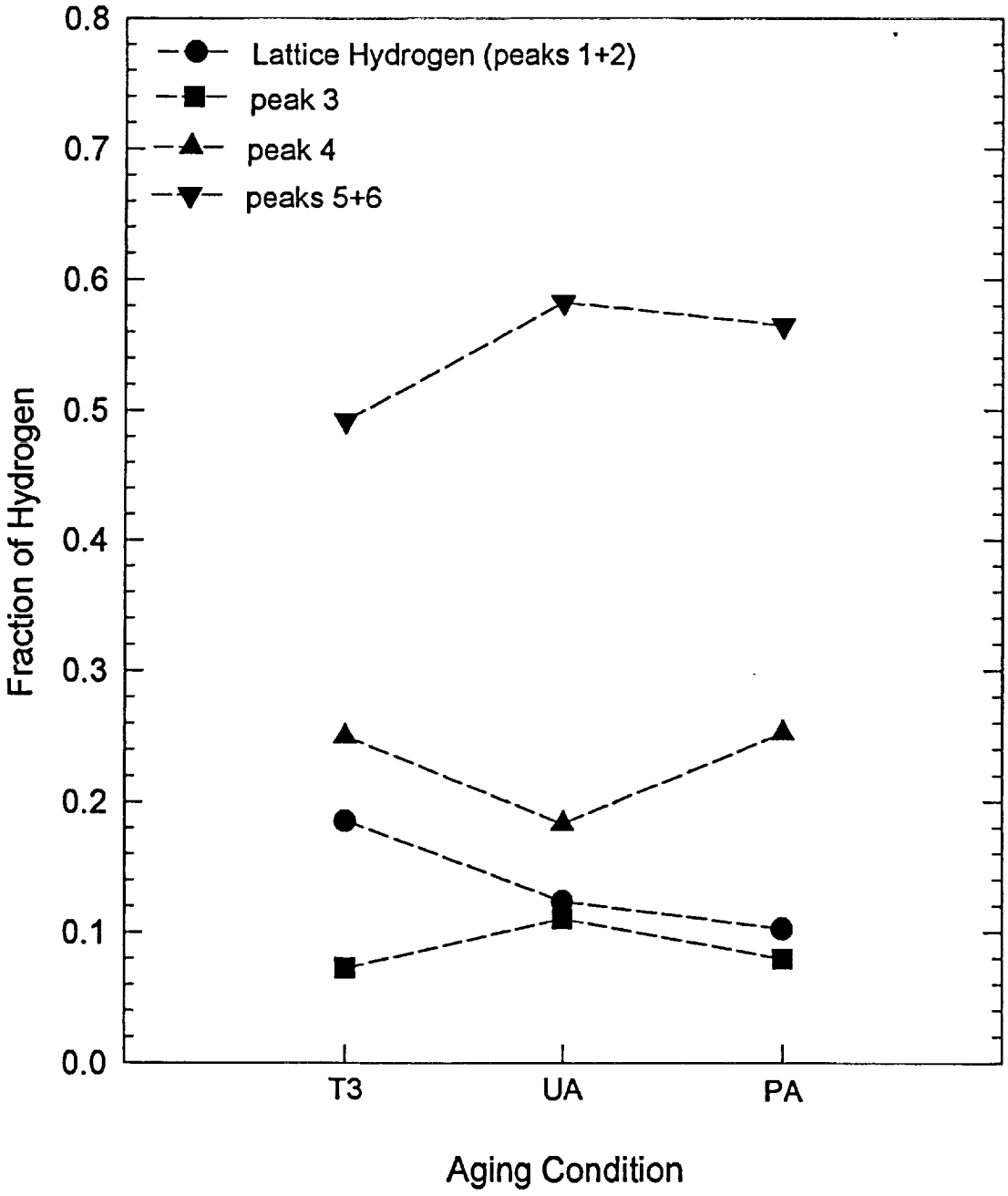

Binding Energy Calculations

Approximate Desorption Rate:

$$F_d = \nu_d \exp\left(\frac{S_d}{R}\right)\exp\left[\frac{-(E_m+E_B)}{RT}\right]$$

solve for maximum desorption rate:

$$\frac{\partial \ln(\phi/T_{max}^2)}{\partial(1/T_{max})} = -\frac{E_m+E_B}{R}$$

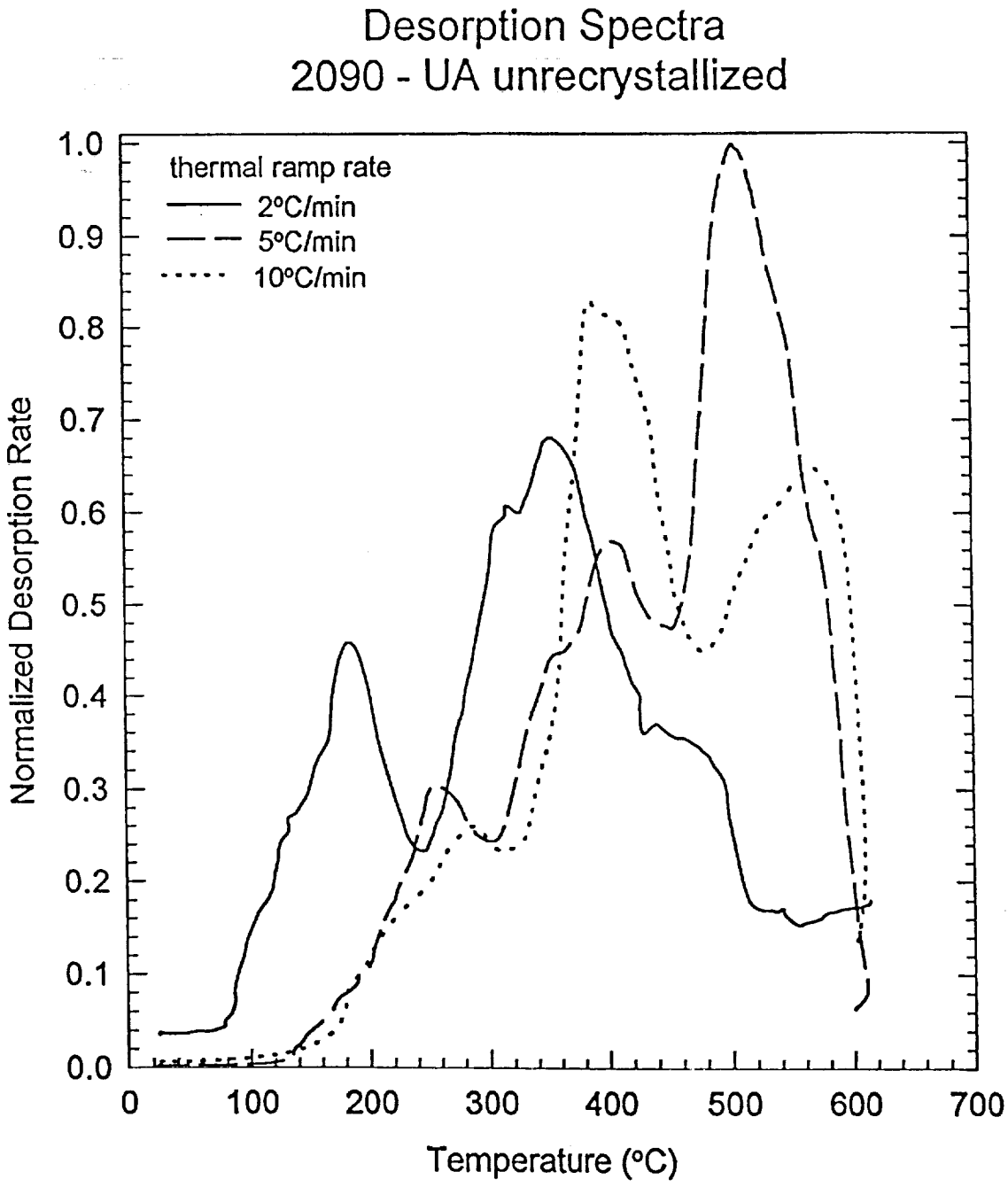
Desorption Spectra
2090 - UA unrecrystallized
thermal ramp rate
2°C/min
5°C/min
10°C/min
Normalized Desorption Rate
Temperature (°C)
0.0
0.1
0.2
0.3
0.4
0.5
0.6
0.7
0.8
0.9
1.0
0
100
200
300
400
500
600
700

Calculated Binding Energies 2090 - UA

peak	$(E_m+E_B)/R$ (°K)	E_m+E_B (kJ/mol)	E_B (kJ/mol)
1	1775	14.76	-3.45
2	2756	22.92	4.71
3	6551	54.46	36.25
4	8849	73.57	55.36
5	10657	88.60	70.39
6	----	----	----

using: E_m = 18.21 kJ/mol (Anyalebechi, Talbot and Granger)

Reported Binding Energies

H - vacancy	48 kJ/mol	ΔH_{sol} Al - 1 Li	6.67 kJ/mol
		Al - 2 Li	13.7 kJ/mol
grain boundary	14 kJ/mol	Al - 3 Li	23.6 kJ/mol

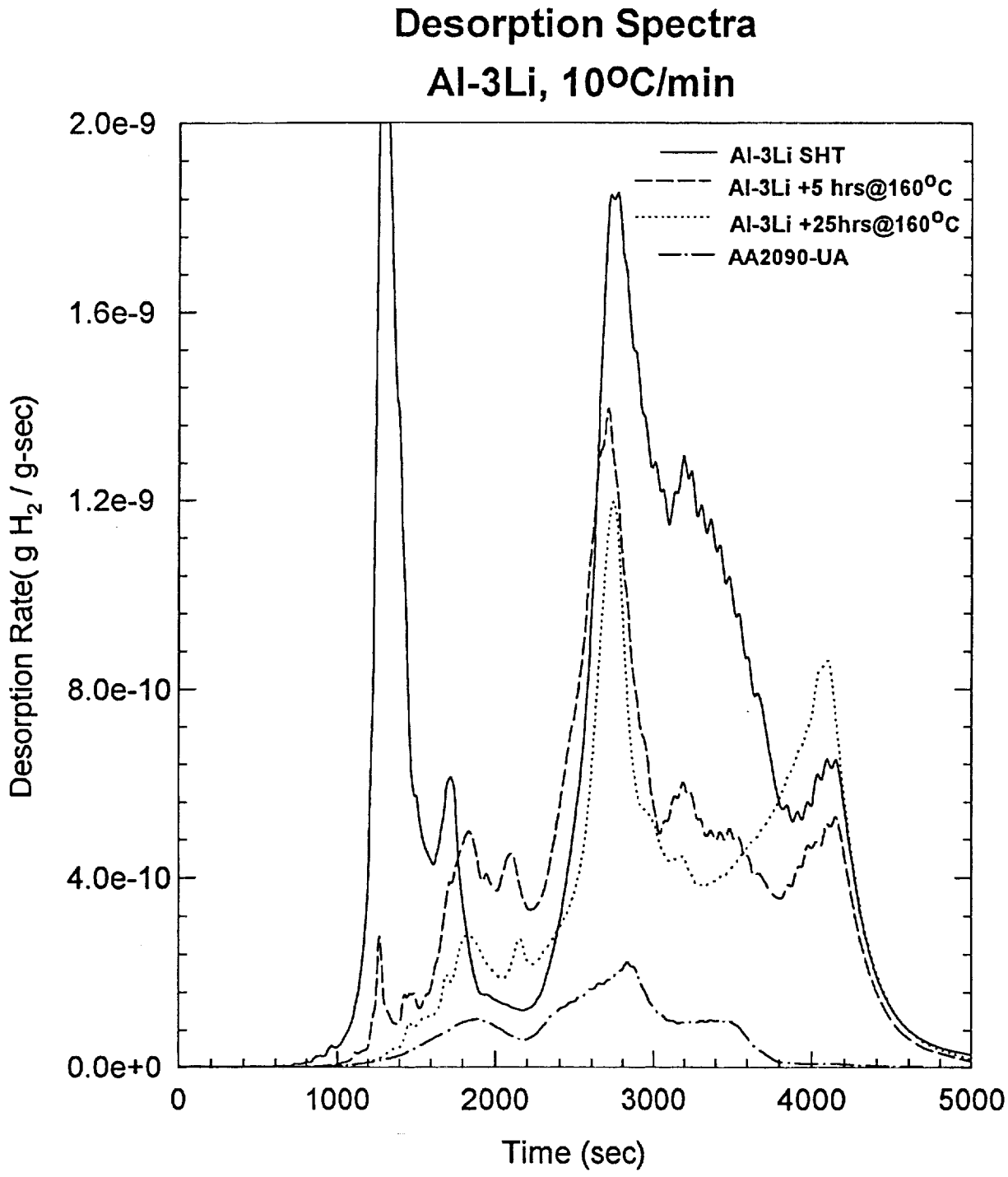

Specimens cathodically polarized at -1V_{SCE} in pH 7 Na_2SO_4 for 28 days

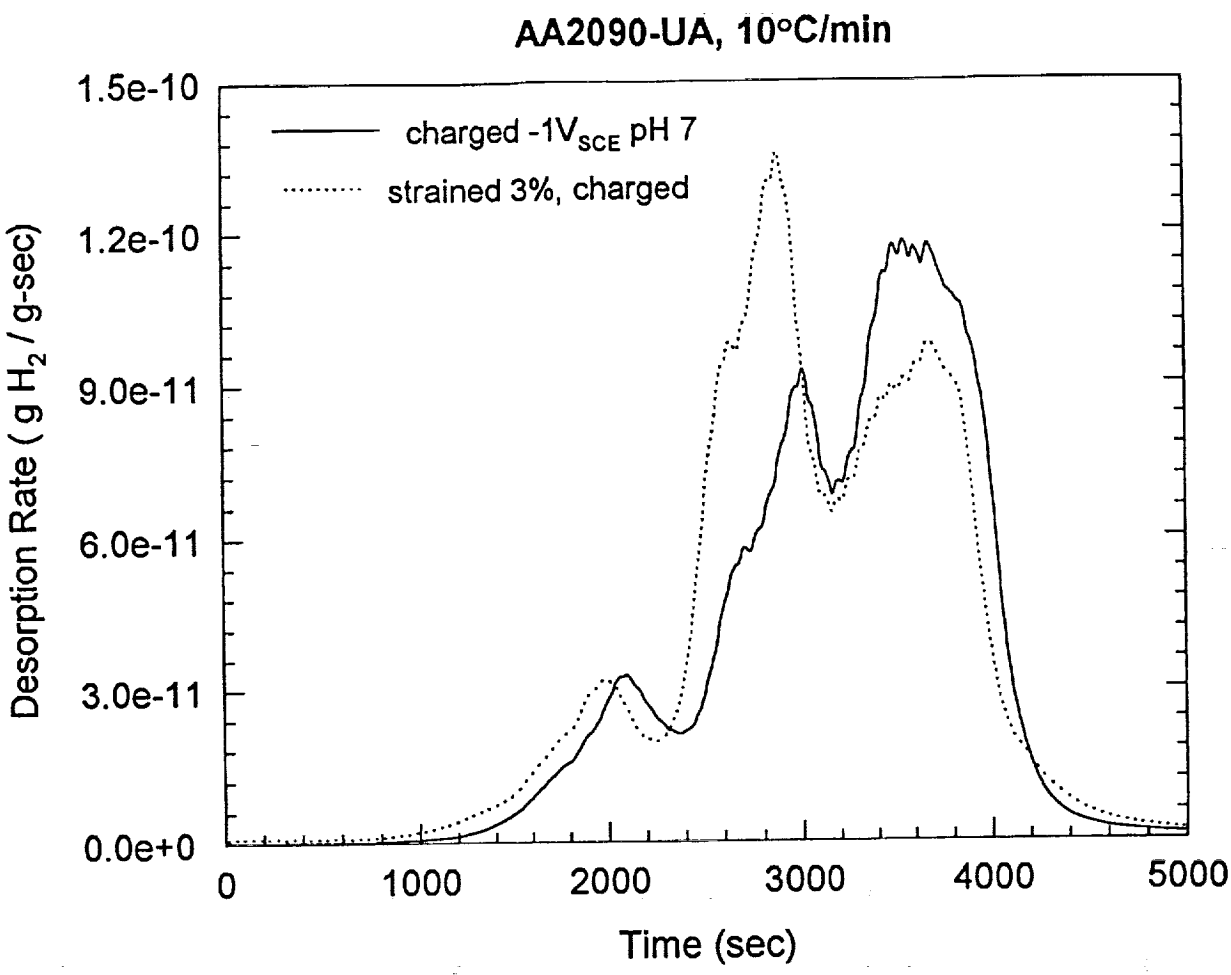
AA2090-UA, 10°C/min
charged -1V$_{SCE}$ pH 7
strained 3%, charged
Desorption Rate (g H$_2$ / g-sec)
1.5e-10
1.2e-10
9.0e-11
6.0e-11
3.0e-11
0.0e+0
0
1000
2000
3000
4000
5000
Time (sec)

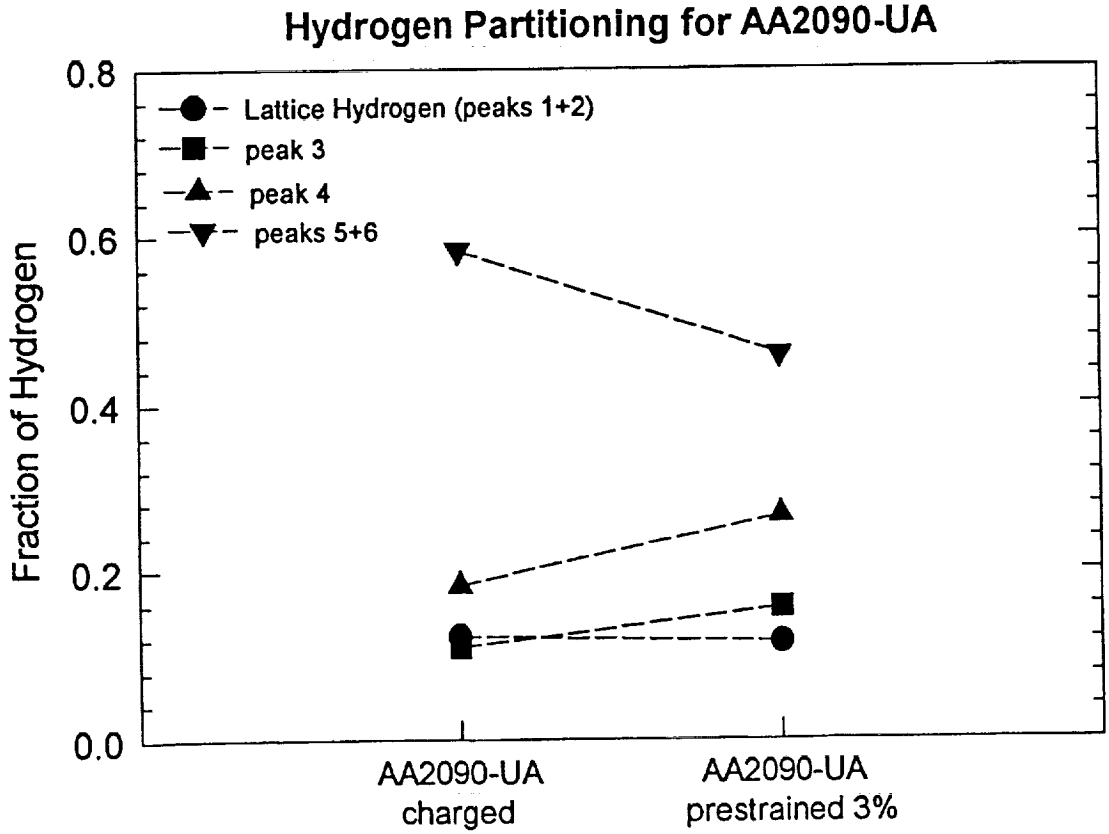
Hydrogen Partitioning for AA2090-UA
Lattice Hydrogen (peaks 1+2)
peak 3
peak 4
peaks 5+6
Fraction of Hydrogen
0.8
0.6
0.4
0.2
0.0
AA2090-UA
charged
AA2090-UA
prestrained 3%

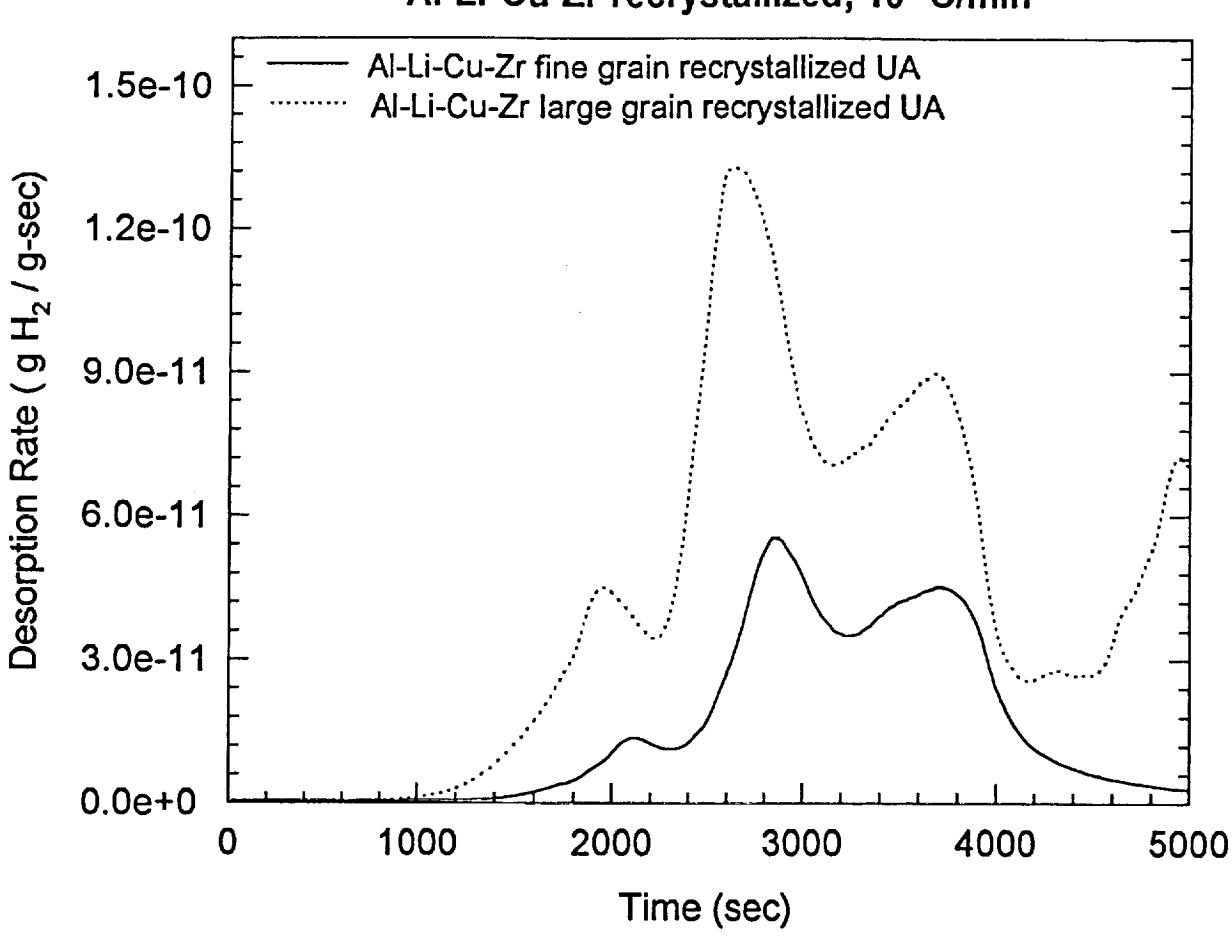
Al-Li-Cu-Zr recrystallized, 10°C/min
Al-Li-Cu-Zr fine grain recrystallized UA
Al-Li-Cu-Zr large grain recrystallized UA
Desorption Rate (g H2 / g-sec)
1.5e-10
1.2e-10
9.0e-11
6.0e-11
3.0e-11
0.0e+0
0
1000
2000
3000
4000
5000
Time (sec)

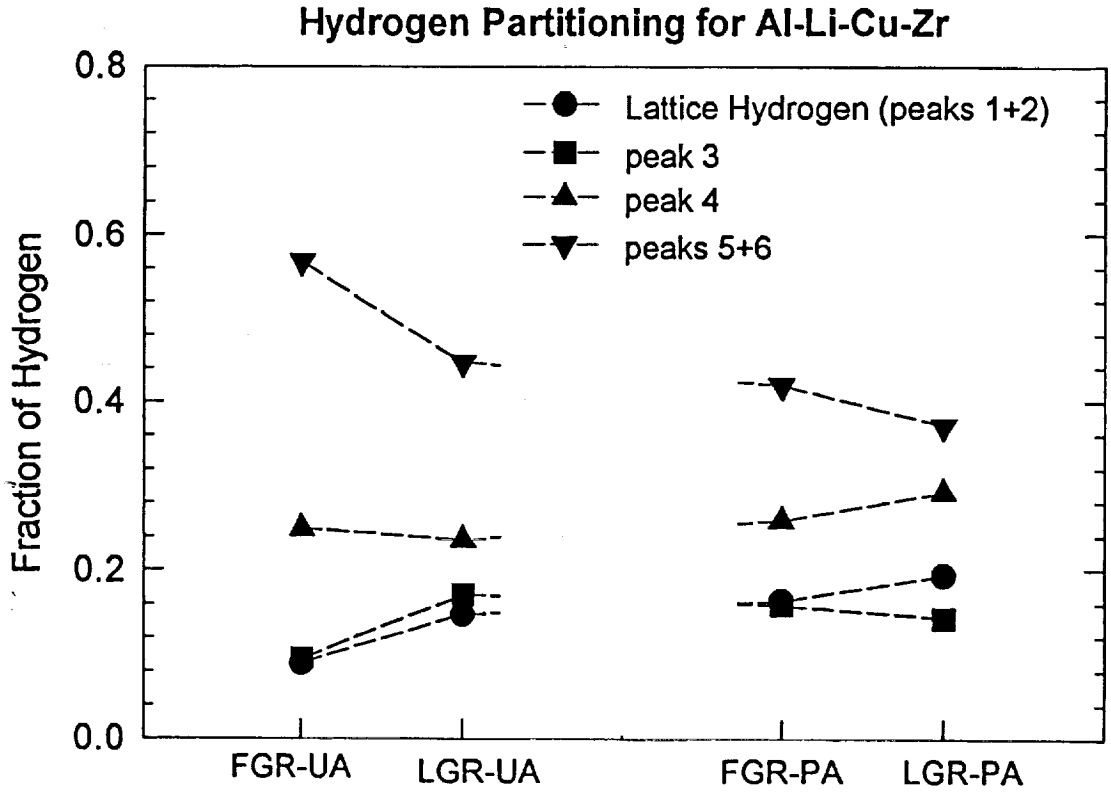
Hydrogen Partitioning for Al-Li-Cu-Zr
Lattice Hydrogen (peaks 1+2)
peak 3
peak 4
peaks 5+6
Fraction of Hydrogen
0.8
0.6
0.4
0.2
0.0
FGR-UA
LGR-UA
FGR-PA
LGR-PA

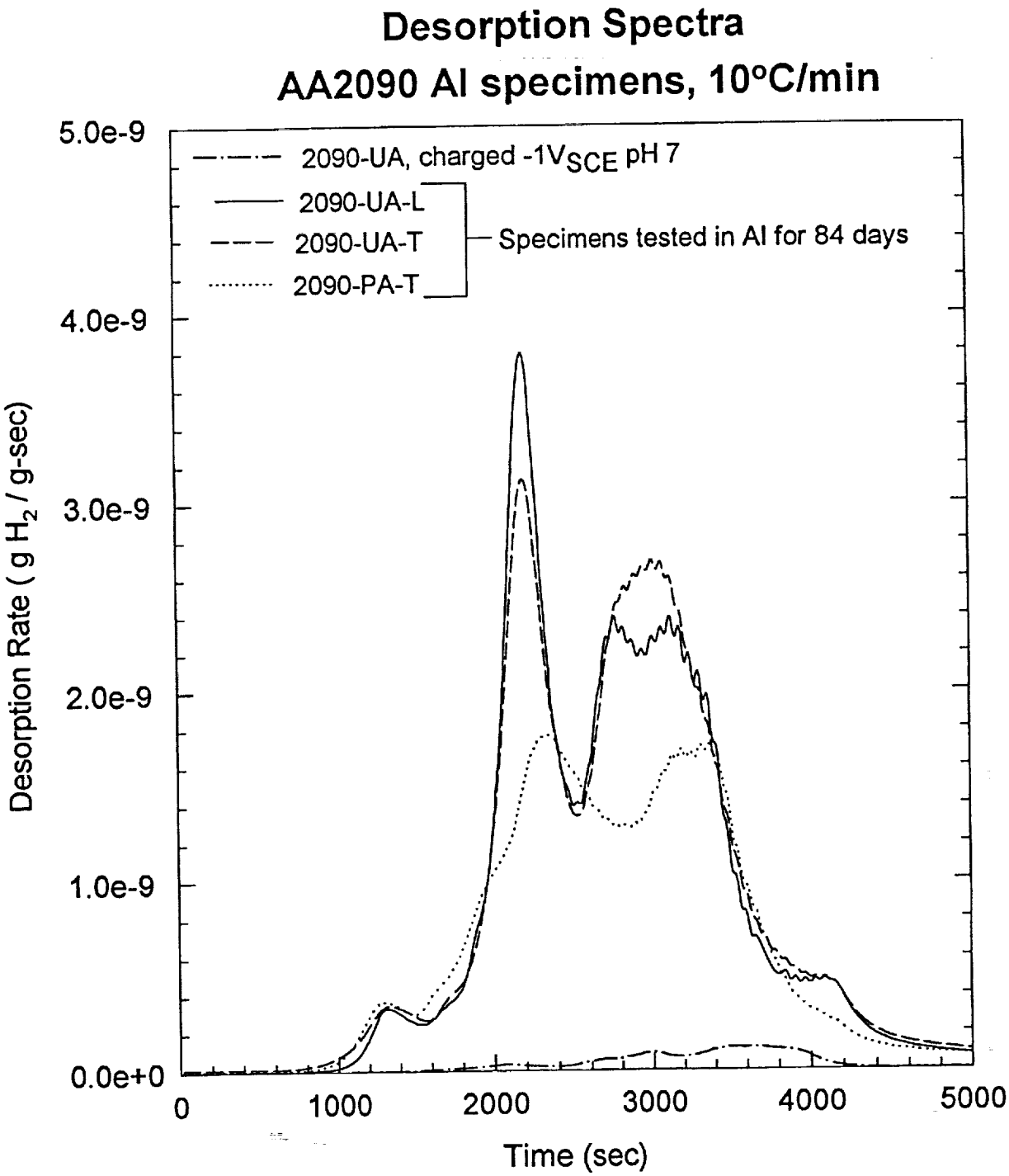
Desorption Spectra
AA2090 Al specimens, 10°C/min
2090-UA, charged -1V$_{SCE}$ pH 7
2090-UA-L
2090-UA-T
2090-PA-T
Specimens tested in Al for 84 days
Desorption Rate (g H_2 / g-sec)
5.0e-9
4.0e-9
3.0e-9
2.0e-9
1.0e-9
0.0e+0
0
1000
2000
3000
4000
5000
Time (sec)

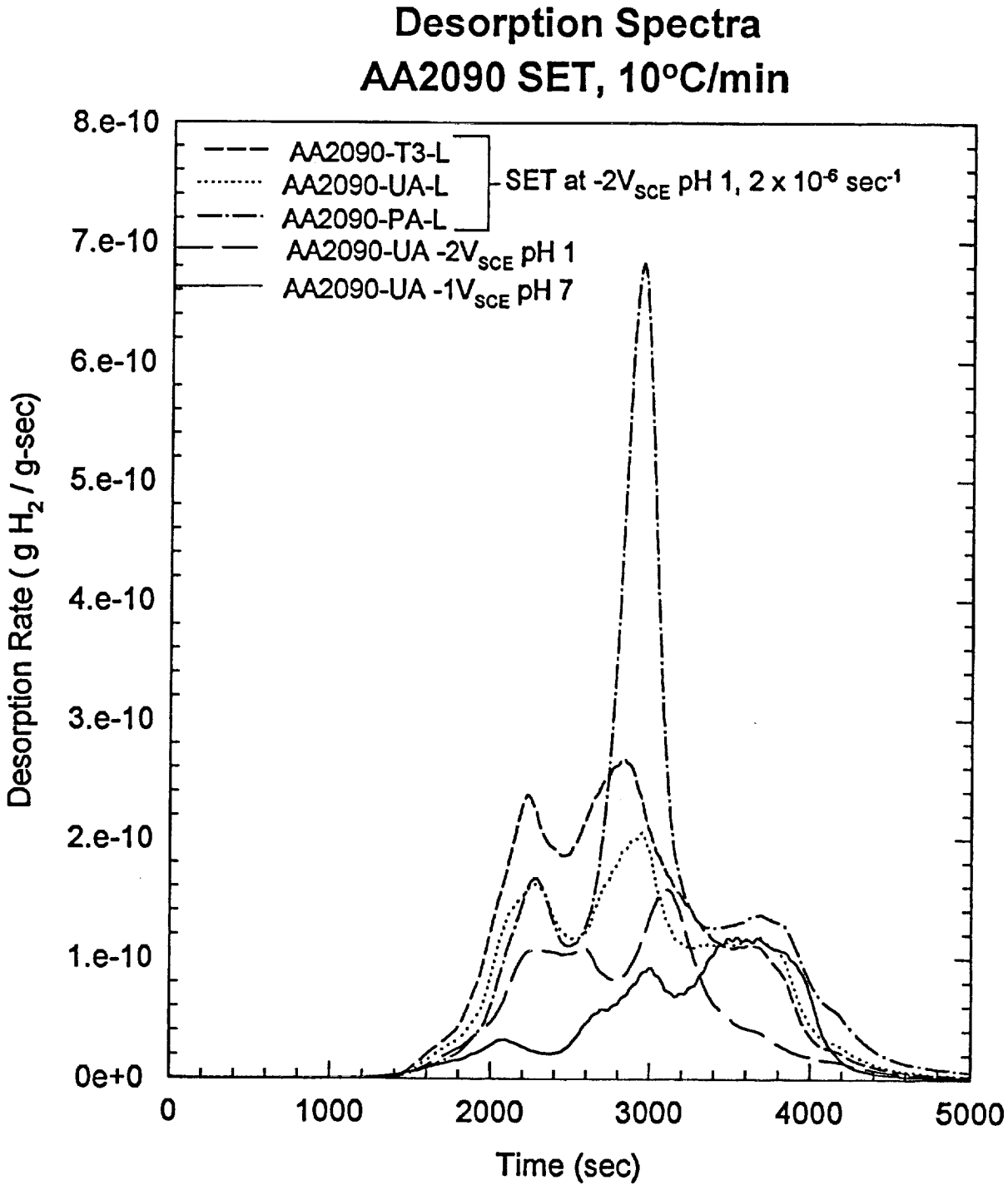
Desorption Spectra
AA2090 SET, 10°C/min
AA2090-T3-L
AA2090-UA-L
AA2090-PA-L
SET at -2V$_{SCE}$ pH 1, 2 x 10^{-6} sec^{-1}
AA2090-UA -2V$_{SCE}$ pH 1
AA2090-UA -1V$_{SCE}$ pH 7
Desorption Rate (g H$_2$ / g-sec)
8.e-10
7.e-10
6.e-10
5.e-10
4.e-10
3.e-10
2.e-10
1.e-10
0e+0
0
1000
2000
3000
4000
5000
Time (sec)

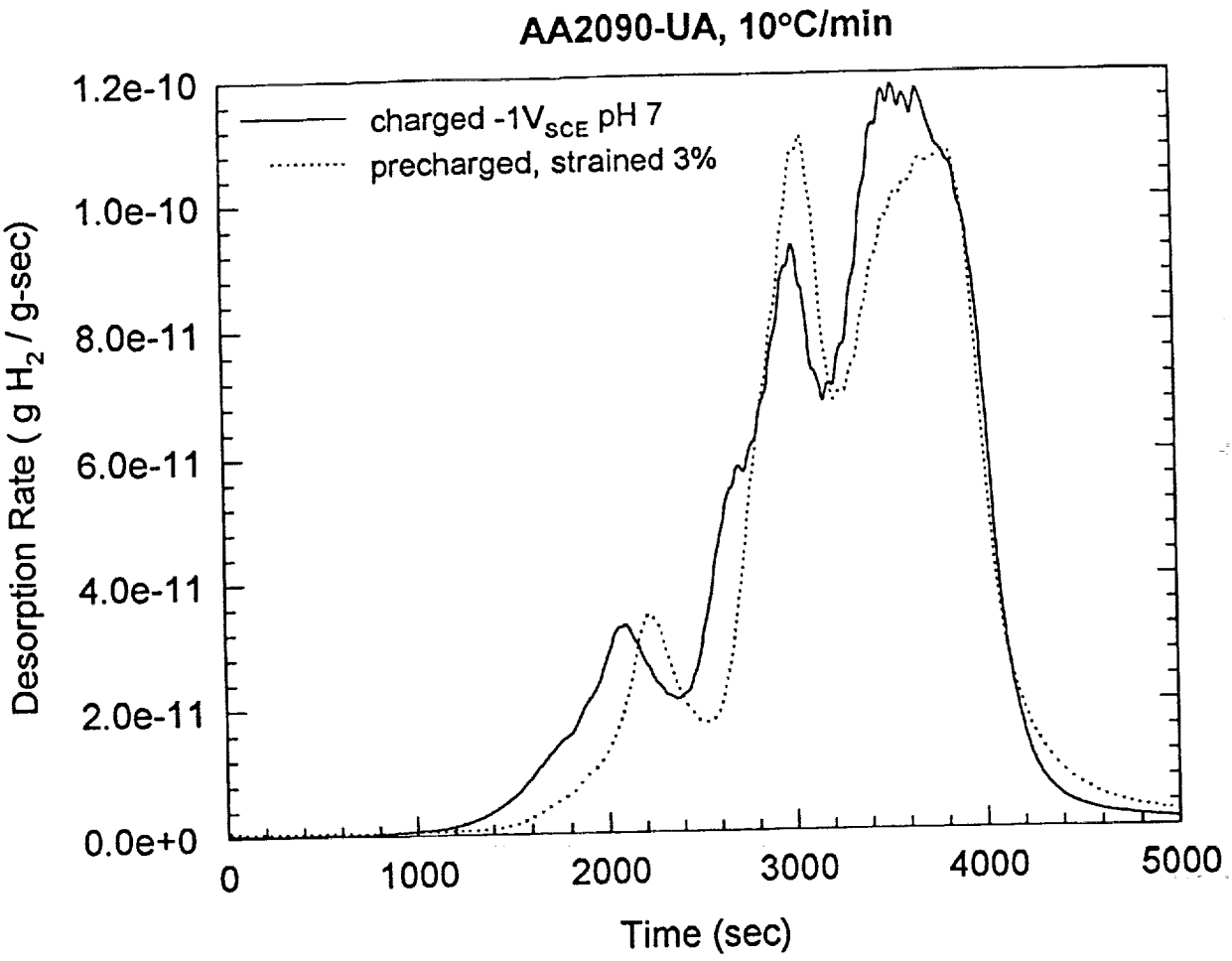
AA2090-UA, 10°C/min
charged -1V$_{SCE}$ pH 7
precharged, strained 3%
Desorption Rate (g H$_2$ / g-sec)
1.2e-10
1.0e-10
8.0e-11
6.0e-11
4.0e-11
2.0e-11
0.0e+0
0
1000
2000
3000
4000
5000
Time (sec)

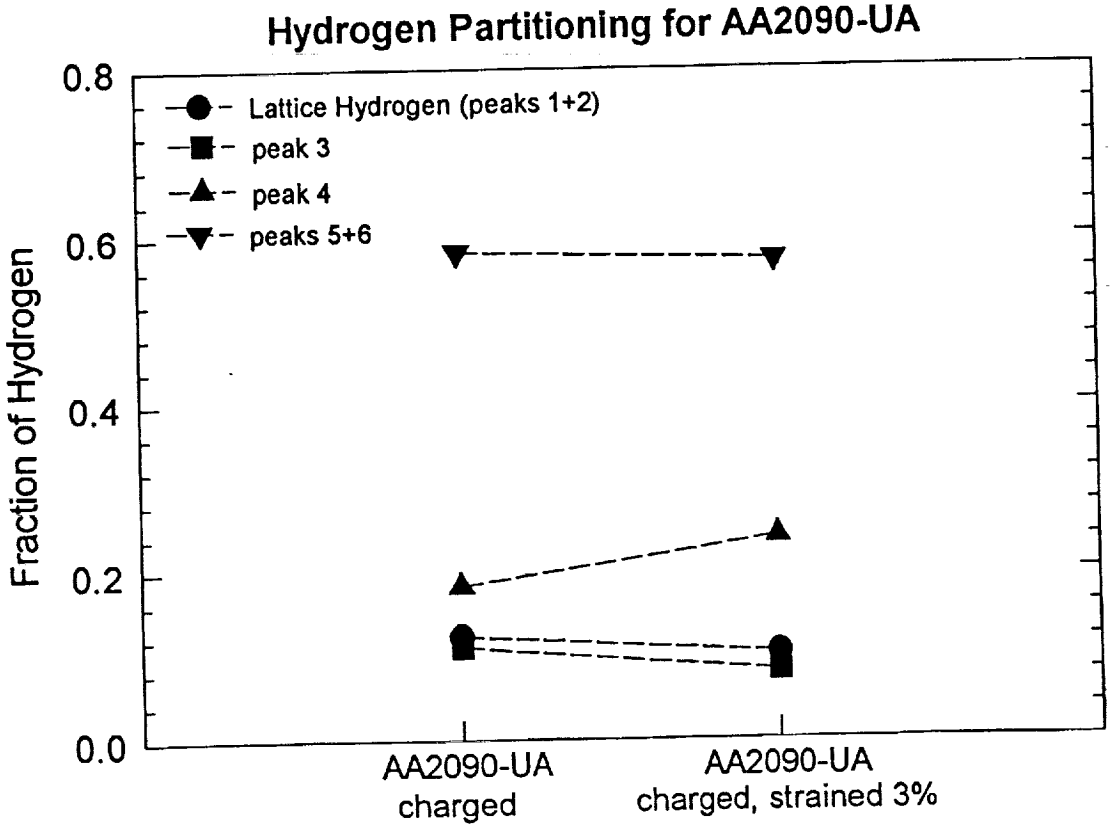
Hydrogen Partitioning for AA2090-UA
Lattice Hydrogen (peaks 1+2)
peak 3
peak 4
peaks 5+6
Fraction of Hydrogen
0.8
0.6
0.4
0.2
0.0
AA2090-UA
charged
AA2090-UA
charged, strained 3%

Conclusions: TDS

- Hydrogen solubility within the matrix decreases with aging of AA2090 and is directly related to a decrease of Li in solid solution.
- Trap state 3 is associated with δ' as seen from studies with aged and solutionized Al-3Li alloys.
- The presence of an increased dislocation density increases the amount of hydrogen associated with trap state 4.
- Recrystallized alloys show an increased fraction of total hydrogen being partitioned to trap states 5 and 6 for materials with larger high angle grain boundary areas.
- Increased hydrogen absorption relative to Ni coated specimens has been shown during AI/SCC of AA2090.
- Hydrogen absorption and possibly transport is enhanced during dynamic straining with cathodic polarization.
- A fixed concentration of internal hydrogen can be repartitioned during straining of precharged specimens.

Future Work

- Determine if increased absorbed hydrogen levels during concurrent straining/charging are due to:
  a) increased dislocation transport
  b) mechanical destabilization of passive film and high local fugacity
  c) increased solubility due to elastic loading

- Determine trap binding energies for T3, UA, PA and overaged AA2090, taking into consideration the possibility of aging effects during TDS.

- Determine if HEAC of Al-Li-Cu-Zr alloys is more strongly related to deformation mode, strain-induced trap evolution and dislocation transport or is dominated by microstructural based trapping.

Project #6 Metastable Pitting of Al Alloys in Halide Solutions

S.T. Pride, J.L. Hudson and J.R. Scully

Objective

Metastable pitting of high purity Al, aged Al-2%Cu and AA2024-T3 were characterized by analyzing the electrochemical transients associated with metastable pitting, stable pitting and intergranular corrosion in room temperature NaCl solutions. The project contains three elements each with its own objective:

1. *Stabilization criteria for the transition from metastable to stable pitting.*

Little is understood about pit nucleation and the stabilization criteria for pit growth. The objective of this element is to define the factors which govern the transition from metastable to stable pit growth in Al. Are the properties of metastable pits different from stable pits or do all metastable pits have some finite probability of survival which increases with proximity to the pitting potential?. The answers to these questions have significant implications with regard to the design of corrosion resistant alloys, aqueous phase inhibitors, and aging aircraft.

2. *Evaluation of the utility of electrochemical noise analysis methods as a forecasting tool for prediction of the transition from metastable to stable pitting growth.*

The objective of this phase is to ascertain the best approach for forecasting the transition from metastable to stable pit growth using electrochemical noise methods. Spectral and statistical analysis methods such as power spectral density plots, noise resistance and pitting index were examined. Important considerations such as electrode area and alloy composition (pure Al, aged Al-2%Cu and AA2024 T3) were investigated.

3. *Existence of correlations or coupling of metastable pitting events.*

The objective of this project element is to determine whether or not metastable pitting events are completely independent of each other or whether some "memory" exists in the pitting process which leads to interactions between older pits and newer pits. The relevancy of this work is related to the construction of feedback models describing the pit stabilization process. Testing for "pit interdependency" will forward the establishment of rules regarding the spatial and temporal coupling of pits. This knowledge in turn would govern the development of feedback models of pitting.

Current Status

Analysis and reduction of experimental data are nearing completion. Sheldon Pride is now writing his Ph.D. dissertation. He has accepted employment as a staff engineer at the Rohm and Haas Chemical Co. in Bristol, PA, and is completing thesis writing on a part-time basis. Two publications have been submitted and accepted (project elements 1 and 2) and a third is planned in the area of project element 3.

Findings

This section details the important final conclusions from each project element.

1. *Stabilization criteria for the transition from metastable to stable pitting.*

Pits formed at more positive potentials, approaching the mean pitting potential, grew according to faster growth laws than pits formed at more negative potentials. This factor contributed to the ability of such prestable pits to meet the stabilization criteria.

A stabilization criterion for transition from metastable to stable

pit growth was identified. Stable pits must achieve a growth rate such that the ratio of pit current to pit radius is constant with time and exceeds the ratio: $I/r > 10^{-2}$ A/cm. It was established that this ratio is associated with the need to form and maintain the concentrated acidified $AlCl_3$ chemistry in open pits.

The origins of statistical distributions in pitting potentials were clearly linked with distributions of metastable pit properties.

Pit growth behavior near the pitting potential was found to be ohmically controlled. Pit growth at high anodic potentials was mass transport controlled. These controlling factors significantly influence pit growth behavior and the effect of a variety of variables on pit growth behavior.

The beneficial effect of chromate inhibitor was linked to both the growth rates of metastable pits (which was lowered with chromate) and the metastable pit occurrence rate (which was lowered with chromate).

2. *Evaluation of the utility of electrochemical noise analysis methods as a forecasting tool for prediction of the transition from metastable to stable pitting growth.*

Concerning statistical analysis methods, the pitting index and noise resistance were found to be of limited value in forecasting the transition from metastable to metastable pit growth.

Concerning spectral analysis methods, current power spectral density data successfully indicated both the increasing aggressiveness of NaCl solutions of increasing concentration and increasing alloy susceptibility for AA 2024 T3 ST in comparison

to AA2024 T3 LT as well as aged Al-Cu and high purity Al. However, since spectral analysis provides no information on pit size, it was not as successful as the I/r ratio from single pit analysis in predicting the transition to stable pit growth.

Concerning spectral analysis methods, voltage power spectral density data were less successful than current PSD in indicating the increasing aggressiveness of NaCl solutions of increasing concentration or increasing alloy susceptibility.

3. *Existence of correlations or coupling of metastable pitting events.*

Inter-event times (the elapsed time period between pit events for a large population of metastable pitting events) were analyzed to ascertain whether or not metastable pitting processes are completely stochastic or, instead, indicate inter-relationships. Some interdependency of pitting events was indicated using the auto-correlation function. This result was supported by spectral analysis, return map analysis, and event distribution plots which differed from Poisson's distribution behavior normally associated with random events. These results confirm that pitting is not a stochastic process and that interdependency exists.

Milestones

In the next 6 months a thesis dissertation will be completed and defended by S. Pride. A third archival publication will be completed and published.

Presentation Graphic Captions

1. Title page.

2. Project elements and objectives.

3. Experimental materials studied.

4. Stabilization criteria for localized corrosion.

5. Pitting potentials for Al, Al-4%Cu with Cu in solid solution, and 2024-T3 of two orientations.

6. Current versus time behavior showing the transition from metastable pitting to stable pit growth for high purity Al in 10^{-4} M NaCl.

7. Faraday's Law was used to calculate pit sizes assuming a hemispherical pit geometry. Good agreement was obtained between calculated pit sizes and those observed via microscopy.

8. Peak pit current vs. pit radius at peak pit current for pure Al at various applied potentials in 10^{-4} M NaCl. The data corresponding to potentials between -0.75V and -0.1V (SCE) are metastable pits. The data corresponding to potentials between 0.1V and 1V (SCE) are for stable pits evaluated at equivalent growth times. The average pitting potential for pure Al in 10^{-4} M Cl^- is -0.3V(SCE). The I_{pit}/r_{pit} line is the criterion for stable pit formation.

9. Criterion for maintenance of pit chemistry assuming spherical diffusion, H_2 production, and taking into consideration migration. For formation and stabilization of a pit site the local chemistry in the pit must maintained at a level from about 1 to 3M $AlCl_3$, otherwise repassivation may occur.

10. Ratio of pit current to pit radius indicating that the growth rates for stable pits are fast enough to maintain a concentrated pit environment over long time periods. In contrast, metastable pits will likely repassivate once the remnants of the oxide cover over the pit (which limits dilution of the pit solution) is ruptured by hydrogen evolution.

11. Calculation of pit growth laws for stable pits in comparison to metastable pits demonstrating the link between pit growth law and pit stabilization.

12. Effect of Na_2CrO_4 on pure Al pitting potentials, metastable pit formation rate and cumulative number of pit events with time. The number of

metastable pitting events decrease with increasing CrO_4^- concentrations. NaCl concentration = 10^{-3}M. Applied potential = -0.5V (SCE).

13. Effect of Na_2CrO_4 on metastable pit properties. Peak pit current vs. pit current density at peak pit current and peak pit current versus pit radius data are both shown. On average the larger metastable pit current density are removed with the addition of CrO_4^-.

14. Conclusions concerning pit stabilization criteria.

15. Electrochemical noise analysis procedures.

16. Time series showing galvanic coupling of two identical AA 2024-T3 (ST) electrodes in 0.1M NaCl.

17. Power spectral density plots showing the ability of the noise method to qualitatively rank pitting susceptibility but provide little mechanistic information.

18. Summary conclusions on utility of electrochemical noise methods

19. Summary viewgraph justifying the significance of memory and feedback in pitting phenomena.

20. Methods used to study memory, and/or interdependency of pitting events.

21. Use of the autocorrelation function as a test for memory in pitting (Fe-Cr alloy).

22. Use of the autocorrelation function as a test for memory in pitting (Al-2%Cu).

23. Summary of findings regarding spatial and temporal coupling of pitting events.

24. Example of the incorporation of memory into a pitting initiation model.

25. Factors controlling pit growth in Al. Low potentials - ohmic control. High Potentials - mass transport control..

26. Published pit growth laws for Al.

27. Future directions.

Metastable Pitting of Aluminum Alloys in Halide Solutions

S.T. Pride[+], J.R. Scully[*], J.L. Hudson[#]

+ Formerly Department of Chemical Engineering
University of Virginia.
Present address - Rohm and Hass Chemical Co., Bristol, PA.

*** Department of Materials Science and Engineering**
University of Virginia

 # Chemical Engineering Department
University of Virginia

Project Elements and Objectives

1. **Stabilization criteria for the transition from metastable to stable pitting:**

   The objective of this element is to define the factors which govern the transition from metastable to stable pit growth. The findings have significant implications with regard to the design of corrosion resistant alloys, aqueous phase inhibitors, and aging aircraft.

2. **Evaluation of the utility of electrochemical noise analysis methods as a forecasting tool for prediction of the transition from metastable to stable pitting growth.**

   The objective of this phase is to ascertain the best approach for forecasting the transition from metastable to stable pit growth using electrochemical noise methods.

3. **Existence of correlations or coupling between metastable pitting events**

   The objective of this project element is to determine whether or not metastable pitting events are completely independent of each other or whether some "memory" exists in the pitting process which leads to interactions between older pits and newer pits.

Materials

- **High purity Al (99.999% wire)**

- **Aged Al-2%Cu**

  510°C 2 hrs/quench/246°C for 24 hrs
  Θ', Θ'', grain boundary Θ-Al_2Cu

- **AA 2024-T3 (LT and ST orientations)**

  SHT, cold work, naturally aged
  GP zones, undissolved excess S or S'-Al_2CuMg
  $(Mn,Fe)_3SiAl_{12}$, $Cu_2Mn_3Al_{20}$

Stabilization criteria and the transition from metastable to stable localized corrosion

Criteria - local site:

1. **Solution compositional changes are required at the local site and must be maintained for stabilization** - coupled mass transport modelling is required to understand factors responsible for chemistry alteration

2. **Salt film formation may be a precursor to stabilization** - coupled mass transport modelling is required to understand factors controlling salt film precipitation

3. **An ohmic voltage difference is often required between the local site and external surface** - current and potential distribution modelling is required

Criteria - cathode site:

4. **Local site growth rates may become cathode limited** - transient and steady state current and potential distributions govern capacitive and faradaic currents which support anodic processes at the local site

Pitting Potentials Obtained from Anodic Polarizations in Deaerated NaCl Solutions

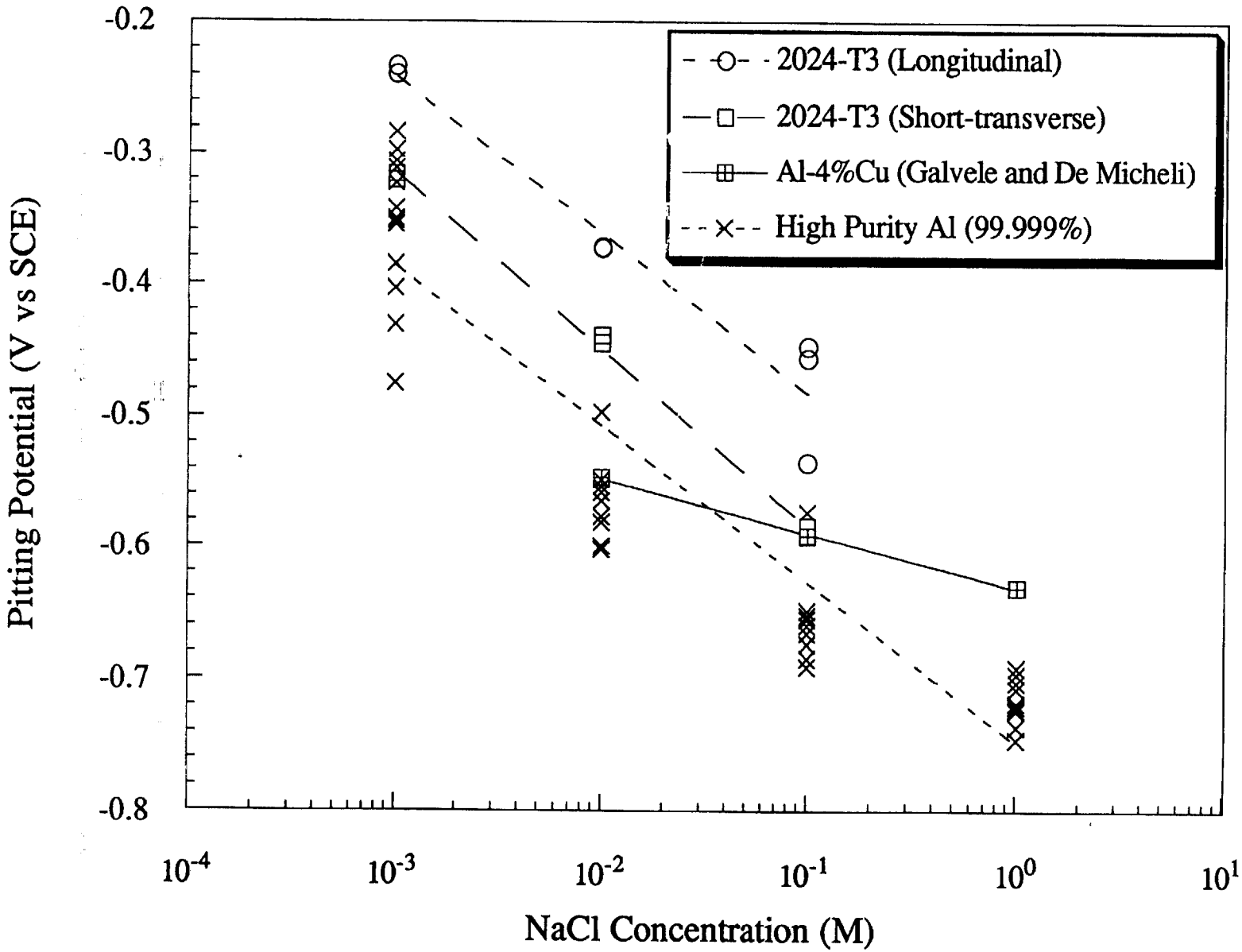

Metastable pitting behavior of pure Al in 10^{-4} M NaCl showing transition to stable pit growth

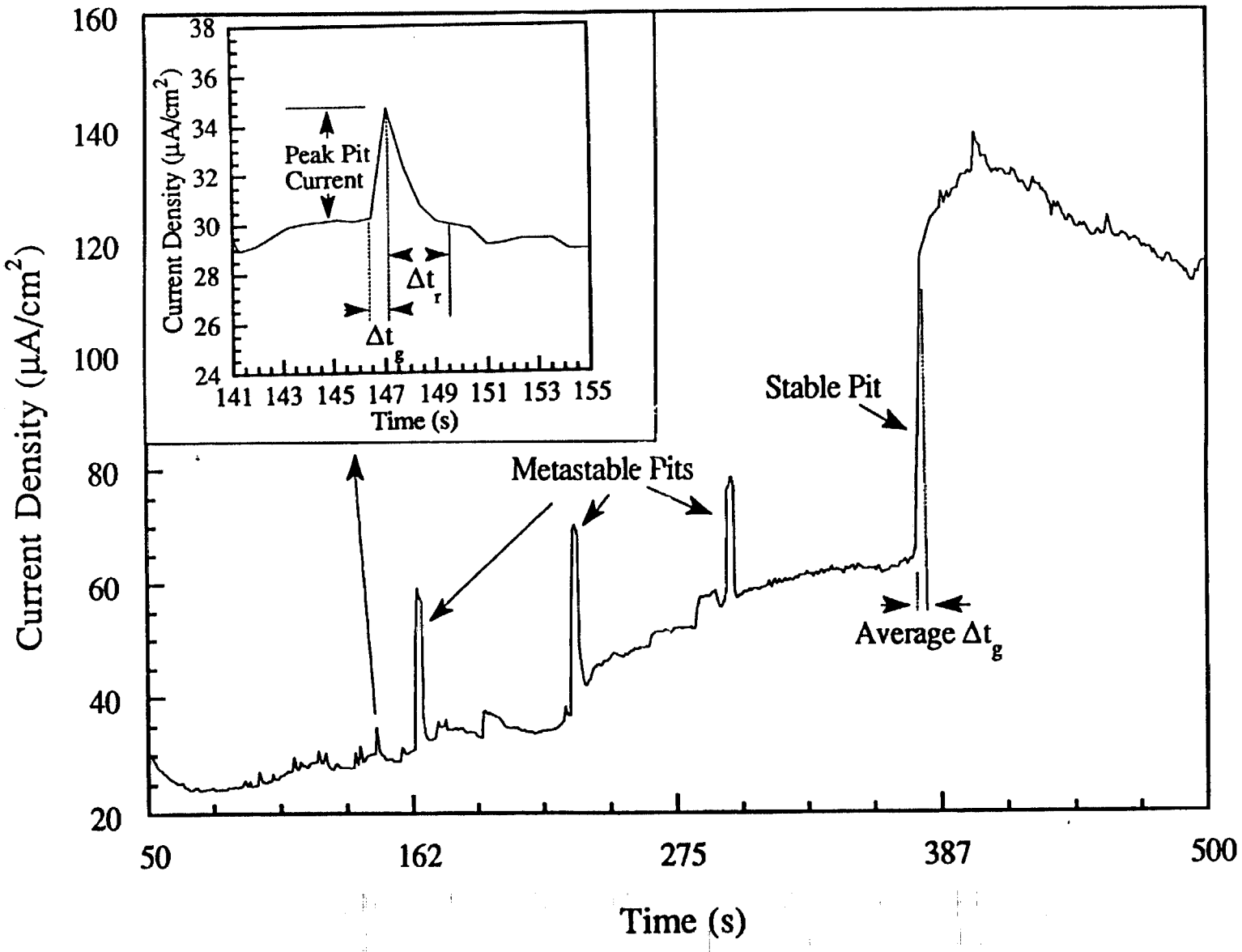

Good agreement is observed regarding the number of current spikes and the number of metastable pits as well as between the pit sizes calculated from Faraday's law and microscopy. (Pride, Scully, Hudson, J. Electrochem. Soc., 1994)

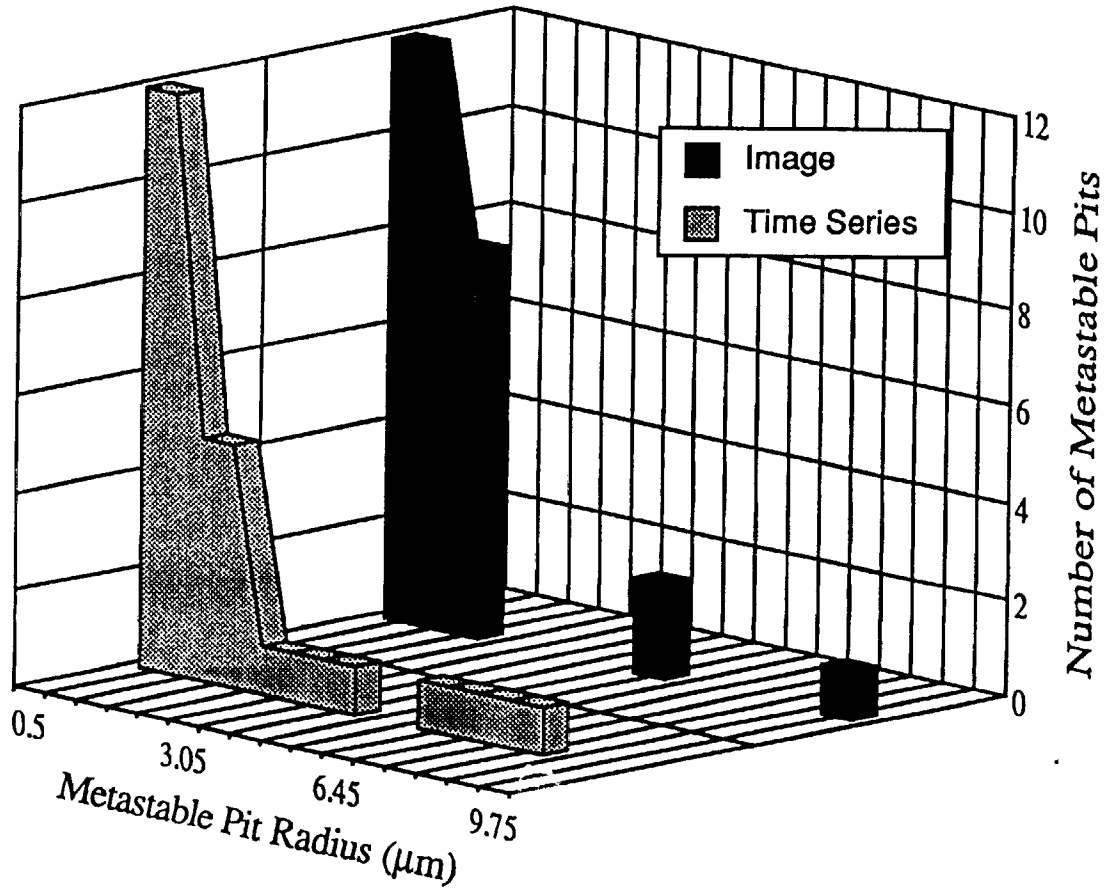

High purity Al in 10^{-3} M NaCl at -0.5V SCE

A transition from metastable to stable pitting occurs when the ratio of peak pit current to pit radius exceeds a threshold value. (Pride, Scully, Hudson, J. Electrochem. Soc. 1994)

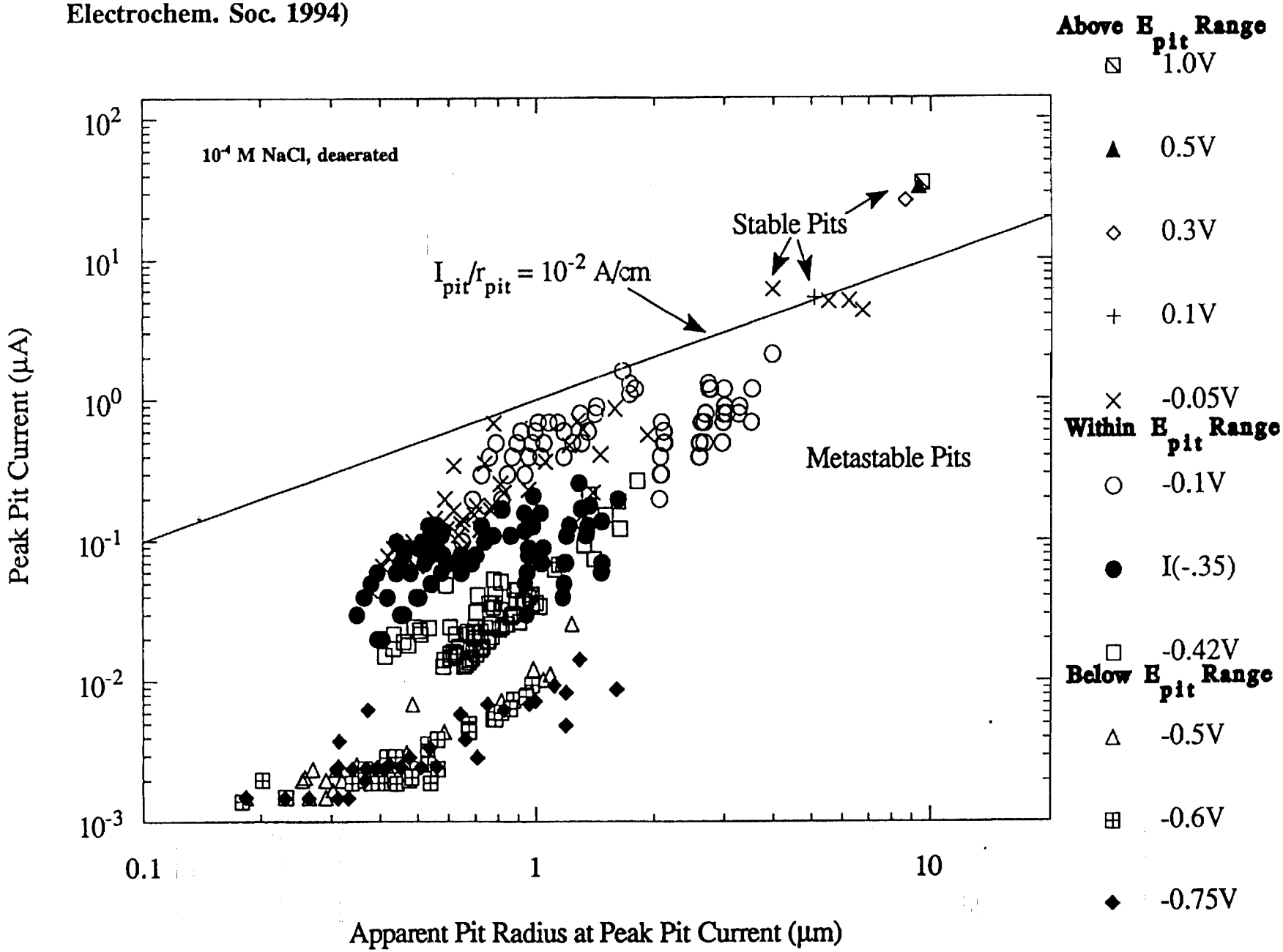

The transition from metastable to stable pitting in Al is linked to the requirement that a concentrated $AlCl_3$ solution must be maintained in the open pit at all times during growth. (Pride, Scully, Hudson, J. Electrochem. Soc. 1994)

Pit current density:

$$i = -F^2 \nabla\phi \sum_i z_i^2 u_i c_i - F \sum_i z_i D_i \nabla C_i + Fv \sum_i Z_i c_i$$

Considering hemispherical diffusion from a mirco-electrode disk in an insulating flat plane with mixing due to hydrogen evolution:

$$i_{pit} = nFD_{Al^{+3}} \Delta C_{Al^{+3}} \left[\frac{1}{\delta_{H_2}} + \frac{1}{r_{pit}} \right] - \nabla\phi \sum \kappa_I$$

The following relationship between $AlCl_3$ concentration and the product i_{pit} x r_{pit} is readily established for micrometer size pits. The transference number corrects for Al^{+3} transport by migration.

$$C_{Al^{+3}} = \frac{i_{pit} r_{pit} (1 - t_{Al^{+3}})}{nFD_{Al^{+3}}}$$

Conclusion: A 3 molar $AlCl_3$ concentration can be maintained when i_{pit} x $r_{pit} > 0.2 \times 10^{-2}$ A/cm or $I_{pit}/r_{pit} > 1.3 \times 10^{-2}$ A/cm.

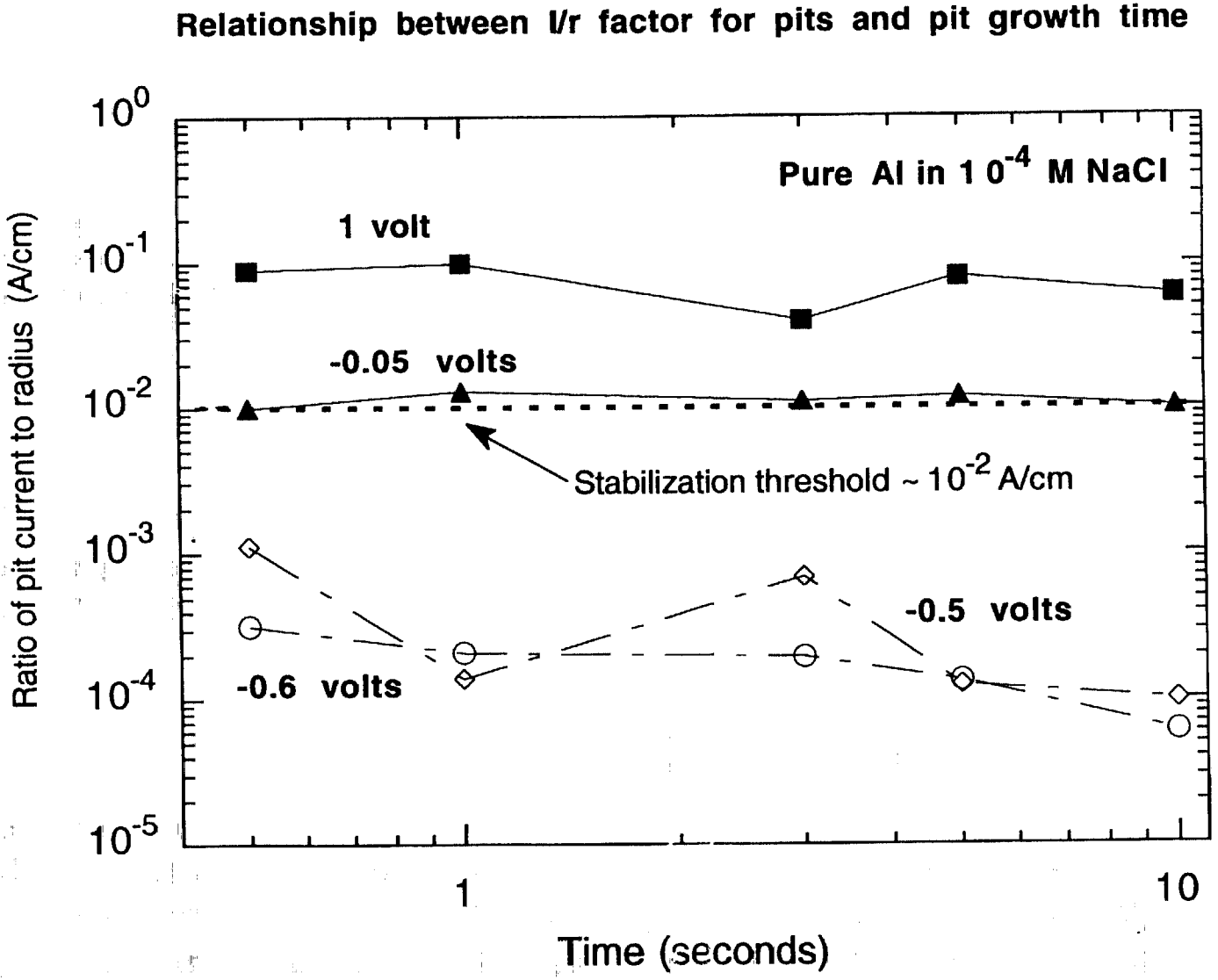
Relationship between I/r factor for pits and pit growth time
Pure Al in 1 0^-4 M NaCl
1 volt
-0.05 volts
Stabilization threshold ~ 10^-2 A/cm
-0.5 volts
-0.6 volts
Ratio of pit current to radius (A/cm)
10^0
10^-1
10^-2
10^-3
10^-4
10^-5
1
10
Time (seconds)

Pit Growth Laws for Metastable and Stable Pits

If $I_{pit} = At^{0.5}$ and hemispherical pits are formed, then it follows from Faraday's law that $r_{pit} = Bt^{0.5}$ and $i_{pit} = Ct^{-0.5}$, where A, B and C are constants.

For stable pits growing according to these conditions:

$I/r_{pit} = A/B$ and $i*r_{pit} = BxC$ A constant pit chemistry is maintained !

For metastable pits growing at $I_{pit} = At^{0.25}$, it follows that $r_{pit} = Bt^{0.42}$ and $i = Ct^{-0.58}$.

For metastable pits the stabilization criterion is even more difficult to meet with time:

$I/r_{pit} = (A/B)t^{-0.17}$ and $i*r_{pit} = BxCxt^{-0.17}$

Chromate inhibitor added to NaCl reduces the chance for pit stabilization on Al by lowering metastable pit nucleation rates (Pride, Scully, Hudson, J. Electrochem. Soc. 94)

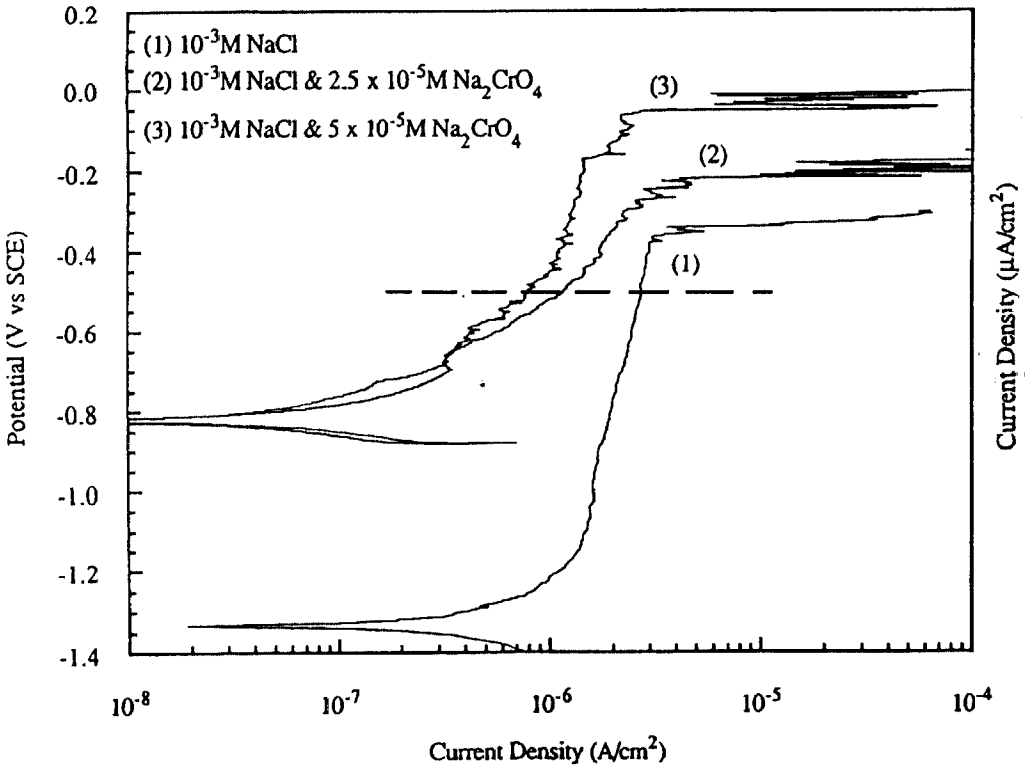

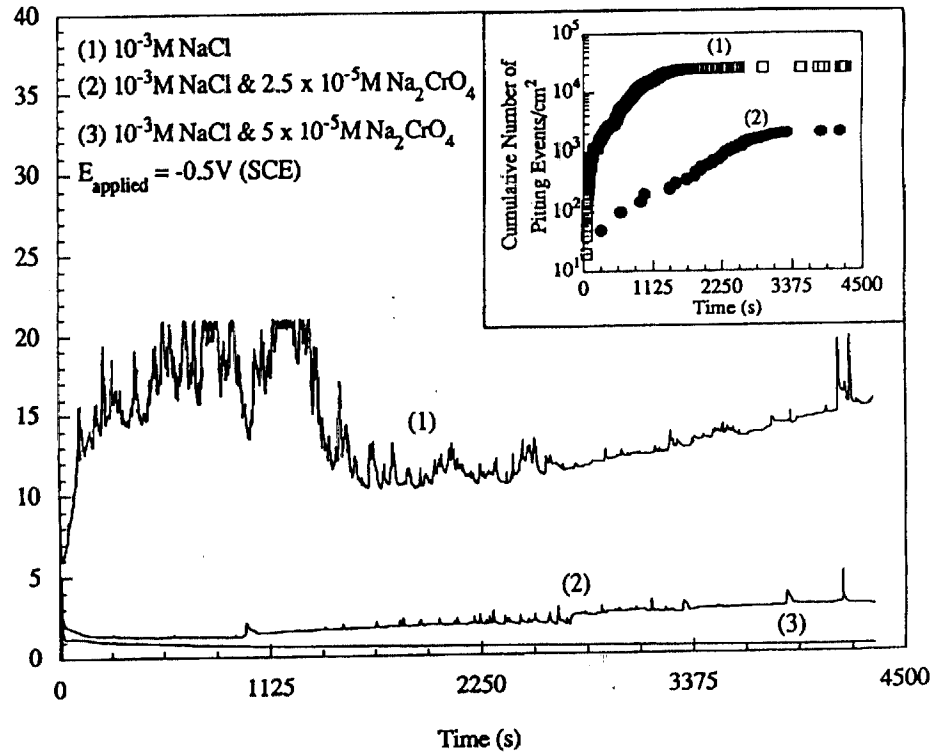

Chromate inhibitor added to NaCl reduces the chance for pit stabilization on Al by eliminating the fastest growing pits (Pride, Scully, Hudson, J. Electrochem. Soc., 1994)

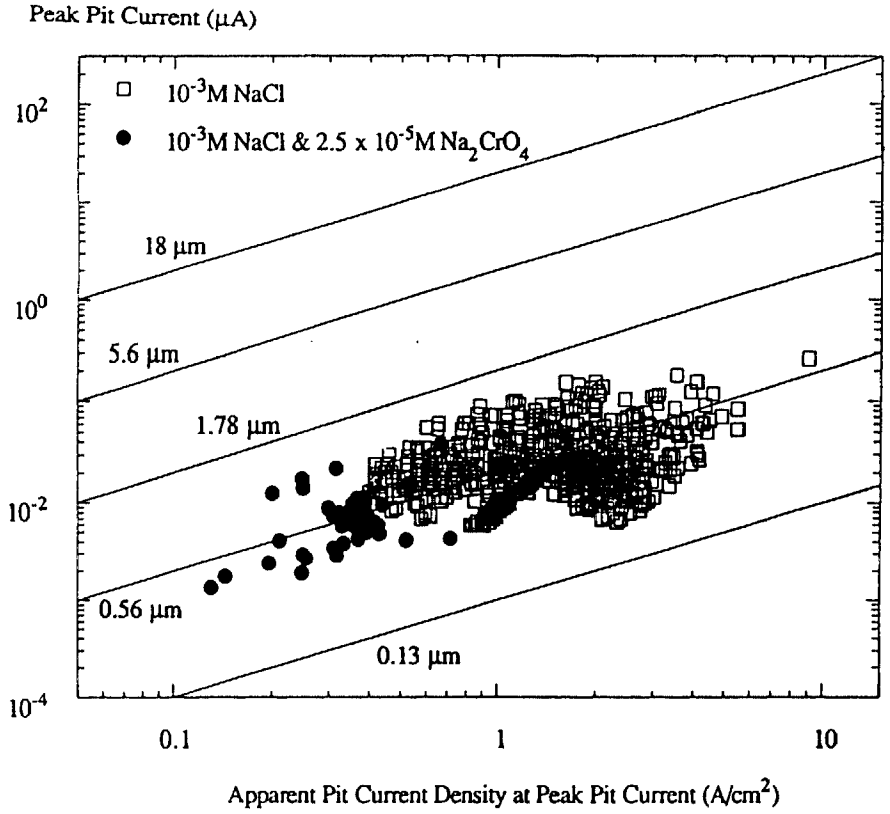

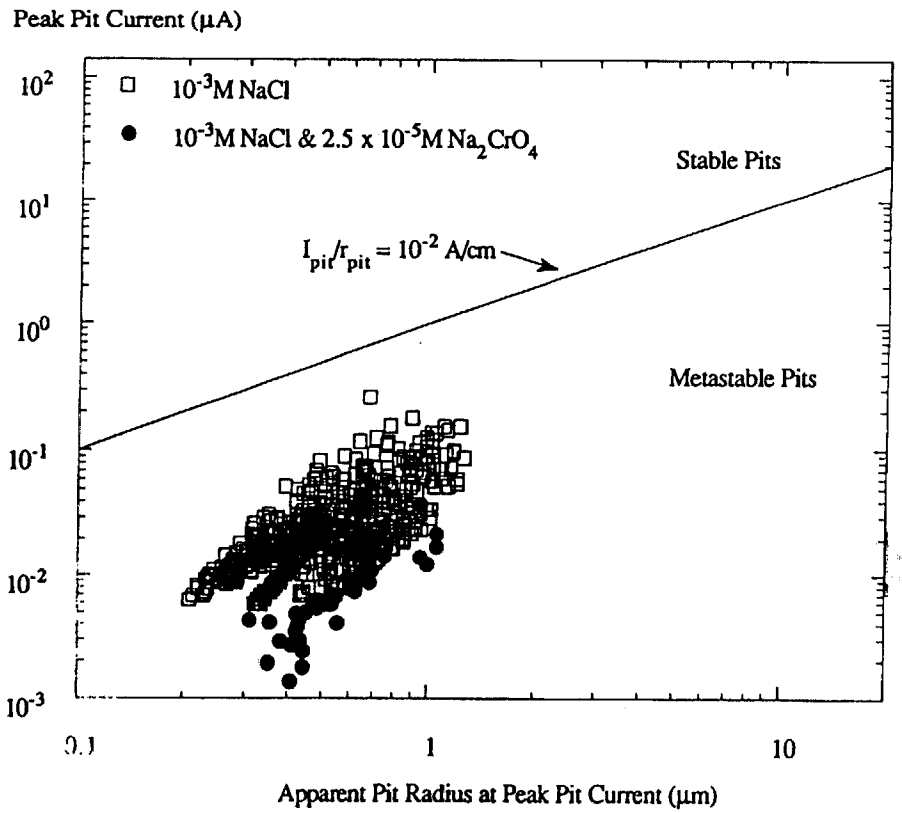

Stabilization and the transition from metastable to stable pit growth

1. **Factors which promote the transition from metastable to stable pitting:**

   - the product of pit current density and pit radius must exceed a critical value ($>0.3 \times 10^{-2}$ A/cm) to maintain a minimal pit chemistry. (SS and Al)

   - Salt film precipitation is required prior to oxide cover rupture in order to supply the necessary ohmic drop to sustain active dissolution. (SS)

   - A re-entrant pit geometry or metastable pit initiation at a previous site aids in pit development. (Exception: depletion of MnS inclusions)

2. **Factors contributing to pitting inhibition by alloying or solution additions:**

   - metastable pit nucleation frequency is lowered at a given halide ion concentration and applied potential

   - fast growing metastable pits are selectively eliminated.

   - pit repassivation rates are enhanced (Fe-Cr)

EN Time Series Analysis Methods

1. Raw electrochemical analysis of individual pitting events using Faraday's law to determine pit volumes and pit current densities.

- pit volume after elapsed time periods
- pit current density at peak pit current
- *pit stabilization criterion*
- repassivation time constant

2. Statistical Analysis

- *statistical pit stabilization criterion*
- Noise resistance
- RMS, variance and standard deviation of EN current and/or voltage time series
- Pitting index

3. Spectral analysis

- *FFT and MEM: power spectral density plots*

4. Tests for Stochastic Processes

- Poisson distributions
- next maxima analysis
- attractor reconstruction
- auto-correlation

Time Series of Galvanically Coupled 2024-T3 (ST) in Aerated 0.1M NaCl

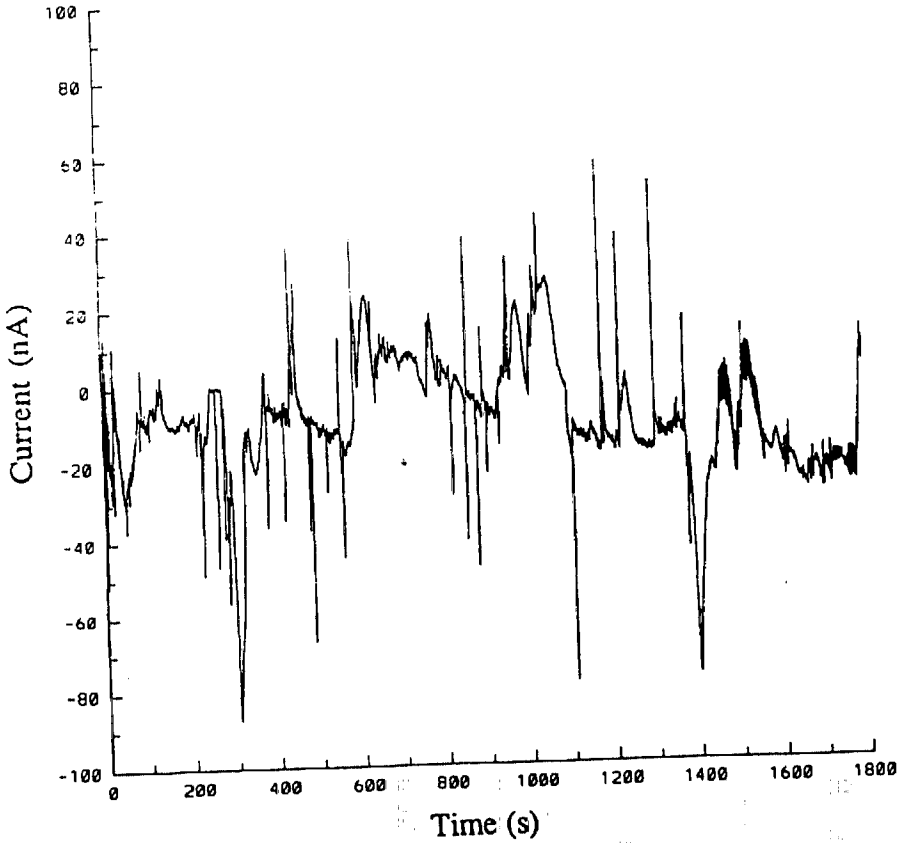

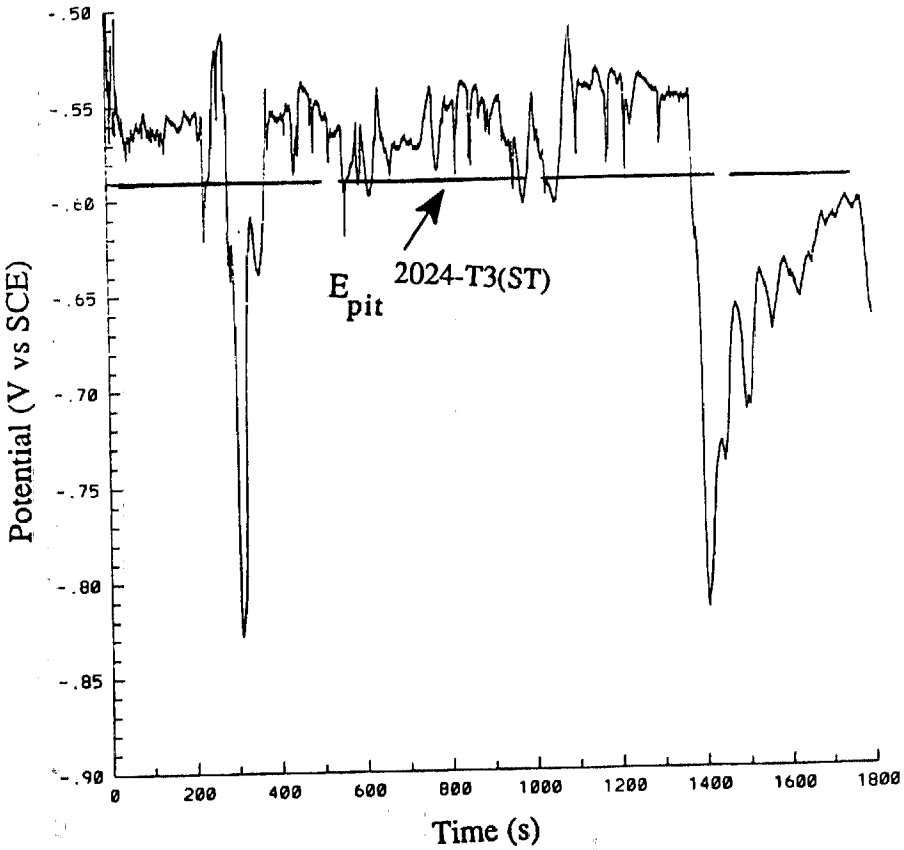

Power Spectral Density of Galvanically Coupled Metals in Aerated 0.1M NaCl

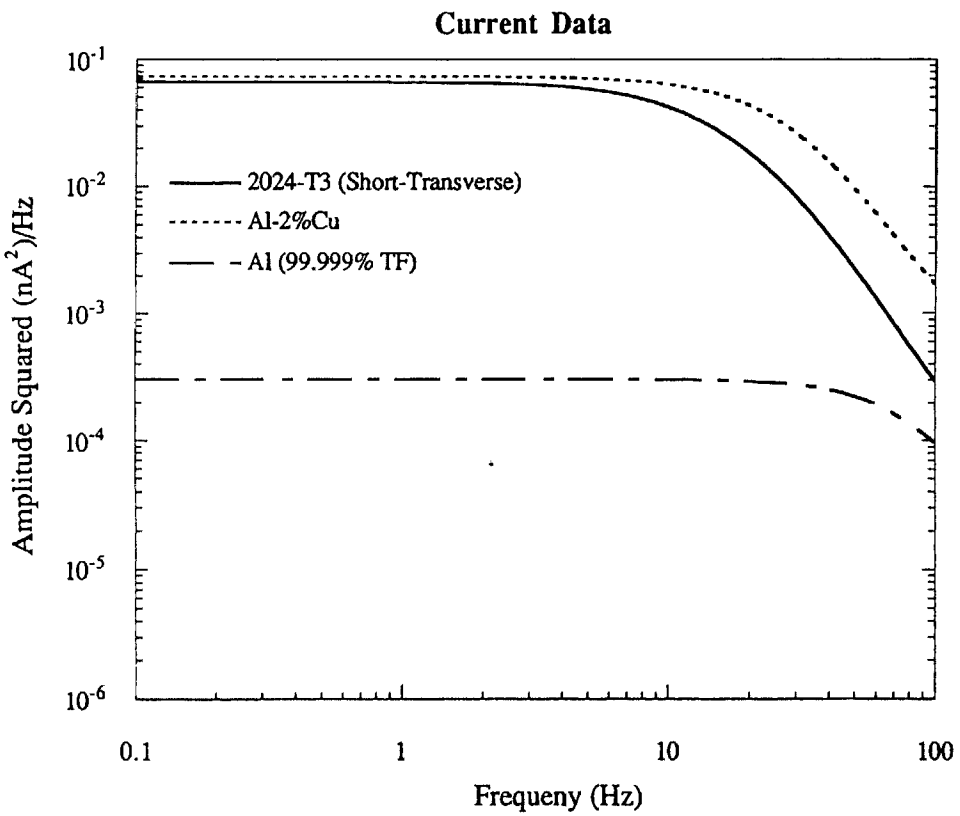

Power Spectral Density of Galvanically Coupled Metals in Aerated 0.1M NaCl

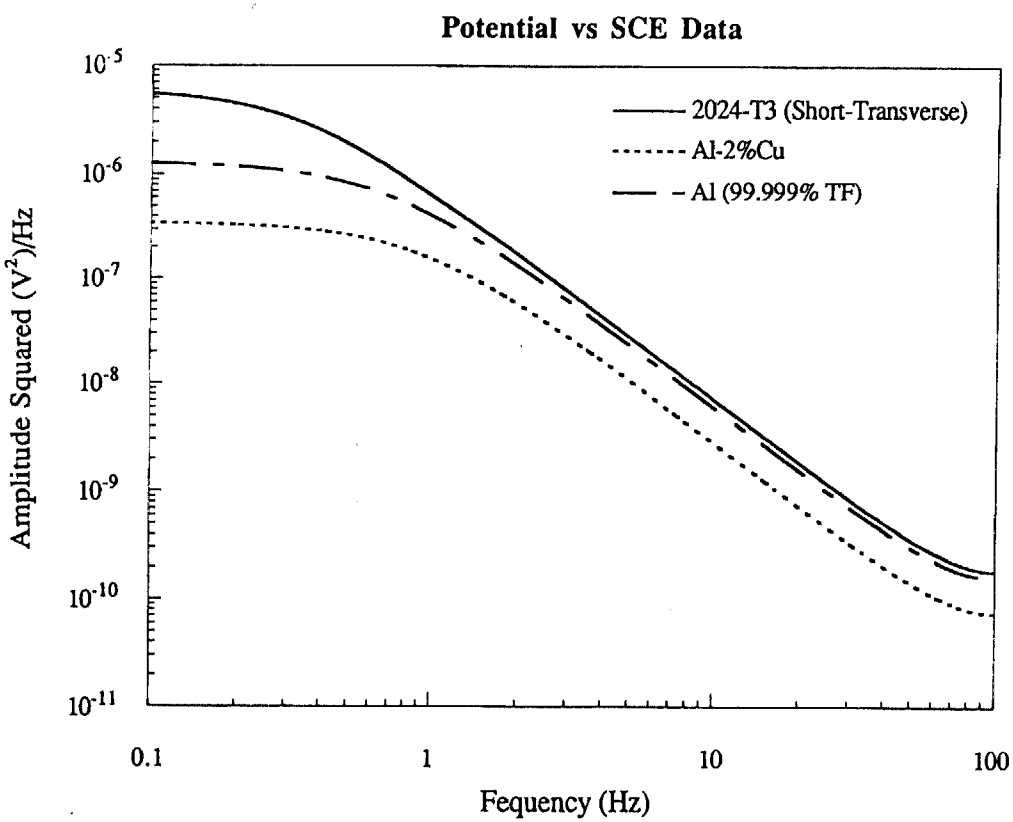

Conclusions

- An electrochemical criterion for stabilization of a single pit site in Al was defined. The ratio of pit current to pit radius must exceed 10^{-2} A/cm at all times during growth for pits to avoid death.

- Of all of the statistical parameters explored, the ratio I_{rms}/r_{total} best distinguishes between the trend for increasing metastable pitting with Cl^- and absence of metastable pitting in chromate. Alloy susceptibility was also predicted.

- The electrochemical noise resistance (ERN) and pitting index (PI) tracked with increasing Cl^- and alloy susceptibility. However, PI did not properly distinguish between the complete absence of pitting in chromate and metastable pitting in high Cl^-.

- ERN data neither corresponds to low frequency impedance data for passive aluminum nor data for Al in simulated pit environments

- The magnitude of the low frequency portion of Power Spectral Density plots (current-PSD) increased with the intensity of metastable pitting.

- High frequency PSD behavior did not indicate a completely stochastic process.

- Current PSD plots provided more useful information than potential PSD plots.

Understanding of the degree of dependence or memory associated with metastable pitting events allows the rational construction of feedback models which improve the probability of pit stabilization when events are spatially and temporally close.

Rationale and justification for limited memory and feedback:

1. Local passive current fluctuations, dealloying, or pit precursor events change alloy or solution chemistry. These affect growth and repassivation rates. (Williams, et al., Nature, 91; Balkwill, et al., 1989; Riley, et al., Corros. Sci., 91, Lott and Alkire, J. ECS, 1989)

2. Local changes in passive film properties near pits affect nucleation frequency, stability of oxide cover, chance of pit stabilization (Sugimoto, J. ECS., 1985; Isaacs and Kissel, J. Electrochem. Soc., 1972; Bardwell, ECS Proc. 92).

3. Ability to support early pit growth with local capacitive current may be temporarily exhausted (Isaacs, Ishikawa, J. ECS, 1985)

Lott and Alkire, 304 SS:

$2MnS + 3H_2O = S_2O_3^{2-} + 2Mn^{+2} + 6H^+ + 8e^-$

and $2H^+ + MnS = Mn^{+2} + S + H_2$

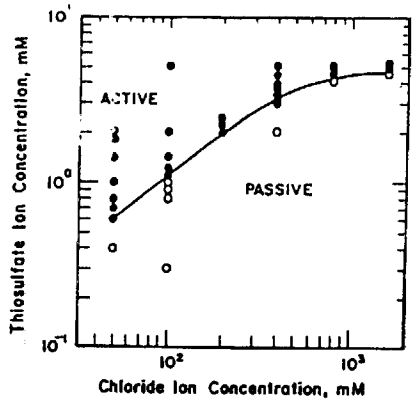

The study of inter-relationships, correlations and/or memory associated with localized corrosion events is relatively new. Analysis methods provide diagnostic procedures to test for "correlations, memory, chaos or stochasticity."

Methods applied to metastable pitting of metals

1. **Spectral** - power and amplitude spectral density to test for white noise
2. **Intensity plots** - rate of event occurrence with time
3. **Event distribution plots** - compare to the Poisson distribution as a test for event randomness
4. **Methods of non-linear dynamical analysis** - test for chaos, methods: return maps such as Δt, I_{max}, dimension calculations
5. **auto-correlation function** - test for correlation of event properties

The inter-event times from the unstable pitting of an Fe-Cr alloy have been tested for memory using the autocorrelation function and intensity plots. Events are not completely independent. (Bertocci, J. Electrochem. Soc., 86)

$$ACF = \frac{\sum_{t=1}^{n} (x_t - X_{mean})(x_{t+k} - X_{mean})}{\sum_{t=1}^{n} (x_t - X_{mean})^2}$$

k = the lag time

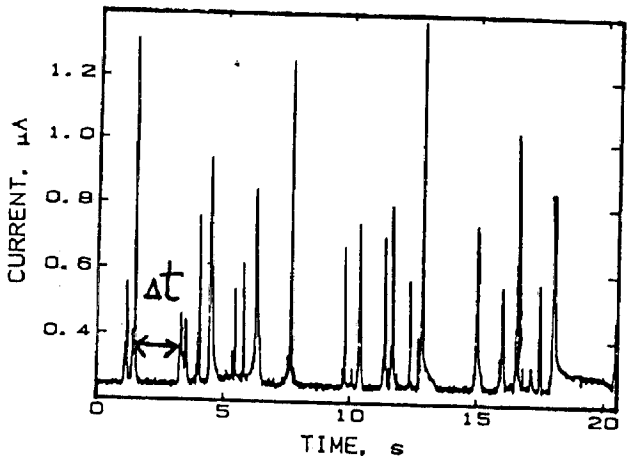

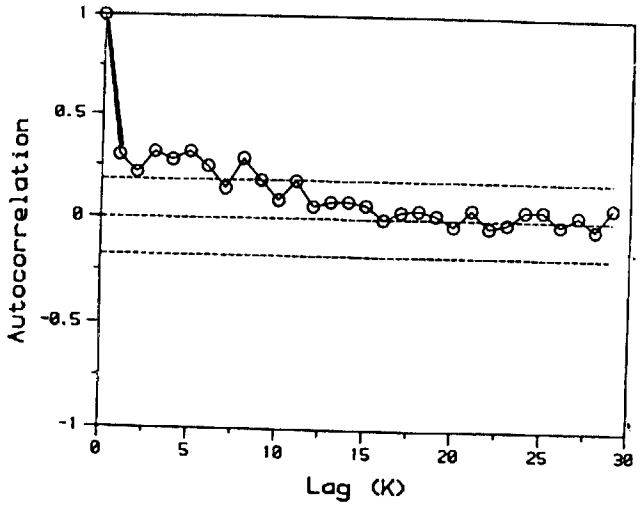

Tests for memory during metastable pitting of aged Al-2%Cu using the autocorrelation function suggest that events are not completely independent. (Pride, Scully, Hudson, Unpublished)

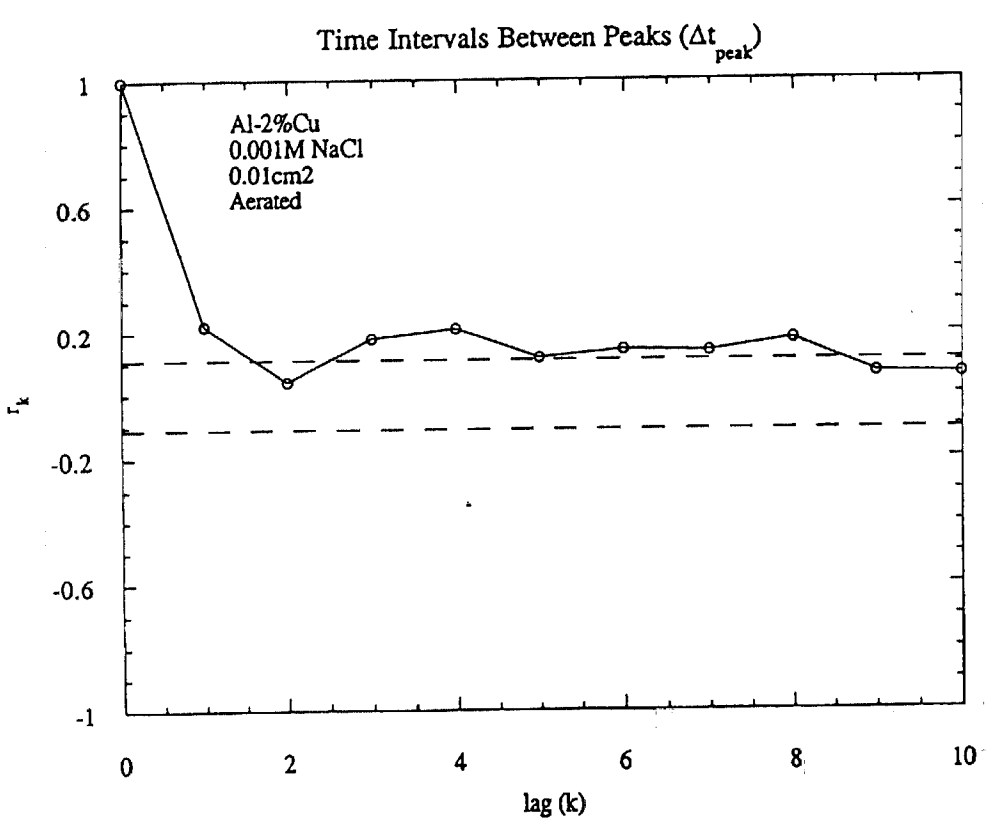

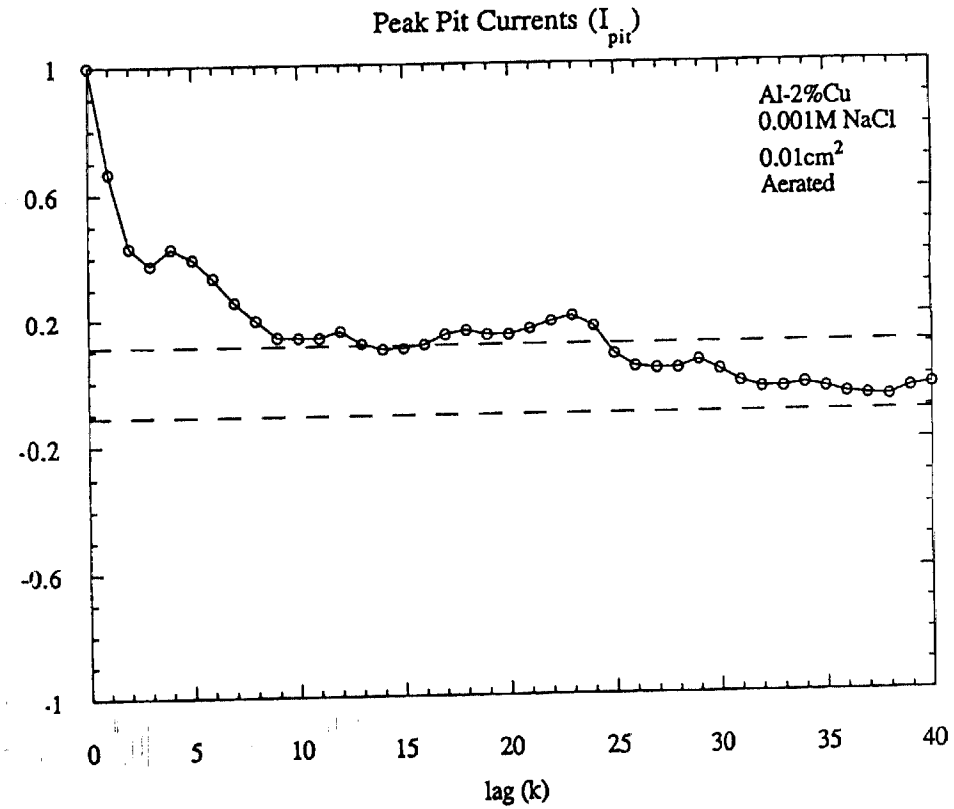

Summary - Spatial and temporal coupling, memory and feedback associated with localized corrosion events

- Analysis of metastable pitting inter-event times indicate short-term memory in Fe-Cr and Al systems

- Analysis of spatially and temporally discrete metastable pitting events does not indicate low dimensional chaos

- much more work needs to be done !

- Feedback models for pit stabilization require incorporation of memory and weighing factors that are based on experimental evidence.

Stochastic models of stable pit initiation develop criteria for the formation of stable pits based upon the nucleation frequency of metastable pits (D.E. Williams, C. Westcott, M. Fleischmann, J. Electrochem. Soc. 85)

Expected induction time for stable pitting:

$$<\tau_{stable}>(\text{sec}) = \left(\frac{1}{A\lambda}\right)\exp(\mu\tau_c) + \tau_c$$

λ = metastable pitting event nucleation frequency (s^{-1}-cm^{-2})
μ = probability of event death (s^{-1})
τ_c = critical age for survival (s)
A = electrode area (cm^2)

The nucleation frequency for metastable pitting, λ, is: (Bohni, Holliger and Pride,Scully):

$$\lambda\ (cm^{-2}\text{–}\sec^{-1}) = B\exp(-Ct)$$

B,C = applied potential, $\epsilon_t/\dot{\epsilon}_{rate}$, $[SO_4^{-2}]/[Cl^-]$, metallurgy (e.g.MnS) and temp. dependent constants
t = elapsed time

The relationship between applied potential and pit current density after equivalent pit growth times suggests regions of ohmic and mass transport controlled pit growth (Pride, Scully, Hudson, J. Electrochem. Soc. 1994)

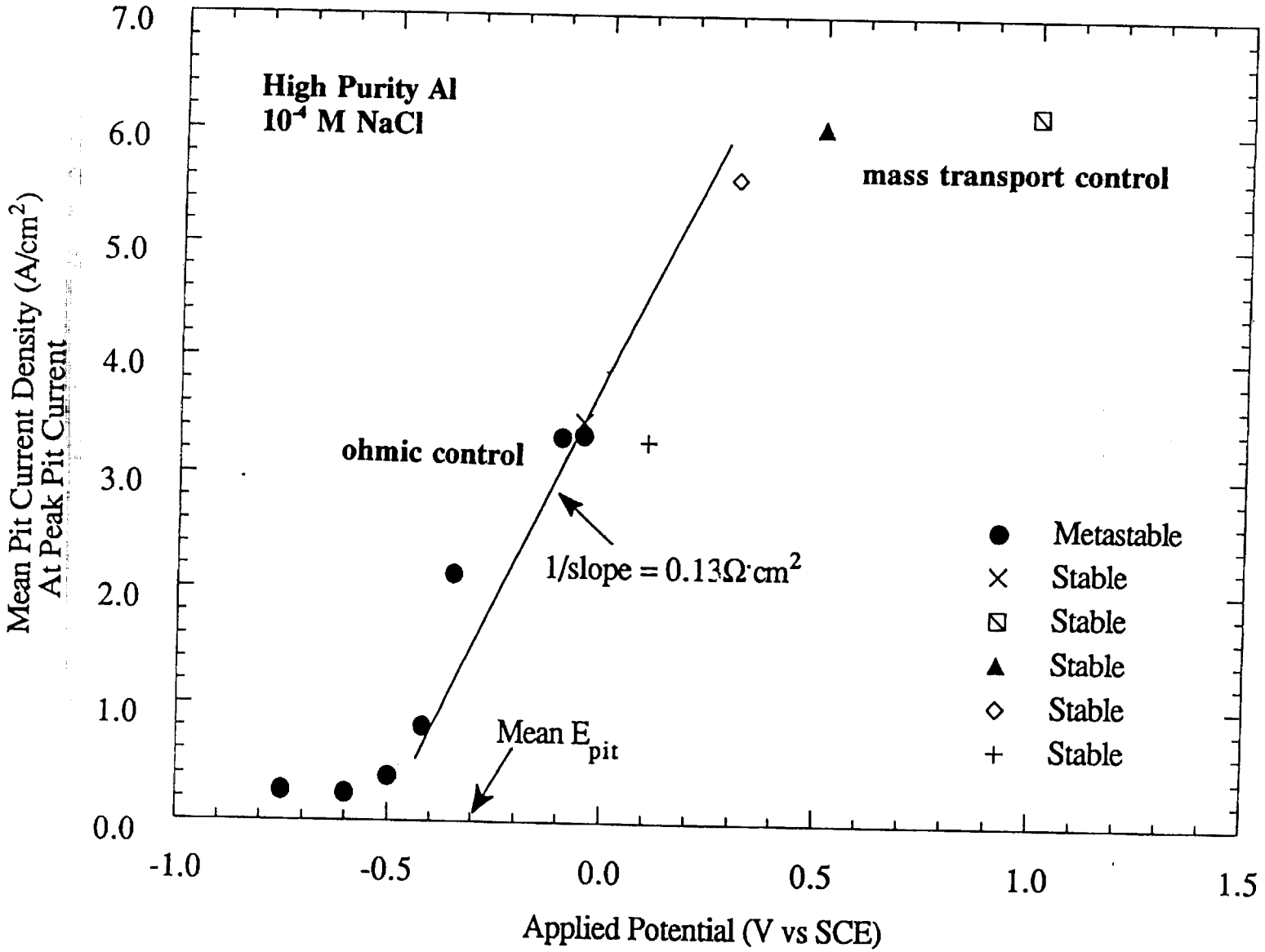

Empirical pit growth laws for metals and alloys where hydrogen evolution in pits increases the effective solution resistance

Metal or Alloy	Penetration law	Growth Rate Law	Controlling factor	Author
Bulk Al in Cl^-, stable pits*	$r = Axt^{1/2}$	$dr/dt = Kxt^{-1/2}$	Ohmic control by R_Ω in pit	Hunkeler and Bohni
Stable pitting on Al in natural waters at open circuit*	$r = Axt^{1/3}$	$dr/dt = Kxt^{-2/3}$	Ohmic control by R_Ω outside of the pit	Godard, analyzed by Hunkeler and Bohni
1-D pencil electrodes Mg or Al in Cl^- Similar for Ti in Br^-	$l = Axt^{1/2}$ high E_{app}	$dl/dt = Axt^{-1/2}$ high E_{app}	Ohmic - low E_{app} Mass transport - high E_{app}: i_{pit} increase with flow, decreases with high conc C_{bulk}	T.R. Beck T.R. Beck and S.G. Chan

* - assumed hemispherical
r = pit radius, l = depth of 1-D pit
diagnostic
dr/dt increase with flow - mass transport
dr/dt decrease with flow - ohmic

Future Directions

Aging aircraft:

1. **Determine the "windows" of applied potential, cyclic strain, and lap-joint chemistry which lead to a) intergranular corrosion and b) corrosion fatigue crack initiation from precursor metastable and/or stable pit sites in AA 2024-T3.**

2. **Use electrochemical noise methods as a high resolution tool to characterize the pitting behavior of AA 2024-T3 of various vintages in aqueous solutions relevant to aging aircraft.**

3. **Characterize the metastable pitting behavior and pre-stable as well as stable pit growth laws for AA 2024-T3 under applied cyclic strain in aqueous solutions relevant to aging aircraft.**

Project #7 Evaluation of Wide-Panel Aluminum Alloy Extrusions

Mark Lyttle and John A. Wert

Objectives

The overall objective of this project is to experimentally observe and to model the effects of microstructure and texture on yield strength in wide panel aluminum alloy extrusions. The modeling results will enable the prediction of locations and tensile axis orientations corresponding to minimum yield strength where localized yielding could occur in service. A generalized form of these models could be applied to any combination of microstructure and texture found in other aluminum alloys.

Current Status

A model has been constructed to predict the variations in yield strength due to grain orientation and precipitate plane orientation for plastic inclusions. Using specimen texture obtained from pole figure data, a Taylor factor can be determined for any stress axis orientation in the specimen. Combining specimen texture and precipitate plane orientation, the contribution to strengthening from precipitates with the specified habit plane orientation can be calculated [1-3].

Experimental verification of predicted Taylor factors and precipitate strengthening parameters has been conducted on two aluminum alloys, 1100 and 2024. These systems have been more thoroughly analyzed than the wide panel extrusions, which should provide an easier route to evaluate the applicability of the modeling results. Experimentally observed yield strengths appear to follow the general trends predicted by the models.

Because of texture variation on a microscopic scale and the desirability of conducting out-of-plane testing, compression testing on small samples is necessary to precisely isolate the variation of yield strength on a local scale. A compression apparatus has been developed which allows accurate and replicable determination of yield strengths.

Recent Important Findings

Prediction of average Taylor factor and precipitate strengthening effects is fairly accurate for the 1100 and 2024 alloys. These preliminary results are encouraging, indicating that, with refinement, our models should be capable of predicting the anisotropy in yield strength given texture, precipitate, and grain morphology data for a wide range of alloys. For the wide panel extrusions to be studied, more compression tests will be performed in each orientation to obtain more reliable data.

Several interesting observations emerge from the plastic inclusion model predictions studied thus far. Because the degree of strengthening is dependent on precipitate plane, it is possible that for a given texture, a weaker precipitate growing on a "stronger" habit plane can cause a greater strength increase than a strong precipitate with a "weaker" habit plane. Precipitates of any habit plane can be separated into two types, which represent the extremes of the precipitate, indicating where the greatest strengthening contribution to yield strength for uniaxial strain occurs, either the <100> or <111> direction. For the greatest uniaxial strength increase in the rolling/extrusion direction, either a cube or copper texture is desirable depending on which type of precipitate is observed to form.

Future Work

The development of the initial models is virtually complete and the models appear to predict the general trends of yield strength for 1100 and 2024 aluminum alloys. Characterization of microstructure and texture of the wide panel extrusions is the next major step. Since these extrusions contain a greater variation of texture and are the more technologically interesting material, more thorough and repeated compression testing will be conducted in numerous orientations in- and out-of-plane. Texture and microstructure will be determined for several different locations in the extrusion.

The capability to predict average Taylor factor and the strengthening ratio of precipitates in the plastic inclusion model is complete. Development of the elastic inclusion model for precipitate strengthening will be completed

within a month. Determining the effect of grain shape on Taylor factor is an important modeling goal for the next year [4].

References

1. P. Bate, W. T. Roberts and D. V. Wilson, Acta Metallurgica, **29** (1981) 1797.

2. P. Bate, W. T. Roberts and D. V. Wilson, Acta Metallurgica, **30** (1982) 725.

3. W. F. Hosford and R. H. Zeisloft, Metallurgical Transactions, **3** (1972) 113.

4. U. F. Kocks and H. Chandra, Acta Metallurgica, **30** (1982) 69.

Presentation Visual Aids

1. Title and Objectives - Evaluating wide panel aluminum alloy extrusions.

2. Introduction - Provides the technological and scientific impetus for this research.

3. Approach - Outlines the methods to be used to characterize the microstructure of the alloy and subsequently predict yield strength anisotropy. Initial verification of models is performed on 1100 and 2024 alloys.

4. Factors Influencing Yield Strength Anisotropy- Basic effects of texture, grain morphology, and precipitate morphology and orientation on yield strength anisotropy are outlined.

5. Predicting the Effect of Texture on Anisotropy - Describes the conversion of pole figure data to average Taylor factor.

6. Effect of Orientation and Texture on Taylor Factor - A table of standard textures and the variation of Taylor factor with tensile orientation. A plot of average Taylor factor varying with tensile orientation for a random texture and for a typical rolling texture.

7. Flow Stress Predictions for the Precipitate Strengthened Condition - General descriptions of the plastic inclusion and elastic inclusion models.

8. Predicting the Effect of Precipitate Orientation on Anisotropy - Displays the variation in amount of precipitate strengthening for three common precipitate habit planes.

9. Precipitate Plane Dependence of Precipitate Strengthening Ratio for Observed Textures - Table of precipitate strengthening ration for combinations of common textures and common precipitate planes. Stereographic triangle showing the stress axis orientations that generate the greatest strengthening for a given habit plane.

10. Compression Testing - Justification for using compression testing.

11. Comparison of Predicted and Experimental Taylor Factors for Cold Rolled 1100 Aluminum - Calculated average Taylor factors are compared with experimental results for 1100 aluminum.

12. Comparison of Predicted and Experimental Taylor Factors for 2024 Solution Treated - Calculated average Taylor factors are compared with experimental results for 2024 solution treated.

13. Comparison of Predicted and Experimental Yield Strengths for 2024 Aged - Calculated average Taylor factors and precipitate strengthening ratios are compared with experimental results for 2024 aged.

14. Conclusions and Future Work - Development of simple models for average Taylor factor and calculation of level of precipitate strengthening are complete and have been verified using 1100 and 2024 alloys. Future work will involve the characterization of the wide panel extrusions.

15. Wide Panel Integrally Stiffened Extrusions on Alloys 2096 and 2195 - Such materials are available for laboratory characterization under the auspices of the LA^2ST Program.

Evaluation of Wide-Panel Aluminum Alloy Extrusions

M. T. Lyttle
J. A. Wert

University of Virginia
Department of Materials Science and Engineering

Objectives

- Characterize the effects of texture and microstructure on the yield strength in wide panel aluminum alloy extrusions
- Develop models which enable the prediction of locations in the extrusion and tensile axis orientations of minimum yield strength where localized yielding could occur in service

Introduction

- Traditional construction
  Sheet and stiffener fabricated separately
  Joined

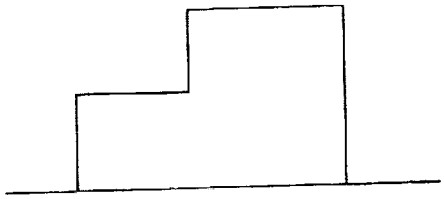

Conventional microstructure and texture

- Wide panel extrusions
  Shape produced by flattening a tubular extrusion with integral stiffeners

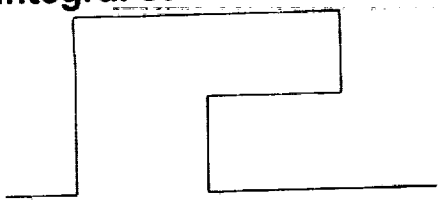

Complex and rapidly varying microstructure and texture

Technological Question-
Are there soft directions in some locations in the wide panel extrusion that could cause localized yielding in service?

Scientific Question-
Can a model be formulated to predict the effects of grain morphology, texture, precipitate orienation, and stress axis orientation on yield strength?

Approach

- Examine factors that influence the yield strength anisotropy of a material

1. Texture - Determines average Taylor factor for a specified stress axis orientation
   Grain Shape - Deviation from spherical grains causes a relaxation in the constraints of the Taylor/Bishop-Hill analysis
2. Precipitate Orientation - Affects the amount of strengthening due to the precipitates

- Conduct compression tests in various orientations on 1100 and 2024 to validate simple model predictions

- Plan to use same modeling and experimental methods for wide panel extrusion when available

Factors Influencing Yield Strength Anisotropy

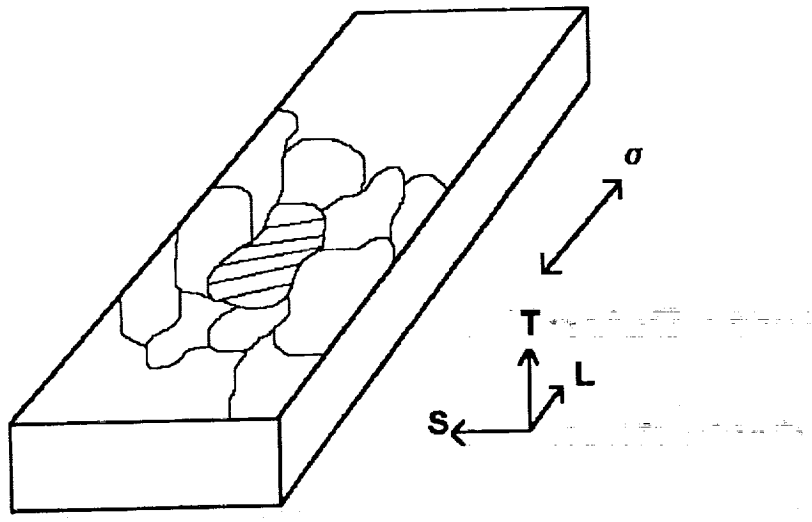

1. Texture: Specified by {plane parallel to LT} <direction parallel to L>

effect on σ_y due to slip plane orientation

2. Grain morphology: Specified by deformation matrix relative to a spherical grain

effect on σ_y due to degree of constraint from neighboring grains

3. Precipitate morphology and properties: Specified by habit plane orientation and precipitate modulus and strength

effect on σ_y due to interaction of precipitates with dislocations

Present models

Plastic Inclusion Model: $\sigma_y = M\tau(1-f) + f\, N\sigma_p$

Elastic Inclusion Model: $\sigma_y = M\tau(1-f) + 2\mu f\,|\gamma|\,\varepsilon^p$

Predicting the Effect of Texture on Anisotropy

- Using pole figure data, generate a weighted grain set representative of the specimen texture
- Calculate the Taylor factor for each of these grains in the tensile direction
- Assuming fully constrained grains, average Taylor factor can be calculated directly
- Elongated grains can relax the constraints on grains resulting in a reduced average Taylor factor

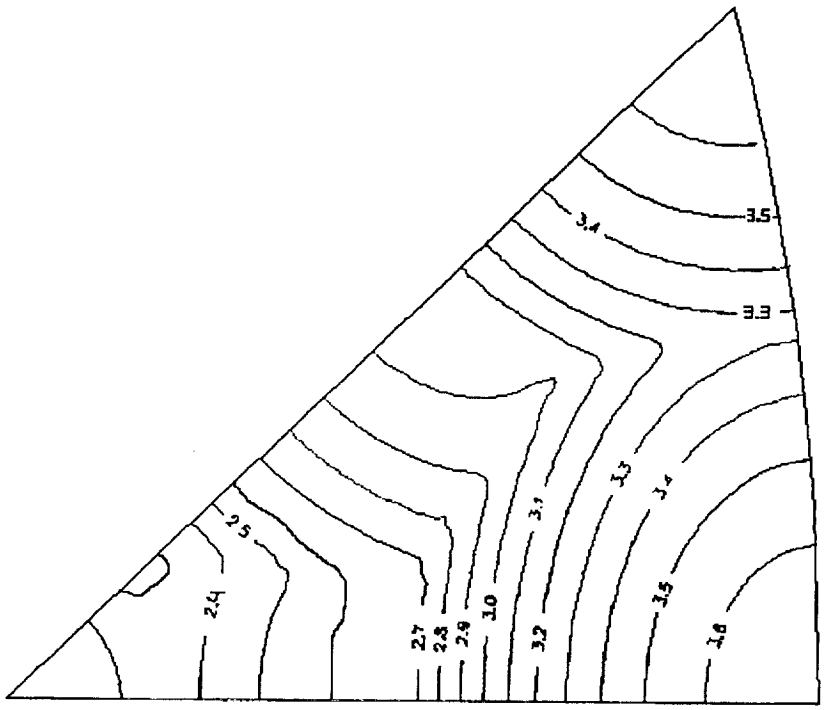

Effect of Orientation and Texture on Taylor Factor

Orientation Dependence of Taylor Factor for Observed Textures

	Angle in LT plane between tensile axis and rolling direction		
Textures	0°	45°	90°
Cube {100} <001>	2.45	3.67	2.45
Goss {112} <111>	2.45	3.52	3.67
Copper {110} <112>	3.06	2.96	3.67
Brass{110}<001>	3.67	2.72	3.67
S {123} <634>	3.18	3.58	2.56
{001}<320>	3.39	2.40	3.39
M(random)	3.07	3.07	3.07
M(rolling)	3.10	2.95	3.10

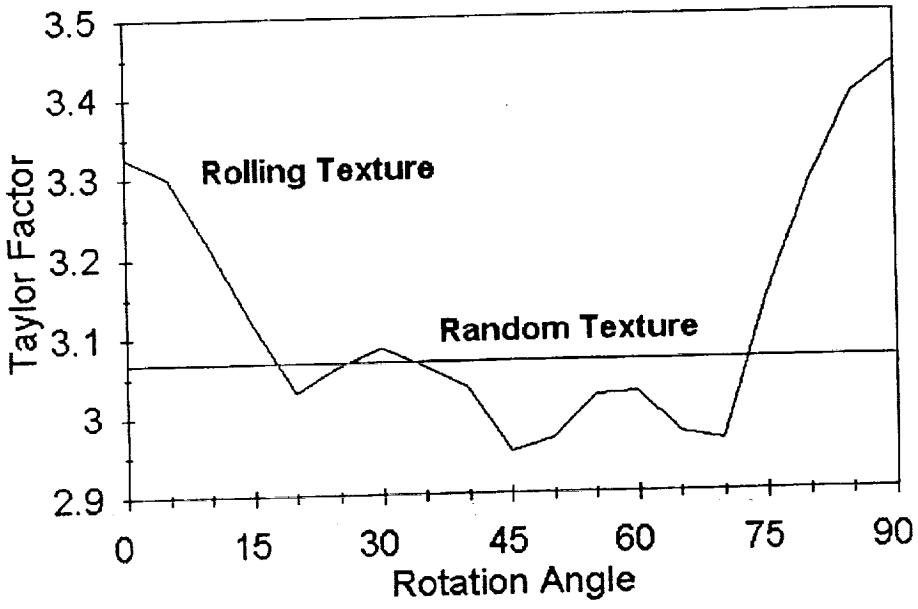

Flow Stress Predictions for the Precipitate Strengthened Condition

Plastic Inclusion Model

- Compatibility between matrix and precipitate is maintained partly by rotation and partly by plastic deformation of the precipitates
- Significant parameter is the ratio of strain in the precipitates to that of strain in the matrix
- May be more appropriate for sheared precipitates

Elastic Inclusion Model

- Assumes an elastic precipitate in a plastically deformed matrix
- Calculates the internal stress field associated with the elastic deformation of the precipitate
- Significant parameter is an accommodation tensor representing the back stress generate in the matrix
- May be more appropriate for looped precipitates

Predicting the Effect of Precipitate Orientation on Anisotropy

Plastic Inclusion Model: $\sigma_y = M\tau(1-f) + f\,N\sigma_p$

- With platelike precipitates, shear strains out of the plane of the precipitate will rotate the precipitate, instead of straining the precipitate
- Because of the possibility of strains in the matrix rotating a precipitate instead of shearing it, the strain in the precipitate will always be less than or equal to the strain in the matrix
- N, the ratio of strain in the precipitate to strain in the matrix is the governing factor of the variation in precipitate strengthening due to stress axis orientation

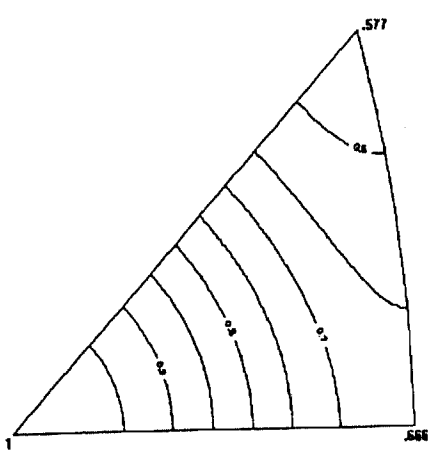

100 precipitates (θ′)

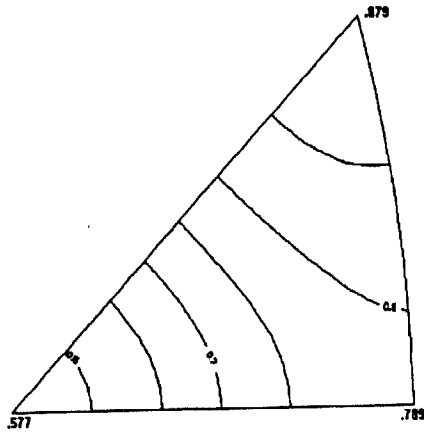

111 precipitates (γ′)

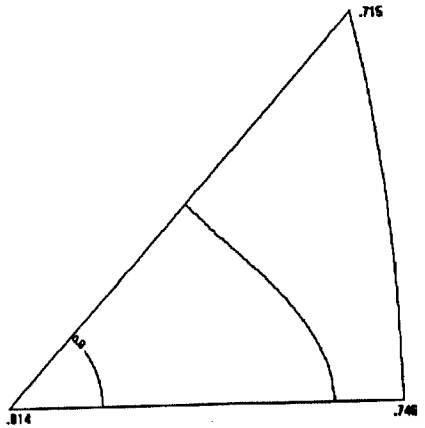

210 precipitates (S′)

N values for three common precipitate planes

Precipitate Plane Dependence of Precipitate Strengthening Ratio for Observed Textures

N: Ratio of strain in precipitate to strain in matrix

Textures	Precipitate Planes		
	100 (θ′)	111 (γ′)	210 (S′)
Cube {100} <001>	1	.58	.81
{110}<110>	.67	.79	.75
Copper {112} <111>	.58	.88	.71
Brass {110} <112>	.70	.81	.74
S {123} <634>	.65	.93	.73
N(random)	.77	.74	.76
N(rolling)	.65	.84	.73

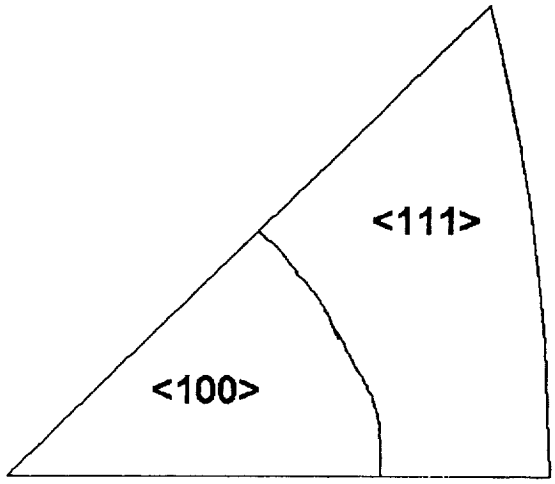

- For a given precipitate habit plane, the greatest strengthening occurs in either the <100> or <111> tensile direction

Compression Testing

- Texture and microstructure vary on a small scale in the extrusions
- Small specimens reduce the likelihood of variations in texture and microstructure in a specimen
- Allows testing in orientations out of the extrusion/rolling plane

Comparison of Predicted and Experimental Yield Strengths for Cold Rolled 1100 Aluminum

Variation of Yield Strength of 1100 Aluminum due to Texture

Angle w/ RD	M	$M\tau(1-f)$
0	2.96	163
15	2.98	164
30	3.02	166
45	3.04	167
60	3.04	167
75	3.03	167
90	3.02	166

$\sigma_y = M\tau(1-f) + f\, N\sigma_p$ $\quad\quad$ $\tau = 55$ MPa

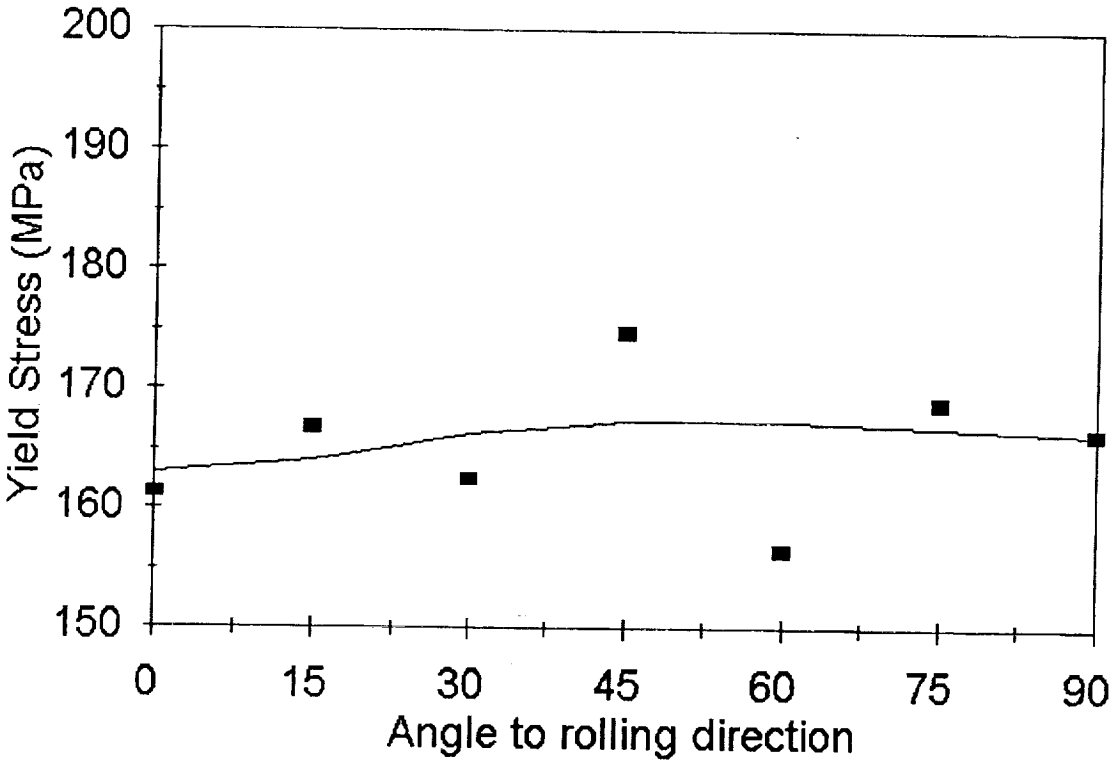

Comparison of Experimental and Predicted Yield Strengths for 2024 Solution Treated

Variation of Yield Strength of 2024 Solutionized due to Texture

Angle w/ RD	M	$M\tau(1-f)$
0	2.98	155
15	2.98	155
30	3.03	158
45	3.04	158
60	3.04	158
75	3.01	156
90	2.99	155

$\sigma_y = M\tau(1-f) + f\, N\sigma_p$ τ= 52 MPa

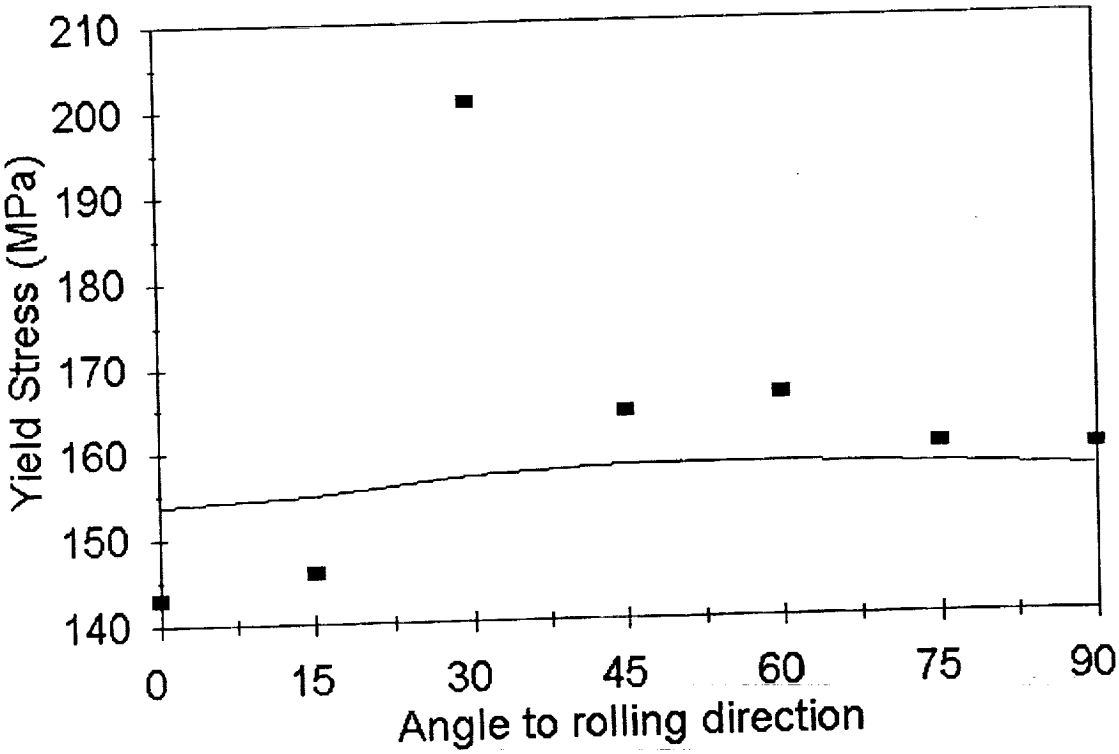

Comparison of Experimental and Predicted Yield Strengths for 2024 Aged

Variation of Yield Strength of 2024 due to Texture (M) and Precipitate Orientation (N)

	M	$M\tau(1-f)$	N	$f\,N\sigma_p$	σ_y
0	2.96	154	.760	81	235
15	2.98	155	.749	80	235
30	3.02	157	.770	82	239
45	3.04	158	.753	80	238
60	3.04	158	.755	80	238
75	3.03	158	.753	80	238
90	3.02	157	.757	81	238

$\sigma_y = M\tau(1-f) + f\,N\sigma_p$ $\quad \tau(1-f) = 52$ MPa $\quad f\,N\sigma_p = 106$MPa

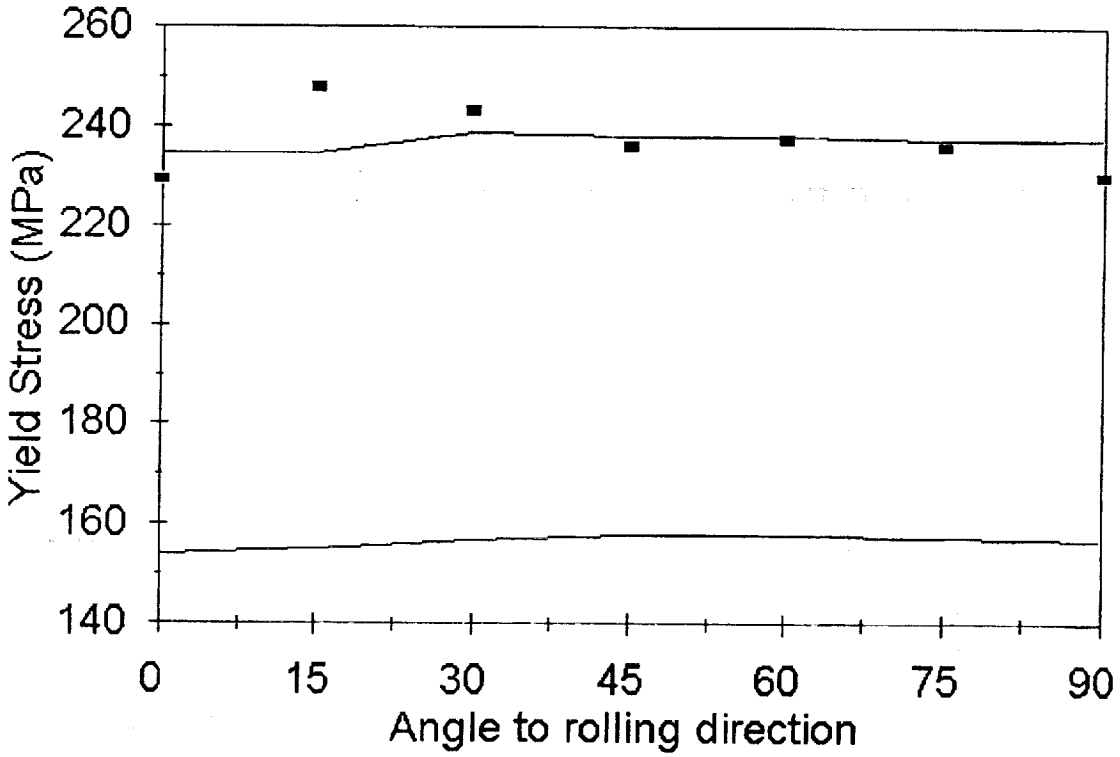

Conclusions

- Using texture and precipitate orientation information, the orientation dependence of average Taylor factor and precipitate strengthening contribution can be determined.

- Initial models accurately predict the variability of yield strength in 1100 and 2024 alloys. With more complete data, accurate prediction of the yield strength anisotropy of more complex systems should be achieveable.

Future Work

- Use modeling and experimental methods developed on 1100 and 2024 alloys to investigate the yield strength anisotropy of wide panel extrusions in greater detail

- Develop the elastic inclusion model

- Confirm the reliability of the inclusion models using an alloy with precipitates on other habit planes

- Experimentally characterize the effect of grain shape on yield strength and Taylor Factor

Wide Panel Extrusions

Reynolds/Alcoa/UVa

- Concept: Fabricated by extrusion of a tube with integral stiffeners
  Tube is slit and flattened
  Result is a flat panel with integral longitudinal stiffeners

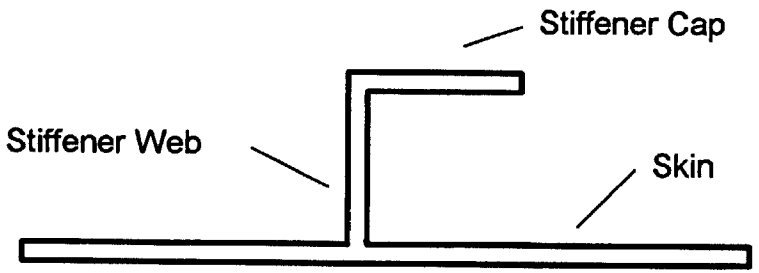

- Status: Ten panels have arrived in Pittsburgh
  Panels are in the process of being shipped to McCook facility to check chemical composition and temper condition

- Alloys: Five panels 2195 (Al - 4.1Cu - 0.9Li - 0.4Mg - 0.3Ag - 0.12Zr)
  Five panels 2096 (Al - 2.7Cu - 1.6Li - 0.6Mg - 0.4Ag - 0.12Zr)

Project #8 PRECIPITATION HARDENING AND MICROSTRUCTURAL STABILITY IN Al-Si-Ge AND Al-Si-Ge-Cu ALLOYS

H.J. Koenigsmann and E.A. Starke, Jr.

Objectives

The objectives of this project are to investigate the thermal stability and the mechanical properties of recently developed Al-Si-Ge and Al-Si-Ge-Cu alloys.

Current Status

The coarsening behavior of SiGe diamond structure precipitates in ternary Al-Si-Ge and quaternary Al-Si-Ge-Cu alloys aged at 120°C and 160°C has been investigated using Transmission Electron Microscopy (TEM). Tensile tests have been performed at room temperature and the volume fraction of voids in a ternary Al-Si-Ge alloy has been determined as a function of strain and aging time through a pycnometer by measuring densities of the deformed gage section and the grip part.

Important Findings

The relationship between the cube of the average radii of the SiGe precipitates in both the ternary and the quaternary alloys and the aging time at 120°C and 160°C is linear as predicted by the coarsening theory by Lifshitz and Wagner. The difference between the average diameters of the SiGe precipitates in the ternary and quaternary alloys at a given aging time and temperature is well within the errors of measurement suggesting that the presence of Cu has no significant effect on the nucleation and coarsening of the SiGe precipitates. The estimated precipitate-matrix interfacial free energy of $400 mJm^{-2}$ to $800 mJm^{-2}$ is in the expected range.

The experimentally determined yield strength of all peak-aged alloys agrees well with the theoretical upper limit described by the modified Orowan equation. A significant increase of the yield strength can be achieved by choosing the composition in such a way that the atomic size misfit is

compensated after the formation of pairs of Si and Ge.

The volume fraction of voids determined in a ternary alloy decreases with increasing aging time, i.e. increasing diameter of the SiGe precipitates, at a given true strain value. Higher void volume fractions are observed at higher tensile ductilities corresponding to shorter aging times. The critical strain to nucleate cavities determined from the experimental data by linear regression corresponds approximately to the theoretical prediction of the cavity nucleation model developed by Brown and Stobbs based upon an energy criterion. However, the experimental data for the overaged alloys suggest that the critical strain is not independent of the particle size as predicted by this energy criterion, but increases linearly with particle size in agreement with a stress criterion by Brown and Stobbs.

Future Work

In order to understand the separate effects of void nucleation and growth, void density and void size measurements will be performed as a function of strain and aging time using Scanning Electron Microscopy (SEM). Furthermore, the experimental data for the void volume fractions as a function of strain and aging time will be analyzed in more detail using the finite element method.

Presentation Viewgraphs

1. Topics.
2. Background.
3. Objectives.
4. Experimental Procedure. Composition of alloys.
5. Experimental Procedure. Heat treatments, quantitative TEM measurements, tensile tests, and pycnometer measurements.
6. TEM Micrograph. The microstructure of the quaternary alloy aged for 16 days at 160°C shows SiGe precipitates and θ' (Al_2Cu) plates. <001> Al orientation.

7. Coarsening. The theory of Lifshitz and Wagner predicts that, when the rate of coarsening is controlled by the diffusion of solute species through the matrix, the cube of the average particle radius increases linearly with aging time.

8. Experimental Coarsening Data (120°C). The agreement between the data and the prediction by Lifshitz and Wagner is good. Cu seems to have no significant effect on the nucleation and coarsening of the SiGe precipitates. The precipitate-matrix interfacial free energy (Y) estimated from the experimental data is in the expected range.

9. Experimental Coarsening Data (160°C). The agreement between the data and the prediction by Lifshitz and Wagner is good. Cu seems to have no significant effect on the nucleation and coarsening of the SiGe precipitates. The precipitate-matrix interfacial free energy (Y) estimated from the experimental data is in the expected range.

10. Results of Tensile Tests. The increase of the yield strength of the third alloy by a factor of about 1.4 as compared to the first alloy is due to a decrease of the average precipitate diameter from 8.0nm to 5.0nm. The decrease of the precipitate diameter has been achieved by choosing the composition of the third alloy in such a way that the atomic size misfit cancels.

11. Modified Orowan Equation. The experimentally determined yield strength is for all peak-aged alloys in good agreement with the theoretical upper limit described by the modified Orowan equation.

12. Cavity Nucleation Models. Brown and Stobbs developed two models to describe cavity nucleation: the one based upon an energy criterion predicts that the critical strain to nucleate cavities is independent of the particle size, whereas the one based upon a stress criterion predicts that the critical strain increases linearly with particle size.

13. Cavity Nucleation. The correction factor takes into account that cavities nucleate at particle poles in the direction of the tensile axis.

14. Experimental Coarsening Data. The precipitate-matrix interfacial free energy (Y) estimated from the experimental data is a parameter in the above mentioned energy criterion by Brown and Stobbs.

15. Results of Tensile Tests. With increasing aging time, the tensile ductility decreases significantly, whereas the decrease of both the yield strength and the tensile strength is almost negligible contrary to the prediction of the modified Orowan equation.

16. Determination of Void Volume Fractions. The volume fraction of voids as a function of strain and diameter of the SiGe precipitates has been determined through a pycnometer by measuring densities of the deformed gage section and the grip part. The void volume fraction decreases with increasing particle diameter at a given true strain value. The critical strain to nucleate cavities (ϵ_c) has been determined from the experimental data by linear regression.

17. Comparison between Cavity Nucleation Models and Experimental Data. The critical strain to nucleate cavities determined from the experimental data agrees approximately with the prediction of the energy criterion by Brown and Stobbs. However, the experimental data suggest that the critical strain is not independent of the particle size as predicted by this criterion, but increases linearly with particle size in agreement with the stress criterion by Brown and Stobbs.

18. Comparison between Stress Criterion and Experimental Data. The experimental data agree well with the stress criterion by Brown and Stobbs if the critical stress is chosen as $\mu_p/50$, where μ_p is the shear modulus of the SiGe particles.

19. Conclusions.

20. Future Work.

Al-Si-Ge Alloy Development

H.J. Koenigsmann and E.A. Starke, Jr.
Department of Materials Science and Engineering
University of Virginia

Topics

* Background and Objectives
* Experimental Procedure
* Coarsening of SiGe Precipitates (120°C, 160°C)
* Tensile Properties
* Void Volume Fraction (Strain, SiGe Diameter)
* Conclusions
* Future Work

Background

* Uniform distribution of very small diamond structure SiGe particles
* High degree of hardening for a small volume fraction of particles
* Low solubility of both Si and Ge in Al results in better thermal stability than other age-hardenable aluminum alloys
* Low strength of ternary Al-Si-Ge alloys can be increased by about 60% by the addition of less than 2.5wt.% Cu

Objectives

* Investigate the thermal stability of ternary Al-Si-Ge and quaternary Al-Si-Ge-Cu alloys: coarsening of SiGe precipitates, comparison of experimental data with theory by Lifshitz and Wagner, effect of Cu
* Investigate and improve the tensile properties of the ternary and quaternary alloys
* Investigate cavity nucleation and growth in a ternary Al-Si-Ge alloy:
  volume fraction of voids as a function of strain and diameter of the SiGe precipitates, comparison of experimental data with cavity nucleation models, theoretical analysis of experimental data

Chemical Composition of Alloys

No.	Alloy	Composition (at.%)					
		Si	Ge	Cu	Mg	Mn	Al
1	Al-1.02Si-0.95Ge	0.99	0.36	--	--	--	Balance
2	Al-1.00Si-0.99Ge-2.57Cu	0.98	0.38	1.12	--	--	Balance
3	Al-0.55Si-2.02Ge	0.54	0.76	--	--	--	Balance
4	2014-T4	0.84	--	1.95	0.57	0.40	Balance

Experimental Procedure

* Homogenization: 30hrs at 500°C (ternary alloys) or 490°C (quaternary alloy) based on DSC
* Hot rolling: at 300°C to 350°C to 2mm sheets
* Solution heat treatment: 1hr at 490°C (ternary alloys) or 480°C (quaternary alloy)
* Cold water quenching
* Aging: up to 60 days at 120°C and up to 16 days at 160°C in air furnaces
* TEM: Philips EM 400T - quantitative stereology, correction for truncation and overlap, CBED
* Tensile Tests: 810 MTS - according to ASTM standard E8-91, strain rate of $10^{-3}s^{-1}$
* Pycnometer measurements: $V_f = (\rho_g - \rho_n)/\rho_g$

  V_f - volume fraction of voids

  ρ_g - density of the grip part

  ρ_n - density of the deformed gage section (neck)

Al-1.00Si-0.99Ge-2.57Cu (wt.%)

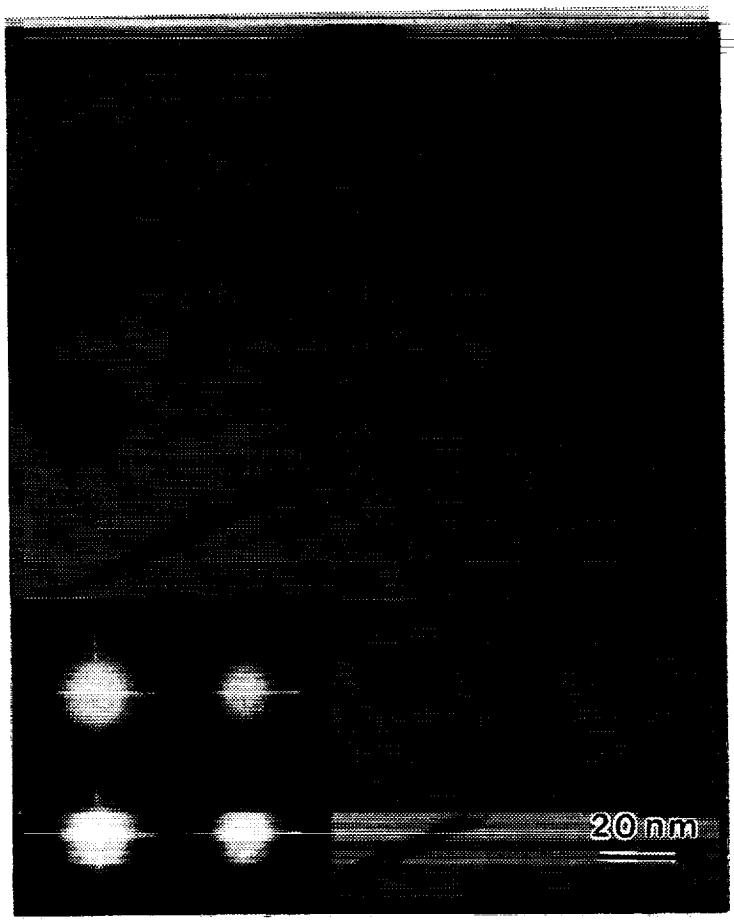

The microstructure of the quaternary alloy at a magnification of 500,000 times after aging for 16 days at 160°C: SiGe precipitates and θ' (Al_2Cu) plates. <001> Al orientation.

Coarsening Theory (Lifshitz & Wagner)

$$r^3 - r_o^3 = 8\gamma D c_o V_m^2 (t - t_o)/9RT$$

r - mean particle radius

r_o - initial mean particle radius

γ - precipitate-matrix interfacial free energy

D - diffusivity of the solute species in the matrix

c_o - equilibrium concentration of solute species

V_m - molar volume of the precipitate

t - time

t_o - time when coarsening commences

R - gas constant

T - temperature

Coarsening of Diamond Precipitates in Al-Si-Ge/Al-Si-Ge-Cu at 120°C

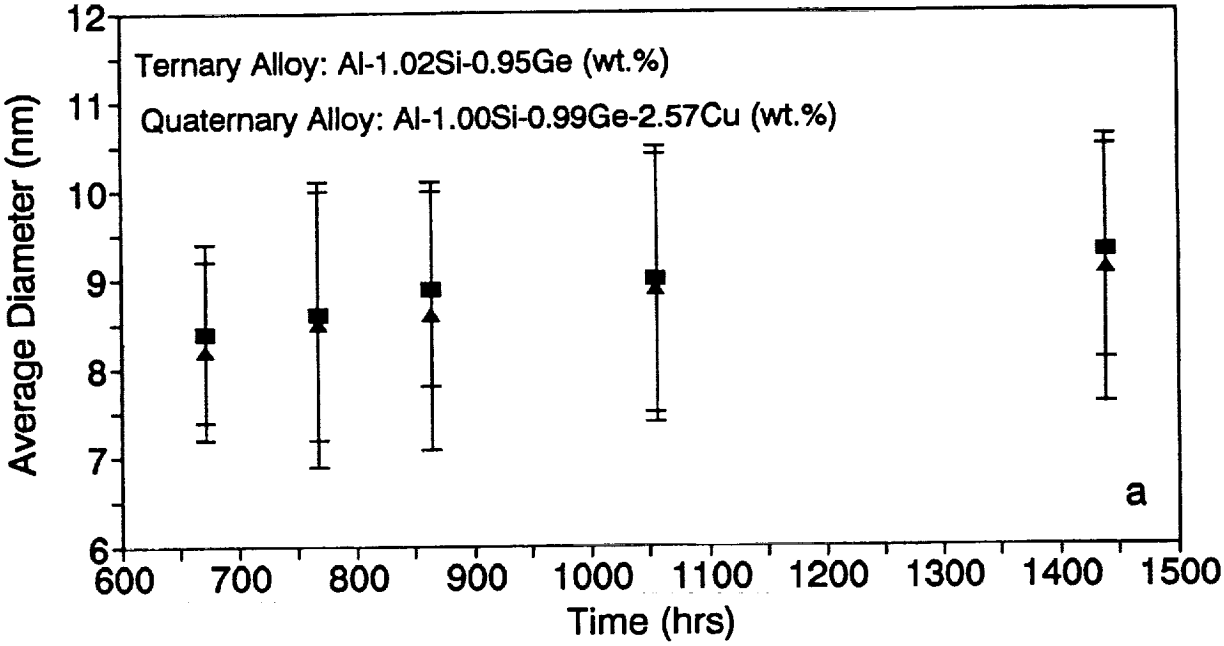

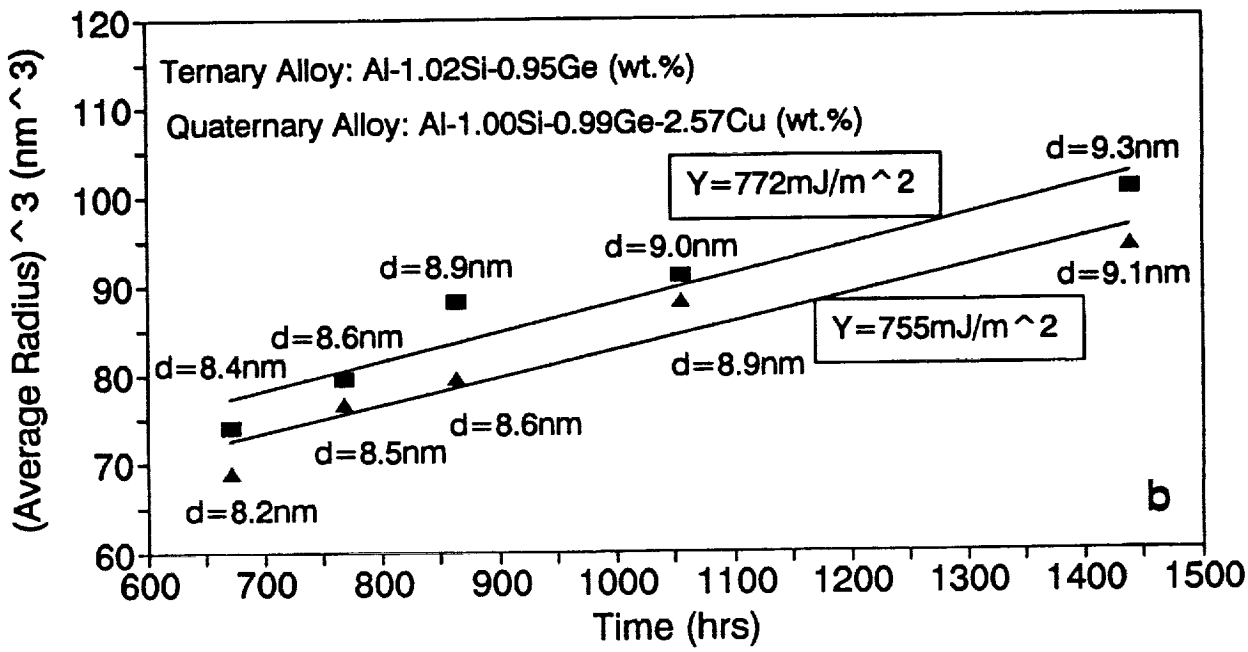

Corrected for truncation and overlap.

▲ Ternary Alloy ■ Quaternary Alloy

Coarsening of Diamond Precipitates in Al-Si-Ge/Al-Si-Ge-Cu at 160°C

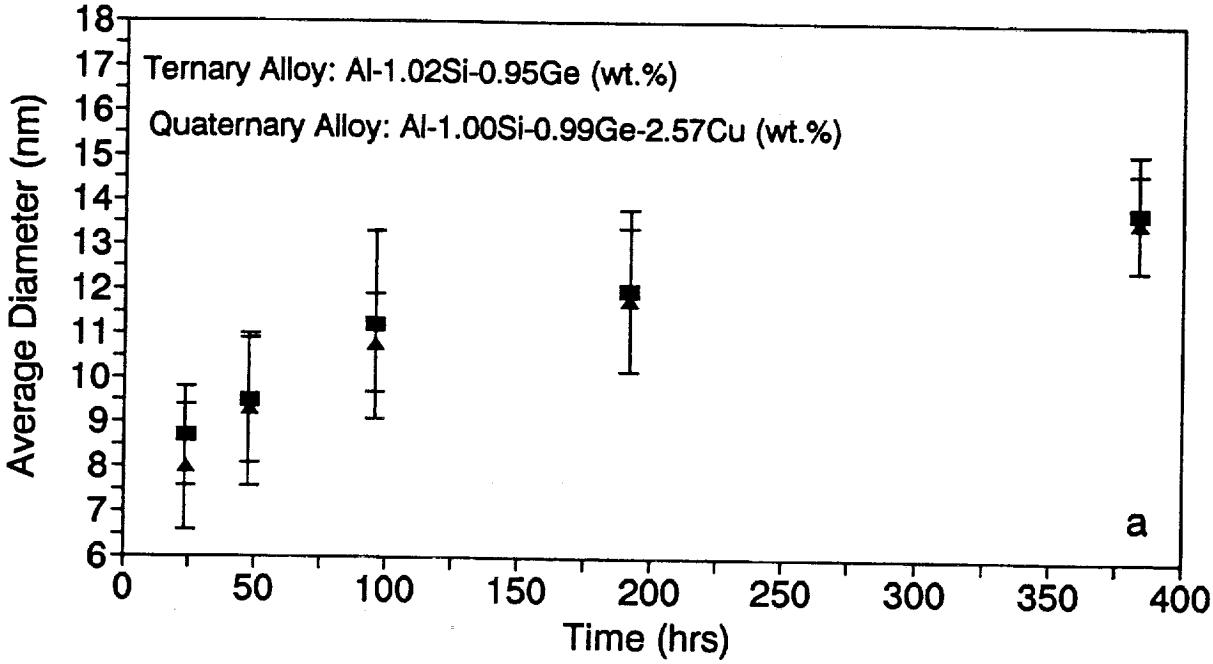

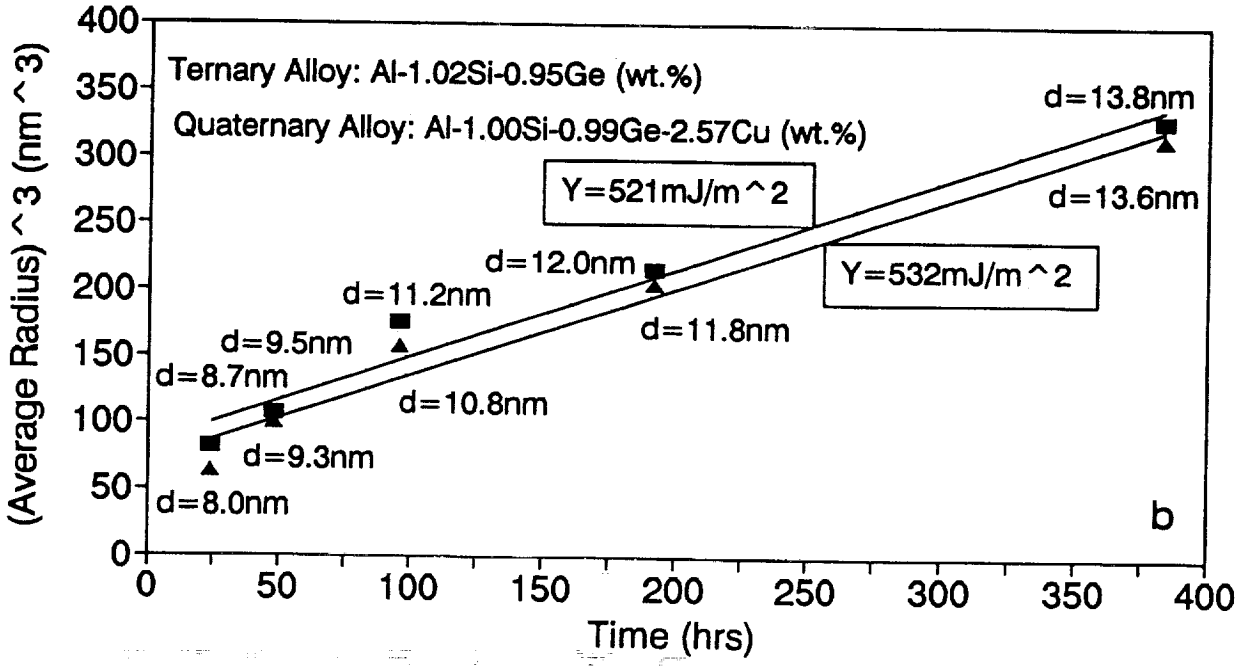

Corrected for truncation and overlap.

▲ Ternary Alloy ■ Quaternary Alloy

Comparison of Tensile Properties

Alloy	$\Delta\sigma_p^*$ (Mpa)	σ_y^* (MPa)	σ_{TS}^* (MPa)	ϵ_f^* (%)
Al-1.02Si-0.95Ge	77	73	137	24
Al-1.00Si-0.99Ge-2.57Cu	76	168	280	10
Al-0.55Si-2.02Ge	112	105	164	17
2014-T4	--	344	486	21

* $\Delta\sigma_p$ - theoretical contribution of SiGe particles to the yield strength, σ_y - yield strength, σ_{TS} -tensile strength, ϵ_f - strain after fracture

Strain rate: $10^{-3}s^{-1}$
Orientation of first three alloys: 0° to rolling direction
The first three alloys were peak-aged at 160°C.

Modified Orowan Equation

$\Delta\sigma_p \approx \mu b\sqrt{f/d}$

$\Delta\sigma_p$ - particle contribution to the yield strength

μ - shear modulus of the matrix (26GPa)

b - Burgers vector (0.284nm)

f - volume fraction of the particles

d - particle diameter

Cavity Nucleation Models (Brown & Stobbs)

Energy Criterion:

$\Delta E_{el} + \Delta E_s \leq 0 \Rightarrow \epsilon_c \geq \gamma(1-\cos\theta)/2\mu_p b\sin^2\theta$

ΔE_{el} - internal elastic energy of the particle

ΔE_s - energy increase in forming new surfaces

ϵ_c - critical strain for cavity nucleation

γ - precipitate-matrix interfacial free energy

θ - geometrical correction

μ_p - shear modulus of the particle

b - Burgers vector

Stress Criterion:

$\sigma_c \approx 4.2\alpha\mu_p b\sqrt{\rho}$, $\rho \approx 3.4\epsilon_c/db \Rightarrow \epsilon_c \geq \sigma_c^2 d/60\alpha^2\mu_p^2 b$

σ_c - critical stress ($\mu_p/50$ for Fe-Fe_3C)

α - numerical parameter (1/7)

ρ - local dislocation density

d - particle diameter

Cavity Nucleation

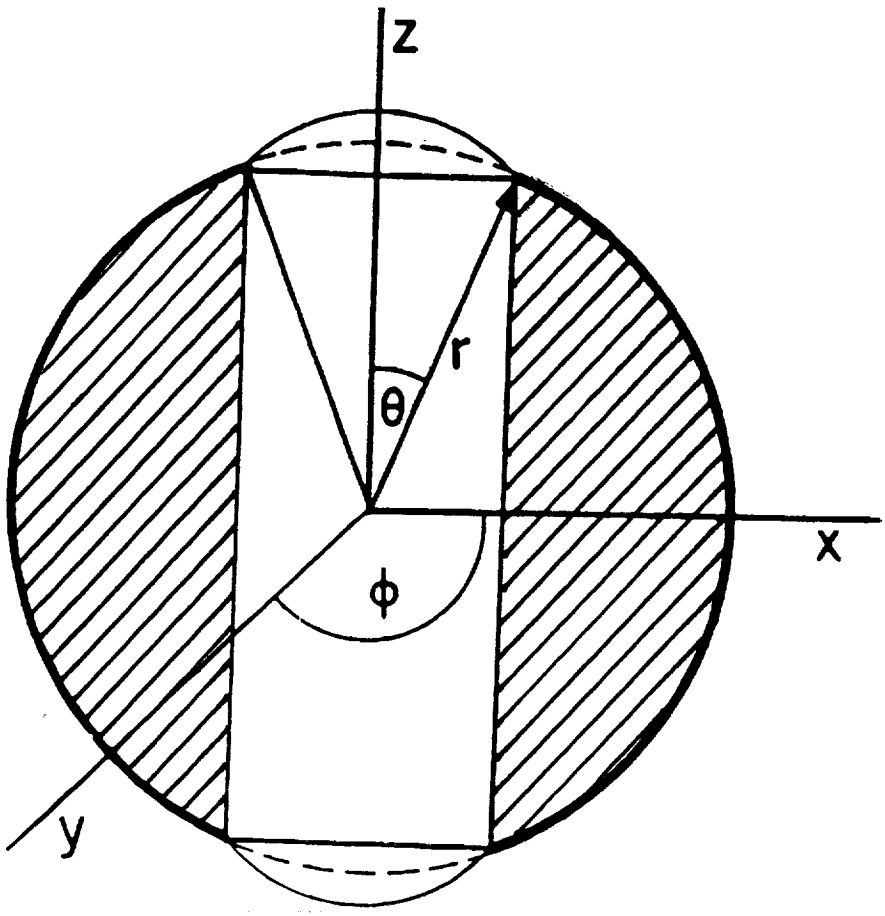

The internal surfaces are formed from only a small fraction of the particle-matrix interface. Elastic energy release occurs from the cylinder bounded by the cavity caps. The resulting correction factor is $(1-\cos\theta)/4\sin^2\theta$.

Coarsening of Diamond Precipitates in Al-0.55Si-2.02Ge (wt.%) at 160°C

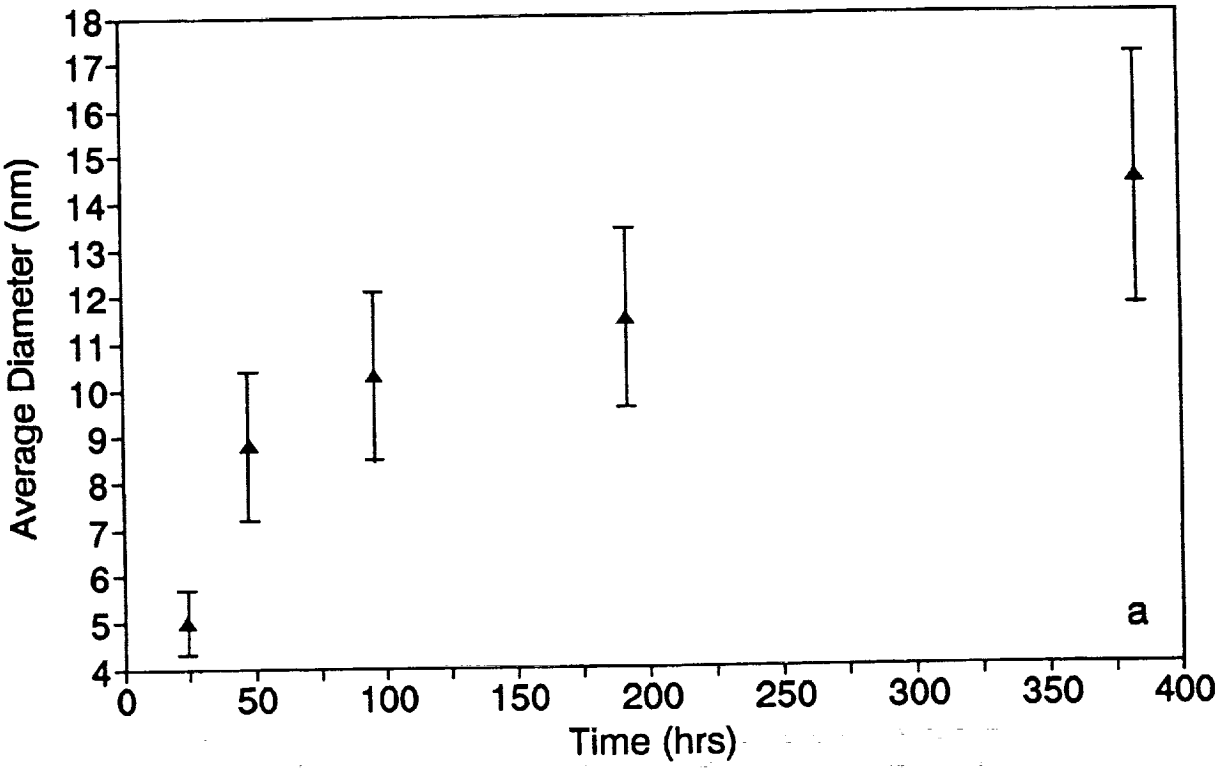

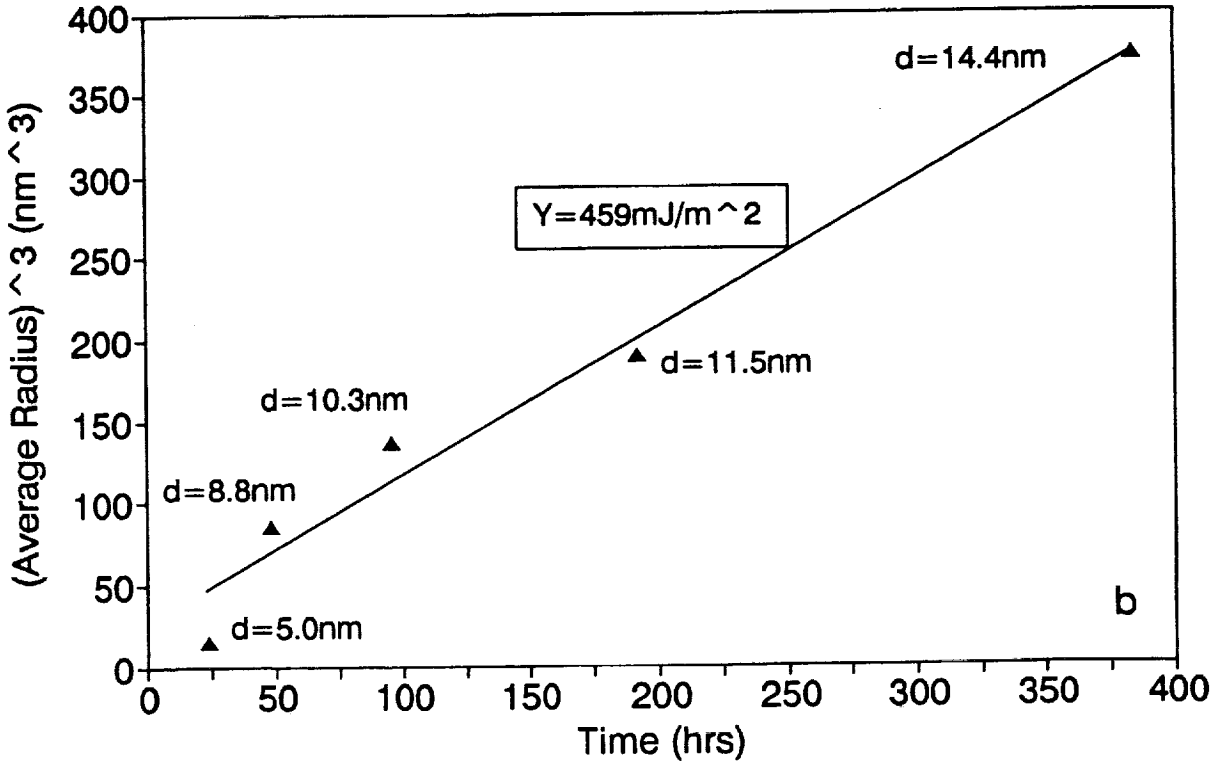

Corrected for truncation and overlap.

Tensile Tests (Al-0.55Si-2.02Ge (wt.%))

Aging Time (d)	σ_y^* (MPa)	σ_{TS}^* (MPa)	ϵ_f^* (%)
1	105	164	17
2	103	162	16
4	100	158	13
8	100	155	9
16	94	153	9

* σ_y - yield strength, σ_{TS} - tensile strength, ϵ_f - strain after fracture

Strain rate: 10^{-3} s^{-1}
Orientation: 0° to rolling direction

Determination of Void Volume Fraction

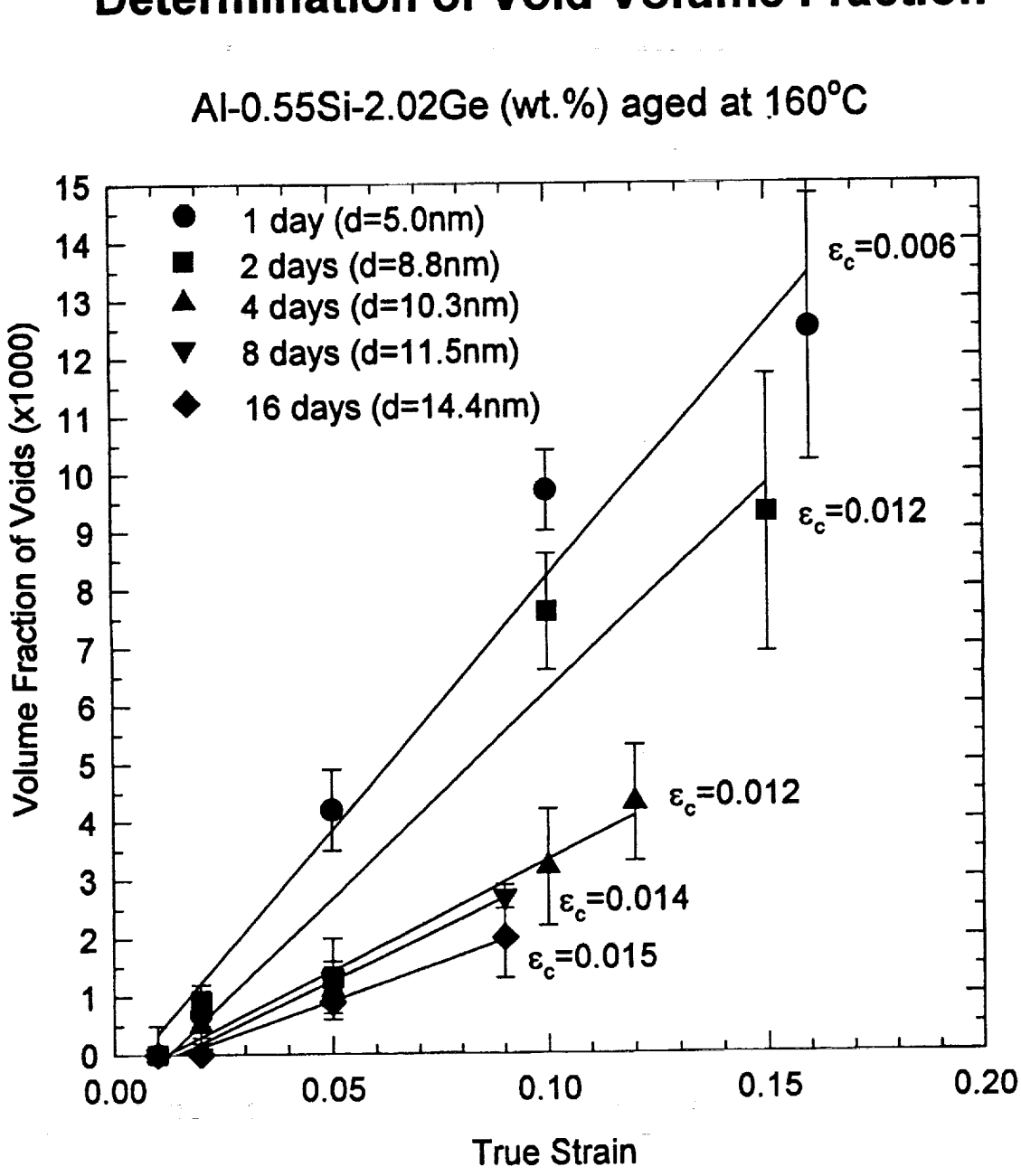

Evaluation of Cavity Nucleation Models

Energy Criterion (Brown & Stobbs):

$\epsilon_c \geq 0.012$ independent of particle size

using $\gamma = 459 mJm^{-2}$, $\theta = 15^o$,

$\mu_p = 34GPa$, $b = 0.284nm$

experimental data between 0.006 and 0.015, but

<u>not</u> independent of the particle size

Stress Criterion (Brown & Stobbs):

$\epsilon_c \geq 0.00115 nm^{-1} \times d$

using $\sigma_c = \mu_p/50$, $\alpha = 1/7$, $b = 0.284nm$

linear dependence on particle size in agreement with experimental data, but quantitative agreement difficult to evaluate

Comparison of Stress Criterion with Experiment

Al-0.55Si-2.02Ge (wt.%) aged at 160°C

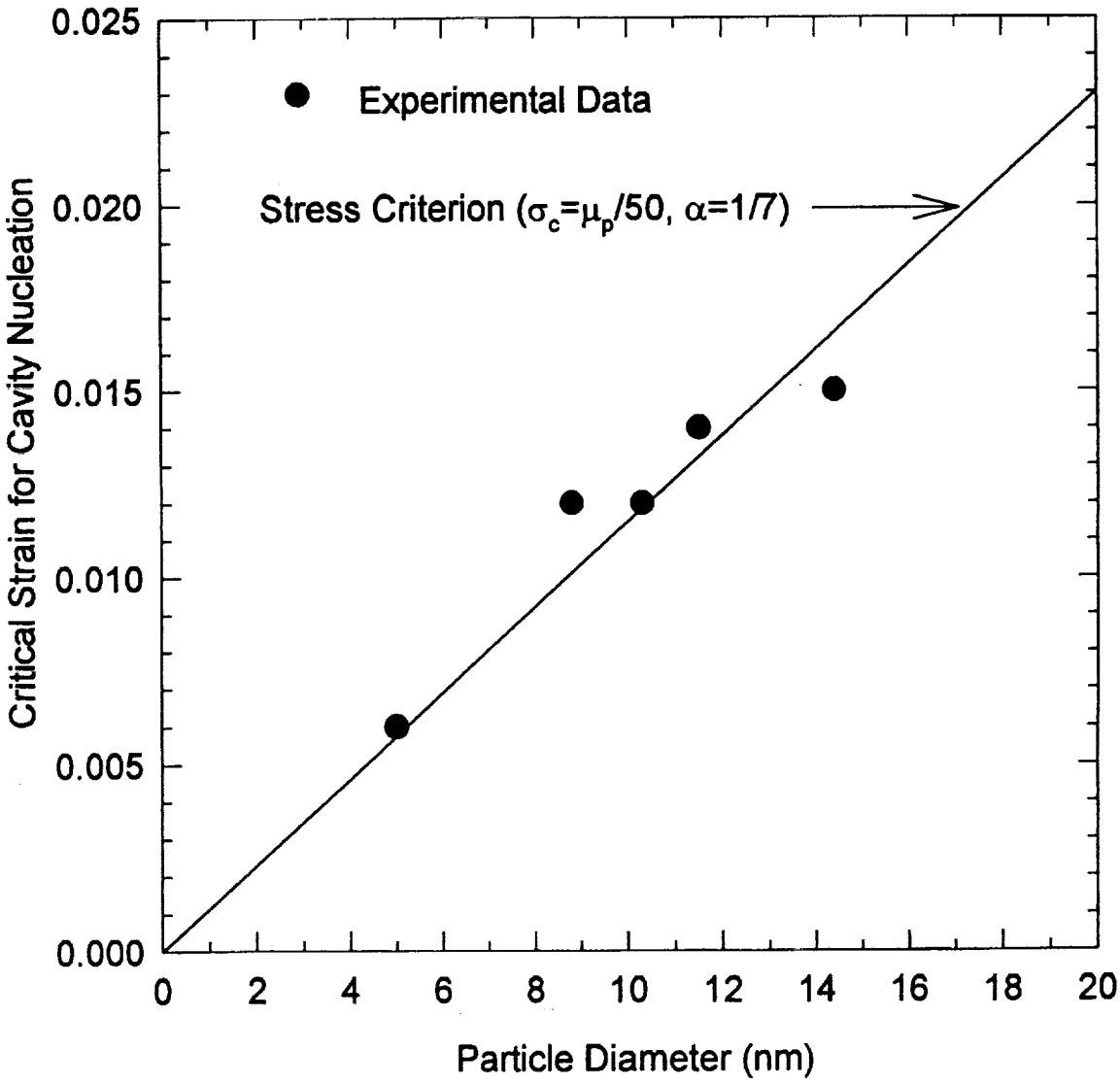

Conclusions

* Linear dependence between the cube of the radii of the SiGe precipitates (in both the ternary and the quaternary alloys) and the aging time at 120°C and 160°C as predicted by Lifshitz & Wagner
* Presence of Cu has no significant effect on the nucleation and coarsening of the SiGe precipitates
* Agreement between experimentally determined yield strength and Orowan equation only for peak-aged alloys
* Volume fraction of voids determined in a ternary alloy decreases with increasing diameter of the SiGe precipitates at a given true strain value
* Critical strain to nucleate cavities determined from the experimental data by linear regression increases linearly with particle size in agreement with the stress criterion by Brown & Stobbs

Future Work

* Perform void density and void size measurements as a function of strain and aging time in order to understand the separate effects of void nucleation and growth, analyze the experimental data
* Analyze the experimental data for the void volume fractions as a function of strain and aging time in more detail using the finite element method

Project #9 Environmental Effects in Fatigue Life Prediction: Modeling Crack Propagation in Light Aerospace Alloys

Mark E. Mason, Edward Richey III, Zuhair Gasem and Richard P. Gangloff

Objectives

The objective of this project is to establish data and models for estimating and ultimately predicting environment enhanced fatigue crack propagation (FCP) kinetics for light aerospace structural alloys, particularly titanium and high strength aluminum alloys. This work is necessary to enhance computer-based fatigue life prediction codes such as NASA-FLAGRO.

As outlined in the 1993 renewal proposal, there are four approaches to this goal. One task is focusing on improved linear superposition predictions of FCP in the AA7075/aqueous NaCl system. A second study emphasizes environment-crack closure interaction effects which govern the complex shape of FCP rate versus stress intensity range laws in Ti-6Al-4V. A third program is focused on environmental FCP in advanced 7000 series alloys and on mechanistic modeling of crack tip damage. The fourth task is considering empirical interpolation models of environmental fatigue crack propagation kinetics, with emphasis on the titanium/NaCl system. The first and fourth tasks will continue through 1994, as Messrs Mason and Richey achieve the MS degrees in the late Fall to Winter of this year. The second project was terminated at the beginning of this reporting period. The third program was initiated in January of 1994, upon the arrival of a new graduate student, Mr. Zuhair Gasem. Only the first and fourth programs are reported here.

Project #9A Time-dependent Chloride Environmental Fatigue Crack Propagation in AA7075

Mark E. Mason and Richard P. Gangloff

Objective

The objectives of this research on an SCC-susceptible 7000-series aluminum alloy in aqueous chloride are four-fold: (1) to test static load or displacement-based linear superposition predictions of da/dN vs ΔK and frequency, (2) to determine if quasi-static load stress corrosion crack growth rates are affected sufficiently by crack tip strain rate to enable improved linear superposition predictions of da/dN, (3) to measure the frequency, load waveform and hold-time dependencies of environmental FCP da/dN, and (4) to speculate on the metallurgical and electrochemical origin(s) of the variability in the time-dependence of environmental FCP in 7000 series aluminum alloys. The output of this work will be improved data and understanding on time-cycle-dependent EFCP kinetics for use in NASA-FLAGRO.

Current Status

Constant load/displacement, monotonically rising load, and ripple load experiments are conducted with a cracked fracture mechanics specimen to determine the stress intensity and crack tip strain rate dependencies of da/dt_{scc}. Computer-automated constant ΔK and ΔK-decreasing experiments are employed to determine da/dN as a function of loading frequency, waveform and hold-time.

The experimental work for 7075-T651 in acidified chloride was completed during this reporting period. The results of work prior to May, 1994 were presented to the FAA/NASA International Conference on Ageing Aircraft, and are being published in the conference proceedings as "Modeling Time-Dependent Corrosion Fatigue Crack Propagation in 7000 Series Aluminum Alloys". The graduate student, Mr. Mark E. Mason, will complete

and defend his Master's of Science thesis in September. A paper reporting the complete findings and observations is planned for journal publication.

Recent Results

Fatigue crack propagation rates for 7075-T651 (S-L orientation) in chromate inhibited, acidified NaCl solution are enhanced five to ten-fold over rates in moist air and are over an order of magnitude faster compared to fatigue cracking in helium. Measured time-based crack growth rates for 7075-T651 (S-L), subjected to quasi-static load or displacement, are an order of magnitude too small to predict the effect of NaCl on FCP rates for loading frequencies above 0.001 Hz and by linear superposition. Alternate methods of establishing da/dt, based on enhanced crack tip strain rate, do not provide a means of enabling linear superposition modeling of EFCP in peak-aged 7075/NaCl. Imposed constant crack mouth opening displacement rate does not accelerate da/dt. Da/dt is not enhanced by high frequency-low amplitude cyclic loading, designed to increase crack tip surface strain rate, in conjunction with a high sustained stress intensity.

Crack propagation rates for corrosion fatigue of 7075-T651 (S-L) in NaCl show two regimes of frequency (f) dependence; da/dN is proportional to f^{-1} below 0.001 Hz, and is proportional to $f^{-\lambda}$, where λ is between 0 and 0.1, for frequencies above 0.001 Hz. Da/dN and da/dN_{CF} increase mildly with increasing rise-time for a range of loading waveforms, but may not depend on hold-time at K_{MAX}. The strong frequency dependence (f^{1}) is modeled based on simple linear superposition, while the mild time-dependence (f^{λ}) is due to cycle-time-dependent corrosion fatigue.

The NaCl environmental effect on time-cycle-dependent fatigue crack growth is identical for the S-L and L-T orientations of peak aged 7075, suggesting a minimal involvement of anisotropic high angle grain boundaries. The frequency response of EFCP in 7000 series alloys is variable and depends on an undefined compositional or microstructural variable. Crack solution cations, from segregant or a second phase in the alloy, could alter hydrogen production kinetics, or H diffusion within the crack tip process zone could

C-4

vary based on dislocation and grain boundary processes. High hydrogen production/uptake and rapid hydrogen diffusion favor f-independent cracking persisting to higher frequencies and crack growth rates.

EFCP in the 7075/NaCl system is adequately described for computer life prediction by linear superposition for long load-cycle periods, and by a time-independent upper bound relationship between da/dN and ΔK for moderate frequencies and load rise-times.

Presentation Graphics Captions

1. Title

2. Program objectives and current work.

3. Mechanical properties and representative microstructure of AA7075-T651.

4. Schematic of environmental testing set-up.

5. Models to quantitatively predict environmental fatigue crack propagation have been developed from several perspectives, however, each has its limitations. The linear superposition model has been shown by this work to have limited use for AA7075/NaCl; this approach is accurate for loading frequencies below 0.001 Hz.

6. Stress corrosion crack velocity (da/dt_{scc}) vs stress intensity (K) for cracking susceptible 7075-T6 (S-L) fully immersed in aqueous chloride. Points represent the results of the current work, while the lines are published results for 1N NaCl (Le and Foley), NaCl at pH 2 (Thompkins et al.), and neutral 3.5% NaCl (Holroyd).

7. The superposition model was integrated numerically to yield predicted EFCP rates that are shown here for fixed frequencies between 0.01 Hz and 20 Hz with K varying sinusoidally as a function of time. These predictions are compared with corrosion fatigue data generated with sinusoidal loading at 5 Hz.

8. Effect of frequency on corrosion fatigue crack propagation in 7000-T6 series aluminum alloys in aqueous chloride. This plot presents the results from several investigations of EFCP in 7000 series aluminum alloys, fully immersed in aqueous chloride: 7079 and 7075-T73 (Speidel); 7017 (Holroyd and Hardie); 7475 (Green and Knott); and 7075 (Rechberger).

9. Two reasons why linear superposition fails to predict environmental FCP kinetics for AA7075-T651/NaCl.

10. Conclusions from dynamic load testing to increase crack tip strain rate. The results of this study show that various forms of increased crack tip strain rate do not exacerbate da/dt for 7075-T6 (S-L) in chloride.

11. K_{th} versus crack mouth opening displacement rate (CMOD) showing results for 7075-T651 in air and chloride for comparison with results for 2024 (after Dietzel and Schwalbe) in chloride. K_{th} does not decrease, and da/dt does not increase, with increasing CMOD rate.

12. Crack length versus time showing the results of constant-K (11 to 13 MPa$\sqrt{m}$) loading, with and without applied small amplitude ripple loading (ΔK = 0.7 MPa$\sqrt{m}$ at first 5 Hz then 30 Hz). Da/dt does not increase in response to the application of the small amplitude cyclic load.

13. EFCP da/dN versus cycle hold time at K_{MAX} for constant applied ΔK (15 and 9 MPa$\sqrt{m}$) for 7075-T651 (S-L) in aqueous chloride solution at a stress ratio of 0.1.

14. Effect of sine-wave loading frequency on EFCP da/dN at two applied ΔK levels (15 and 9 MPa$\sqrt{m}$), showing a mild time-cycle dependency. These results confirm results from other investigators (Fig 8., Rechberger). Linear superposition cannot account for this time-cycle dependence.

15. Summary of da/dN versus frequency data for peak aged 7000 series aluminum alloys, comparing extensive da/dN results from this investigation with published trends in frequency dependence.

16. Schematic showing two time-cycle dependencies of environmental da/dN at a single ΔK for 7000 series aluminum alloys. The important issue is why the critical frequency for time-cycle dependent environmental cracking depends on alloy composition and/or microstructure.

17. The time-cycle dependence of environmental fatigue crack growth in 7000 series alloys can be modeled based on hydrogen diffusion, over a distance (Δa) and a number of cycles (ΔN), with $da/dN = \Delta a/\Delta N$. f_{Crit} represents the critical loading frequency above which hydrogen diffusion in the crack tip process zone is insufficient to sustain the power-law ΔK-dictated rate of fatigue crack advance. Based on a simple diffusion-based equation for da/dN, one can identify three alloy-dependent factors that could influence f_{Crit}. This argument is speculative.

18. Results from asymmetric loading waveforms implicate rise time from K_{Min} to K_{Max}, t_R, (equalling 1/2f for symmetric sinusoidal and triangular waveform loading), not total time between K_{Min} and the beginning of unloading, as governing the time-cycle dependence of environmental fatigue in 7075/NaCl..

19. A plot of crack length versus loading cycles for constant ΔK segments of environmental fatigue experiments with variable loading waveforms. An increase in slope of a long rise-time waveform, compared to a short rise-time case, is shown for a single ΔK.

20. The Effect of cycle rise-time for five waveforms (sine, trapezoidal, asymmetric triangle, and triangle) showing increased EFCP da/dN with increasing rise time. L-T results are from Selines and Pelloux. Note that the environmental fatigue crack propagation behavior of 7075-T6 is equivalent for the S-L and L-T crack orientations, in contrast to quasi-static load cracking.

21. A summary of EFCP data for 7075-T651/NaCl under several loading frequencies, waveforms, and ΔK control formats. An upper bound on da/dN versus ΔK can be established for engineering fatigue life calculations.

22. Conclusions

Time-Dependent Environmental Fatigue Crack Propagation in AA7075

Mark E. Mason and Richard P. Gangloff

Department of Materials Science and Engineering
University of Virginia

Robert S. Piascik
and
James C. Newman

NASA-LaRC

Objective

Quantitatively model environmental fatigue, da/dN(ΔK, R, f, waveform,..), for use in NASA-FLAGRO life prediction.

Current Work

- oo Test linear superposition predictions of da/dN vs ΔK and f based on static load or constant displacement da/dt_{scc}.
- oo Determine if da/dt_{scc} is affected sufficiently by crack tip strain rate to enable improved linear superpostion predictions of da/dN.
- oo Measure frequency, load waveform, and hold-time dependencies of da/dN.
- oo Identify metallurgical and electrochemical origin(s) of wide variability in frequency dependency of 7000 series aluminum alloys.

Mechanical Properties	
Yield Strength MPa (ksi)	472 (68.4)
Tensile Strength MPa (ksi)	540 (78.2)
Elongation Pct	4.0
K_{IC} MPa√m (ksi√in)	22.2 (19.3)

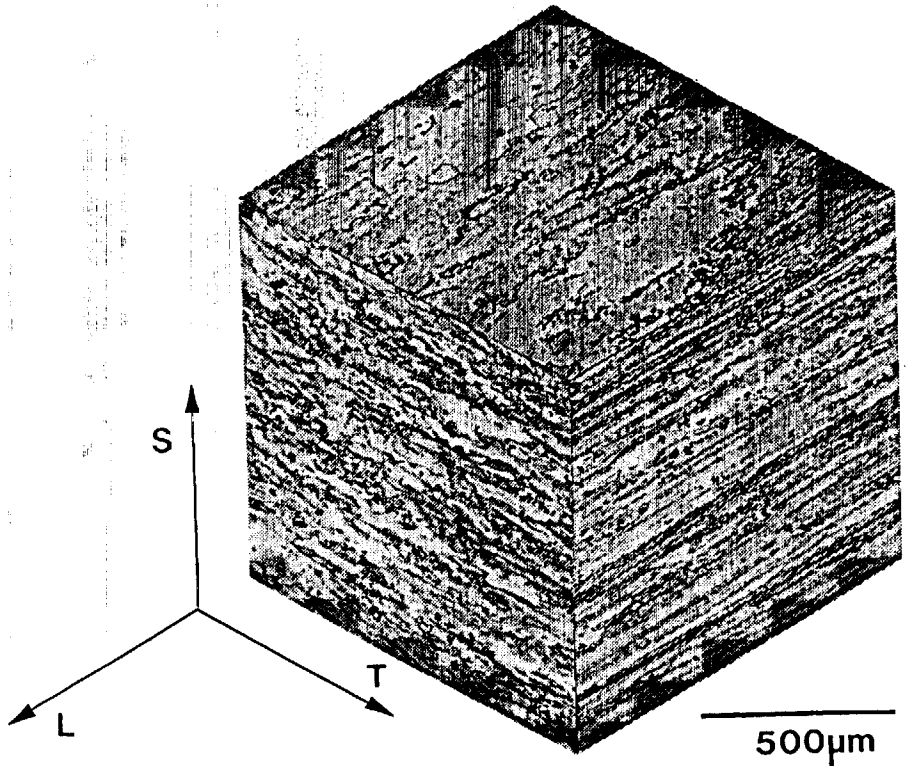

Representative Microstructure

Environmental Testing Set-up

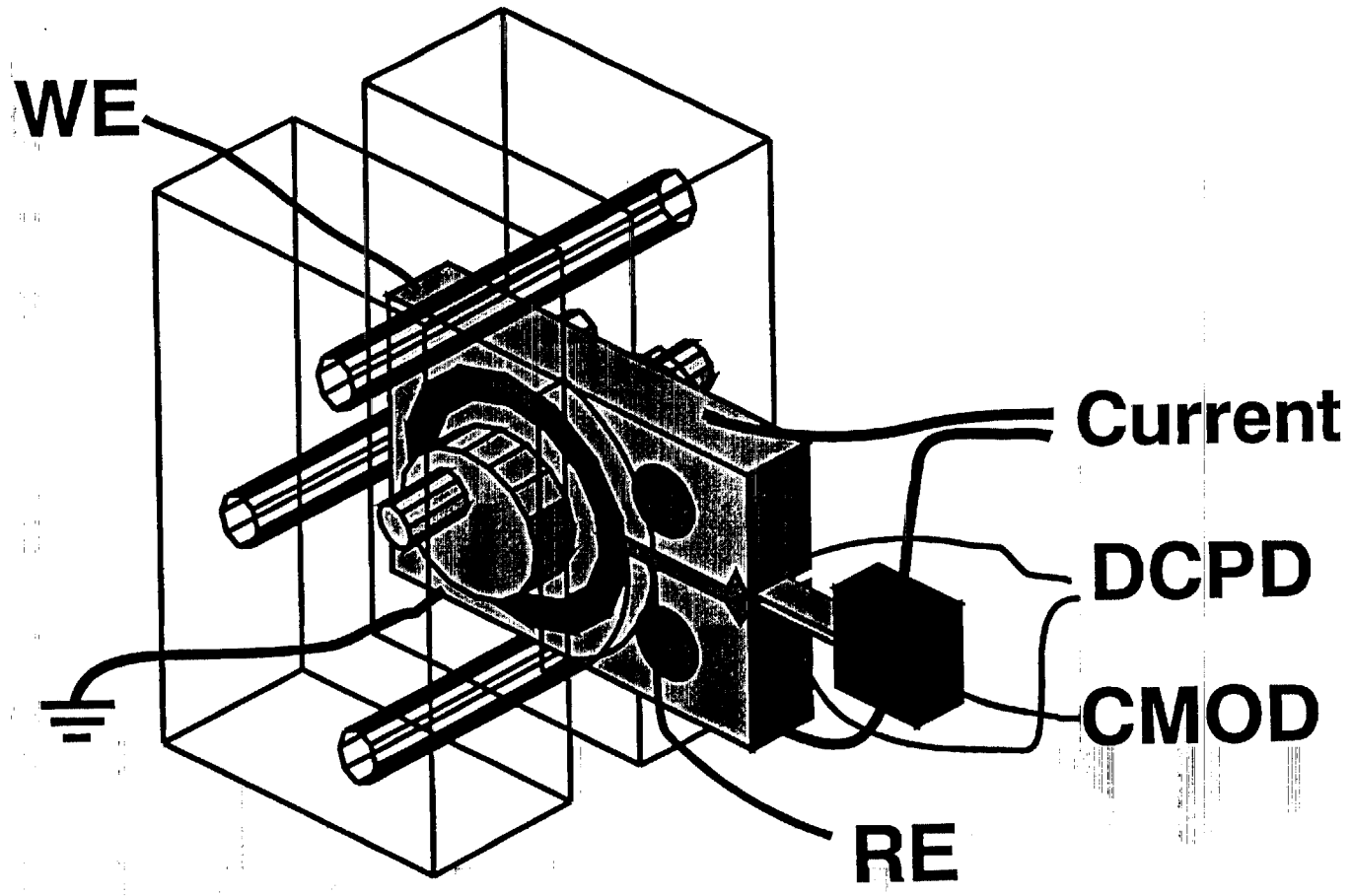

Models to interpolate and extrapolate environmental da/dN-(ΔK, R, f, waveform, ...) have been developed from several perspectives:

Linear Superposition

$$\frac{da}{dN} = \frac{da}{dN_{Inert}} + \int_{\tau} [\frac{da}{dt}(K)]\, K(t)\, dt$$

Empirical Curve Fitting

$$\frac{da}{dN} = \frac{C(1-f)^n\ \Delta K^n\ (1-\Delta K_{TH})^p}{(1-R)^n\ (1-\frac{\Delta K}{(1-R)K_C})^q}$$

Mechanism-based

$$\frac{da}{dN} = \frac{da}{dN_{Inert}} + \frac{da}{dN_{SCC}} + \frac{da}{dN_{CF}}$$

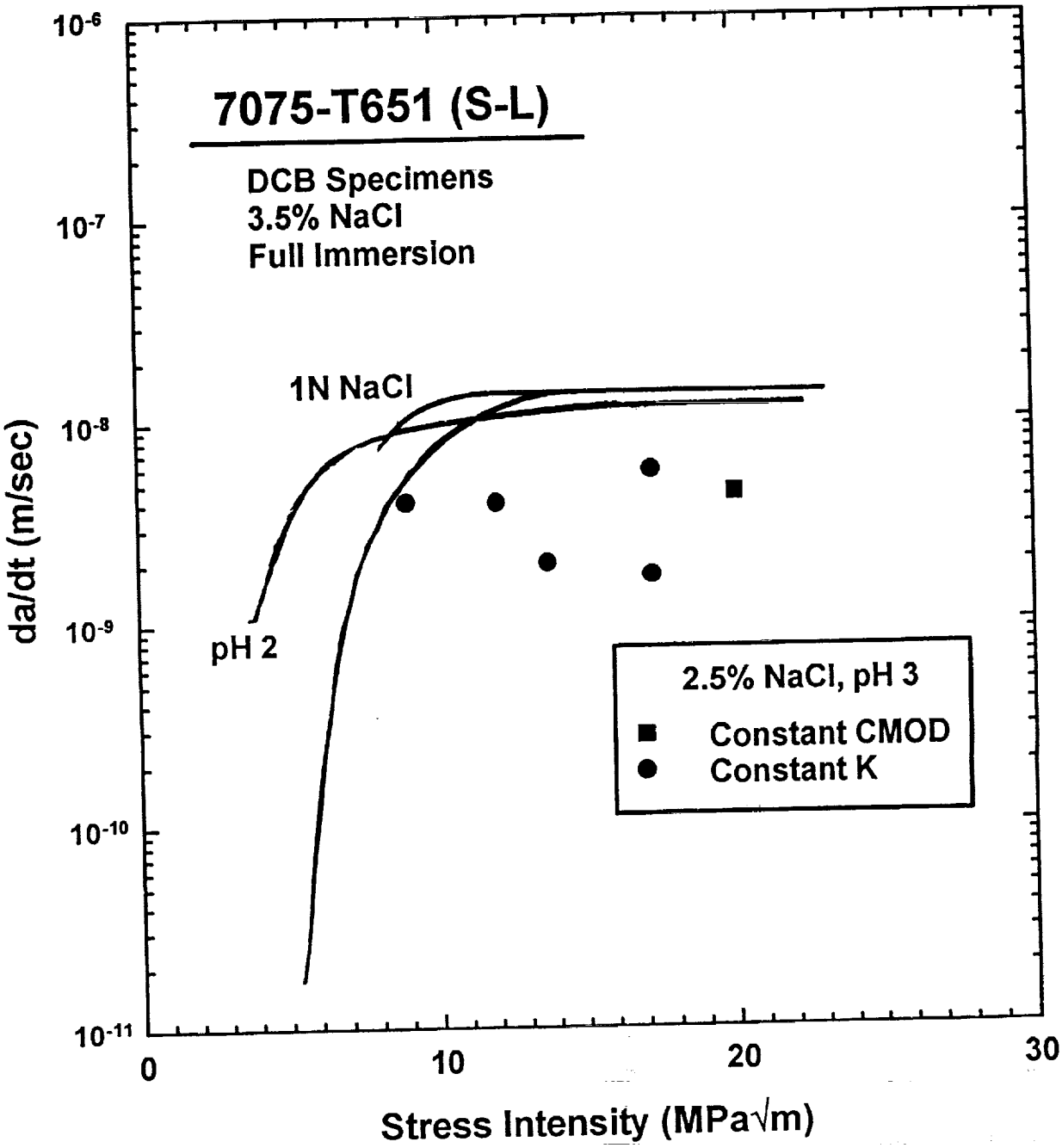
7075-T651 (S-L)
DCB Specimens
3.5% NaCl
Full Immersion
1N NaCl
pH 2
2.5% NaCl, pH 3
Constant CMOD
Constant K
da/dt (m/sec)
Stress Intensity (MPa√m)
10-6
10-7
10-8
10-9
10-10
10-11
0
10
20
30

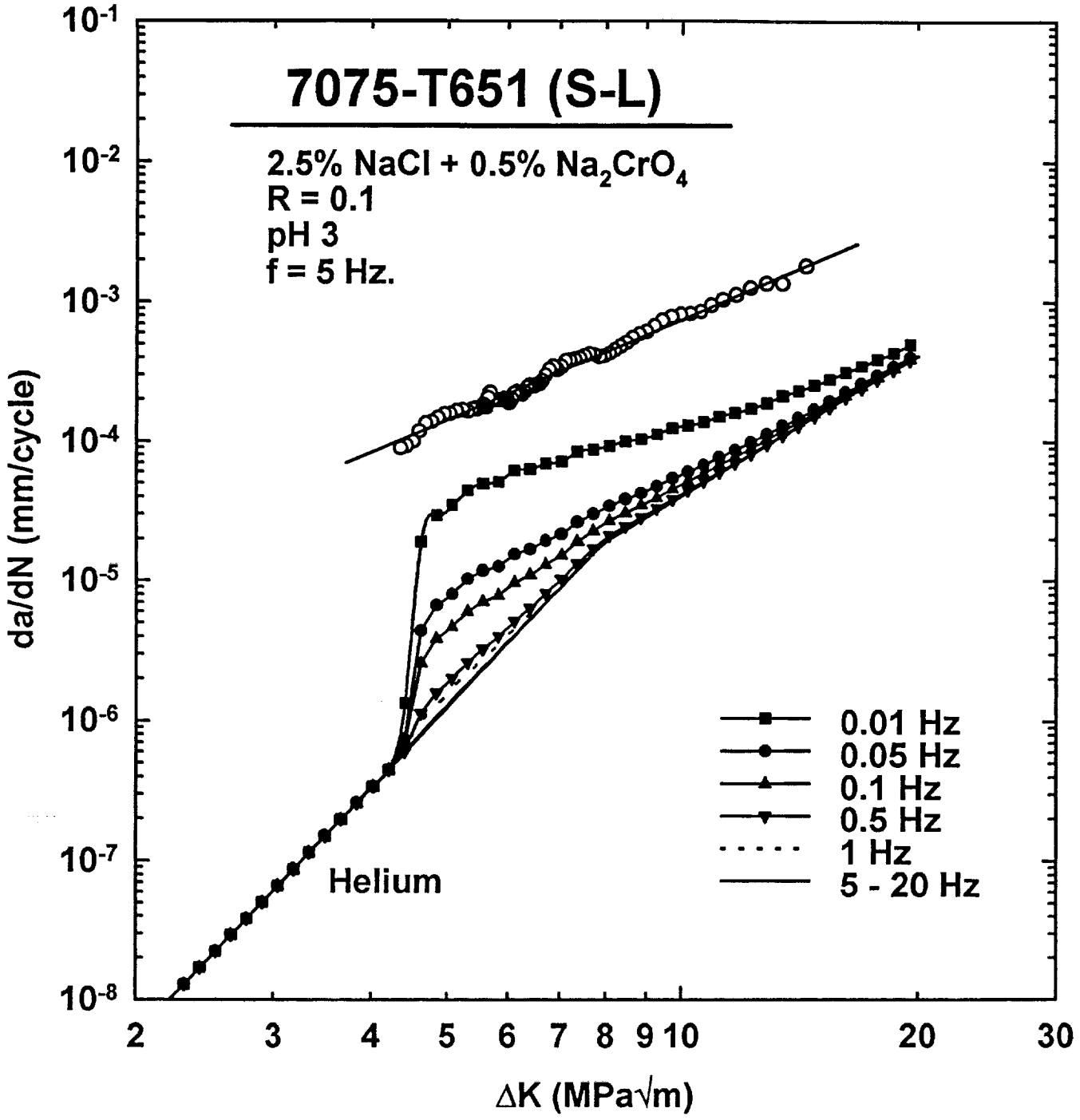
7075-T651 (S-L)
2.5% NaCl + 0.5% Na2CrO4
R = 0.1
pH 3
f = 5 Hz.
Helium
0.01 Hz
0.05 Hz
0.1 Hz
0.5 Hz
1 Hz
5 - 20 Hz
da/dN (mm/cycle)
ΔK (MPa√m)
10-1
10-2
10-3
10-4
10-5
10-6
10-7
10-8
2
3
4
5
6
7
8
9
10
20
30

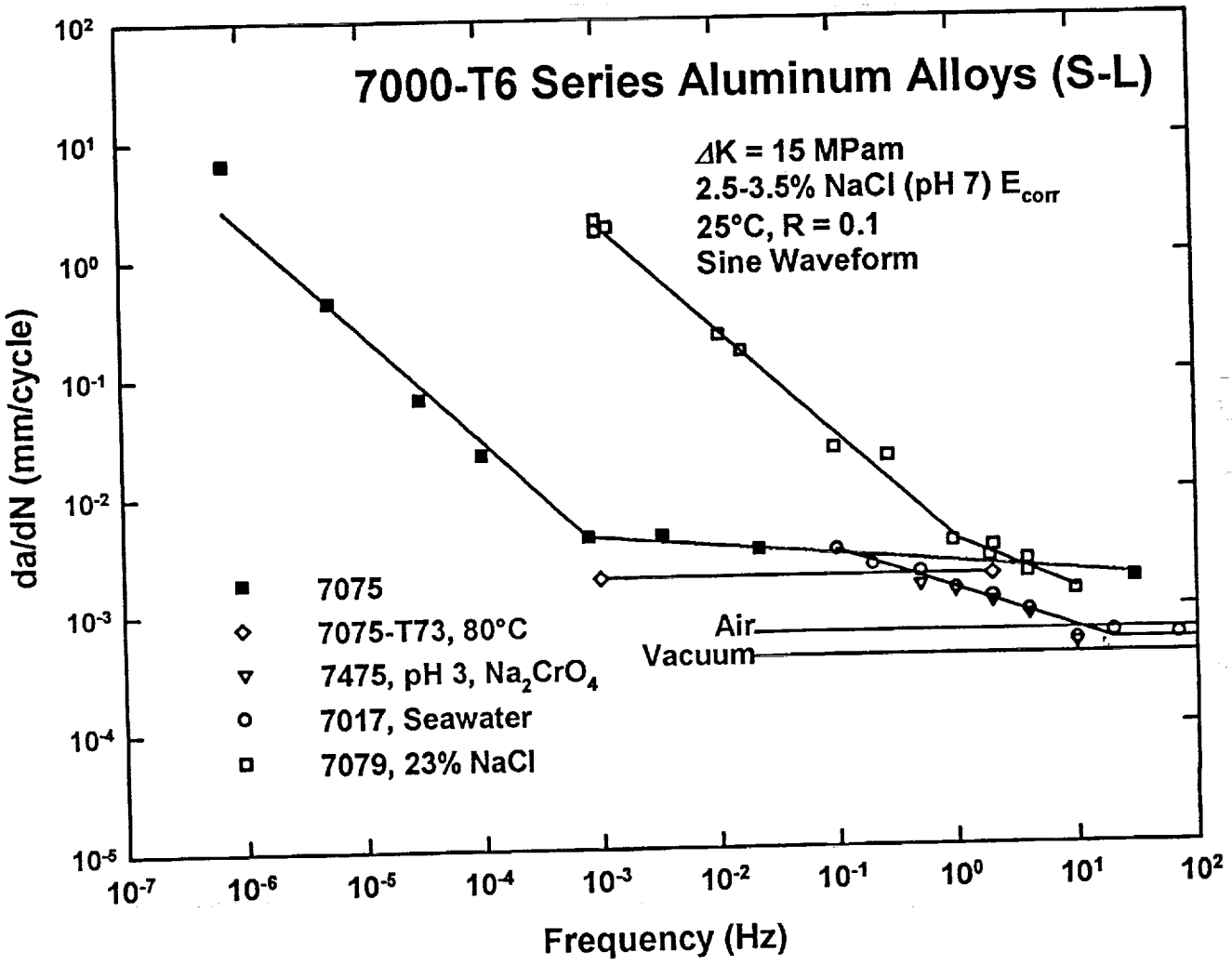
7000-T6 Series Aluminum Alloys (S-L)
ΔK = 15 MPam
2.5-3.5% NaCl (pH 7) E_corr
25°C, R = 0.1
Sine Waveform
7075
7075-T73, 80°C
7475, pH 3, Na2CrO4
7017, Seawater
7079, 23% NaCl
Air
Vacuum
da/dN (mm/cycle)
Frequency (Hz)
10^2
10^1
10^0
10^-1
10^-2
10^-3
10^-4
10^-5
10^-7
10^-6
10^-5
10^-4
10^-3
10^-2
10^-1
10^0
10^1
10^2

Two reasons why linear superposition fails to predict environmental FCP kinetics for AA7075-T651/NaCl:

- oo Static load/displacement crack tip strain rates are slower than dynamic rates in fatigue crack tip process zone, affecting hydrogen production, uptake, and or transport in the process zone.

- oo Environmental FCP competes with static load cracking and occurs by a different crack tip damage mechanism unique to cyclic deformation.

CONCLUSIONS

Increasing strain rate from the static displacement case does not enhance environmental cracking:

- **Imposed constant crack mouth opening displacement rate does not accelerate da/dt.**

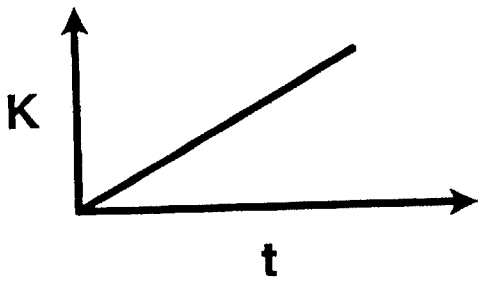

- **Da/dt is not enhanced by high frequency-low amplitude cyclic loading, designed to increase crack tip surface strain rate, in conjunction with $K_{MAX} > K_{ISCC}$.**

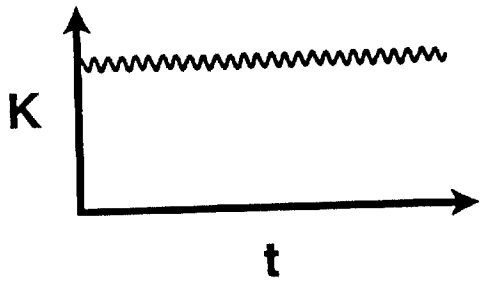

- **Corrosion fatigue propagation rates are independent of hold time at K_{MAX}. Hold time based EFCP experiments do not provide improved da/dt_{SCC} for linear superposition.**

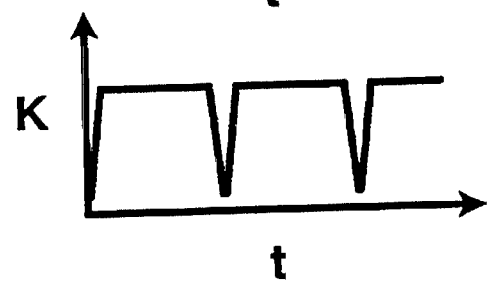

In all cases, measured da/dt_{SCC} for 7075-T651/ NaCl is an order of magnitude too small to predict chloride enhancement of EFCP for loading frequencies above 0.001 Hz and by linear superposition.

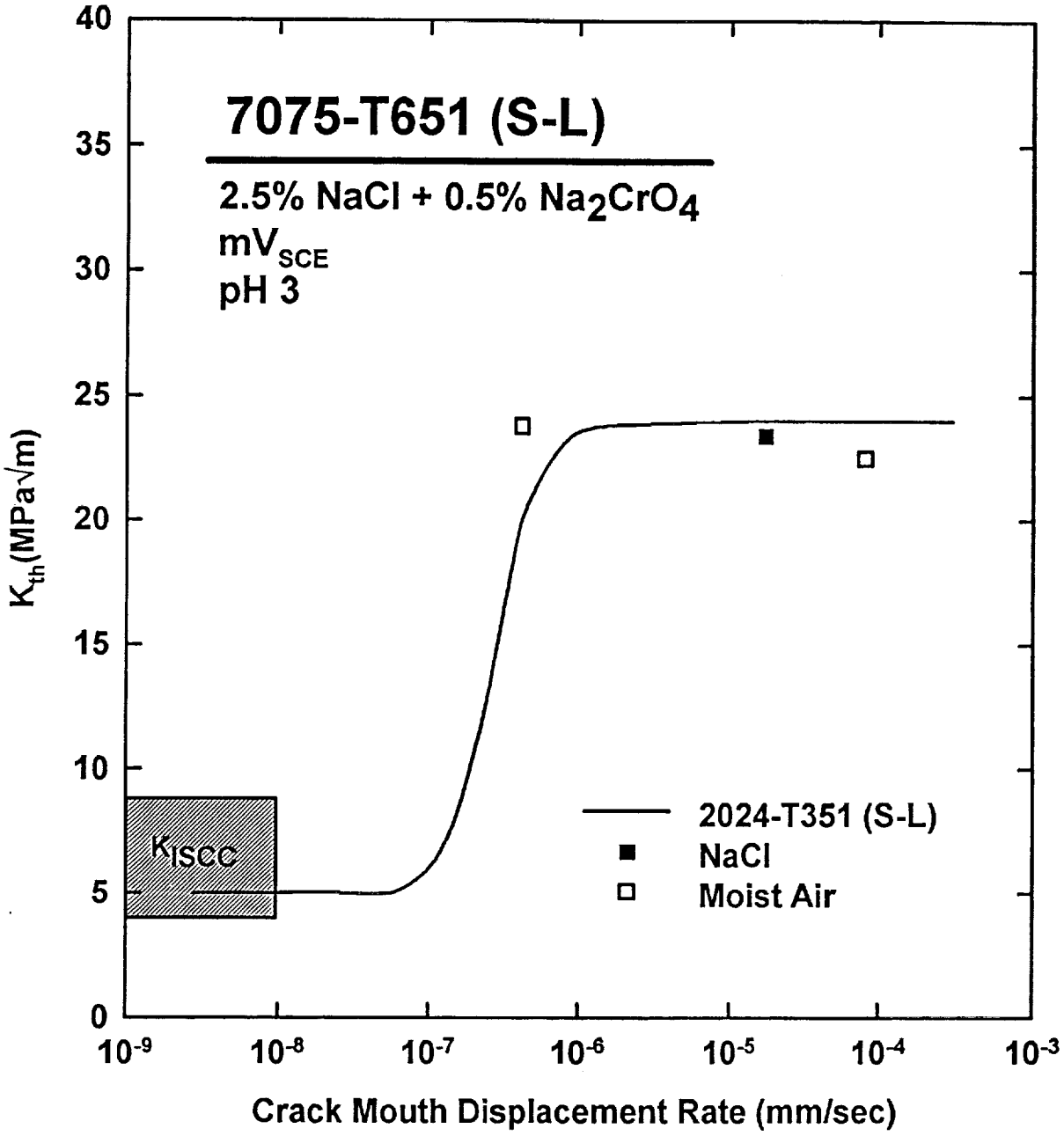
7075-T651 (S-L)
2.5% NaCl + 0.5% Na2CrO4
mVSCE
pH 3
Kth(MPa√m)
KIscc
2024-T351 (S-L)
NaCl
Moist Air
Crack Mouth Displacement Rate (mm/sec)
0
5
10
15
20
25
30
35
40
10-9
10-8
10-7
10-6
10-5
10-4
10-3

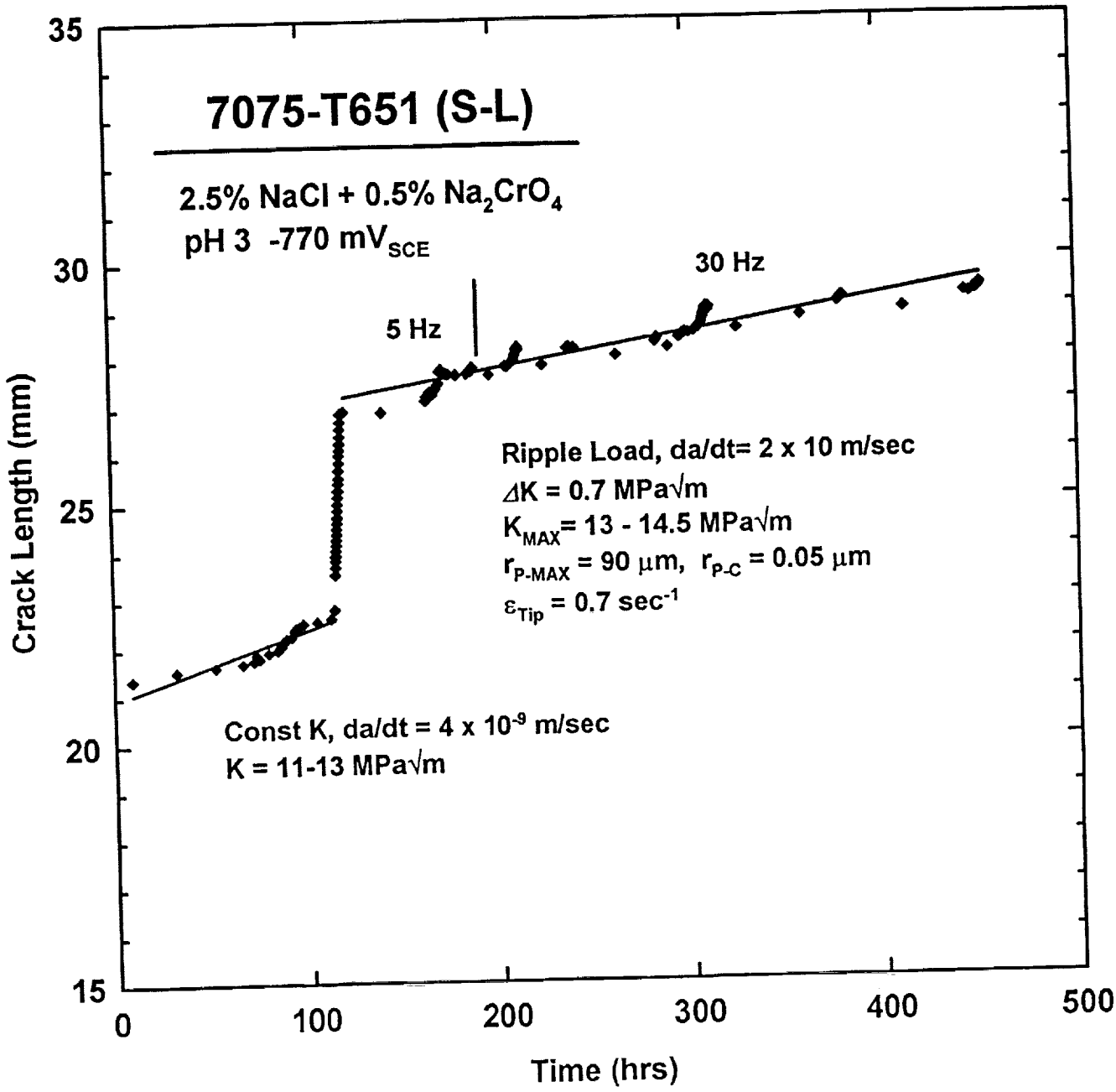
7075-T651 (S-L)
2.5% NaCl + 0.5% Na2CrO4
pH 3 -770 mVSCE
5 Hz
30 Hz
Ripple Load, da/dt= 2 x 10 m/sec
ΔK = 0.7 MPa√m
KMAX= 13 - 14.5 MPa√m
rP-MAX = 90 μm, rP-C = 0.05 μm
εTip = 0.7 sec-1
Const K, da/dt = 4 x 10-9 m/sec
K = 11-13 MPa√m
Crack Length (mm)
Time (hrs)
35
30
25
20
15
0
100
200
300
400
500

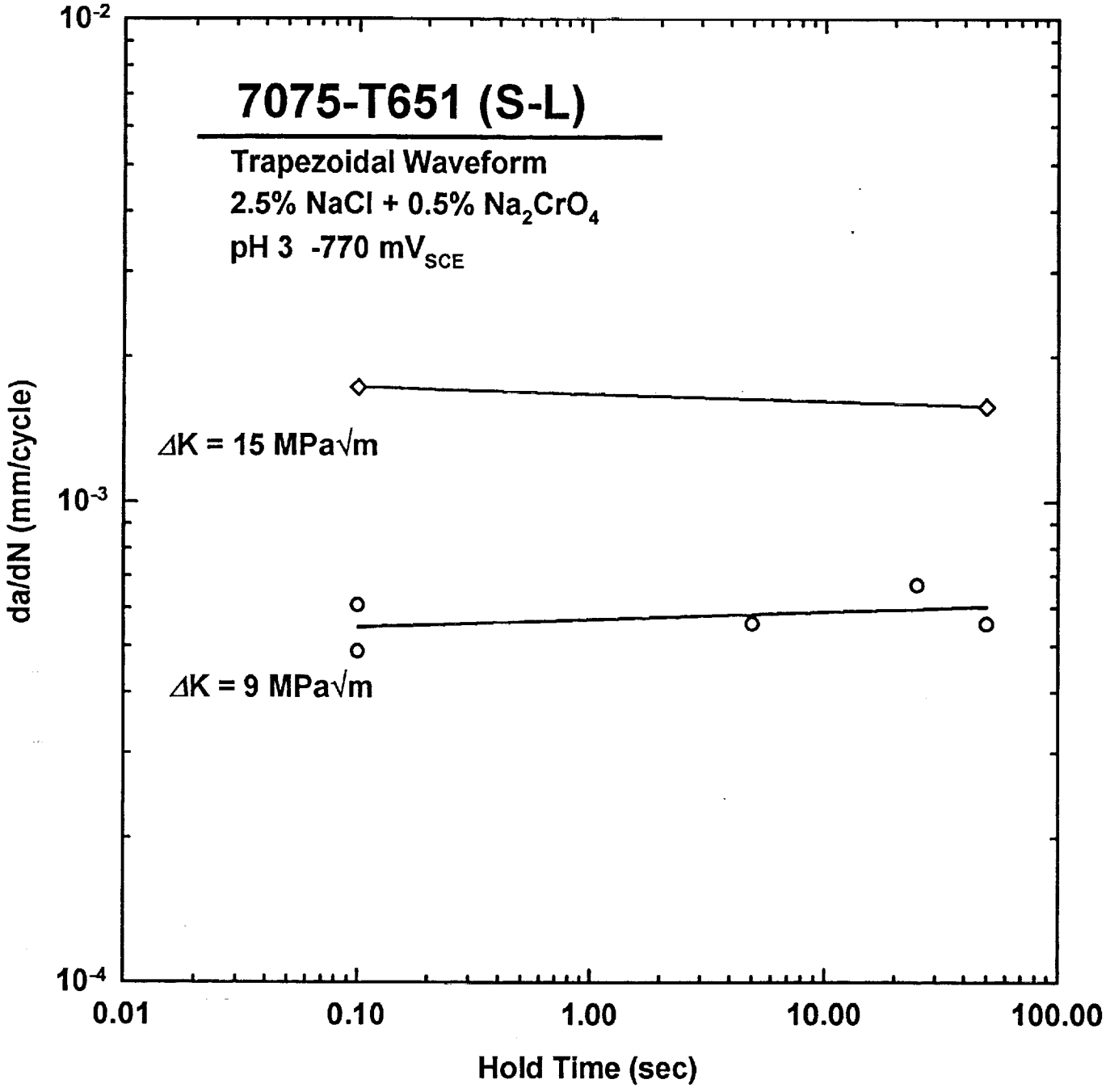
7075-T651 (S-L)
Trapezoidal Waveform
2.5% NaCl + 0.5% Na2CrO4
pH 3 -770 mVSCE
ΔK = 15 MPa√m
ΔK = 9 MPa√m
da/dN (mm/cycle)
10-2
10-3
10-4
0.01
0.10
1.00
10.00
100.00
Hold Time (sec)

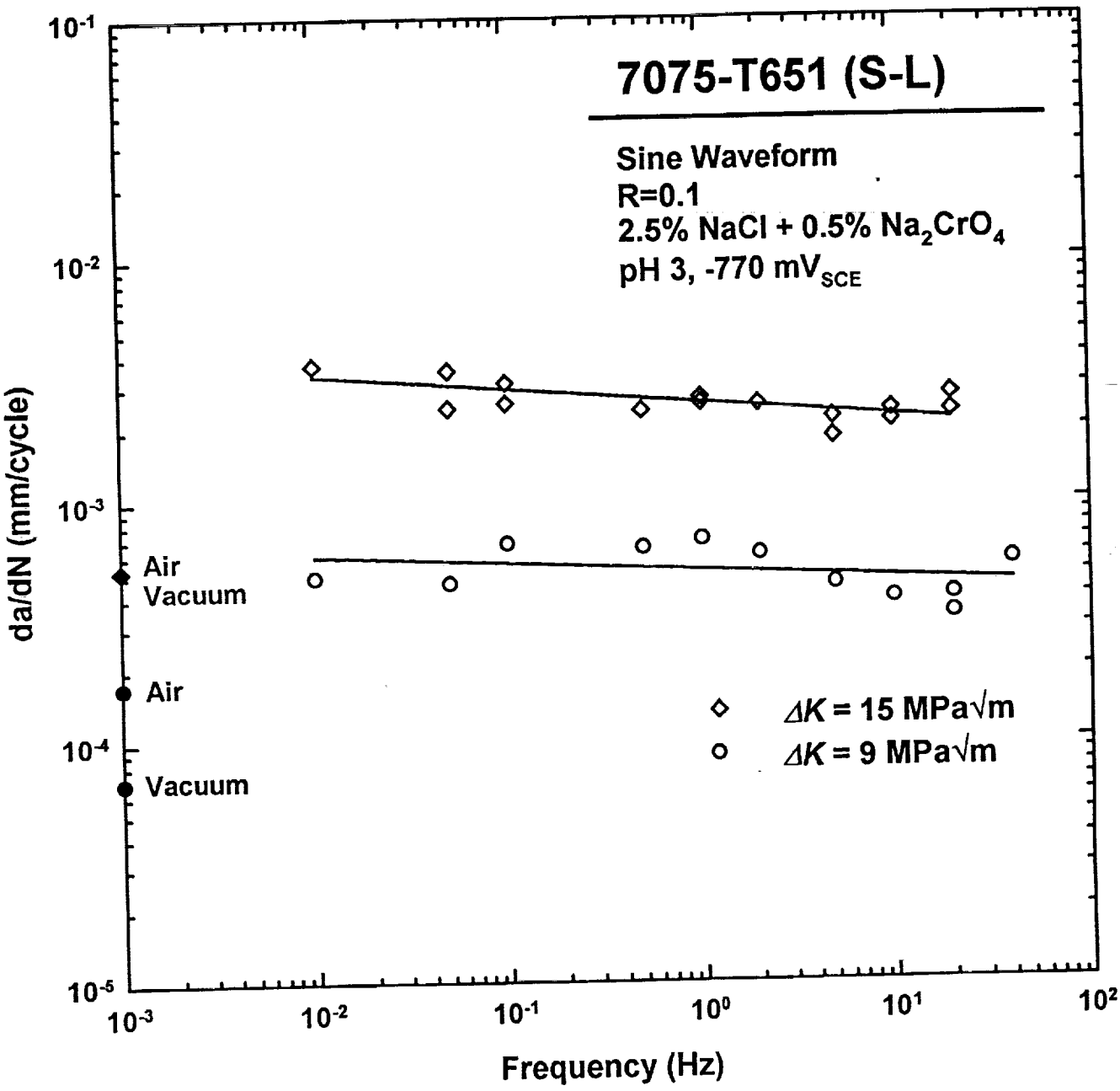
7075-T651 (S-L)
Sine Waveform
R=0.1
2.5% NaCl + 0.5% Na2CrO4
pH 3, -770 mVSCE
da/dN (mm/cycle)
Frequency (Hz)
Air
Vacuum
Air
Vacuum
ΔK = 15 MPa√m
ΔK = 9 MPa√m
10-1
10-2
10-3
10-4
10-5
10-3
10-2
10-1
100
101
102

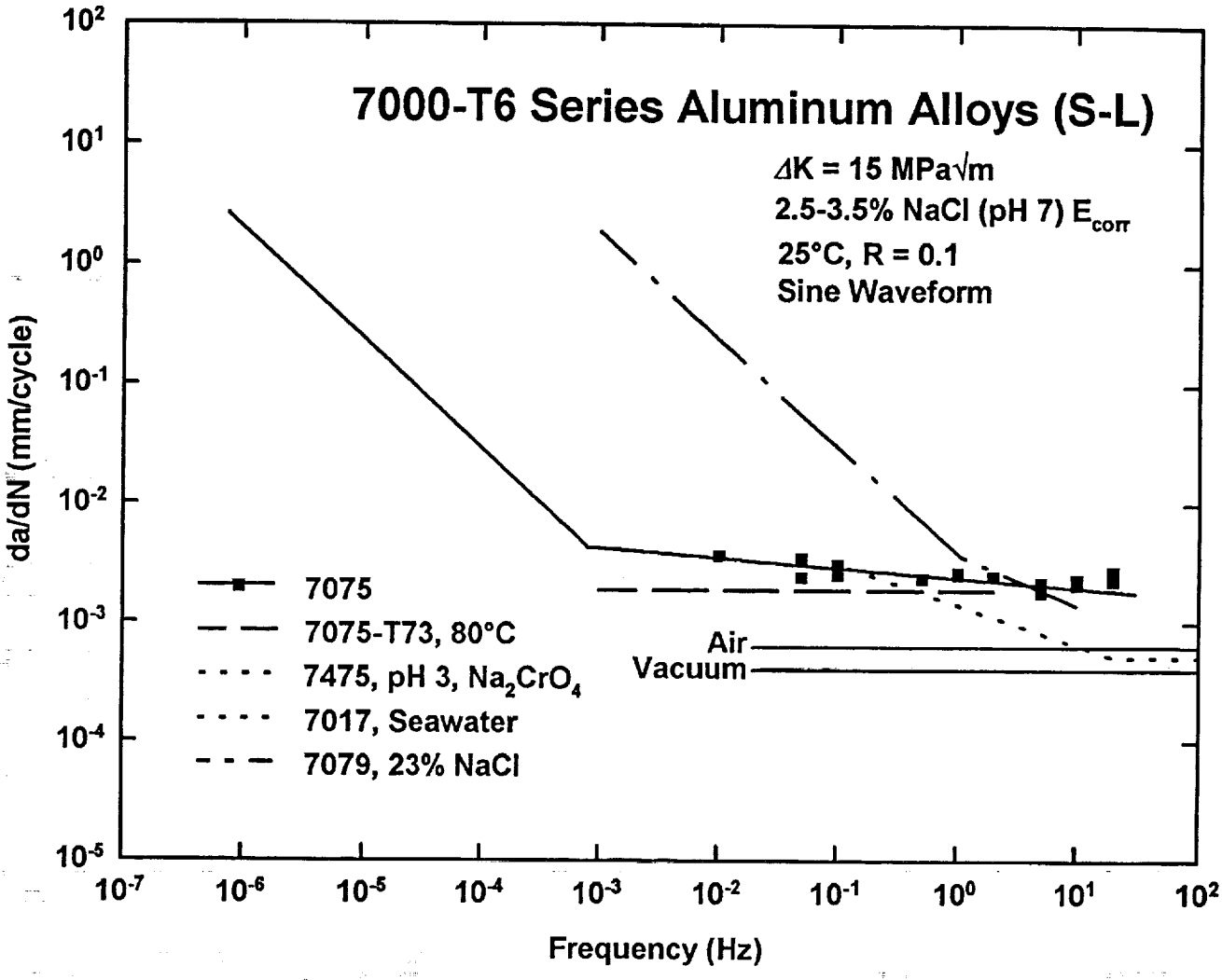
7000-T6 Series Aluminum Alloys (S-L)
ΔK = 15 MPa√m
2.5-3.5% NaCl (pH 7) E_corr
25°C, R = 0.1
Sine Waveform
da/dN (mm/cycle)
Frequency (Hz)
7075
7075-T73, 80°C
7475, pH 3, Na2CrO4
7017, Seawater
7079, 23% NaCl
Air
Vacuum
10^2
10^1
10^0
10^-1
10^-2
10^-3
10^-4
10^-5
10^-7
10^-6
10^-5
10^-4
10^-3
10^-2
10^-1
10^0
10^1
10^2

Time-Cycle Dependency -- 7000 Series Aluminum Alloys

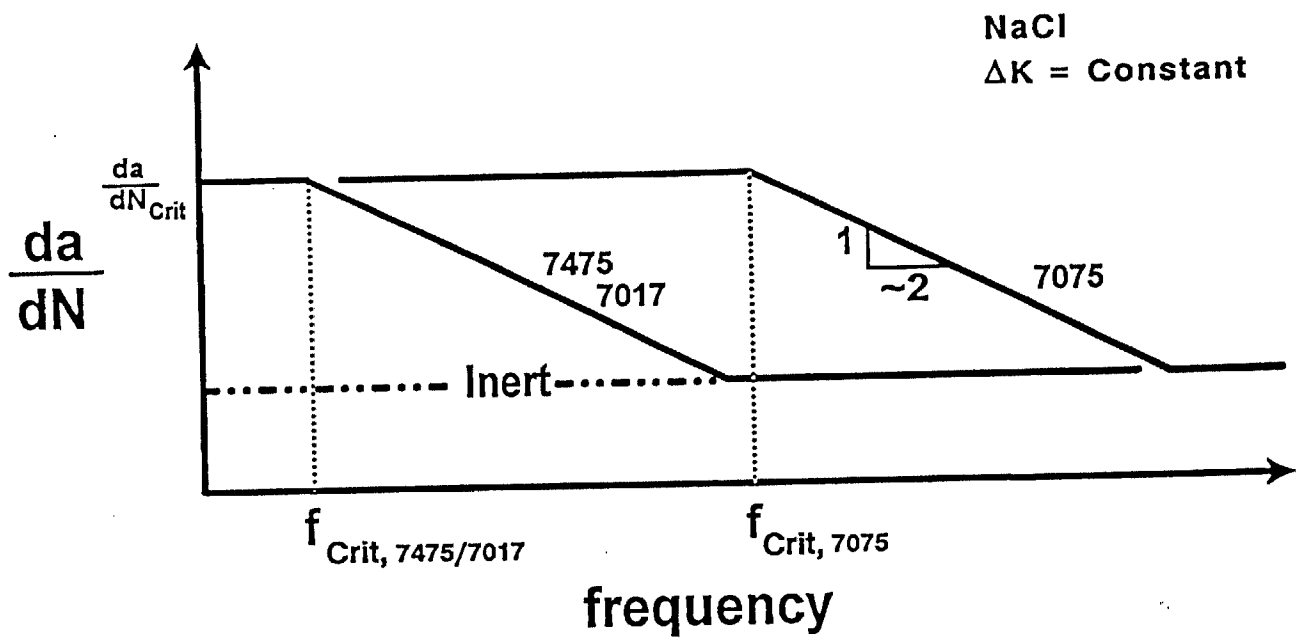

- For short cycle periods ($f \geq f_{Crit}$) diffusion of embrittling hydrogen over the fatigue advance distance, defined by ΔK, is time-limited, reducing hydrogen enhanced da/dN.

- Lower frequencies allow sufficient hydrogen diffusion and there is no time dependency due to hydrogen enhanced da/dN.

Why does f_{Crit} depend on the alloy?

f_{Crit} ⇒ **frequency above which H diffusion over Δa during ΔN is insufficient to sustain da/dN which is dictated by ΔK.**

$$\frac{\Delta a}{\Delta N} \propto \frac{\sqrt{Dt}}{\Delta N} \quad \Rightarrow \quad \frac{da}{dN} = \frac{2\sqrt{D_H}}{\sqrt{fN}} \, erf^{-1}\left(1 - \frac{C_{Crit}}{C_S}\right)$$

- **Hydrogen diffusion within the crack tip process zone could vary based on dislocation and grain boundary processes. f_{Crit} ↑ as D_H ↑**
- **As the critical hydrogen concentration (C_{Crit}) necessary for cracking decreases, f_{Crit} increases.**
- **As the concentration of hydrogen at the crack tip surface (C_S) increases, f_{Crit} increases. Crack solution cations from segregant, or a second phase in the alloy, could alter hydrogen production kinetics; could Mg^{+2} increase C_S?**

High hydrogen production/uptake and rapid hydrogen diffusion favor f-independent cracking persisting to higher frequencies and crack growth rates.

Results from asymmetric loading waveforms implicate rise time from K_{MIN} to K_{MAX}, t_R (= 1/2f for symmetric sinusoidal and triangular waveforms), NOT total time from K_{MIN} to the first unloading, as governing da/dN for time-cycle dependent corrosion fatigue.

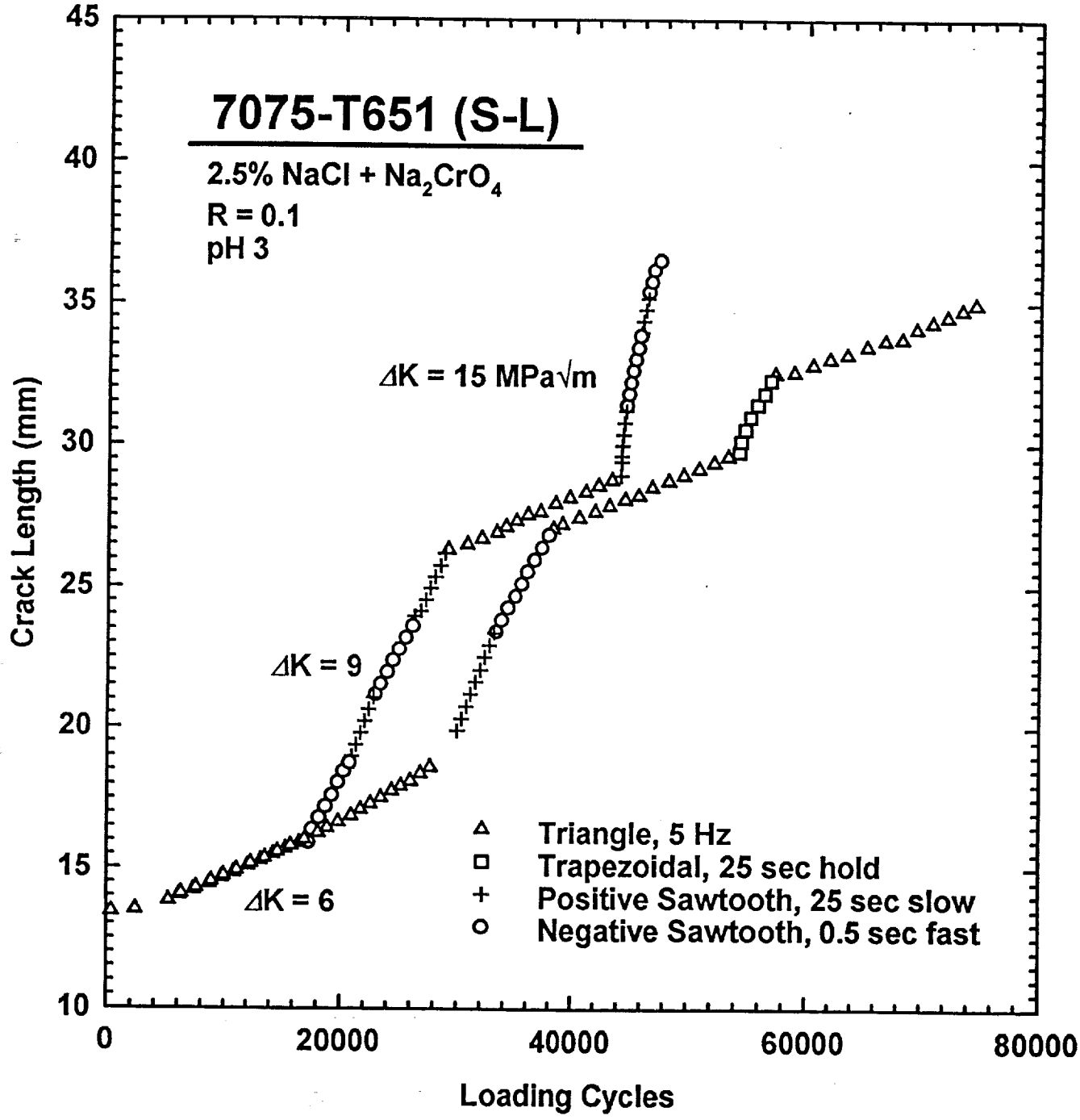
7075-T651 (S-L)
2.5% NaCl + Na2CrO4
R = 0.1
pH 3
ΔK = 15 MPa√m
ΔK = 9
ΔK = 6
Triangle, 5 Hz
Trapezoidal, 25 sec hold
Positive Sawtooth, 25 sec slow
Negative Sawtooth, 0.5 sec fast
Crack Length (mm)
Loading Cycles
45
40
35
30
25
20
15
10
0
20000
40000
60000
80000

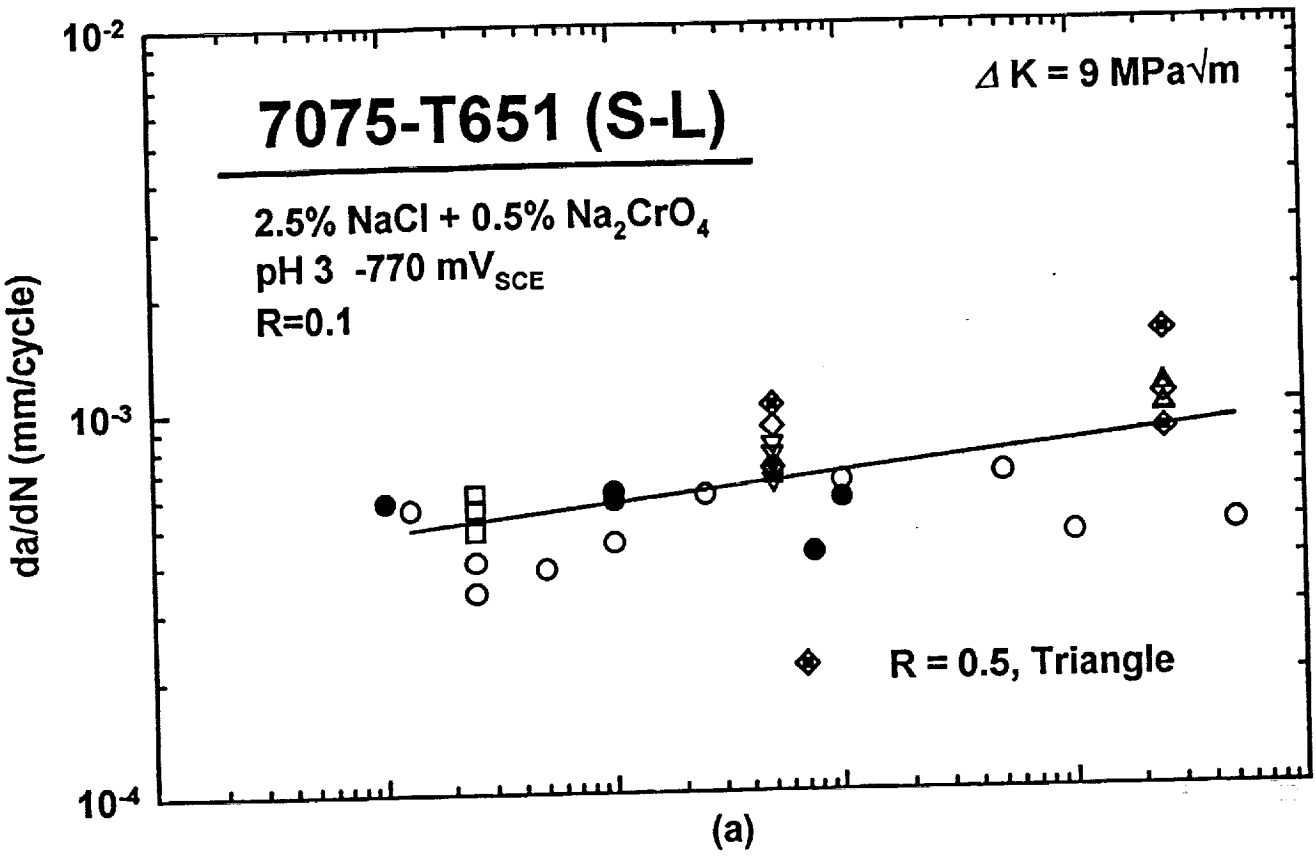
7075-T651 (S-L)
2.5% NaCl + 0.5% Na2CrO4
pH 3 -770 mVSCE
R=0.1
Δ K = 9 MPa√m
R = 0.5, Triangle
da/dN (mm/cycle)
10-2
10-3
10-4

(a)

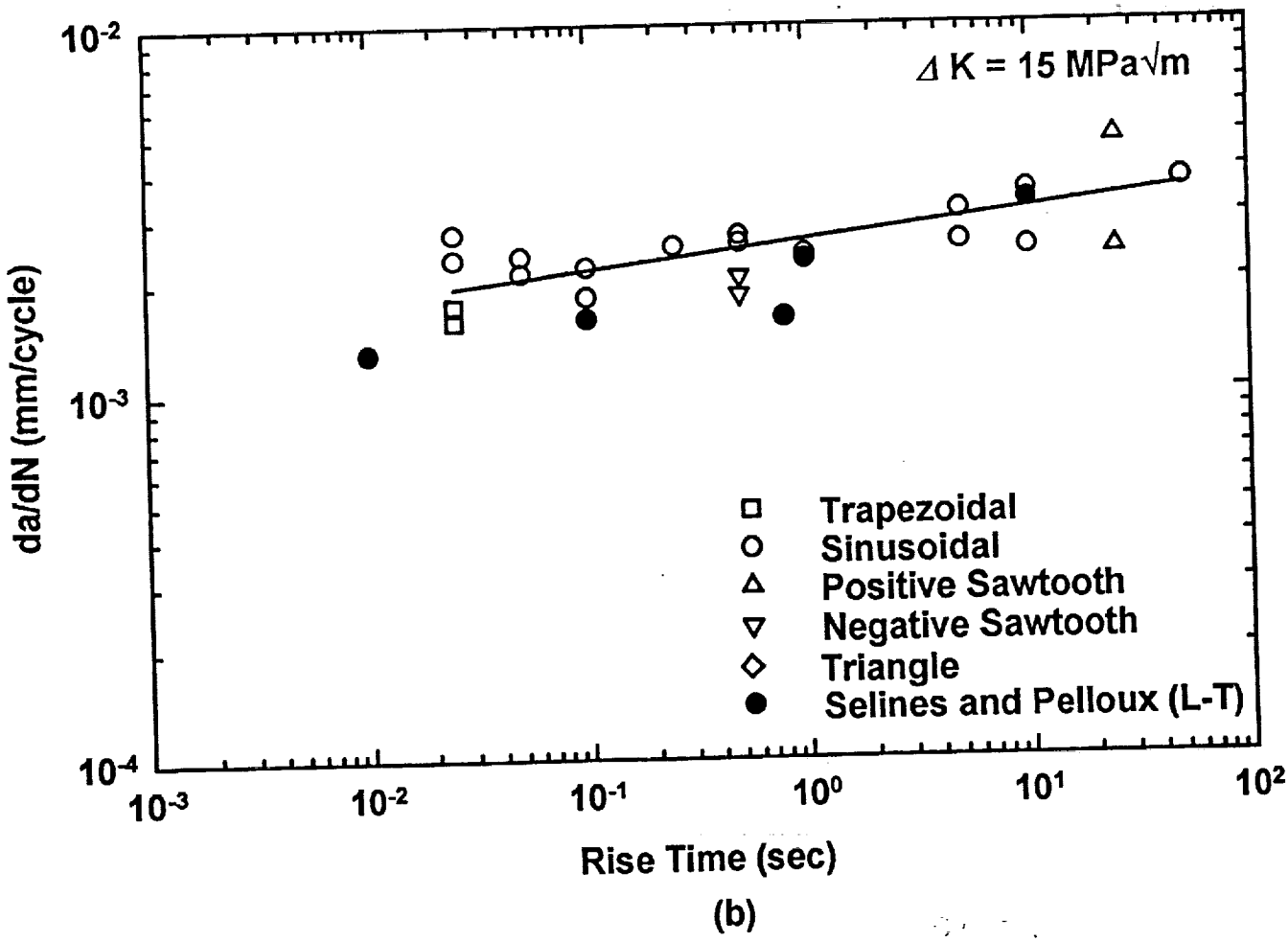
Δ K = 15 MPa√m
Trapezoidal
Sinusoidal
Positive Sawtooth
Negative Sawtooth
Triangle
Selines and Pelloux (L-T)
da/dN (mm/cycle)
10-2
10-3
10-4
10-3
10-2
10-1
100
101
102
Rise Time (sec)

(b)

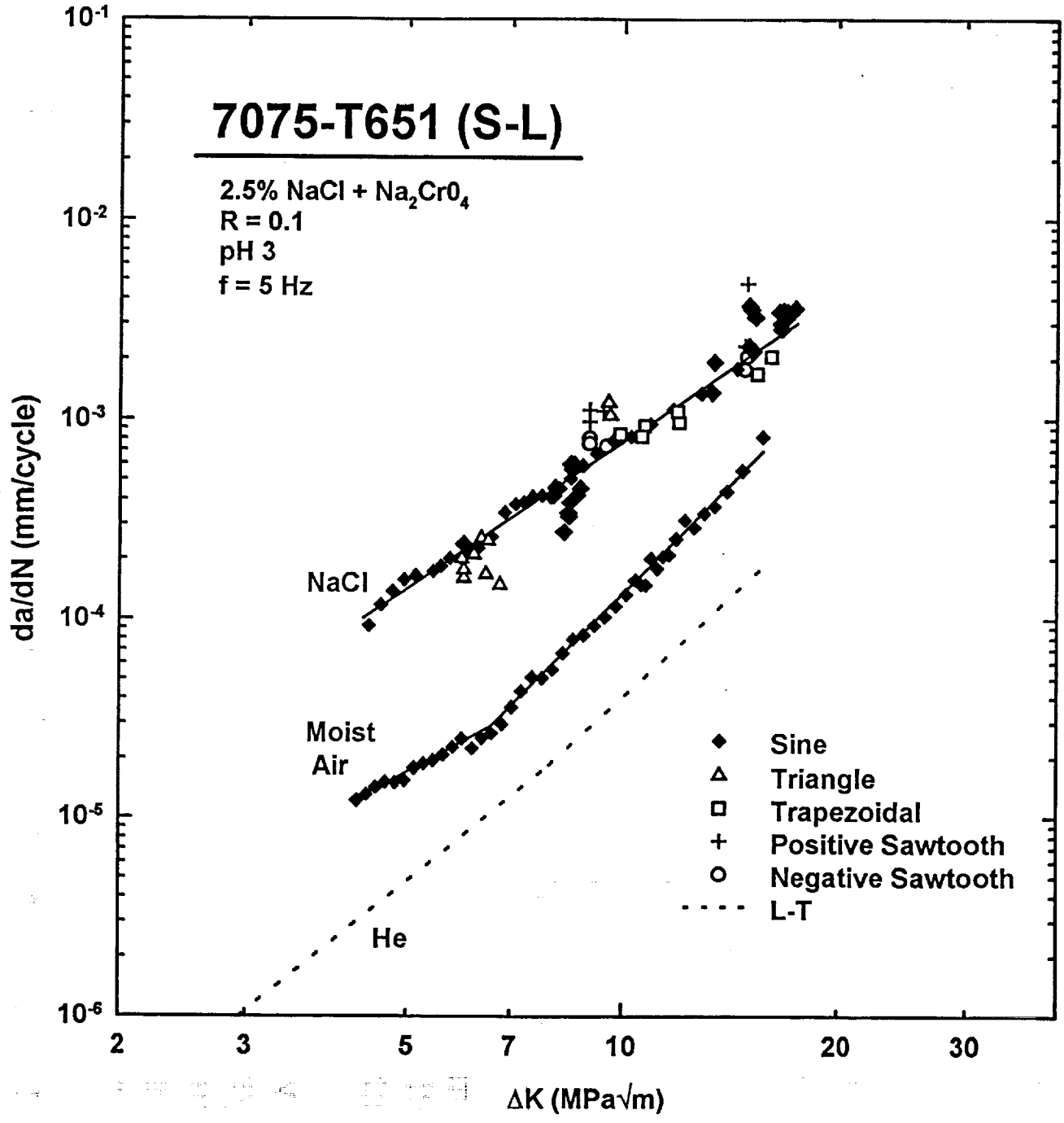
7075-T651 (S-L)
2.5% NaCl + Na2Cr04
R = 0.1
pH 3
f = 5 Hz
da/dN (mm/cycle)
ΔK (MPa√m)
NaCl
Moist Air
He
Sine
Triangle
Trapezoidal
Positive Sawtooth
Negative Sawtooth
L-T

CONCLUSIONS

- oo Da/dN for corrosion fatigue of 7075-T651/NaCl is enhanced five to ten-fold over moist air and He da/dN.

- oo Da/dN for 7075-T651 in NaCl shows two regimes of frequency dependence:

  - ▸ $da/dN \propto f^{-1}$ below 0.001 Hz, time-dependent FCP, modeled by linear superposition

  - ▸ $da/dN \propto f^{0 \text{ to } -0.1}$ above 0.001 Hz, due to cycle-time-dependent crack propagation

- oo Minimal involvement of grain boundaries in EFCP is suggested by identical chloride time-cycle dependent EFCP for S-L and T-L orientations.

- oo The variable frequency response of EFCP in 7000 Series aluminum alloys depends on an undefined compositional and microstructural variable. High hydrogen production/uptake and rapid hydrogen diffusion favor f-independent cracking persisting to higher frequencies and crack growth rates.

- oo EFCP in 7075/NaCl is adequately described for life prediction by linear superposition for long load-cycle periods, and by a time-independent upper bound relationship for faster load rise-times.

Project #9B Computer Modeling Environmental Effects on Fatigue Crack Propagation in Light Aerospace Alloys

Edward Richey III and Richard P. Gangloff

Objective

The objective of this research is to develop an effective method for estimating stress intensity-dependent and time-dependent environmental effects on rates of fatigue crack propagation (FCP) in aerospace alloys. Such information is necessary for use in damage tolerant fatigue life prediction codes such as NASA FLAGRO. The method being developed will estimate the rate at which a crack grows when a structural alloy is exposed to cyclic loads in a corrosive or embrittling environment. Data from previous tests will be analyzed by empirical curve-fitting and interpolation methods.

Status

Work in this project has been conducted by undergraduates in Mechanical and Aerospace Engineering, and has focused on three tasks. Jonathan Pope developed a method for electronically reading data points from literature graphs in order to create ASCII data files. Allen Wilson developed a computer program which implemented the Wei and Landes method of linear superposition. Edward Richey developed an interpolative model which allows the user to fit sets of da/dN data to empirical equations, including the Forman Equation contained in FLAGRO. Assumed interpolation relationships are then used to account for the effects of loading time and other variables that influence fatigue crack growth in a corrosive environment.

Recent Results

A method for digitizing the points on a literature graph and transforming them to da/dN versus ΔK values was developed using a Numonics 2400 Digitablet. The data points are read using the Digitablet, and the numbers transformed to file-values using a FORTRAN program called DIGITIZE.EXE. An error analysis was performed on the digitization and

transformation process. All errors are negligible when compared to the typical uncertainty associated with laboratory testing. The largest average error in any test was 2.1%.

A computer program was created which predicted corrosion FCP rates using the linear superposition method. Although this approach is not accurate for all (or even most) material-environment systems, the method has proven to be reliable in those cases where environment has a strong effect on subcritical crack growth. The program incorporates the conditions which affect environmental fatigue cracking including ΔK, stress ratio (R), frequency of the applied load (f), hold time of the applied load (τ), loading wave form, and material (inert environment) fatigue and stress corrosion behavior.

A stand-alone computer program, incorporating elements of NASA FLAGRO, was developed to regression curve-fit da/dN versus ΔK data, as well as interpolate trends in fatigue behavior. The program currently contains five crack growth rate equations: the Forman Equation with closure, the Forman Equation without closure, the Paris Equation, the Hyperbolic Sine Equation, and the Sigmoidal Equation. The ability of all five crack growth rate equations to fit da/dN data was tested. Each fit FCP data for Ti-6Al-4V in air and a 1% NaCl solution. All of the crack growth rate equations were able to interpolate trends in da/dN versus ΔK data for Ti-6Al-4V in 3.5% NaCl solution, when the frequency at which data were interpolated was within the range for which data were entered.

The three computer programs are compiled on a program disk in executable form. A menu system was developed, and can be executed by typing *MENU* at the DOS prompt. The source codes for the programs are included on the disk. This program has been forwarded to Dr. R.S. Piascik in the Mechanics of Materials Branch at the NASA-Langley Research Center, and to Dr. R.G. Forman at the Johnson Space Center.

Future Work

Several tasks must be completed to improve the usefulness of the computer programs for estimating the fatigue behavior of metals in corrosive

environments.. The following studies constitute the final portion of Mr. Richey's MS thesis in Mechanical and Aerospace Engineering.

(1) Experimentally produce corrosion fatigue data for Ti-6Al-4V (ELI) in an aqueous chloride environment as a function of loading frequency, hold-time, waveform and perhaps stress ratio.

(2) Improve the logarithmic assumptions contained in the interpolative modeling program which relate constants in the crack growth rate equations to load-time characteristics. This will be done by exploring the forms of the observed relationships, coupled with a physical understanding of time-cycle dependent environmental FCP in titanium alloys exposed to aqueous chloride.

Presentation Viewgraph Captions

1. Title.

2. Presentation outline.

3. Objective and current work. The objective of the research is to develop an effective method for estimating environmental effects on fatigue crack propagation rates for use in damage tolerant codes such as FLAGRO.

4. Summary of the program disk. The digitization program and both computer models are included on a disk with the FORTRAN source code. These programs are discussed in the NASA Contract Report (to be published), *Computer Modeling the Fatigue Crack Growth Rate Behavior of Metals in Corrosive Environments.* A preprint is available upon request from Professor Gangloff.

5. Summary of method developed to digitize points on a literature graph, with transformation to accurate da/dN versus ΔK values. An error analysis was conducted on the complete digitization process. The largest error was 2.1%, and errors are negligible when compared to the typical uncertainty associated with laboratory testing.

6. Summary of the computer program embodying the Wei and Landes linear superposition model developed to predict corrosion fatigue crack propagation rates. The program incorporates material properties [$(da/dN)_{mechanical}$ and da/dt(K)], as well as the applied loading history of interest [K(t)] to predict the effects of ΔK, stress ratio, frequency, hold time, and loading wave form on the environmental fatigue crack growth rate. The method is only reliable for limited cases where environment strongly affects subcritical crack growth.

7. Computer-program-modeled linear superposition predictions of corrosion fatigue crack growth kinetics in a stress corrosion cracking susceptible aluminum alloy in aqueous chloride solution. The results are most accurate for cyclic stress intensity levels above K_{ISCC} which is about 5 MPa$\sqrt{m}$ for this material/environment system.

8. Computer-program-modeled linear superposition predictions of the effect of stress ratio on elevated temperature environmental fatigue cracking in IN718. Stress ratios of 0.1 and 0.5 are included for a temperature of 649 °C.

9. Summary of the equations available in the interpolative computer modeling program for representing da/dN versus ΔK. Five different crack growth rate equations are available in the program including the Forman Equation with and without closure, the Paris Equation, the Hyperbolic Sine Equation, and the Sigmoidal Equation.

10. Description of the interpolative model, compared with NASA FLAGRO. The new program can use all material property constants that are currently included in FLAGRO, in conjunction with the Forman Equation. Major differences between the programs include the interpolative model's capability to describe any one of five FCP rate equations, the ability to regression-fit any combination of equation constants to input da/dN versus ΔK data, the ability to hold K_{max} or K_{min} constant for a given data set, the ability to optimize the value of K_C and ΔK_{th} for input data, and the addition of statistical parameters including the coefficient of determination for a fitted data set and confidence interval estimates of the fitted equation constants.

11. Summary of the results when the least squares regression subroutines in the interpolative modeling program were bench marked against FLAGRO and results published by Haritos for the Hyperbolic Sine Equation. The linear least squares subroutine in the interpolative model yielded the same results as FLAGRO, when fitting data to the Forman Equation with closure. The nonlinear least squares algorithm yielded different results than those published by Haritos, but yielded a better fit based on the coefficients of determination.

12. Forman Equation (with closure) fit of fatigue data for Ti-6Al-4V in 1.0% NaCl with R = 0.4 at 5 Hz. Results are included for fitting C, n, p, and q, as well as results for fitting only C and n while p was set to 0.25, and q to 0.75. (Fatigue data for Ti-6Al-4V were produced by Kim and Gangloff, as reported in the last LA^2ST progress report: R.P. Gangloff, "NASA-UVa Light Aerospace Alloy and Structures Technology Program", UVa Report No. UVA/528266/MSE93/114, March, 1994.)

13. Forman Equation (without closure) fit of fatigue data for Ti-6Al-4V in 1.0% NaCl with R = 0.4 at 5 Hz. Results are included for fitting C, n, p, and q, as well as results for fitting only C and n while p was set to 0.25, and q to 0.75.

14. Hyperbolic Sine Equation fit of fatigue data for Ti-6Al-4V in 1.0% NaCl with R = 0.4 at 5 Hz. Notice that near the threshold the fitted curve does not show a sharp decrease in da/dN as ΔK decreases. Instead, the curve levels. This demonstrates the fact that the fitted curves are only accurate within the range of data fit to the equation.

15. Sigmoidal Equation fit of fatigue data for Ti-6Al-4V in 1.0% NaCl with R = 0.4 at 5 Hz.

16. Summary of the coefficients of determination calculated for fitting the crack growth rate equation to data for Ti-6Al-4V in an air and a 1.0% NaCl environment. The Forman Equation (with and without closure) yields the "best" fit for all data tested, with an average coefficient of determination of 0.9735. The Sigmoidal Equation displays similar accuracy, with a coefficient of determination value of 0.9730, followed by the Hyperbolic Sine Equation with a value of 0.9552. The equations generally describe complex shapes within the data range, but are often not accurate outside the range of fitted data.

17. Plot of da/dN versus ΔK_{eff} for Ti-6Al-4V (ELI,MA) in 1.0% NaCl and moist air for a stress ratio of 0.4, a frequency of 5 Hz, and an LT orientation. Notice the transition points in the power law da/dN versus ΔK segments based on an approximation with linear segments. While the various wide-range da/dN-ΔK relationships are reasonable for engineering life prediction, they may not sufficiently preserve information that is important for mechanistic studies. Since these fitting equations are not physically based, they may not describe complex da/dN dependencies on ΔK, particularly of the "power-law transition type" typical of environmental FCP in titanium alloys.

18. Summary of the method proposed to interpolate trends in environmental fatigue behavior using an approach similar to that reported by Haritos et al. Trends are interpolated by relating equation constants to load-time characteristics using empirical relationships.

The forms of these relationships are selected so that they are defined for allowable ranges of load characteristics. As future work, these functions will be altered to reflect the complex and interactive effects of the variables on da/dN.

19. Summary of equations used to interpolate equation constants based on load characteristics. The load characteristics are stress ratio, hold time and frequency. The form of the interpolation equation depends on the number of data sets fit to a crack growth rate equation, and the form of the basic crack growth rate equation.

20. Fitted (top two figures) and interpolated (bottom left plot) data for Ti-6Al-4V in a 3.5% NaCl solution, using the Forman Equation with closure, and fitting the constants C, n, p, and q. The effect of frequency on the curves is summarized by the figure in the bottom right of the page. The curves show the frequency "crossover" effect reported by Dawson and Pelloux for $\alpha + \beta$ titanium alloys in passivating electrolytes. (The data in these figures were reported in: D.B. Dawson and R.M. Pelloux, Metall. Trans. A., Vol. 5A, pp. 723-731 (1974).)

21. Fitted and interpolated data for Ti-6Al-4V in a 3.5% NaCl solution, using the Forman Equation without closure and fitting the constants C, n, p, and q.

22. Fitted and interpolated data for Ti-6Al-4V in a 3.5% NaCl solution, using the Hyperbolic Sine Equation.

23. Fitted and interpolated data for Ti-6Al-4V in a 3.5% NaCl solution, using the Sigmoidal Equation.

24. Conclusions for the empirical/interpolative model. The regression subroutines in the empirical/interpolative model are accurate when bench marked against FLAGRO and results published by Haritos. All of the crack growth rate equations are able to fit da/dN data with accuracy inside the range of data. All of the equations may be able to interpolate trends in fatigue data when the frequency where data are interpolated is within the range for which data are entered. Additional work is, however, required to develop physically-based interpolation equations.

25. Summary of future work, including generating corrosion fatigue data for Ti-6Al-4V in an aqueous chloride environment. These data must be analyzed so that a physical understanding of time-cycle dependent environmental fatigue crack propagation can be gained and coupled with improving the logarithmic assumptions which relate equation constants to load-cycle characteristics.

Computer Modeling the Fatigue Crack Growth Rate Behavior of Metals in Corrosive Environments

Edward Richey and Richard P. Gangloff

LA^{2}ST Program Review

NASA Langley Research Center

July 25-26, 1994

Presentation Outline

I. Objective

II. Data Collection and Preparation

III. Linear Superposition Model
   A. Summary
   B. Results

IV. Interpolative Model
   A. Crack Growth Rate Equations
   B. Computer Modeling Program / Comparison to FLAGRO
   C. Testing and Results
      1. Bench Marking Stand-Alone Program
      2. Ability of Program to Fit da/dN Versus ΔK Data
      3. Ability of Model to Interpolate Time - Cycle - Dependent Fatigue Behavior

V. Summary and Conclusions

Objective

Develop an effective method for estimating environmental effects on fatigue crack propagation rates in metals for use in damage tolerant codes such as NASA FLAGRO.

Current Work

- Develop method to electronically read data from literature graphs.
- Implement Wei and Landes linear superposition method in a stand-alone computer program.
- Test reliability of the superposition method in predicting fatigue crack propagation rates for metals in corrosive environments.
- Develop a curve-fitting based interpolative computer modeling program, extending approach used in FLAGRO.
- Test accuracy of the interpolative model in estimating the fatigue behavior of Ti-6Al-4V in 3.5% NaCl solution.
- Couple three programs into single PC based program.

Program Disk

- Programs available in executable form.
- Source code included on program disk.
- Menu system developed to run programs.
- Discussed in *Computer Modeling the Fatigue Crack Growth Rate Behavior of Metals in Corrosive Environments* (NASA-CR to be published).

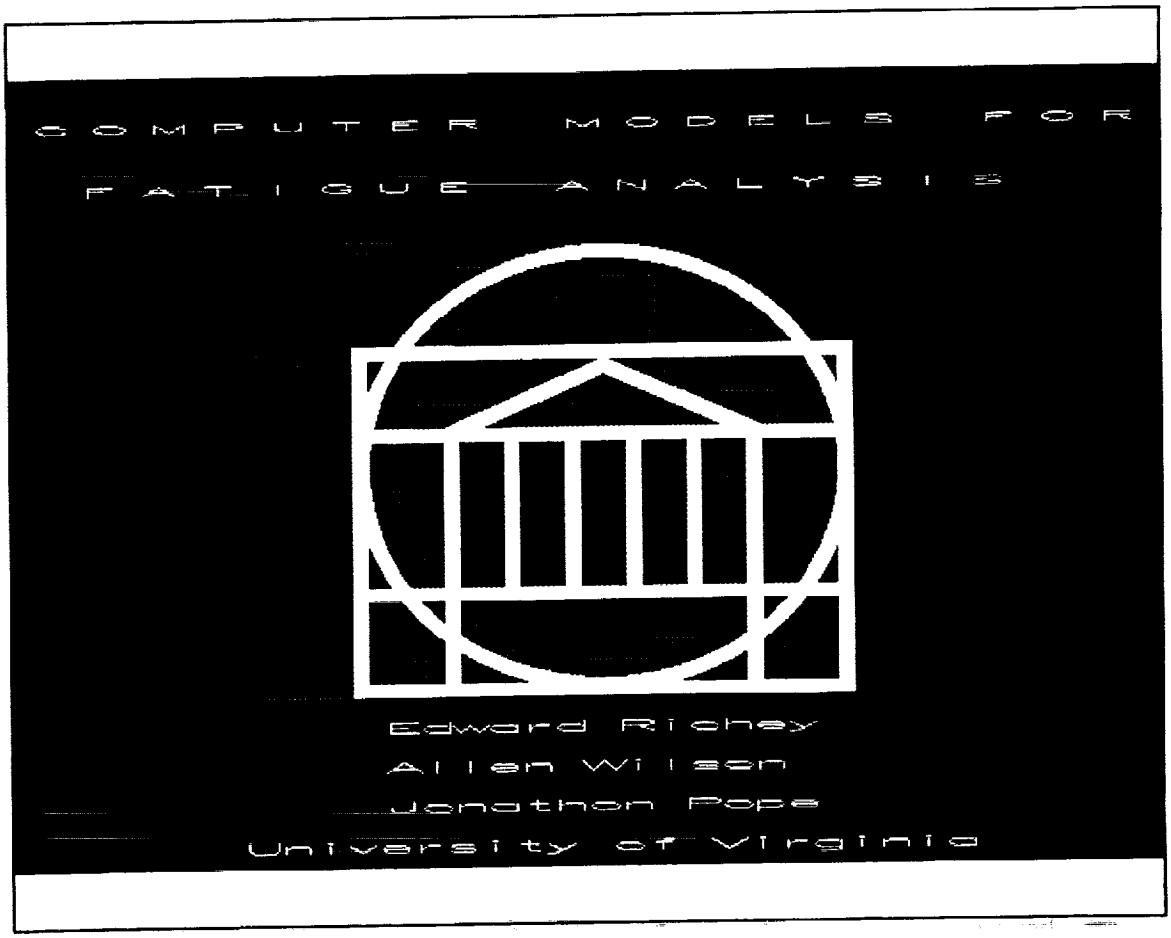

Data Collection and Preparation (Jonathan Pope)

- A method was developed to digitize fatigue crack propagation kinetics data.
- The method developed is specific to the Numonics 2400 Digitablet and is comparable to commercially available software products such as Digimatic™.
- The file produced by the Numonics 2400 Digitablet is processed with the FORTRAN program DIGITIZE.EXE, which produces accurate sets of fatigue data.
- An error analysis was performed on the complete process of digitizing and transforming a set of data. The largest average error in any test was 2.1%, while the smallest was 0.10%
- Errors are negligible when compared to the typical uncertainty associated with laboratory testing.

Linear Superposition Model (Allen Wilson)

- The Wei and Landes method of linear superposition has been implemented in a FORTRAN program.

- The program incorporates :
  - $(da/dN)_{Mechanical}$
  - da/dt(K)
  - K(t)

  to predict the effects of :
  - ΔK
  - Stress ratio (R)
  - Frequency of the applied load (f)
  - Hold time of the applied load (τ)
  - Loading wave form

  on environmental fatigue.

- The method is reliable only for limited cases where environment strongly affects subcritical crack growth. Such alloys are often not selected for applications.

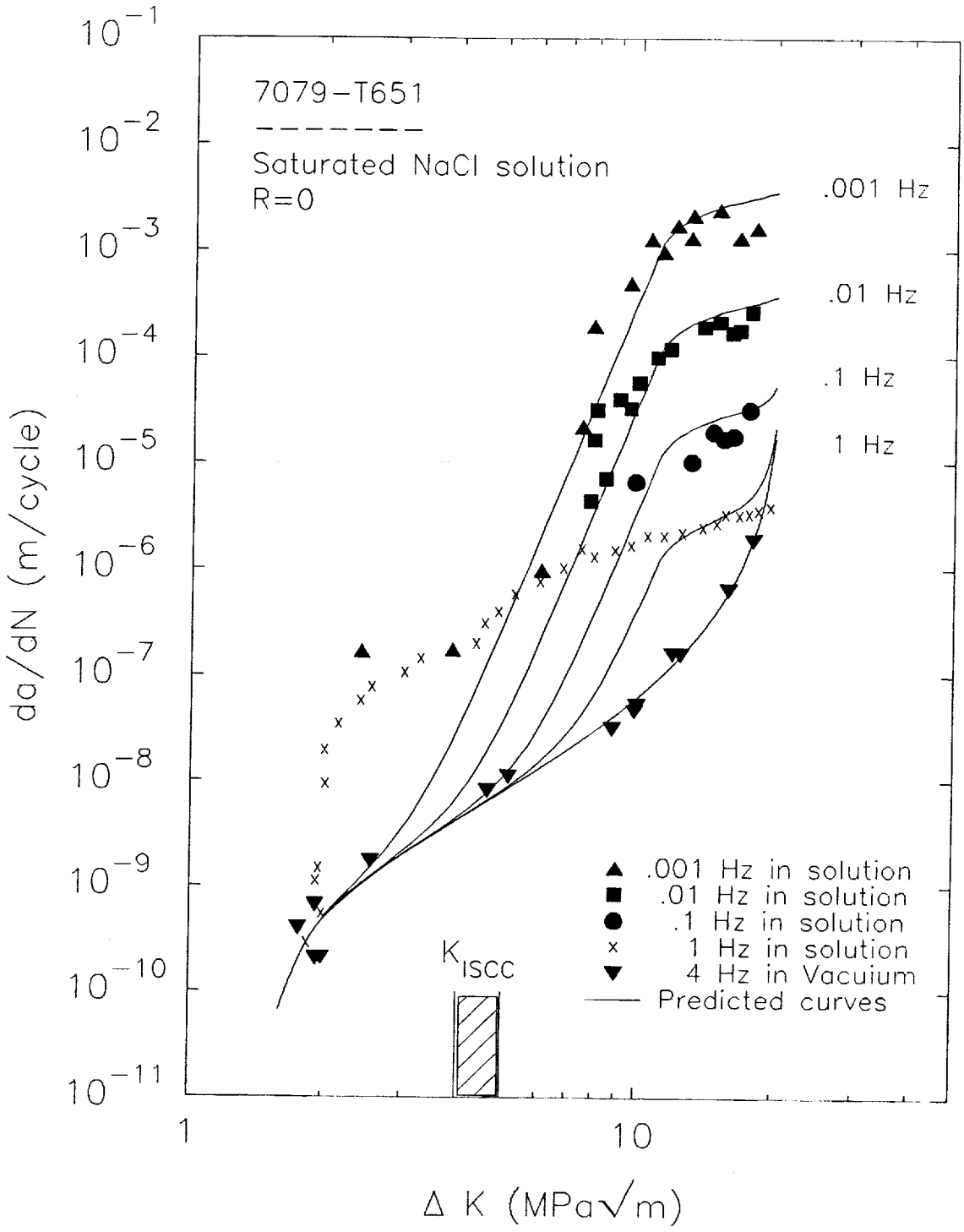
7079-T651
Saturated NaCl solution
R=0
.001 Hz
.01 Hz
.1 Hz
1 Hz
.001 Hz in solution
.01 Hz in solution
.1 Hz in solution
1 Hz in solution
4 Hz in Vacuum
Predicted curves
K_{ISCC}
da/dN (m/cycle)
10^{-1}
10^{-2}
10^{-3}
10^{-4}
10^{-5}
10^{-6}
10^{-7}
10^{-8}
10^{-9}
10^{-10}
10^{-11}
1
10
Δ K (MPa√m)

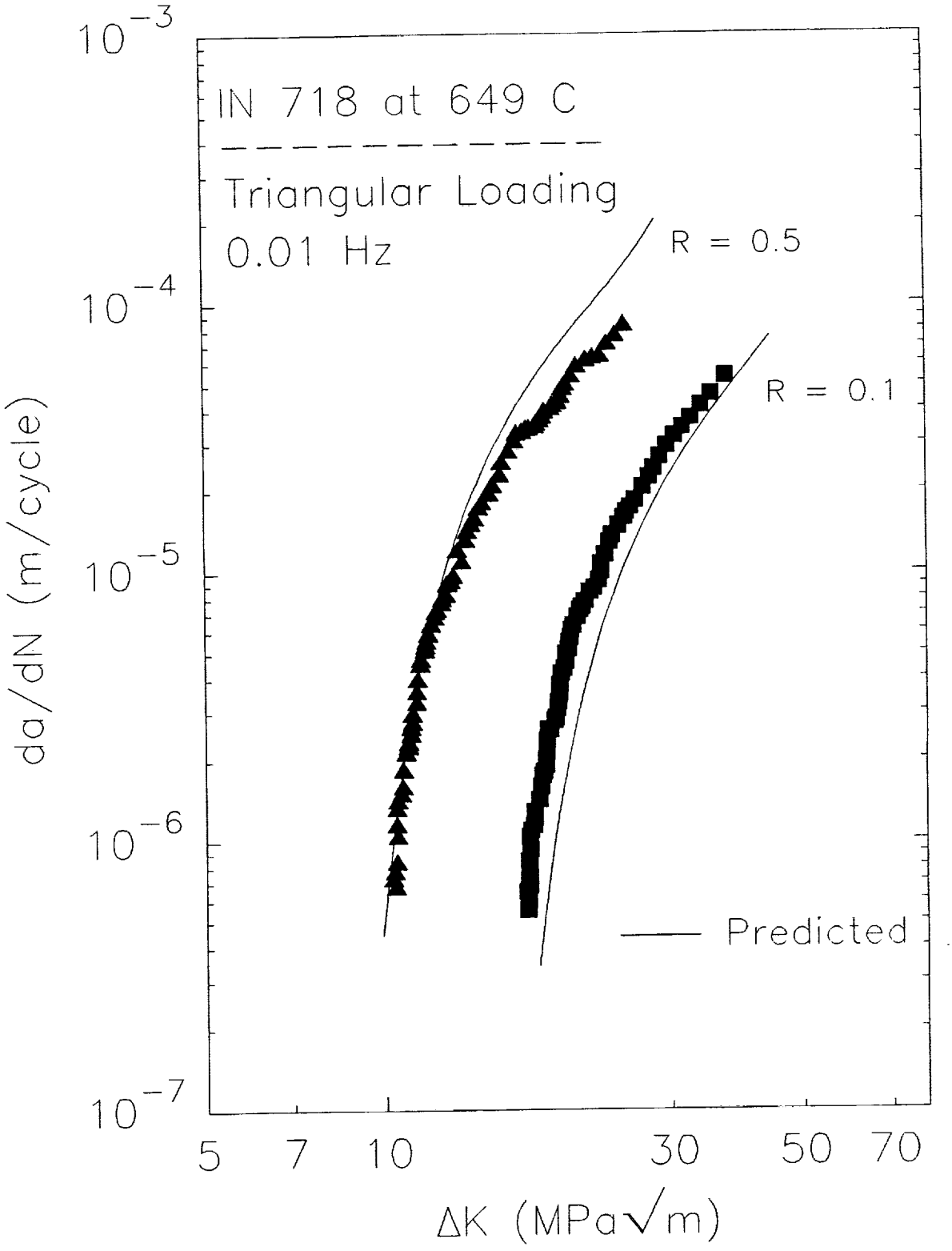
IN 718 at 649 C
Triangular Loading
0.01 Hz
R = 0.5
R = 0.1
Predicted
da/dN (m/cycle)
ΔK (MPa√m)
10^-3
10^-4
10^-5
10^-6
10^-7
5
7
10
30
50
70

Crack Growth Rate Equations

- **Forman With Closure**

$$\frac{da}{dN} = \frac{C\,(1-f)^n\,\Delta K^n \left(1 - \frac{\Delta K_{th}}{\Delta K}\right)^p}{(1-R)^n \left(1 - \frac{\Delta K}{(1-R)K_C}\right)^q}$$

- **Forman Without Closure**

$$\frac{da}{dN} = \frac{C\,\Delta K^n\,(1-R)^m \left(1 - \frac{\Delta K_{th}}{\Delta K}\right)^p}{\left(1 - R - \frac{\Delta K}{K_C}\right)^q}$$

- **Paris**

$$\frac{da}{dN} = C\,\Delta K^n$$

- **Hyperbolic Sine**

$$\log\frac{da}{dN} = C_1 \sinh\left(C_2\left[\log(\Delta K) + C_3\right]\right) + C_4$$

- **Sigmoidal**

$$\frac{da}{dN} = e^B \left(\frac{\Delta K}{\Delta K_{th}}\right)^P \left[\ln\left(\frac{\Delta K}{\Delta K_{th}}\right)\right]^Q \left[\ln\left(\frac{\Delta K_C}{\Delta K}\right)\right]^D$$

Description of Interpolative Model and Comparison to NASA FLAGRO Program

- The interpolative modeling program uses material constants available with the NASA FLAGRO program.
- Interpolative model allows user to fit any combination of equation constants to da/dN versus ΔK data.
- The interpolative model allows the user to hold K_{max} or K_{min} constant for a data set instead of the stress ratio.
- Interpolative model contains an option to optimize the values of ΔK_{th} and K_C using a cubic equation.
- Coefficient of determination is calculated for every data set fit to a crack growth rate equation.
- Confidence interval estimates are calculated for the fitted equation constants.

Bench Marking Of Interpolative Model

- Linear least squares regression subroutines in the interpolative model were bench marked against FLAGRO.

- Subroutines used in interpolative model yielded same result as FLAGRO when fitting data to the Forman Equation with closure.

- Non-linear least squares algorithm was bench marked against results published by Haritos for the Hyperbolic Sine Equation. Values selected by interpolative model yielded a better fit based on the Coefficients of Determination.

Forman Equation With Closure

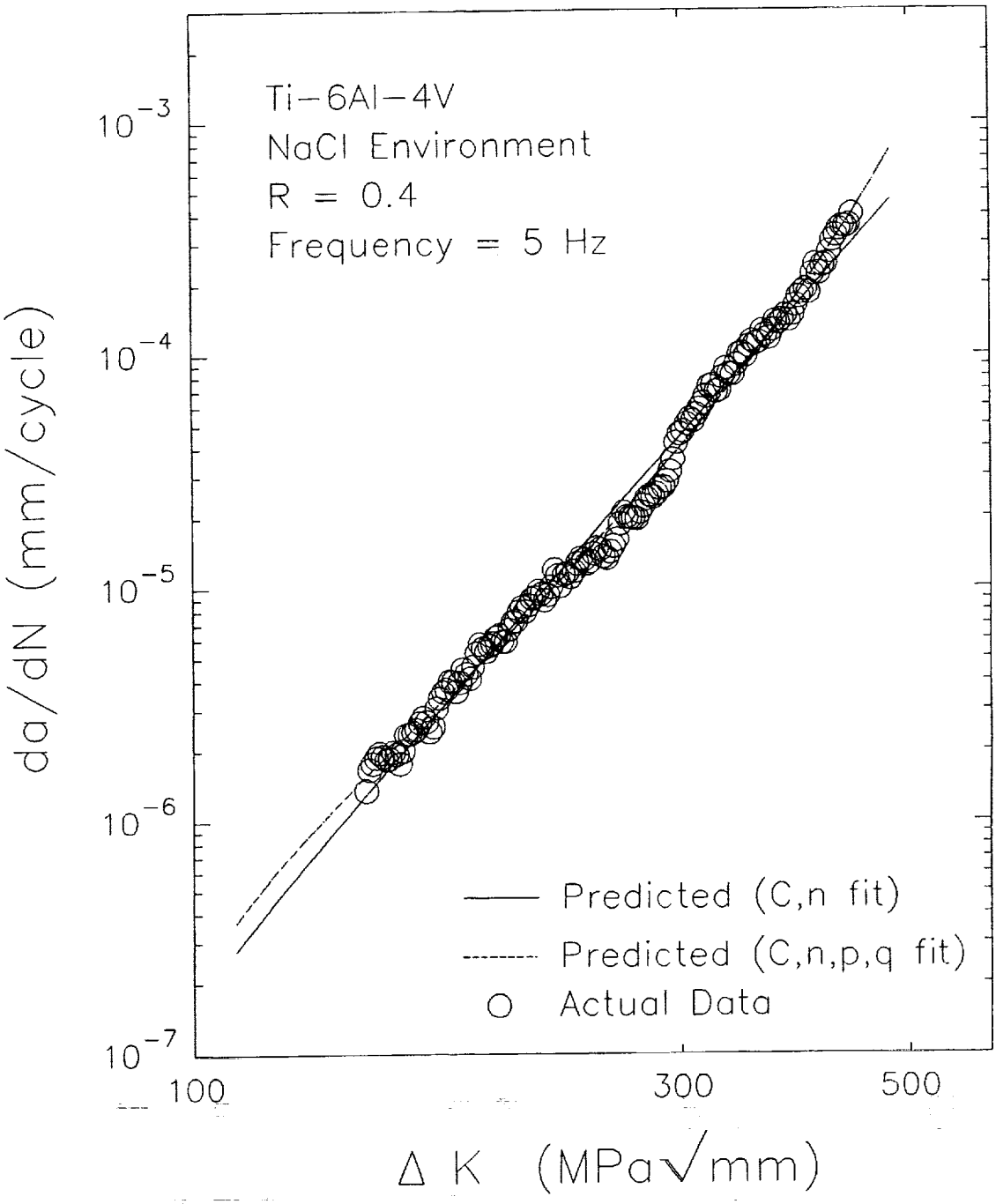

Forman Equation Without Closure

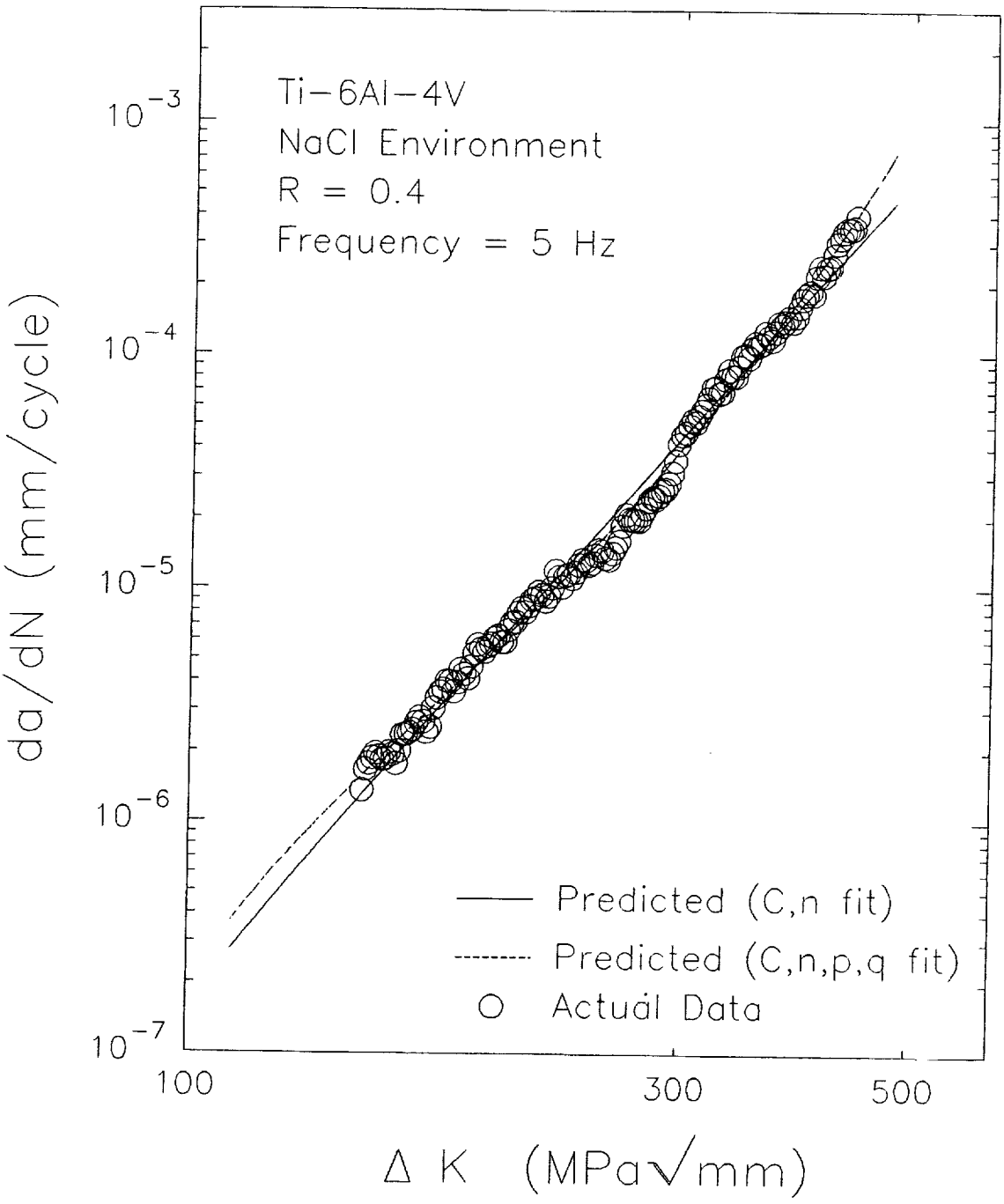

Hyperbolic Sine Equation

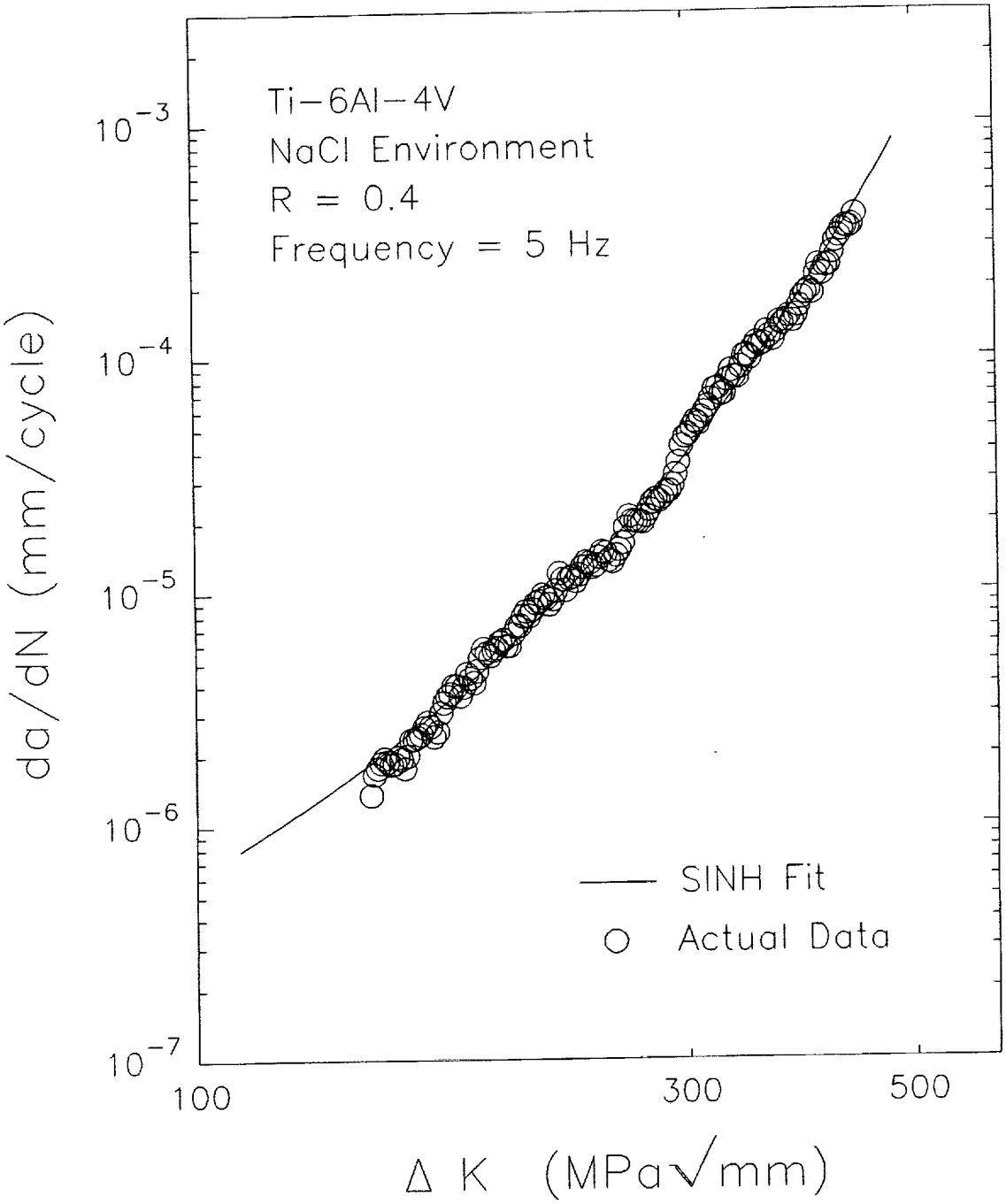

Sigmoidal Equation

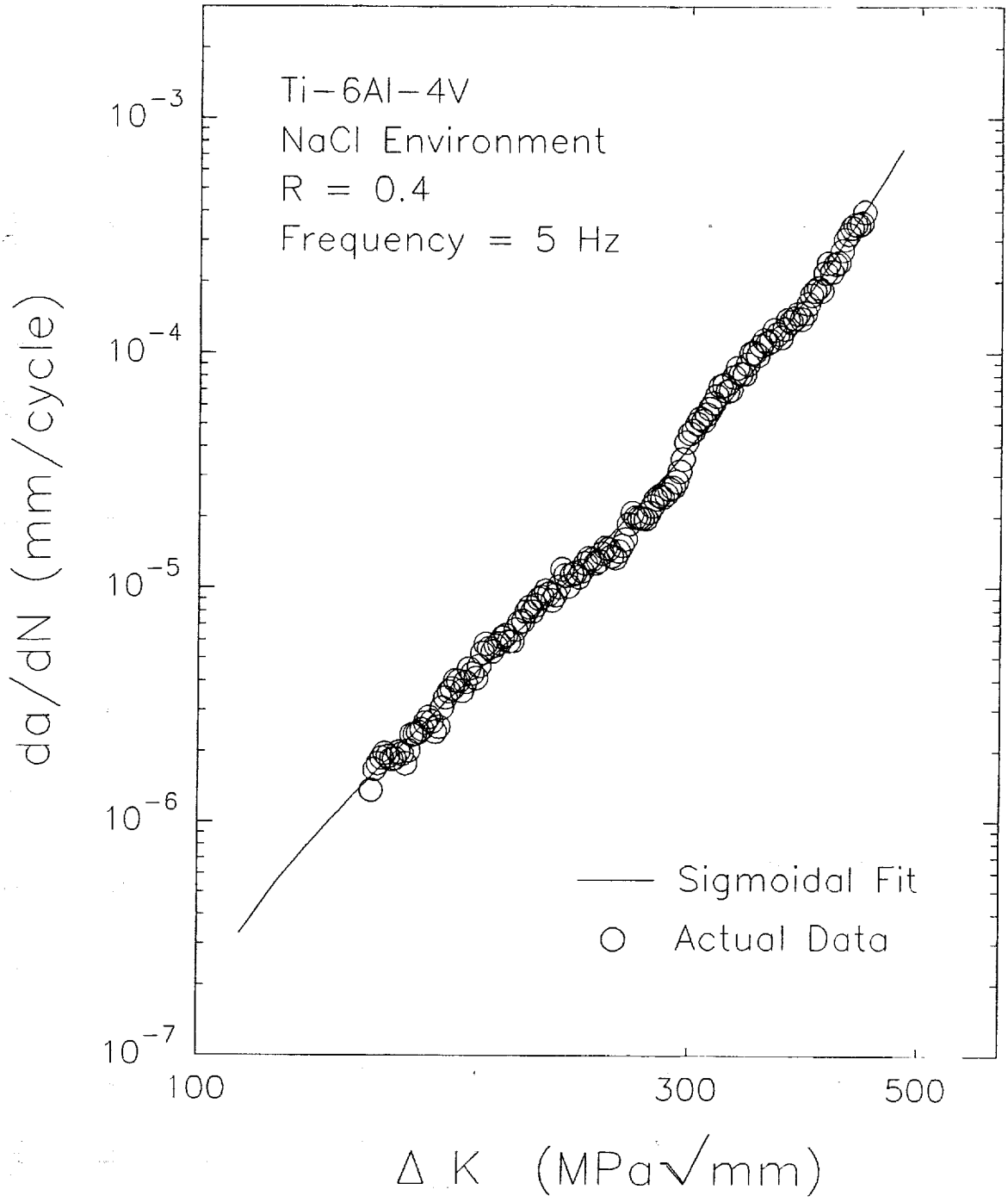

Coefficients of Determination

Equation Type	Parameters Fit	Environment	Coefficient	Average
Forman (with closure)	C, n, p, q	Air	0.9916	0.9735
		1.0% NaCl	0.9554	
Forman (no closure)	C, n, p, q	Air	0.9916	0.9735
		1.0% NaCl	0.9554	
Sigmoidal	B, P, Q, D	Air	0.9916	0.9730
		1.0% NaCl	0.9543	
Hyperbolic Sine	C_2, C_3, C_4	Air	0.9754	0.9552
		1.0% NaCl	0.9349	

- Forman Equation yielded "best" fit for all data tested.
- Equations can describe complex shapes within the data range.
- Equation shapes are not always accurate outside data range.

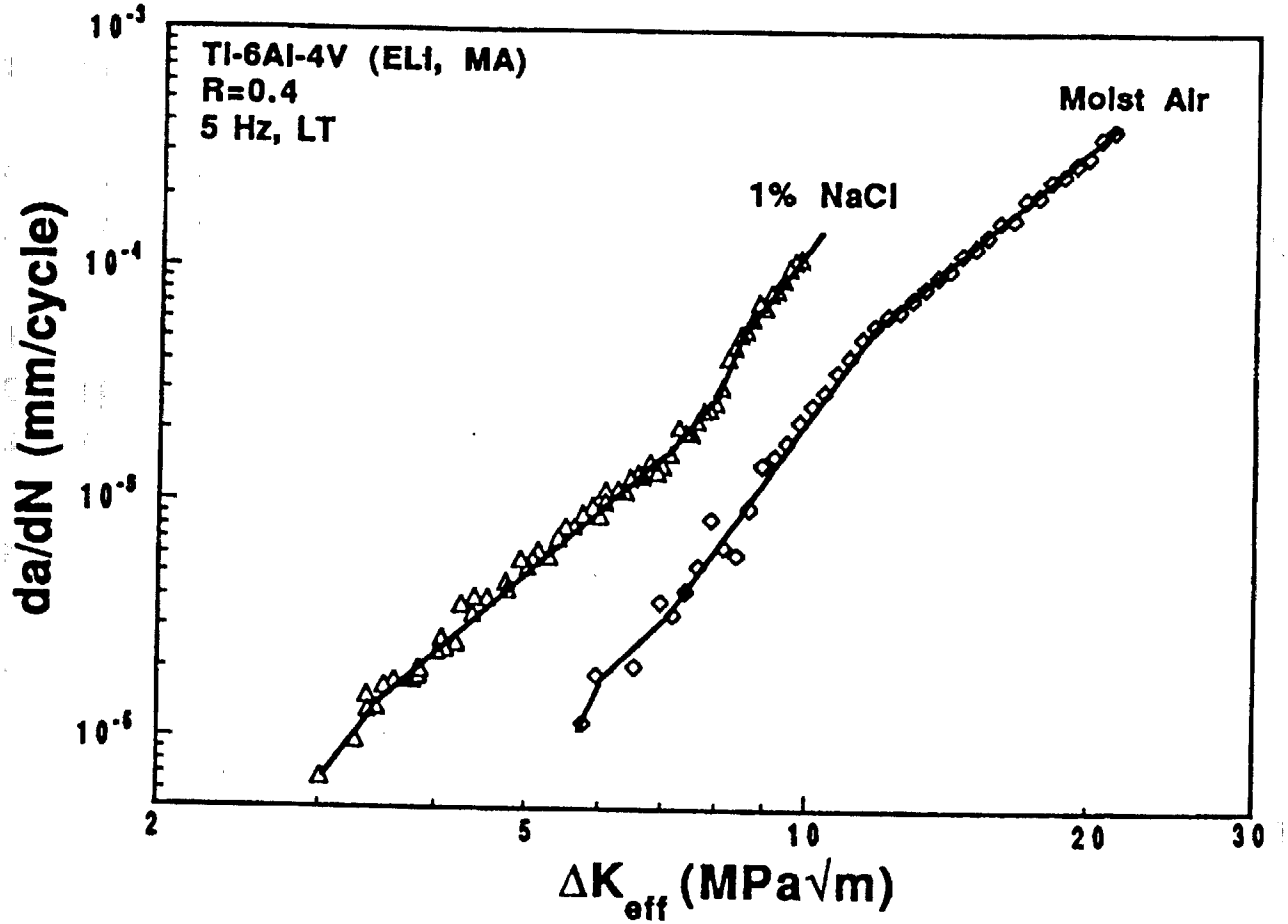
Ti-6Al-4V (ELI, MA)
R=0.4
5 Hz, LT
Moist Air
1% NaCl
da/dN (mm/cycle)
10^-3
10^-4
10^-5
10^-6
2
5
10
20
30
ΔK_eff (MPa√m)

Interpolating Equation Constants

- FLAGRO is primarily accurate for fatigue in moist air.
- Need: estimate time and load-waveform-dependent trends in fatigue behavior for corrosive environments.
- Interpolate trends by relating equation constants to load-time characteristics.
- If η is an equation constant then: $\eta = \mathrm{f}\ (f, \tau, \mathrm{R})$
  - f = frequency
  - τ = hold time
  - R = stress ratio
- Forms of relationships selected so that functions are defined for allowable values of load characteristics.
- Based on a procedure discussed by Haritos.

Functions Used to Interpolate Equation Constants

- If one data set entered :

$$\eta = a_1 \log\left[\left(\frac{1}{f}\right) + 1\right]$$

- If two data sets entered using Forman Equation:

$$\eta = a_1 \log\left[\left(\frac{1}{f}\right) + 1\right] + a_2 \log\left[\frac{\tau + 1}{0.1}\right]$$

- If two data sets entered using Paris, SINH, or Sigmoidal Equations:

$$\eta = a_1 \log\left[\left(\frac{1}{f}\right) + 1\right] + a_2 \log\left[\frac{1 - 0.1\ R}{0.1}\right]$$

- If three data sets entered:

$$\eta = a_1 \log\left[\left(\frac{1}{f}\right) + 1\right] + a_2 \log\left[\frac{1 - 0.1\ R}{0.1}\right] + a_3 \log\left[\frac{\tau + 1}{0.1}\right]$$

- If K_{max} is constant, replace log [(1-0.1R)/0.1)] with log (K_{max})

Forman Equation With Closure (C, n, p, q fit)

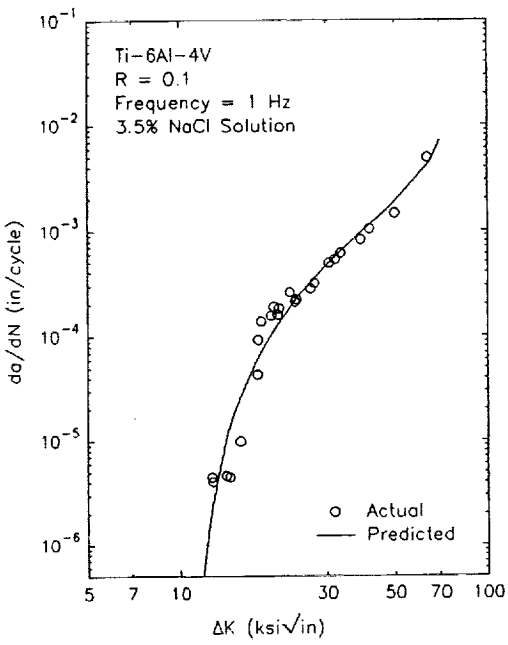

Fitted data for 1 Hz.

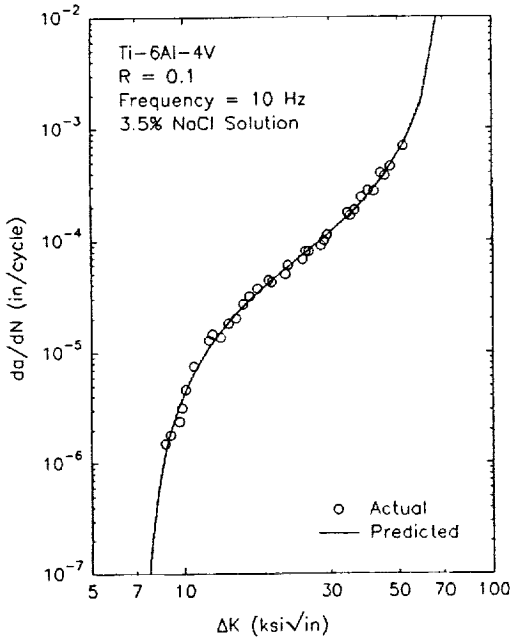

Fitted data for 10 Hz.

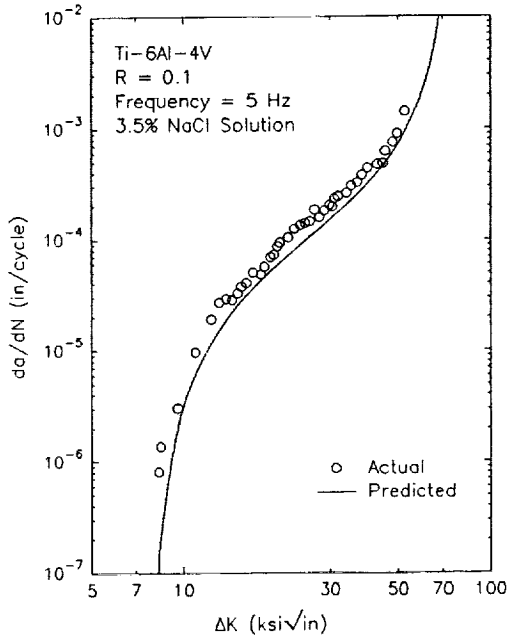

Interpolated data for 5 Hz.

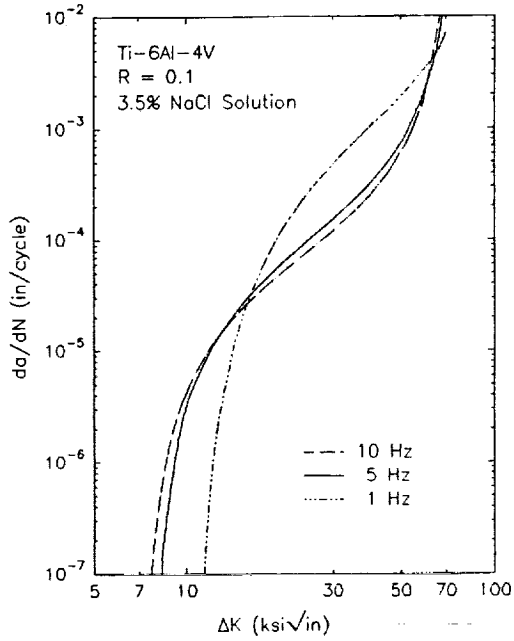

Effect of frequency.

Forman Equation Without Closure (C, n, p,q fit)

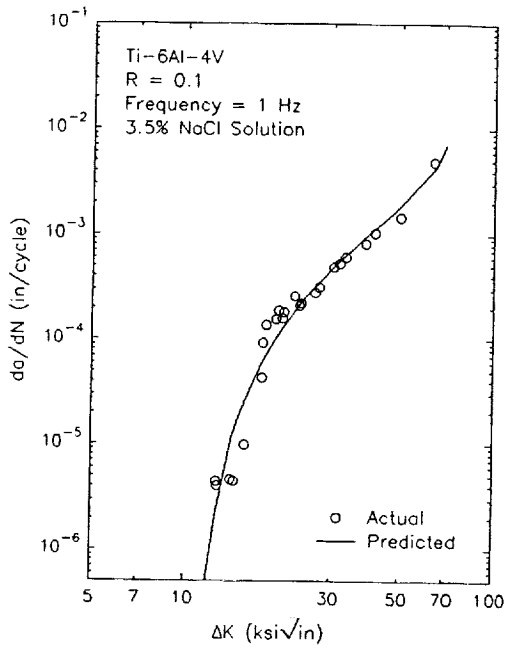

Fitted data for 1 Hz.

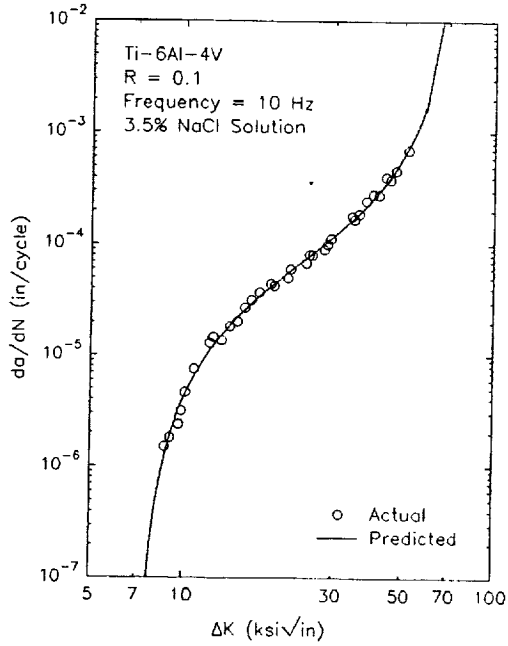

Fitted data for 10 Hz.

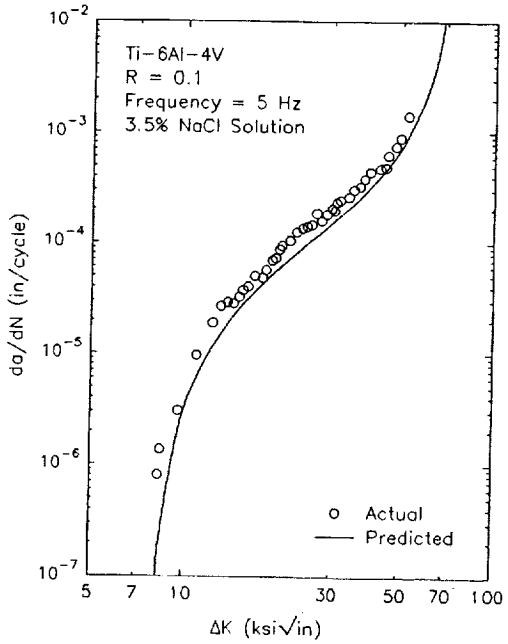

Interpolated data for 5 Hz.

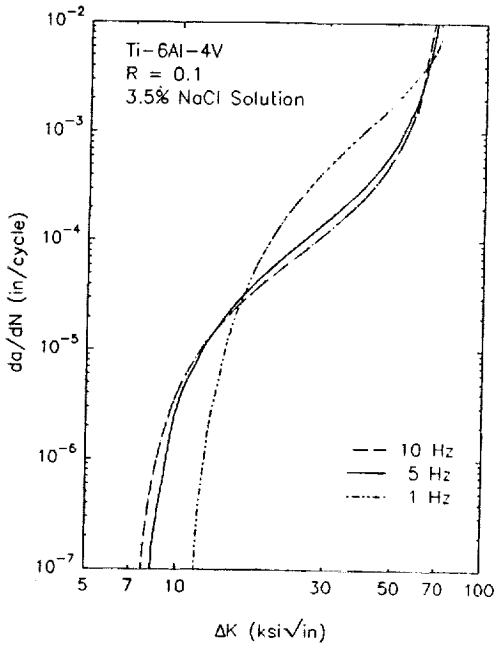

Effect of frequency.

Hyperbolic Sine Equation

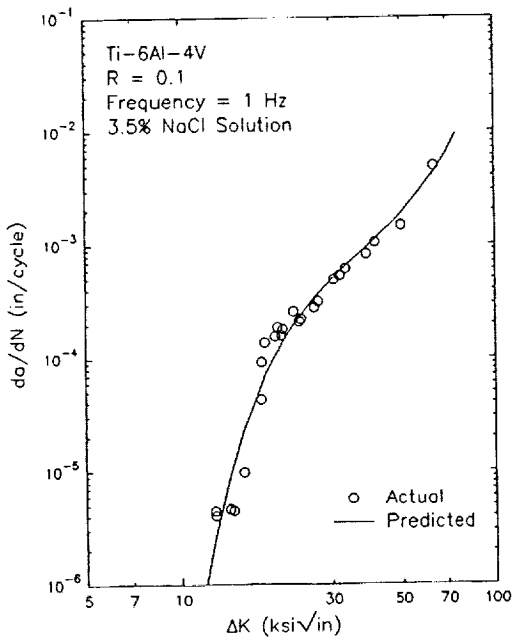

Fitted data for 1 Hz.

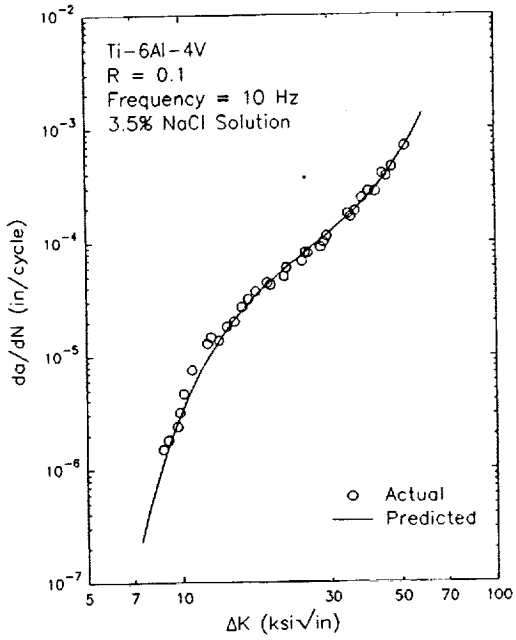

Fitted data for 10 Hz.

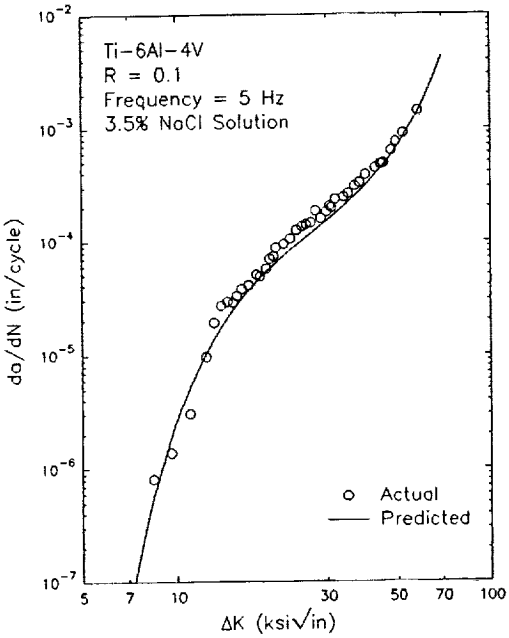

Interpolated data for 5 Hz.

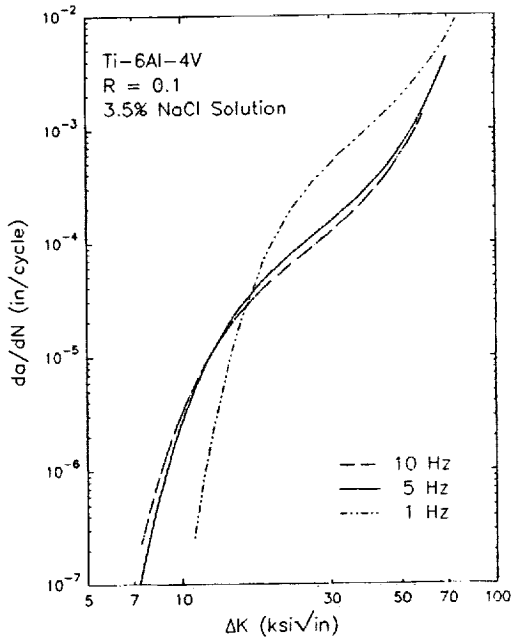

Effect of frequency.

Sigmoidal Equation

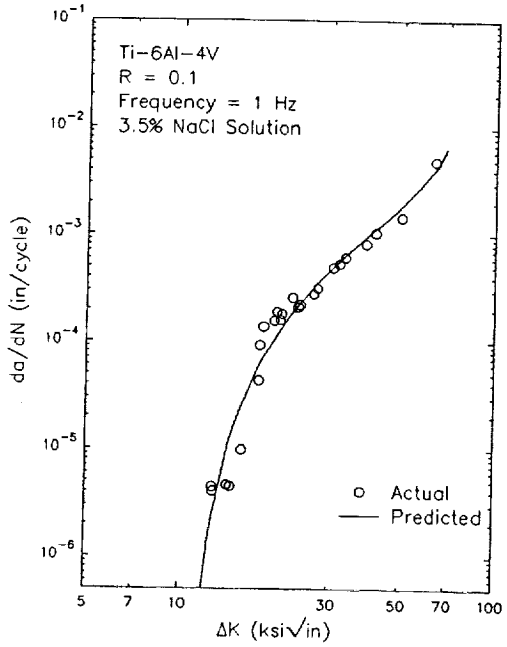

Fitted data for 1 Hz.

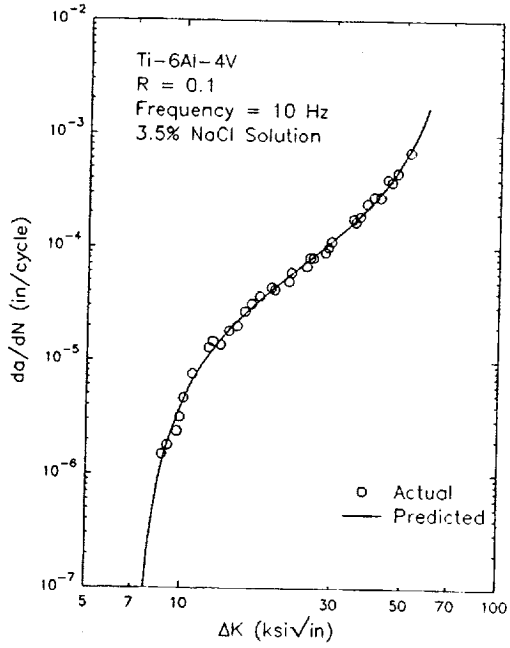

Fitted data for 10 Hz.

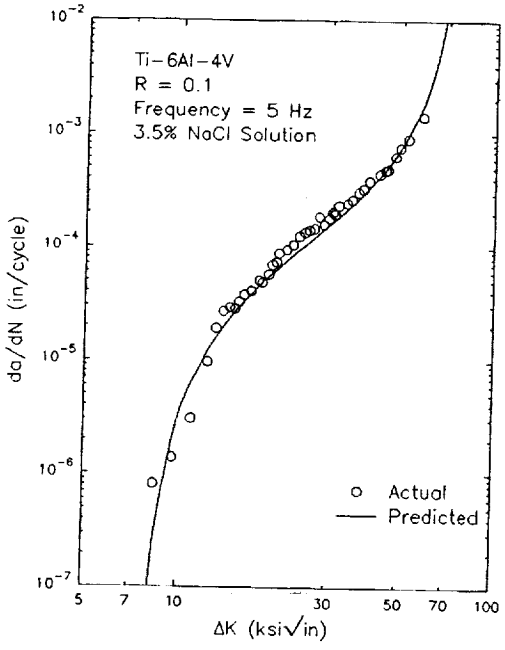

Interpolated data for 5 Hz.

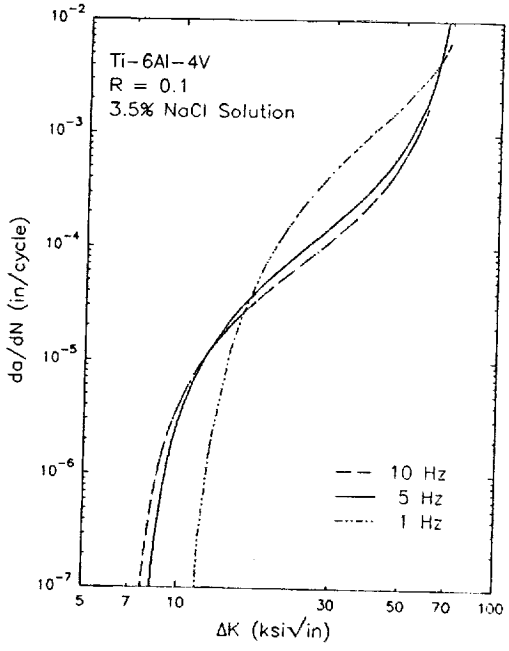

Effect of frequency.

Conclusions for the Interpolative Model

- The regression subroutines used in the interpolative modeling program were bench marked against FLAGRO and results published by Haritos. The subroutines are accurate.
- All crack growth rate equations fit da/dN data with accuracy inside the range of data. The shape is not always accurate outside the range of data.
- All crack growth rate equations were able to interpolate trends in da/dN versus ΔK when the frequency where data were interpolated fell within the range for which data were entered.
- The data tested displayed the frequency "crossover" effect. The interpolated data also displayed this effect.
- The model accurately shows that ΔK_{th} increases as frequency decreases. This is a result of the functions which relate equation constants to load characteristics.

Future Work

- Generate corrosion fatigue data for Ti-6Al-4V (ELI) in aqueous chloride environment.

- Determine the effects of frequency, hold time, rise time and stress ratio on fatigue crack propagation.

- Gain a physical understanding of time-cycle dependent environmental fatigue crack propagation.

- Improve logarithmic assumptions which relate equation constants to load - cycle characteristics.

- Finish MS thesis by 1/95.

APPENDIX I: GRANT PUBLICATIONS (January 1 to June 30, 1994)

1. Edward Richey, III, A.W. Wilson, J.M. Pope, and R.P. Gangloff, "Computer Modeling the Fatigue Crack Growth Rate Behavior of Metals in Corrosive Environments", NASA CR, NASA-Langley Research Center, press (1994).

2. M.E. Mason and R.P. Gangloff, "Modeling Time-Dependent Corrosion Fatigue Crack Propagation in 7000 Series Aluminum Alloys", in Proceedings of the International Symposium on Advanced Structural Integrity Methods for Airframe Durability and Damage Tolerance, C.E. Harris, et al., eds., NASA-Langley Research Center, Hampton, VA, in review (1994).

3. R.P. Gangloff, "Corrosion Fatigue Cracking", in Manual on Corrosion Tests: Application and Interpretation, R. Baboian, ed., ASTM, Philadelphia, PA, in review (1994).

4. S.S. Kim and R.P. Gangloff, "Localized Deformation Control of Elevated Temperature Fracture in Submicron Grain Aluminum with Dispersoids", Materials Science and Engineering A, in review (1994).

5. F.D. Wall and G.E. Stoner, "Electrochemical Characterization and Occluded Environment Analysis of Localized Corrosion in Advanced Aluminum Alloys", Paper No. 546, Corrosion 94, NACE, Houston, TX, 1994.

6. F.D. Wall and G.E. Stoner, "Critical Electrochemical Potentials Relating to the Rapid Environmentally Assisted Cracking of Advanced Aluminum Alloys", Proceedings of the 1994 Conference on Advanced Earth to Orbit Propulsion Technologies, NASA-Marshall Space Center, Huntsville, Alabama, 1994.

7. M.T. Lyttle and J.A. Wert, "Simulative Modeling of Continuous Recrystallization of Aluminum Alloys", in Advances in Hot Deformation Textures and Microstructures, J.J. Jonas, T.R. Bieler and K.J. Bowman, eds., TMS-AIME, Warrendale, PA, pp. 373-383 (1994).

8. S.T. Pride, J.R. Scully and J.L. Hudson, "Metastable Pitting of Aluminum and Criteria for the Transition to Stable Pit Growth," Journal of the Electrochemical Society, in press (1994).

9. S.T. Pride, J.R. Scully and J.L. Hudson, "Analysis of Electrochemical Noise from Metastable Pitting in Al, Aged Al-2%Cu and AA 2024-T3, ASTM STP," in Electrochemical Noise Methods in Corrosion, ASTM, Philadelphia, PA, in review (1994).

APPENDIX II: GRANT PRESENTATIONS (January 1 to June 30, 1994)

1. M.J. Haynes and R.P. Gangloff, "Elevated Temperature Fracture of RS/PM AA8009 and Wrought AA2519 + Ag", NASA-UVa HSCT Program Review, Hampton, VA, January, 1994.

2. F.D. Wall and G.E. Stoner, "Electrochemical Characterization and Occluded Environment Analysis of Localized Corrosion in Advanced Aluminum Alloys", Corrosion '94, Baltimore, Maryland, March, 1994.

3. R.P. Gangloff and M.E. Mason, "Modeling Environmental Effects on Fatigue Crack Propagation in Light Aerospace Alloys", FAA/NASA International Symposium on Advanced Structural Integrity Methods for Airframe Durability and Damage Tolerance, Hampton, VA, May, 1994.

4. F.D. Wall and G.E. Stoner, "Critical Electrochemical Potentials Relating to the Rapid Environmentally Assisted Cracking of Advanced Aluminum Alloys", Conference on Advanced Earth to Orbit Propulsion Technologies, Huntsville, Alabama, May, 1994.

5. M.T. Lyttle and J.A. Wert, "Simulative Modeling of Continuous Recrystallization of Aluminum Alloys", Materials Week, '93, Pittsburgh, PA, October, 1993.

6. J.A. Wert, "Processing of Aluminum Alloys for Superplastic Forming", Risø National Laboratory, Roskilde, Denmark, June, 1994.

7. J.A. Wert, "Representing and Using Boundary Misorientation Data", Risø National Laboratory, Roskilde, Denmark, June, 1994.

8. S.W. Smith and J.R. Scully, "High Resolution Thermal Desorption Analysis of Internal Hydrogen in Aluminum Alloys", CORROSION '94, Baltimore, Maryland, March, 1994.

9. S.T. Pride, J.R. Scully and J.L. Hudson, "Analysis of Electrochemical Noise from Metastable Pitting in Al, Aged Al-2%Cu and AA 2024-T3," 1st International Symposium on Electrochemical Noise Measurement for Corrosion Application, Montreal, May, 1994.

APPENDIX III: GRANT PROGRESS REPORTS (January, 1988 to December, 1993)

1. R.P. Gangloff, G.E. Stoner and R.E. Swanson, "Environment Assisted Degradation Mechanisms in Al-Li Alloys", University of Virginia, Report No. UVA/528266/MS88/101, January, 1988.

2. R.P. Gangloff, G.E. Stoner and R.E. Swanson, "Environment Assisted Degradation Mechanisms in Advanced Light Metals", University of Virginia, Report No. UVA/528266/MS88/102, June, 1988.

3. R.P. Gangloff, G.E. Stoner and R.E. Swanson, "Environment Assisted Degradation Mechanisms in Advanced Light Metals", University of Virginia, Report No. UVA/528266/MS89/103, January, 1989.

4. R.P. Gangloff, "NASA-UVa Light Aerospace Alloy and Structures Technology Program", UVa Report No. UVA/528266/MS90/104, August, 1989.

5. R.P. Gangloff, "NASA-UVa Light Aerospace Alloy and Structures Technology Program", UVa Report No. UVA/528266/MS90/105, December, 1989.

6. R.P. Gangloff, "NASA-UVa Light Aerospace Alloy and Structures Technology Program", UVa Report No. UVA/528266/MS90/106, June, 1990.

7. R.P. Gangloff, "NASA-UVa Light Aerospace Alloy and Structures Technology Program", UVa Report No. UVA/528266/MS91/107, January, 1991.

8. R.P. Gangloff, "NASA-UVa Light Aerospace Alloy and Structures Technology Program", UVa Report No. UVA/528266/MS91/108, July, 1991.

9. R.P. Gangloff, "NASA-UVa Light Aerospace Alloy and Structures Technology Program", UVa Report No. UVA/528266/MS92/109, January, 1992.

10. R.P. Gangloff, "NASA-UVa Light Aerospace Alloy and Structures Technology Program", UVa Report No. UVA/528266/MS93/111, July, 1992.

11. R.P. Gangloff, "NASA-UVa Light Aerospace Alloy and Structures Technology Program", UVa Report No. UVA/528266/MSE93/112, March, 1993.

12. R.P. Gangloff, "NASA-UVa Light Aerospace Alloy and Structures Technology Program", UVa Report No. UVA/528266/MSE93/113, July, 1993.

13. R.P. Gangloff, "NASA-UVa Light Aerospace Alloy and Structures Technology Program", UVa Report No. UVA/528266/MSE93/114, March, 1994.

APPENDIX IV: GRANT REVIEW MEETING AGENDA

AGENDA

FIFTH ANNUAL NASA-UVa LA^{2}ST MEETING

Room 256, Building 1205
Light Alloys Research Laboratory
NASA-Langley Research Center
Hampton, Virginia

Day 1: Monday, July 25, 1994

1:00-1:15 pm	Dennis L. Dicus: Welcome. Richard P. Gangloff: LA^{2}ST program progress.
1:15-2:00	"Hydrogen Interactions in Aluminum-Lithium Alloys"; Stephen W. Smith and J.R. Scully.
2:00-2:45	"Metastable Pitting of Aluminum Alloys in Halide Solutions"; Sheldon Pride and J.R. Scully.
2:45-3:00	Break
3:00-3:30	"Modeling Environmental Fatigue Crack Propagation for NASA-FLAGRO"; Edward Richey III, Alan Wilson, Jonathan Pope and R.P. Gangloff.
3:30-4:00	"Time-Dependent Environmental Fatigue Crack Propagation in AA7075"; Mark E. Mason and R.P. Gangloff.
4:00-4:45	"Mechanisms of Localized Corrosion in Alloys 2090 and 2095"; F. Douglas Wall and G.E. Stoner.
6:30	Dinner

Day 2: Tuesday, July 26, 1994

8:15-9:00 am	"Effects of Texture and Microstructure on the Anisotropic Yield Strength of Wide Panel Aluminum Alloy Extrusions"; Mark T. Lyttle and John A. Wert
9:00-9:45	"Al-Si-Ge Alloy Development"; Holger Koenigsmann and Edgar A. Starke, Jr.
9:45-10:00	Break
10:00-10:45	"Elevated Temperature Fracture of AA2519 with Ag"; Michael J. Haynes and R.P. Gangloff.
10:45-11:15	"Effects of Temperature and Aging Condition on the Fracture Toughness of AA2095"; Cynthia L. Lach and R.P. Gangloff.
11:15-12:00	"Effects of Temperature and Microstructure on the Fracture Toughness of Alloys 2090 and 2090+In"; John A. Wagner and R.P. Gangloff.
12:00-1:15 pm	Lunch
1:15-2:15	Group discussion between UVa and LaRC participants on the health of the LA^{2}ST Grant, the LA^{2}ST-HSCT program merger, and directions for future NASA/UVa research.
2:15--	Individual discussions between UVa investigators and LaRC technical contacts on the direction and finances for the 1995 renewal. UVa faculty should schedule these meetings as needed.

DISTRIBUTION LIST

1-4	Mr. D. L. Dicus Contract Monitor Metallic Materials Branch, MS 188A NASA Langley Research Center Hampton, VA 23665
5-6*	NASA Scientific and Technical Information Facility P. O. Box 8757 Baltimore/Washington International Airport Baltimore, MD 21240
7	Mr. Neil Price, Grants Officer MS 126 NASA Langley Research Center Hampton, VA 23665
8	Dr. Darrel R. Tenney Materials Division NASA Langley Research Center Hampton, VA 23665
9	Dr. Charles E. Harris Mechanics of Materials Branch NASA Langley Research Center Hampton, VA 23665
10	Mr. W. Barry Lisagor Metallic Materials Branch NASA Langley Research Center Hampton, VA 23665
11	Mr. T.W. Crooker Code RM NASA Headquarters Washington, DC 20546
12	Dr. Robert S. Piascik Mechanics of Materials Branch NASA Langley Research Center Hampton, VA 23665
13	Mr. W. Brewer Metallic Materials Branch, MS 188A NASA Langley Research Center Hampton, VA 23665

14 Mr. Thomas T. Bales
Metallic Materials Branch, MS 188A
NASA Langley Research Center
Hampton, VA 23665

15 Mr. John Wagner/Ms. Cynthia Lach
Metallic Materials Branch, MS 188A
NASA Langley Research Center
Hampton, VA 23665

16 Dr. William F. Bates
Lockheed Aeronautical Systems Co.
86 South Cobb Drive
Marietta, GA 30063-0648

17 Dr. Alex Cho
Reynolds Metals Co.
4th and Canal Street
Richmond, VA 23261

18 Mr. E.A. Colvin
Alcoa Technical Center
Route 780, 7th Street Road
Alcoa Center, PA 15069

19 Dr. L.M. Angers
Alcoa Technical Center
Route 780, 7th Street Road
Alcoa Center, PA 15069

20 Dr. Ravi Kahandal
McDonnell Douglas Aerospace
Mail Stop 36-90
3855 Lakewood Blvd.
Long Beach, CA 90846

21 Mr. Fred Casey
Space Transportation Systems Division
Rockwell International
Dept. 289 MC/AC56
12214 Lakewood Blvd.
Downey, CA 90241

22-23 E.A. Starke, Jr.; MS&E

24-26 R.P. Gangloff; MS&E

27 G.E. Stoner; MS&E

28 J.A. Wert; MS&E

29 J.R. Scully; MS&E

30 C.T. Herakovich; CE and AM

31-32 E.H. Pancake; Clark Hall

33 SEAS Preaward Administration Files

34 Mr. Gwyn Faile
Code ED 24
Marshall Space Flight Center
Huntsville, AL 35812

35 Mr. Brian McPherson
Code ED 24
Marshall Space Flight Center
Huntsville, AL 35812

36 Mr. William E. Quist
Boeing Aerospace and Electronics
Aerospace Group
Mail Stop GH-CJ
P.O. Box 3707
Seattle, WA 98124

37 Dr. Howard G. Nelson
NASA-Ames Research Center
EEM: 213-3
Moffett Field, CA 94035

38 Dr. R.G. Forman
Mail Code ES-5
NASA-L.B. Johnson Space Flight Center
Houston, TX 77058

39 Professor A.K. Noor
Center for Computational Structures Technology
NASA Langley Research Center
Hampton, VA 23665

40 Prof. A.K. Ghosh
Department of Materials Science and Engineering
University of Michigan
2102 Dow Building
Ann Arbor, MI 48109-2136

41 Dr. D. Ferton
Pechiney Centre de Recherches
De Voreppe
B.P. 27 -- 38340 Voreppe
FRANCE

42 Dr. John Papazian
Grumman Aerospace & Electronics
Mail Stop A02-026
Bethpage, NY 11714-3582

43 Dr. Richard Lederich
McDonnell Douglas Aircraft Company
Mail Stop 111-1041
P.O. Box 516
St. Louis, MO 36166

*One reproducible copy

Updated: July, 1994